A Deeper Focus on the Primordial Universe

Develoment of a Metamaterial-based Lenslet coupled with Kinetic Inductance Detectors for Cosmology

Thesis submitted to Cardiff University
For the degree of Doctor of Philosophy

April 2023

Mr. Thomas Gascard

First printing, April 2023

Summary

Modern cosmology is seeking to understand the mechanisms behind the Universe birth and evolution, dynamics at limiting cases of both high energy quantum physics and the theory of gravitation. Since the observation of the Cosmic Microwave Background, primordial light revealed at the Universe's creation, a technological push was made towards the precise detection of its subtle variations, especially with regards to its polarisation states. Directly or not, the scientific impact resulting from this effort is strong. Radio-antennas, optical component at the base of cosmology telescopes, are commonly used for telecommunication purposes in cars, phones, computers, etc. The detectors used in instruments for Cosmic Microwave Background observations are based on superconductors, ground technology for Magnetic Resonance Imaging or quantum-computer qubits. Metamaterials, a recent artificial media tunable to shape the light as desired, enabled microscopy at nanometric scales for instance.

This thesis presents efforts to prove the concept of the MetaL, a focal optics made of metamaterial surfaces. Details on the Cosmic Microwave Background current knowledge and considerations on future experiments are discussed. Compliance with the requirements dressed for Cosmic Microwave Background instrumentation is partly demonstrated through a full experimental characterisation of a prototyped device. Excellent optical performances, similar to an existing optics counterpart, are demonstrated in a warm setup. Further plans and preliminary results to prove the coupling with a detecting element cold are laid out.

Acknowledgements and Funding

To Michel Betremieux...
The wind rustles as a bird flies off a branch, somewhere in the marches. The peaceful silence that follows will always have your imprint in my heart.

Under rainfall or sunshine, in cold and warmth, together, even when only by mind, our lives turns into wonderful adventures. Thank you, Louise Betremieux, my partner in life, as always...

Thank you both with all my heart Corinne Gascard, my Mother, and Jacques Gascard, my Father. I could not have managed this daunting task without knowing that, somewhere, my family loved me and was proud.

My undying gratitude to Nathalie, Francois and Marie-Therese Betremieux, Marcelle Bailleul, and Jean-Pierre and Denise Béarez, who welcomed and supported me as they would their own.

Gabrielle & Maxime Chaveroche, Laura Lageard & Anthony Blanquart, Chloe Thuin, Luc Richard, Graziella Mary and Clement Lambin, for the friendship we share and cherish, the rare chemistry that only people knowing each other so well, and for so long, can create.

Leo & Kelsey Brown, here is for your friendship and attentive care in a time when it was most needed. Wyn Davies-Baptista, for your generosity and gentle encouragements. This accomplishment would never have been possible without the times we shared playing, drinking, climbing and hiking in Wales... catching a breath most needed.

Ian Veenendaal, Adam Shorock my thanks for the good times we shared together roaming Cardiff or scratching our heads on 3 hours plus boardgames, extended to Chris Woodhead, without whom I would have stayed in a cave on my own. I hope we will soon all be chilling out around a nice and traditional cup of tea again, with the correct amount of milk of course.

For showing me what being Welsh truly was about, and for your tremendous help with precision engineering parts, Chris Dodd and Julian House, I am in your debt. Christopher Dunscombe, I realise a few of your hairs must have fell off over the consequent efforts you provided in the clean rooms to fabricate the prototype samples required for this work. Thank you for your hard work and disponibility.

I am beholden to the detector team: Sam Rowe, Tom Brien, Amber Hornsby, Gethin Robson and Pete Barry, who took the little time they had to answer my questions and give a little help where they could.

Many thanks, Benjamin Beringue, for your precious help and comments on Cosmology related topics, especially regarding the systematics benchmark analysis.

Rashmikant Sudiwala, I am very appreciative of your tenacity in benevolently drilling knowledge on optical setups inside that bulky head of mine.

Alexey Shitvov, thank you for your active comments and reviews throughout this work. Your efforts and support helped putting me in the right direction when it was most needed during this work.

I am most grateful for Giampaolo Pisano's endeavour to guide me towards independence in my research on metamaterial optics while watching over my progress. Guidance extended over exquisite music suggestions. Simon Doyle, this work would be far from complete if it was not for your decisive, yet kind directions over the last couple years. Thank you both for your contributions towards my journey to become a better researcher.

Water colour paintings contained in this work are the creations and propriety of Louise Betremieux.

This work was supported in part by the Science and Technology Facilities Council [grant number ST/S00033X/1 and ST/W000830/1] and in part by NASA [grant/cooperative agreement number NNX17AE85G].

List of Publications

T. Gascard, G. Pisano, S. Doyle, A. Shitvov, J. Austermann, J. Beall, J. Hubmayr, B. Raymond, N. Halverson, G. Jaehnig, C. M. McKenney, and A. Suzuki, "Design and experimental investigation of a planar metamaterial silicon-based lenslet," in Millimeter, Submillimeter, and Far-Infrared Detectors and Instrumentation for Astronomy X (SPIE, 2020), Vol. 11453, pp. 59–68, DOI: 10.1117/12.2562692

T. Gascard, G. Pisano, S. Doyle, A. Shitvov, P. Barry, T. L. R. Brien, and C. Dunscombe, "Pixel design for FIR/mm/submm astronomy constituted of a set of antenna-coupled superconducting detectors feeding a metamaterial-based lenslet," in Millimeter, Submillimeter, and Far-Infrared Detectors and Instrumentation for Astronomy XI (SPIE, 2022), Vol. 12190, pp. 643–654, DOI: 10.1117/12.2627848

T. Gascard, G. Pisano, S. Doyle, J. Thompson, A. Shitvov, J. Austermann, J. Beall, J. Hubmayer, B. Raymond, N. Halverson, G. Jaehnig, C. McKenney, and A. Suzuki, "Experimental characterisation of a planar phase-engineered metamaterial lenslet for millimetre astronomy," Appl. Opt. (2023), DOI: 10.1364/AO.480933

Foreword

"Il y a deux réponses à cette question,
comme à toute les questions :
celle du poète et celle du savant.
Laquelle veux-tu en premier ?"
P. Bottero, Le Pacte des Marchombres, Tome 1 : Ellana, 2010

"There are two answers to this question,
as for any questions:
that of the poet and that of the scholar.
Which one would you like first?"
P. Bottero, The Pact of the Shadowwalkers, Book 1 : Ellana, 2010

It was dark. As if awakened from a deep slumber, my ears slowly picked up on the sound of the surrounding mountains, the wind rustling against the fabric of the tent and the rumbling of the river stream. Despite the comfortable warmth my duvet was providing, I was driven to go outside, partly because, as they say in Wales, the Dragon needed to be released, but also because I knew from the crisp cold biting my cheeks that the sky was clear and couldn't skip the marvellous spectacle that awaited outside. Minutes later, I stood there looking up, lost in a moment, less than a grain of sand on a minuscule rock spinning around a slightly less minuscule and somewhat shiny thermonuclear reactor, lost in the Orion Spur of the Milky Way... My awareness of the infinities we're lost within arising just as the more immediate awareness of my surroundings did when I woke up earlier. Funny how, with the correct instrument, we can look at the sounds the Universe was making at its birth. How it grew from one infinite to the other in an unimaginably small amount of time. A couple mosquito bites later, I was back asleep inside the tent.

Climbing summits over multiple days on your own is obviously exhausting. The muscle fatigue builds up over hours marching, the prolonged loneliness takes on moral, rest is precarious... In a sense, it is a very good mirror of one's life where multiple factors, internal or external, takes their toll. But then why carrying on climbing?

That's where my very short and somewhat generic story comes to play. Those moments where the mind can wonder freely in a blend of contemplation, curiosity and imagination are the driver. It is my firm belief that as trying times as it may be, we need to preserve this dreamer side under which science is inscribed, providing the answers of the "poet" through the "scholar" perspective.

Contents

Introduction

I Science &Technology Context

II Optical Systematics

III Principle &Design of a Metamaterial-based Lenslet

IV MetaL Prototype Experimental Characterisation

V Detector Coupling

Conclusion

Back Matter

Appendices

List of Figures

List of Tables

Introduction

Inscribed in the effort carried by generations of researchers to give humanity an eye that can see clearly the very origin of the Universe, this thesis present a humble contribution to the development of a focal optics, the Metamaterial-based Lenslet (MetaL). The material constituting this lenslet is essentially reshaping light as it travels through. The proof of concept for that device is further progressed by coupling it to a new generation of detectors that can perceive the faintest variations of primordial light yet achieved, very much like the human eye can distinguish more shades of green than any other colour.

The developments carried through are decomposed as follows. The current scientific perspective under which we describe the origin and evolution of the Universe will be explored first in Part I. Here will be discussed the Cosmic Microwave Background (CMB), the image we can see of the Universe near it's origin, and what kind of instrument are used or currently being developed to observe it, emphasising the potential role our MetaL could play in future instrumentation developments. The requirements set by the community on such telescopes will further be depicted in Part II. Optical systematics, defects generating impurities in the desired CMB picture, will be defined. Followed by the presentation of a method to investigate further the impact of a real lens such as the MetaL on sky observations. To acquire a deeper understanding of this device, its operating principle and design will then be depicted further in Part III. It will be discussed in details how light is being remodelled through metamaterial-based filters, and how this technology has been readapted to produce a MetaL. More practical concerns are looked upon in Part IV, where the fabrication processes involved in the manufacture of a prototype is presented, and the discussion is extended to inherent limitations for other types of design. The optical quality of the prototyped lenslet, measured with a high precision setup, will then be compared with the analytical model dressed so far and validated against the desired characteristics for CMB observations. With this focal optics fully understood, the next concern to prove its concept is to properly transfer the light from the prototyped device down to a detector set. Such pixel design is depicted in Part V. A discussion on the operating principle of the Kinetic Inductance Detector (KID), explaining how this elegant detector responds to the requirements set for future CMB instruments. Understanding both end of the light path, a solution is devised to couple them together. Namely, a broadband planar antenna transfers the light focused by the lenslet to a microstrip architecture matching the propagating signal to the KID. The current status and future plans for the experimental characterisation of this now fabrication device will finally be discussed.

I

Science & Technology Context

Part I Outline

Beginnings. The starting point of something new, evocative of an epoch untainted by time. But there is never such thing as a "clean" start. A child's birth, for instance, is actually an utter mess, predated by a fairly intense and relatively short period of cellular activity. Cosmology, literally the study of (λογία-logía) the Universe (κόσμος-kósmos), modernised through the scientific discoveries made during the XX$^{\text{th}}$ century, is humanity's attempt at understanding the genesis of the Universe and how it evolves. Very much like our own birth, inaccessible to us, the Universe's origins are currently blurry, and so are the dynamics involved. This view will be depicted in Subsection I.1.1 through a short discussion on the Big Bang paradigm, the current scientific consensus born from recent observations of the CMB, the oldest light relic of our Universe, discussed in Subsection I.1.2.1. Further description of the polarisation states of this primordial trace will be given in Section I.1.2.2, linking the Universe's evolutionary model to its observables. Considerations will be laid out in Subsection I.2 on how, to refine the current CMB picture, future observations will be carried out, overviewing the design of the related instruments. By further discussing the current technological options for Focal Plane Unit (FPU) designs, we will finally argue in Subsection I.2.5 why the MetaL is an attractive option that could be implemented there.

I.1. A glimpse at the Primordial Universe

I.1.1 The Big-Bang Consensus

The Big Bang, a paradigm that depicts the Universe at its earliest time, was precursed by Albert Einstein's theory of general relativity, Niels Bohr's efforts to push it towards a dynamic cosmological solution and Edwin Hubble's discovery of nebulae as being other galaxies outside ours [1]. The latter effectively underlined the Copernican principle, essential in Cosmology, stating in essence that our place in the Universe is representative of any other. The detection of the CMB by Arno Penzias and Robert Wilson in 1965 gave the Big Bang paradigm a final evidence and it grew steadily in the end of the XX$^{\text{th}}$ century through the efforts of scientists like Yakov B. Zel'dovich who tried to devise the origin and dynamics of the large scale structures observable on sky in the Far Infra-Red (FIR) range [2]. In 1992, the first detailed map of the CMB is observed by the COsmic Background Explorer (COBE) mission [3], further enhanced by the Wilkinson Microwave Anisotropy Probe (WMAP) mission in 2001 [4, 5] and finally by the Planck satellite in 2013. This newly acquired cartography of our Universe helped shaping the Big Bang theory further, to the chronology it has today.

Planck Era

The current consensus proposes that at the very origin, from $0\,\mathrm{s}$ to the Planck time $10^{-43}\,\mathrm{s}$, the Universe was in a singular state regarding both the theory of general relativity and quantum physics. At this time, the Universe was at the Planck Temperature $1.41 \times 10^{32}\,\mathrm{K}$, 10^{19} times hotter than the surface of the Sun. According to the Heisenberg uncertainty principle and considering the wavelengths of concern, neither the primordial particles spin nor their probability density can be predicted within the scope of quantum mechanics. Furthermore, the mass contained within this region is of order of the Planck Mass $5.5 \times 10^{-8}\,\mathrm{kg}$, which is 10^{15} times bigger than the mass of hydrogen, resulting in a limiting case for general relativity [6]. The four fundamental interactions, namely the strong nuclear interaction, electromagnetism, the weak nuclear interaction and gravity, cannot be directly observed nor predicted in these limit conditions. At present, it is suggested that they were unified under a single interaction.

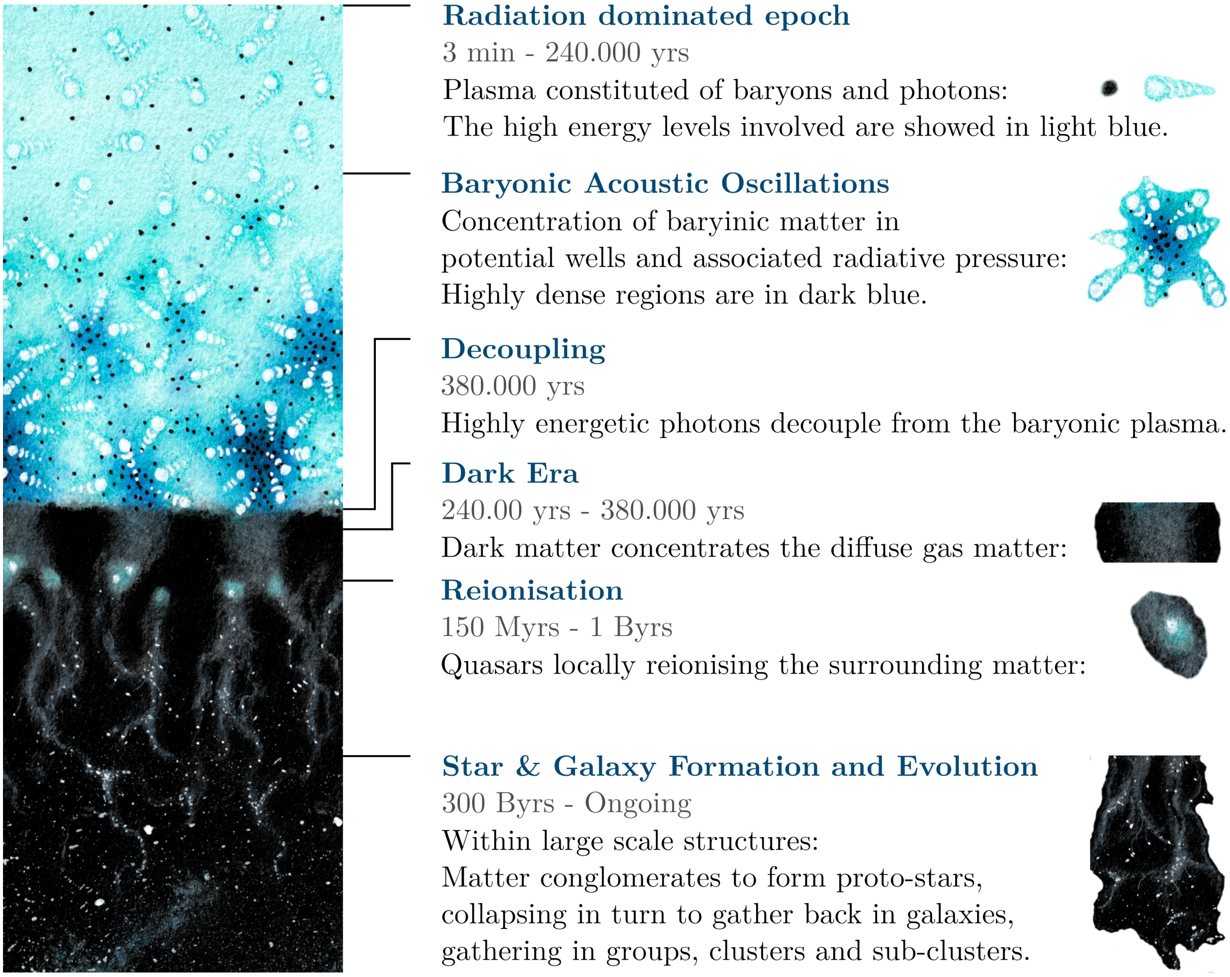

Radiation dominated epoch
3 min - 240.000 yrs
Plasma constituted of baryons and photons:
The high energy levels involved are showed in light blue.

Baryonic Acoustic Oscillations
Concentration of baryinic matter in
potential wells and associated radiative pressure:
Highly dense regions are in dark blue.

Decoupling
380.000 yrs
Highly energetic photons decouple from the baryonic plasma.

Dark Era
240.00 yrs - 380.000 yrs
Dark matter concentrates the diffuse gas matter:

Reionisation
150 Myrs - 1 Byrs
Quasars locally reionising the surrounding matter:

Star & Galaxy Formation and Evolution
300 Byrs - Ongoing
Within large scale structures:
Matter conglomerates to form proto-stars,
collapsing in turn to gather back in galaxies,
gathering in groups, clusters and sub-clusters.

Figure I.1.1: *Artistic impression of the Big Bang Chronology, from the radiation dominated epoch to present times. Watercolour paint created and property of Mme Louise Betremieux.*

Grand Unified Theory (GUT) Epoch

From 10^{-43} s to 10^{-36} s seconds, the Universe is thought to be dominated by photo-radiative energy. The GUT proposes that pairs of proto-particles and their opposite anti-particles form and instantly annihilates with one-another under suspected quantum gravitational interaction, decoupling from the other unified interactions whilst the Universe grows.

Inflation

As will be seen in Subsection I.1.2.1, measurements of the CMB strongly suggests an inflationary scenario where, from 10^{-36} s to 10^{-32} s, the strong nuclear force also decouples from the other unified interactions during the Universe's growth, causing a sudden expansion of the Universe from the Planck length up to roughly the size of a coin on modern scales. A less but still hot and dense plasma of pre-baryonic matter and photons is spread out within these extended dimensions. The expanded quantum fluctuations seeded a characteristic acoustic imprint which slowly triggered the agglomeration of matter during later times.

Pre-baryonic Era

From 10^{-32} s to 10^{-22} s, the conditions settles for massless elementary particles to form as the strong interaction decouples. The intense characteristics of the Universe at this stage maintain a non-baryonic plasma where matter and anti-matter combines to cancel out, immersed in bath of highly energetic photons. Massive particles start forming as the electro-weak interaction decouples.

Baryogenesis & Baryosynthesis

Eventually, as the Universe continues expanding, an asymmetry between matter and anti-matter causes the excess matter to form baryons as the conditions relaxed enough, somewhere between 10^{-22} s and 10^{-15} s.

Radiation Dominated Epoch & Nucleosynthesis

From 3 minutes to 20 minutes, nuclear fusion of some baryons triggers. Hydrogen, helium, deuterium and lithium nuclei form within the plasma whilst the Universe cools and becomes less dense. This nucleosynthesis process sustains for 20 minutes. The Universe is still under extreme conditions, where photons are continuously travelling through matter constituents, either ionising the medium locally or bouncing off electrons through Thomson scattering as is depicted on the top layer of Fig.I.1.1. The resulting photo-energy competes with gravity, causing perpetual density fluctuations in the media, direct result of the acoustic oscillations released during inflation. The Universe carries on expanding and cooling, providing sufficient conditions to maintain this baryonic plasma for the next 240000 years.

Decoupling/Recombination

The constituents of the baryonic plasma finally recombines into neutral atoms, a process that ends approximately 380000 years after the Big Bang. In Fig.I.1.1, the deep blue pockets represents highly dense and hot regions forming through recombination. Eventually, there is enough room for the photons to decouple from the plasma and travel unhindered as gamma rays. The CMB is the remanent picture of this surface of last scattering, shown as a clear transition from the baryonic plasma to the more familiar darkness of the sky in Fig.I.1.1. The CMB depicts the last density perturbation, result of the acoustic oscillations, distribution that subsequently seeded the Universe structures. The Matter Era is entered, where gravity dominates over the other interactions on a cosmic scale.

Dark Era

After full decoupling, up to 150 million years, the Universe is constituted of very diffuse gas matter that slowly gathers into large scale structures, pictured as diffuse white filaments in Fig.I.1.1. Their formation is thought to result from gravitational imprints caused by dark matter.

Reionisation

From 150 million years to 1 billion years, local gravitational potential wells eventually gave birth to the first quasars, an accretion of gas which dynamics causes highly energetic radiation. The energy involved locally reionised matter into a baryonic plasma, shown as blue halos in Fig.I.1.1.

Star & Galaxy Formation and Evolution

Around 300 million years, the gravitation distribution combined with the expansion amplifies density anisotropies, leading to local concentration of ionised gas which eventually entered a new nucleosynthesis cycle, resulting in the creation of the first supermassive stars. As time progresses, those stars collapses into supernovae generating new, less massive stars whilst on a bigger scale, matter conglomerates to form galaxies, attracting each other to form groups, clusters and superclusters. The Universe continues expanding whilst matter is pulled together to present days.

I.1.2 The Cosmic Microwave Background

I.1.2.1 Temperature anisotropy

To acquire a proper understanding of the CMB, it is necessary to look further into the baryonic plasma constituting the Universe during the Radiation Era it originates from. Within this plasma, photons would continuously scatter off electrons and the latter would attract the ionised baryons accordingly through Coulomb interaction. At a given time, the surrounding gravitational distribution, laid out from quantum fluctuations at inflation, presents potential wells where it compresses the plasma by attracting the baryonic matter and peaks where matter rarefies and thus, where the plasma is dilated. The now compressed plasma regions presents an excess of energy, in turn radiated out by the photons. The displaced wells will then attract baryons again, and so on, resulting in a continuous acoustic oscillation of compressions and rarefactions in a dynamic equilibrium happening on all scales, as depicted in Fig.I.1.2. These Baryonic Acoustic Oscillationss (BAOs) were stretched out throughout expansion, eventually resulting in the decoupling of photons from baryons, leaving a map of local density-temperature variations, homogeneously and isotropically distributed [7, 8, 9, 10, 11]. All perturbations are mixed together in a cacophony of superimposed waves at different scales. The temperature fluctuation component $\Delta T/T$ is effectively a spherical cut of these propagating waves. On average, the the temperature component of the resulting surface of last scattering, the CMB, was immensely hot. Its currently observed brightness, presented in Fig.I.2.7 in Section I.2, matches that of a blackbody redshifted down to 2.725 K [12].

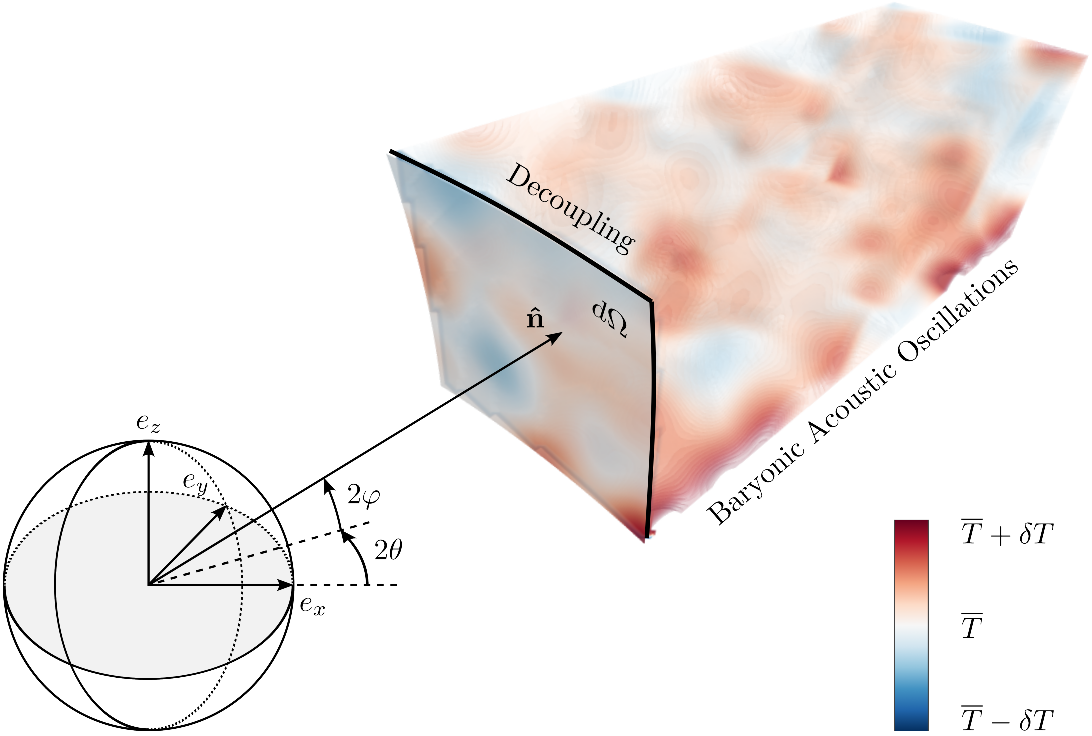

Figure I.1.2: *Section of a single-modded BAO and its surface of last scattering as observed on the celestial sphere in a solid angle $d\Omega$. The azimuth and elevation angles, θ and φ respectively, are defined in a convenient manner for polarisation parameters. Figure made with Python and Inkscape by the author.*

The temperature anisotropies produced from the density perturbations at last scattering, and observed in the coordinate system (θ, φ) of the celestial sphere depicted in Fig.I.1.2, can be expressed as a series of spherical harmonics (I.1.1) [13, 14], weighed by their related expansion coefficients $a^T_{\ell m}$.

$$T(\hat{\mathbf{n}}) = \sum_{\ell m} a^T_{\ell m} Y_{\ell m}(\hat{\mathbf{n}}) \tag{I.1.1}$$

Separate sky projections of weighed $Y_{\ell m}$ are given in Fig.I.1.3. The maps resulting from their successive combination is shown in the bottom part of the figure, ultimately producing a temperature distribution very similar to the observed CMB.

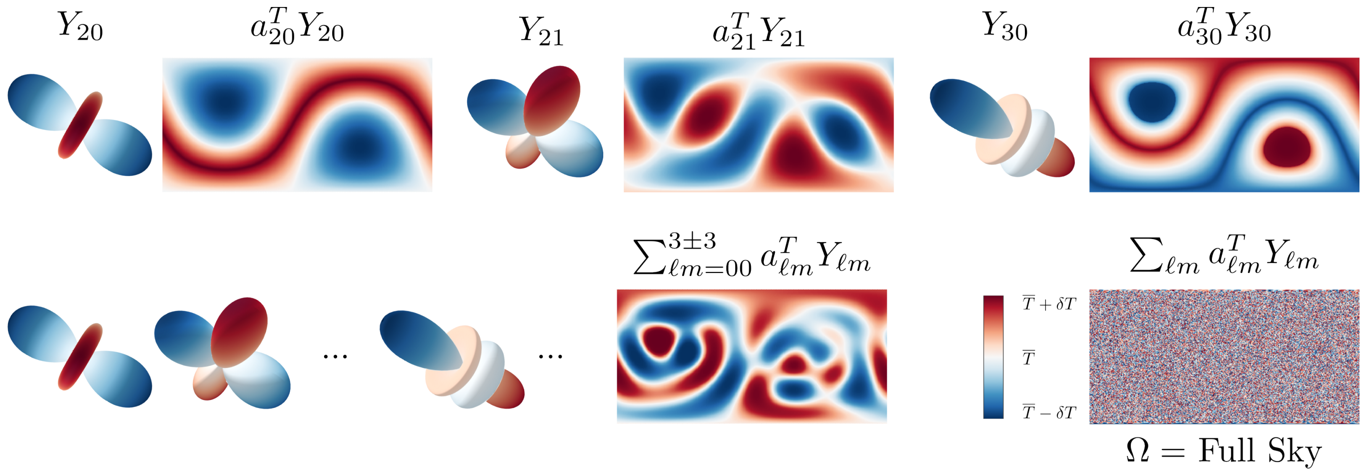

Figure I.1.3: *Sky maps generated from $Y_{\ell m}$ weighed by expansion coefficients $a_{\ell m}$ for $\ell \in [0;3]$ and $m \in [-\ell;\ell]$. The top row shows single element maps and the bottom row presents their combination on the left. The full expansion is finally given on the bottom right with $\ell_{max} = 2500$. Figure made with Python and Inkscape by the author.*

From the last map in Fig.I.1.3 it can intuitively be seen that the temperature fluctuations resemble a white noise distribution. The cyan line in Fig.I.2.7a shows the corresponding CMB temperature brightness Root Mean Square (RMS). A Gaussian distribution is overlaid, illustrating that the CMB temperature seen on sky is accurately modelled as a rotationally invariant normal distribution [15]. In practice, some inflationary scenarios predict various levels of non-gaussianities in the distribution of anisotropies, but this hypotheses is sufficient within the scope of this work. Under these conditions, the temperature distribution can be fully described from its power spectrum C^{TT}_ℓ, giving the variance in magnitude $|a^T_{\ell m}|$ of the expansion coefficients weighing each multipole modes as a function of ℓ. C^{TT}_ℓ, expressed in (I.1.2), can either be derived from an Fast Fourier Transform (FFT) of (I.1.1) over a relatively small fraction of the sky, or calculated from the Boltzmann equation for radiation transfer along $\hat{\mathbf{n}}$ [16].

$$C^{TT}_\ell = \frac{1}{2\ell+1} \sum_m \langle a^{T\dagger}_{\ell m} a^T_{\ell m} \rangle \tag{I.1.2}$$

The cosmological parameters of the Λ Cold Dark Matter (ΛCDM) model, the contemporary framework for Cosmology depicting the Universe constituents and dynamics, are fully constrained by the C_ℓ [17]. For instance, the first acoustic peak in the temperature power spectrum imposes limits on the flatness, curvature and dark energy content of the Universe. The temperature map on its own provides limited information, insufficient to efficiently constrain the full set of ΛCDM parameters. This is especially true at large angular scales where the cosmic variance limits the precision at which temperature signals can be measured. Namely, for a given multipole ℓ, the corresponding random Gaussian temperature distribution is encompassed by $(2\ell + 1)Y_{\ell m}$ leading to a variance (I.1.3) of order $2/(2\ell + 1)$, large for low ℓ. The polarisation map offers a useful complementary view as the polarised signals are not limited by cosmic variance since they result from effects on the $Y_{\ell m}$.

$$\delta C_\ell \simeq \frac{4\pi}{\Omega}\left(\frac{2C_\ell}{\sqrt{(2\ell+1)}}\right) \tag{I.1.3}$$

I.1.2.2 Polarisation

Polarisation initiates near recombination, where photons keep scattering off electrons in cold and hot regions [18]. The plasma is subjected to density fluctuations as discussed previously, but also to vorticity, causing electrons to scatter photons coming from surrounding hot and cold regions. As is represented in Fig.I.1.4, showing a given mode of the BAO, electrons may be submitted to a quadrupole anisotropy, scattering off the incoming photons in a linearly polarised wave. Gravitational fluctuations overlays a specific imprint to those locally polarised waves. The mathematical formalism of the ΛCDM model characterises density, vortical and gravitational fluctuations as scalars, vectors and tensors respectively. Spin 1 perturbations would break isotropy as they have a specific direction and are thus discarded in the ΛCDM model. Each perturbation result in a symmetrical set of quadrupole moments, encompassed through spin-2 spherical harmonics ${}_{\pm 2}Y_{2m}$ of order $m = 0, \pm 1, \pm 2$ for the case considered in Fig.I.1.4:

- The central case shows an electron sitting in a hot region, within a density perturbation. The resulting scattering corresponds to ${}_{\pm 2}Y_{2\pm 0}$. This type of symmetrical pattern has the same handedness as that of an electric field between two particles charged oppositely and have therefore been named E-mode.
- Vorticity corresponds to the left case, where the electron rolls between a hot and a cold region. A local Doppler effect within the vortex produces a ${}_{\pm 2}Y_{2\pm 1}$ quadrupole pattern. Such perturbations would have left vortical imprints on large scale structures in the later Universe, which have not been observed. This type of perturbation is thus predicted to be negligible at recombination [19].
- A passing primordial gravitational wave will distort the space locally, thus the scattered photon wavelength as shown in the right case. This ${}_{\pm 2}Y_{2\pm 2}$ distortion has a handedness with temperature. The resulting asymmetrical pattern is called a B-mode as it resembles a magnetic field surrounding two oppositely charged particles.

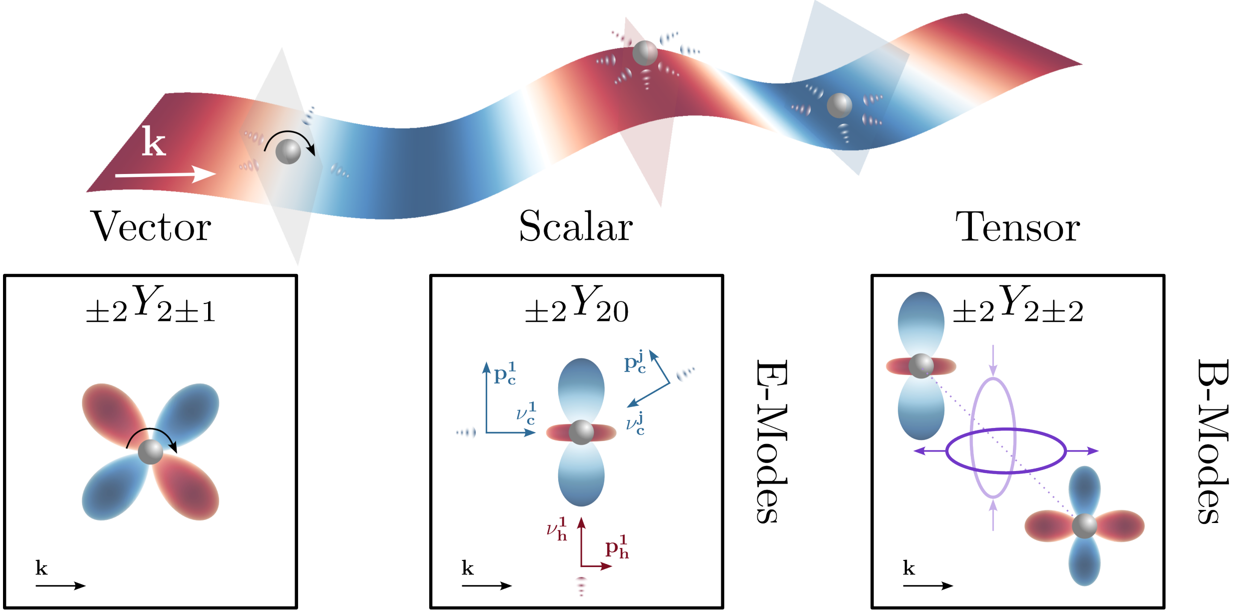

Figure I.1.4: *Electrons Thompson scattering photons in a single-modded BAO propagating along* **k**. *The resulting* $_{\pm 2}Y_{2\pm 0}$ *density-scalar and* $_{\pm 2}Y_{2\pm 1}$ *vorticity-vectorial linear polarisations are pictured as the combination of a virtually infinite number of photons being scattered. The* $_{\pm 2}Y_{2\pm 2}$ *gravitational-tensor imprint is depicted on the right hand side. The scalar case shows various photons coming from hot and cold regions. Their displacement and polarisation states are materialised with the* ν *and* **p** *vectors. A virtually infinite number of photons is scattered to form the* $_{\pm 2}Y_{\ell m}$. *Scalar and tensor perturbations respectively correspond to E and B modes. Figure made with Python and Inkscape by the author.*

Since a virtually infinite number of photons are coming in, and as the process occurs on all scales, or all acoustic modes, all polarisation states superimpose, expanding to higher ℓ. As for the temperature map (I.1.2), the polarisation distribution can be Fourier decomposed with ℓ, matching the various modes of oscillation, and transcribed into a power spectrum (I.1.4).

$$C_\ell^{XY} = \frac{1}{2\ell+1}\langle a_{\ell m}^{X} a_{\ell m}^{Y\dagger}\rangle \tag{I.1.4}$$

The CMB polarisation distribution can be described by the Stokes parameters Q and U (I.1.5) [20, 21], where, on the celestial sphere such as the one depicted by Fig.I.1.2, the first characterises the preponderance of horizontally over vertically polarised light, and the second is the same rotated $\pi/4$ [22]. The overlay of polarised light resulting from scalar, vector and tensor contributions, decomposed into E (I.1.6) and B-modes (I.1.7), is described with the spin ±2 complex polarization $Q \pm iU$ expanded in terms of the spin-2 spherical harmonics $_{\pm 2}Y_{lm}$:

$$(Q \pm iU)(\hat{\mathbf{n}}) = \sum_{\ell m} (E_{\ell m} \mp iB_{\ell m})(\hat{\mathbf{n}})_{\mp 2}Y_{\ell m}(\hat{\mathbf{n}}) = \sum_{\ell m} a_{\pm 2,\ell m \pm 2}Y_{\ell m} \tag{I.1.5}$$

$$E(\hat{\mathbf{n}}) = \sum_{\ell m} a_{\ell m}^{E} Y_{\ell m}(\hat{\mathbf{n}}), \text{ where } a_{\ell m}^{E} = -\frac{a_{2,\ell m} + a_{-2,\ell m}}{2} \tag{I.1.6}$$

$$B(\hat{\mathbf{n}}) = \sum_{\ell m} a_{\ell m}^{B} Y_{\ell m}(\hat{\mathbf{n}}), \text{ where } a_{\ell m}^{B} = i\frac{a_{2,\ell m} - a_{-2,\ell m}}{2} \tag{I.1.7}$$

Appendix A shows C_ℓ^{TT}, C_ℓ^{EE}, C_ℓ^{BB} and C_ℓ^{TE} as released by the Planck and Dark Energy Survey (DES) communities [23, 24]. The TT, EE and TE power spectra are well defined and allow the estimation of the cosmology parameters to a precision up to 1% with the exception of the tensor to scalar ratio r of the density versus primordial gravitational wave fluctuations (I.1.8). The main and secondary peaks in C_ℓ^{EE} are respectively the fundamental and harmonic modes of the BAOs. However, the B-mode polarisation signals are very faint, orders of magnitude below that of the temperature map. Quantitatively, the amplitude A_t of the currently estimated C_ℓ^{BB} spectrum as given in Appendix A is approximately 2 to 3 orders of magnitude below that of the E-mode spectrum A_s. The CMB maps are further affected by effects that occurred between last scattering and the present times which needs to be compensated for.

$$r = A_t/A_s \tag{I.1.8}$$

C_ℓ^{BB}, a direct transcription of r (I.1.8), is expected to be orders of magnitude below C_ℓ^{TT} and C_ℓ^{EE} since density perturbations are predicted to dominate the baryonic plasma. Future experiments are trying to observe the B-mode polarisation signals of the CMB below $\ell = 100$ with pristine sensitivities which should provide $r < 10^{-3}$. Reaching this goal would enable a decisive validation of the inflationary scenario and the ΛCDM model within the Big Bang paradigm. Precision measurements of the CMB over $\ell = 1100$ should also provide information of the late time Universe constituents and evolution, namely large scale structures seeding and formation. Such objective presents considerable technological challenges. An instrument aiming at detecting such faint signals essentially requires high throughput in the bandwidths of interest, calling for pristine optics offering optimal power coupling from the sky to the FPU whilst ensuring efficient out of band rejection on one hand, and for a large number of densely packed, highly sensitive detectors on the other hand. Relying on the cosmology context depicted here, insights on the instrumentation perspective will be given in the next chapter, where the interest in providing an alternative focal optics, the MetaL, will be underlined. A benchmark analysis designed to comparatively analyse the performances of the MetaL option in the context of CMB observations is devised in Part II and applied in Part IV. The associated method and results also necessitate a proper understanding of the cosmological context depicted in this section.

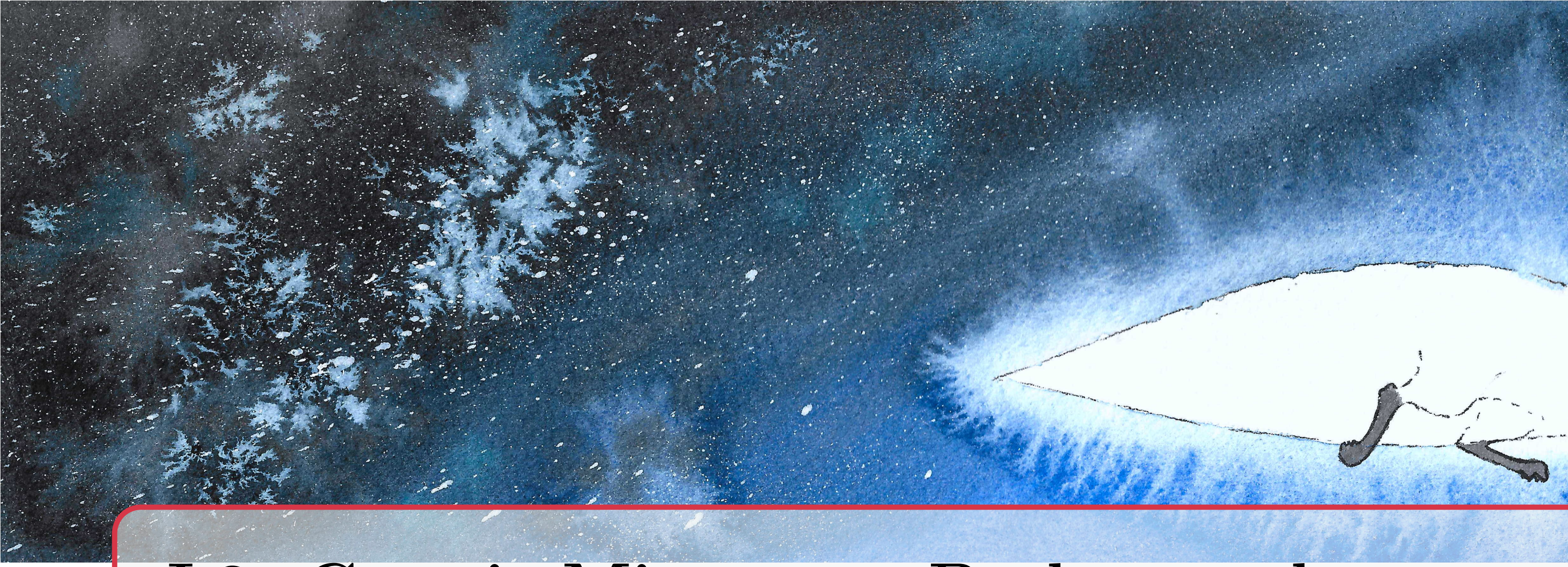

I.2. Cosmic Microwave Background Instrumentation

I.2.1 Observing the sky

I.2.1.1 A brief history of telescopes

A modern telescope essentially aims at gathering the light from the sky onto a set of detectors, converting the incoming photons into a signal that can be handled numerically and processed further. To fully grasp how they are designed for CMB observations, an overview of the basics of their design principle will be given in a chronological manner. Traces of early mirrors and lenses are found as far back as in 3000-2000 B.C. in various parts of the world such as in Ancient Egypt, Anatolia, Mesopotamia and still later in China and in the New World [25, 26, 27]. Understanding the principle of optics was at all times a preponderate theme of research for mankind. The Optica from Ptolemy dated from the II$^{\text{d}}$ century [28] and the premises of the theory of Geometrical Optics from Euclides in the IV$^{\text{th}}$ century [29] were the main references for the work of Al-Kindi, Ibn Sahl, and Ibn al-Haytham in the X$^{\text{th}}$ and XI$^{\text{th}}$ centuries. The latter produced the Book of Optics [30, 31], at the base of Roger Bacon studies three centuries later, which laid the foundation for further developments in optical design [32]. Modern theories on geometrical optics, with an emphasis on refraction, were deepened early on in the XVII$^{\text{th}}$ century by René Descartes [33], Willebrord Snellius (Snell) [34] and Isaac Newton [35], amongst others, ultimately resulting in the creation of the first telescopes by the Dutch spectacle makers Hans Lippershey, Zacharias Janssen and Jacob Metius early in the XVII$^{\text{th}}$ century [36]. In the early times following their fabrication, these devices were used as magnifiers for navigation or land surveys until Galileo Galilei successfully demonstrated a version of his own design capable of astrophysical observations [37], further modified by Johannes Kepler a few years later [38]. Soon after, Isaac Newton, James Gregory [39], Laurent Cassegrain [40] and others investigated the design of reflective telescopes. Both types are represented in Fig.I.2.1.

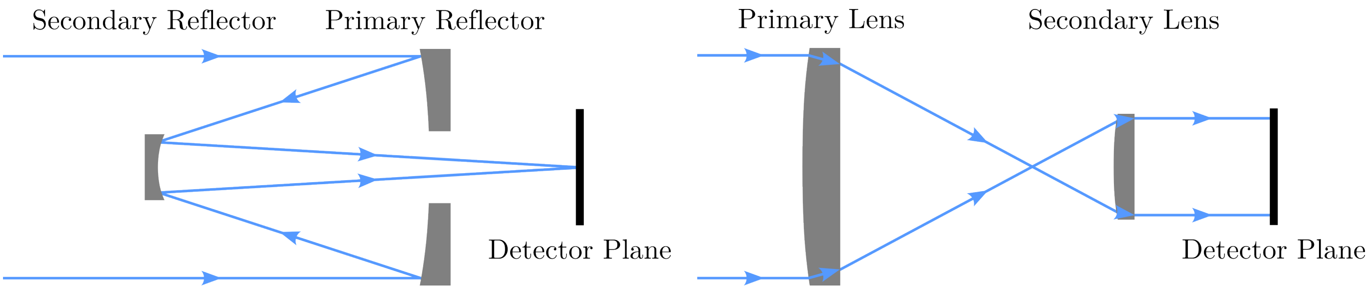

(a) *Gregorian reflective telescope* **(b)** *Two-lens Keplerian refractive telescope*

Figure I.2.1: *(a) Reflective on-axis Gregorian telescope as per devised by James Gregory in 1663 [39]. In a Cassegrain arrangement, the secondary is a convex hyperbola, increasing the telescope focal length in a compact manner. (b) Two-lens refractive on-axis Keplerian telescope, named after Johannes Kepler's redesign of its Galilean counterpart [38]. This arrangement uses a convex set of lenses instead of Galileo's concave ones, resulting in a higher magnification for the same focal length. Figures made with Inkscape by the author.*

I.2.1.2 Inherent optical aberrations and design evolutions

In an on-axis reflective arrangement, the secondary mirror is partially blocking the incoming light which result in a reduction of coupled power and an increase in Signal-to-Noise Ratio (SNR) [41]. To remedy this defect, William Herschel built the first off-axis telescope in 1789, the largest instrument meant for astronomical observations ever built at the time [42]. Apart from blockage, optical aberrations are inherent to the reflector shapes required for such assembly, necessarily asymmetrical paraboloids or hyperboloids inducing astigmatism and coma [43, 41]. It was not until the XX$^{\text{th}}$ century that improvements were made on such designs, as the mirror fabrication techniques improved. For instance, the now classic Ritchey–Chrétien telescope invented early in the XX$^{\text{th}}$ century by George Willis Ritchey and Henri Chrétien [44], offers a focal plane free of coma by using an arrangement of two hyperbolic mirrors. Fig.I.2.2 shows a standard off-axis Gregorian design suffering from astigmatism and coma.

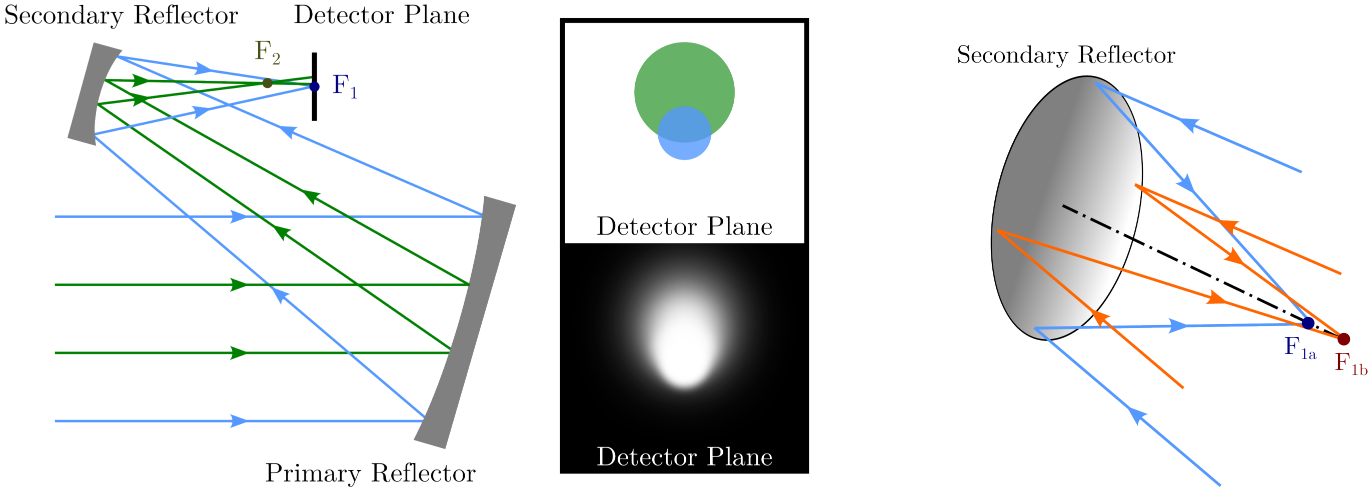

(a) *Coma* **(b)** *Astigmatism*

Figure I.2.2: *(a) Comatic aberration and (b) astigmatism both appear for incoming light rays striking the primary mirror of a reflecting telescope off-axis, resulting in a distorted imaged source. In an off-axis configuration, the sky viewed is inherently not in the Optical Axis (OA) of the first mirror. Stars thus observed would seem to have a coma, as illustrated in the inserts, hence the name of the prior aberration. Astigmatism appears as off-axis rays in a given plane containing the line of sight do not focus in the same spot since they encounter a different mirror profile. Figures made with Inkscape by the author.*

Off-axis Gregorian designs can be modified in a similar manner to mitigate these defects, for instance, coma is cancelled by making the primary slightly elliptical and the secondary a more eccentric ellipsoid [43, 45], as was done for Planck. In 1983, Corrado Dragone described a design that cancels both aberrations on either Gregorian or Cassegrain systems and additionally offers improved polarisation properties [46, 47, 48], especially if the focal optics are following a specific angular position condition derived by Yoshikazu Mizuguchi [49], an attractive trait for CMB experiments [50]. Coma and astigmatism are easily cancelled out in a suitably designed refractive telescope by refining the optics geometry and tuning the secondary lens as to compensate for the defects of the primary [43, 51]. Since such instruments rely on refracting elements, different wavelengths will not focus on the same focal point. This chromatic aberration becomes the main source of defect for such assemblies but can be mitigated by adding a third refractor. To date, the cross-Dragone and the on-axis refractive-only designs are the preferred choice for CMB instruments as they provide the lowest aberration levels [41, 52].

I.2.1.3 Throughput, field-of-view and stray light

In the previous discussion, the light entering the telescopes was only partially depicted through rays parallel to the OA of the concerned assemblies. In practice, all parallel rays incoming at any angles from the instrument Line Of Sight (LOS) are picked up. A telescope Diffraction-Limited Field Of View (DLFOV) is defined as the maximal angle θ_{DLFOV} at which such rays fully focuses down to the focal plane in a diffraction limited manner, which subtend the solid angle Ω observable on sky. For a focal plane of surface area A, the overall brightness the telescope can gather from a source of intensity I over a bandwidth $\Delta\nu$ is encompassed by its étendue E, or throughput (I.2.1).

$$E = A\Omega I\Delta\nu \tag{I.2.1}$$

$$S_{min} = 1.22\mathcal{F}\lambda \tag{I.2.2}$$

$$\mathcal{F} = \frac{F_0}{D_1} \tag{I.2.3}$$

The diffraction limit corresponds to the spatial resolution of the telescope, namely, the admissible separation S_{min} between two focused spots before they become indistinguishable from one another (I.2.2) [53], as depicted by Lord John William Strutt Rayleigh in the XX$^{\text{th}}$ century based on the work of Sir George Biddell Airy in the XIX$^{\text{th}}$ century [54, 55]. Two pixels of an image are resolved when the central peak of one Airy spot lies on or outside the first minimum of the other, as shown in Fig.I.2.3.

Effectively, the detector pixel size should be comparable to the focused Airy spot size for efficient collection of energy from the observed source on sky. Fig.I.2.4 presents a cross-dragonian telescope with these definitions overlaid.

Whilst the solid angle of observation is directly dependant of the telescope primary aperture diameter, its resolution also depends of the instrument focal length F_0. Any unresolved incoming bundle of rays, or stray light, may fall down to the focal plane, over-illuminating the detectors, thus deteri-

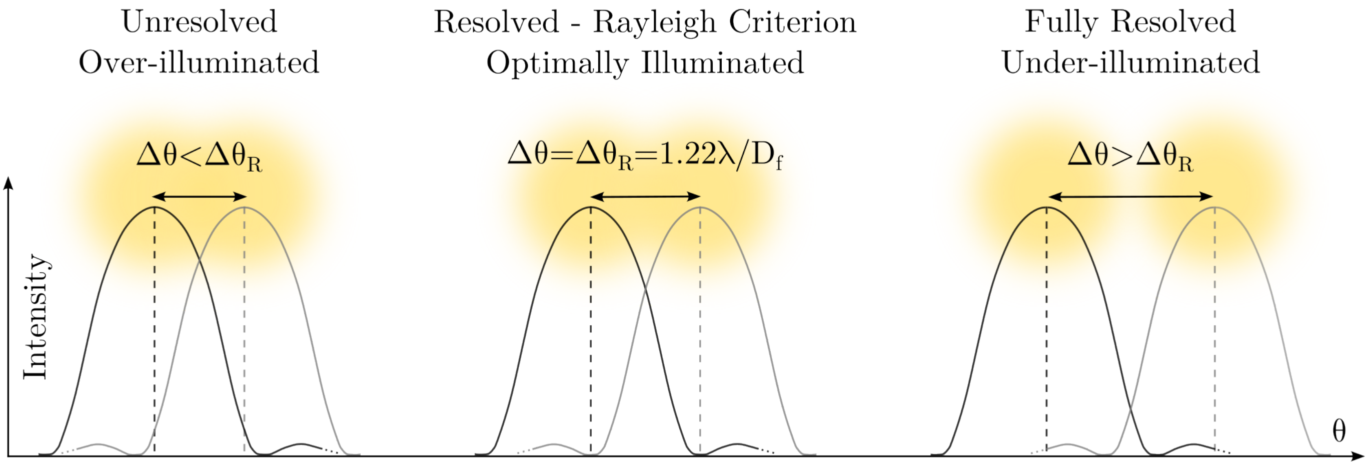

Figure I.2.3: *Illustration of an over, optimally and under-illuminated focal plane. The middle case shows the limiting Rayleigh criterion, minimum $\Delta\theta$ from where the beams are resolved. Figure made with Inkscape by the author.*

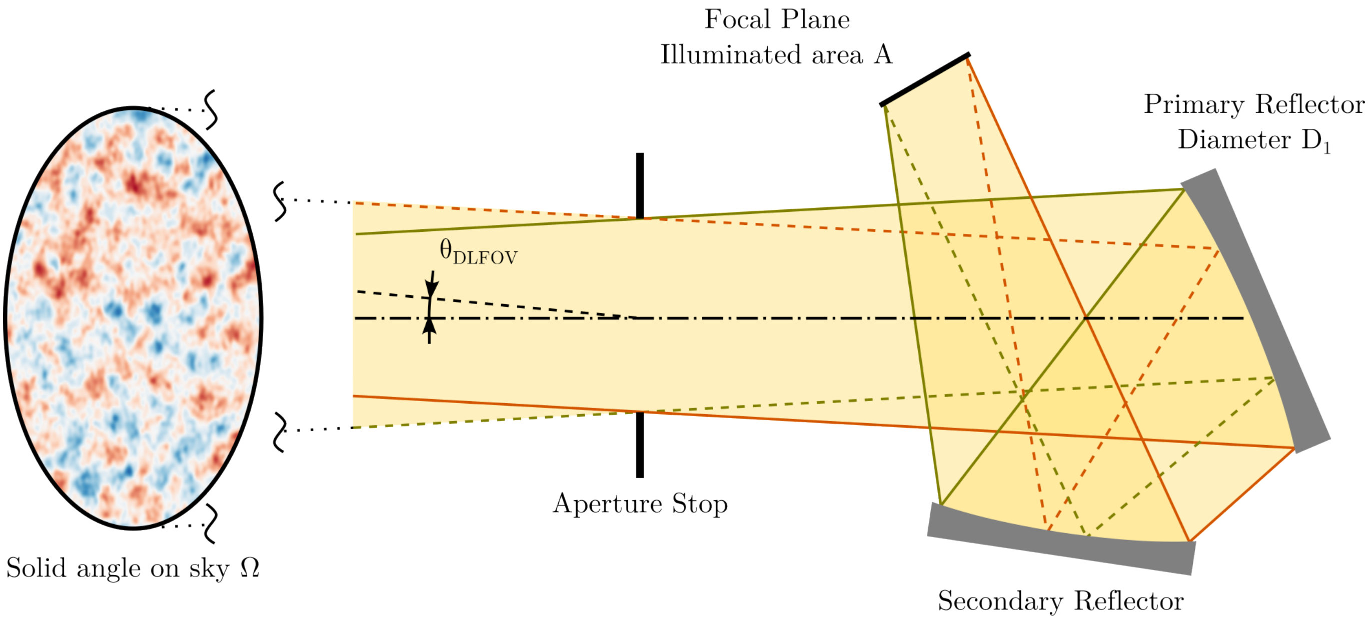

Figure I.2.4: *Cross-dragone configuration [46] observing the CMB at a solid angle Ω with a field of view θ_{DLFOV}, resulting in an illuminated focal plane area A. Figure made with Inkscape by the author.*

orating their performances by causing a decrease in SNR. This is encompassed through the optics focal ratio $\mathcal{F}$, or F-number (I.2.3). To mitigate this, telescopes may include an aperture stop, a series of baffles between the successive optical elements and a field stop near the focal plane, designed to minimise incoming stray light while maximising throughput [51]. A complementary Lyot stop is often used at the entrance pupil, image of the physical aperture stop. These fore-baffles were invented by Bernard Lyot in 1939 [56], who inherited the passion Nicolas Camille Flammarion had for Astronomy. In refracting arrangements, the telescope tube may be coated with Radiation Absorbent Material (RAM) to further absorb leftover vagrant rays.

I.2.2 Imaging the Cosmic Microwave Background

I.2.2.1 Requirements

From an instrumental perspective, the best possible measurement of the CMB signals must be taken with a maximised throughput in band and a full power rejection out of band [57]. The desired bandwidth is conditioned by the brightness temperature RMS of the temperature and polarisation signals raising over the foregrounds contributions on one hand, and the lack of precise measurements of the thermal dust emission from the reionisation era on the other, as depicted in Fig.I.2.7 [12, 58]. The resulting set of power spectra C_ℓ should be cosmic variance limited, meaning essentially that systematic effects would have little to no impact on the measured signals. In order to reach the scientific goals of future CMB experiments, an angular resolution of 1 arcmin or better is desired at $\ell > 1000$ [57], necessary to pick up the fine temperature anisotropies seeding the large scale structures of the universe. At $\ell < 200$, a 25 arcmin beam width ensures a global view on large scales over a full sky map for $r < 10^{-3}$ according to current models. As instrument designs must reflect these conditions, it is worth comparing the arrangements previously depicted. Reflective telescopes are well developed, their large mirrors can be fabricated with a high degree of tolerance, but they are inherently off-axis which induces some degree of coma and astigmatism often compensated by non-telecentric focal planes, as was the case with Planck. Their refractive counterpart, while being on-axis, providing a telecentric focal plane, are limited to 2 m diameter optics by current fabrication techniques. CMB experiments operate in the millimetre and sub-millimetre wavelengths and require arcminute resolution on sky, calling for telescope apertures of order 5 m to 10 m in diameter. To achieve a combination of high throughput and high resolution, the current baseline consists of a combination of reflective fore-optics and refractive back-optics when possible [41, 52].

I.2.2.2 Mapping the sky

The telescope effectively projects on sky the combined and magnified focal optics beams, encompassing a small fraction of the sky. Reconstructing the complete image necessitates scanning at, or below, the proper spatial sample rate (I.2.4), as per depicted by the Shannon theorem [59, 60]. Namely, the digitizing sampler must utilize a sampling interval that is no greater than one-half the size of the smallest resolvable feature of the optical image.

$$\mathcal{R}_s \leq \frac{\Delta\theta_R}{2} = 0.61\mathcal{F}\lambda \tag{I.2.4}$$

$$\theta_{FWHM} \simeq \frac{\lambda}{D_h} \tag{I.2.5}$$

$$\tag{I.2.6}$$

Focal optics will be discussed further in Section I.2.4 but one can grasp that the physical dimensions of such devices may result in an under-sampled image. Horn antennas, a well understood technology extensively used, in Planck for instance, can be cited as an example [61]. Such feedhorns give a tapered illumination of the telescope primary mirror, resulting in an ideal beam profile on sky if suitably designed. The exact details of this optimal profile will be further discussed in Part II where more details on beam characteristics can be found, in particular the description of the Full Width Half Maximum (FWHM) (II.3.1). In the present scenario, the latter is directly dependent on the horn aperture diameter D_h (I.2.5), also limiting the frequency range attainable to those less than $D_h/\lambda \simeq 1/\mathcal{F}\lambda$ [62]. $2\mathcal{F}\lambda$ spaced horns is an optimal focal plane arrangement providing maximum illumination efficiency despite not resolving the sampled image fully. As depicted in Fig.I.2.5, jiggling the telescope pointing or scanning the concerned areas of the sky at the appropriate angle, or the correct velocity, to provide the necessary overlap between beams allows for a full acquisition at the cost of mapping speed.

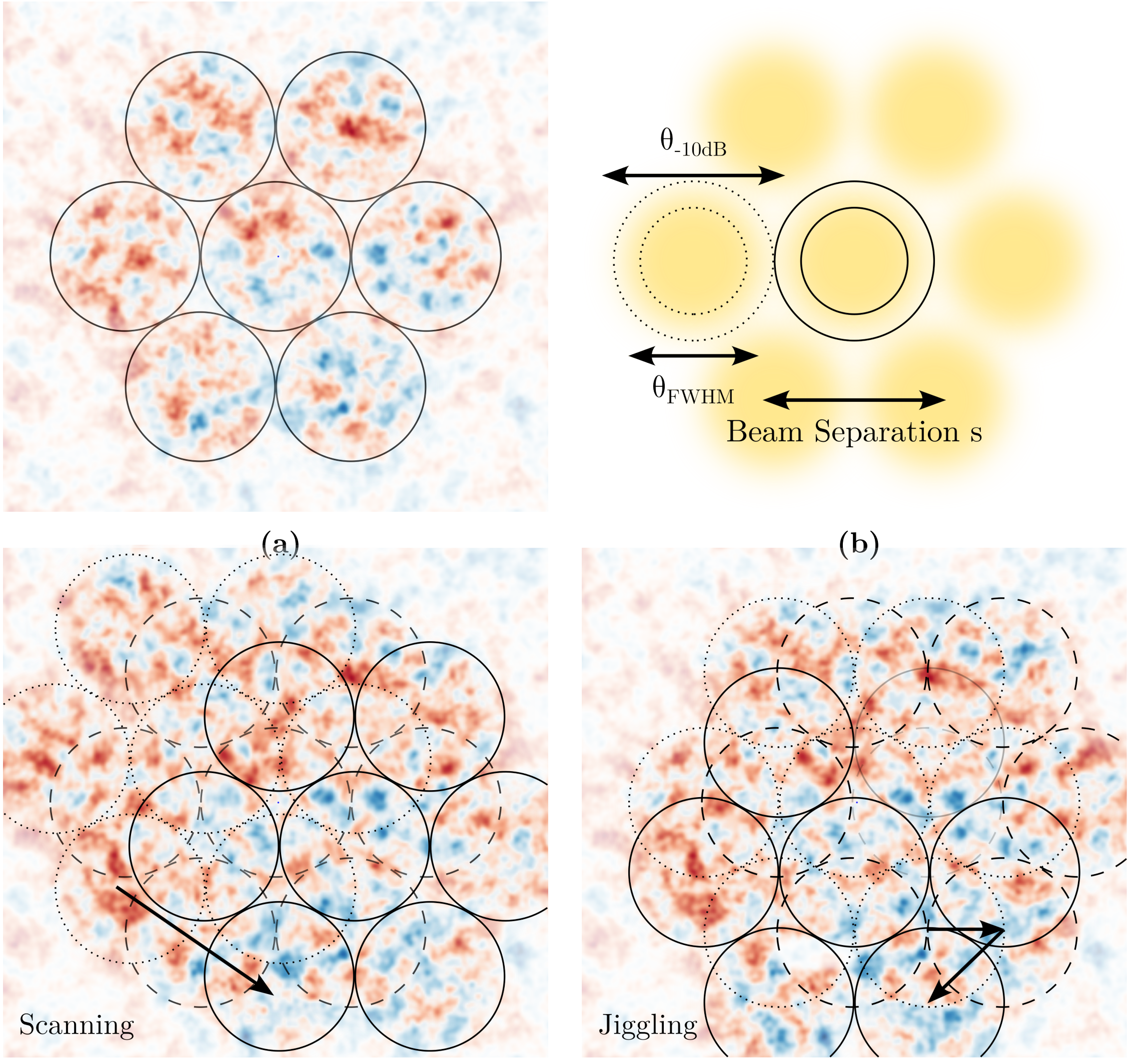

(a) **(b)**

(c) **(d)**

Figure I.2.5: *(a) Telescope observing windows corresponding to a set of seven $2\mathcal{F}\lambda$ spaced feedhorn focal plane arrangement. (b) Associated beam characteristics: FWHM θ_{FWHM}, beam width at 90% power $\theta_{-10_{dB}}$ and separation s. The gaps between beams that can be seen in (a) underline how a (c) sweeping or (d) jiggling scanning strategy needs to be adopted to fully sample the CMB picture observed by the combined focal optics. Reservedly, a shorter separation, potentially available with a different type of focal optics, would immediately allow a direct acquisition. Figures made with Python and Inkscape by the author.*

I.2.2.3 Foregrounds

I.2.2.3.1 Atmospheric windowing and ground pickup

A ground based instrument has to cope with atmospheric optical loading. The proportion of water vapour contained in the atmosphere result in strong absorption of the incoming light at a large range of frequencies, leaving a set of observing windows spanning $\sim$ 70 GHz to $\sim$ 250 GHz. An example for the atmospheric transmission is given in Fig.I.2.6. It was generated with Atmospheric TRANsmission (ATRAN) [63, 64] for a virtual observing site at 30° N latitude and an altitude of 3000 m, with a water vapour content of 0 mm in green, 1 mm in blue and 3.5 mm in red, close to the conditions found at the Mauna Kea observing site.

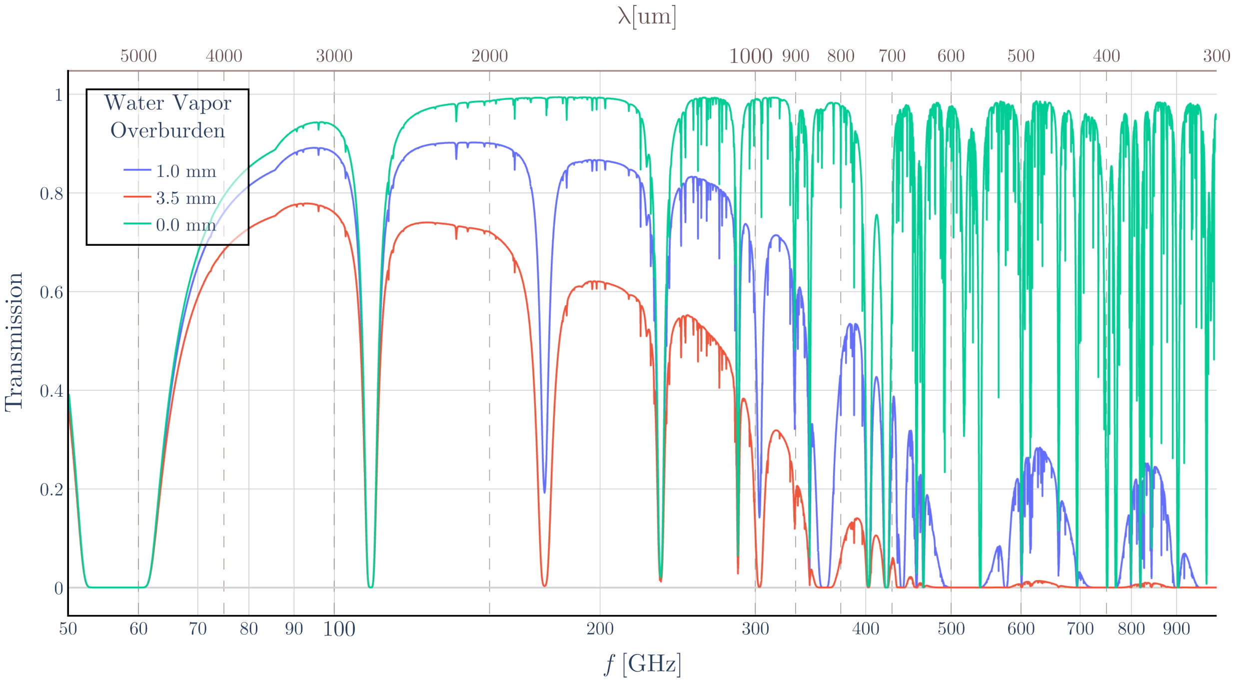

Figure I.2.6: *Atmospheric transmission compiled in Python, using data generated with ATRAN [63, 64] for a water vapour content of* 0 mm *in green,* 1 mm *in blue and* 3.5 mm *in red. Aside the power absorption due to* H_2O, *ATRAN models the impact of other atmosphere constituents such as* O_3, CO_2, *etc., resulting in noticeable drops in transmission as is the case at* 120 GHz *and* 250 GHz.

In band the incoming photons excite the atmosphere constituents, the resulting optical load is treated either by accurately modelling the effect and removing it in the post-processing, or by a pair-differentiating technique [65, 66]. Similarly, the thermal emission of the warmer ground, picked up on the far side of the beam and loading the detectors, is inherently difficult to filter out but can be modelled accurately and removed in the post-processing [65]. Front baffles are often used to partially remove the ground contribution to the signal but induce beam clipping.

I.2.2.3.2 Galactic and extra-galactic foregrounds

Foregrounds affecting the temperature and polarisation maps are of various types. An interesting and complementary effect occurs at reionisation [67], where primordial photons scattered again through locally ionised gases, resulting in a uniform diffusion of power for the temperature spectrum along with lower redshifts z and a cross-correlation between E and B-modes leaving a characteristic peak in their spectra at low ℓ and redshift z. As can be seen on Fig.I.2.7, galactic foregrounds contributes strongly to the polarised signals observable through free-free, synchrotron, spinning dust and thermal dust emissions. The latter, still difficult to fully account for, is currently estimated to affect polarisation imprints up to 5%. Gravitational lensing caused by large scale structures along the light trajectory also causes characteristic E-to-B leakage. The impact resulting from the Sunyaev-Zeldovich (SZ) effect at smaller scales in galaxy clusters is mildly similar. Reionisation signals may be more difficult to constrain below $r = 0.01$ because of these foreground contributions, whilst imprinting various effects on the CMB power spectra. They can be removed through their frequency dependence for the galactic foregrounds and extra-galactic point sources, or via the different angular dependence of their power spectra for the cosmological sources such as gravitational lensing. As for ground pickup, galactic foregrounds may also be limited by adding a front baffle, inherently clipping the beam.

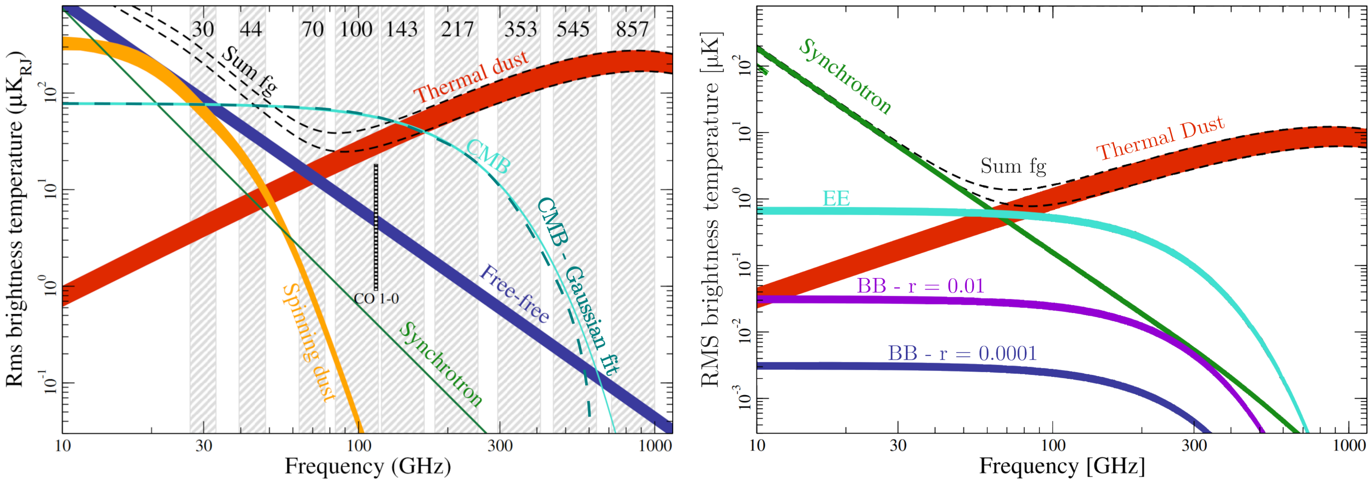

(a) *High-elevation sky brightness temperature RMS for the temperature signal as measured by Planck, borrowed from the 2015 results [12].*

(b) *High-elevation sky brightness polarisation signals RMS for the measured E-mode. Expected B-mode levels are also given for* $r = 10^{-2}$ *and* $r = \mathrm{e}{-4}$. *Figure readapted from [58].*

Figure I.2.7: *Brightness temperature RMS of the CMB for (a) the temperature and (b) the E and B-mode signals as a function of frequency. The foregrounds are overlaid, namely: spinning dust, synchrotron and thermal dust in yellow, green, blue and red, respectively. Their summed thermal brightness RMS is represented in black dashed lines. Typical observational bandwidths are shown in grey bands. Expected B-mode levels are also given for* $r = 10^{-2}$ *and* $r = \mathrm{e}{-4}$.

I.2.2.4 Instrumental systematic effect on polarisation detection

At low ℓ, the cosmic variance of a B-mode power spectrum with a lower limit in amplitude of order $10^{-3}\,\mu\mathrm{K}^2$ is around $10^{-4}\,\mu\mathrm{K}^2$ (I.1.3). Instrumental systematic effects can induce spurious and rotated polarised signals on the detectors, which may result in contributions to the measured power spectrum going off the desired cosmic-variance limit. Effectively, such systematics transcribes themselves into a raise in the absolute magnitude of the polarised signal detected, mainly induced by differential gain, polarisation rotation and cross-polarisation [41], further depicted in Part II. Any other spurious signal is usual stable over scanning and can be removed in the post-processing analysis as an overall offset. The requirement on the differential gain is set below 0.1%, necessary for the power leakage from temperature anisotropy to be below 10% of the predicted C_ℓ^{BB} spectrum with $r = 10^{-3}$. To limit spurious signals raising from polarisation rotation to a factor of 10 below the lensed B-mode signal, they should not deviate more than 0.3° from the incident direction [16, 66].

Polarization modulation by motion of an optical element in the light path constitutes a consistent method of identification and separation of such spurious signals. The modulator can be installed either at ambient temperature on the front-optics level, or inside the cryostat if special care is taken on the heat management of the required driving mechanisms. The rotation of a Half-Wave Plate (HWP) based on a crystalline or a metamaterial structure [68, 69, 70], or the translation of a mirror in front of a polariser, the Variable-delay Polarization Modulator (VPM) [71], are among the standard techniques to achieve such modulation.

Forecasting and removing consistent systematics from the future data acquired in the coming decades is of primary importance. Dedicated pipelines are now a standard to evaluate the performances of an upcoming instrument on sky [72, 73, 74, 75], borne from the experience built with Planck [76, 77, 21], Background Imaging of Cosmic Extragalactic Polarization (BICEP)2 [66], and others. Such end-to-end analysis may be conducted on a partial or full sky, suitably projected onto the instrument Field Of View (FOV) accordingly to its scanning strategy. The signal contributions from the various foregrounds depicted previously are also overlaid. Each optical components of the telescope and their modelled systematics is integrated down to the pixels constituting the focal plane. As depicted further in Section II, two main approaches are taken for such analysis, either Time Ordered Datas (TODs) detector signals are projected on sky and the resulting map gives the observed power spectra, or maps are generated from input spectra, convoluted with the telescope window function and converted back for comparison.

I.2.3 Contemporary and future CMB instruments

A selection of next generation CMB experiments is currently in development or being deployed to reach the precision measurements awaited by the community. Emphasis will be made on the Simons Observatory (SO), a ground based telescope currently being assembled in the Atacama desert in Chile, and on the Lite satellite for the study of B-mode polarization and Inflation from cosmic background Radiation Detection (LiteBIRD) space telescope in its preliminary development phase, led by the Japan Aerospace Exploration Agency (JAXA). The SO consists of a Large Aperture Telescopes (LATs), concerned with high ℓ measurements, and Small Aperture Telescopes (SATs), complementarily observing at large angular scales. As shown in Fig.I.2.8, both telescopes are based on a reflector-refractor combination.

The scanning strategies one may select for ground based experiments are limited by the inherent position of the telescope on Earth and the reachable bore-sight angle. Space telescopes do not suffer from restrained scanning strategy and are not limited in frequency by the atmospheric windows, but they come with their own constraints. In a nutshell, they must remain compact and lightweight in order to be launched, positioned in orbit and maintain for a sufficiently long period. Their operation timescale is inherently shorter than ground based telescopes, which can be maintained and upgraded. To match the lightweight and compactness required, LiteBIRD is planned to be constituted of a fully refractive telescope for the low frequency range and a set of fully reflective

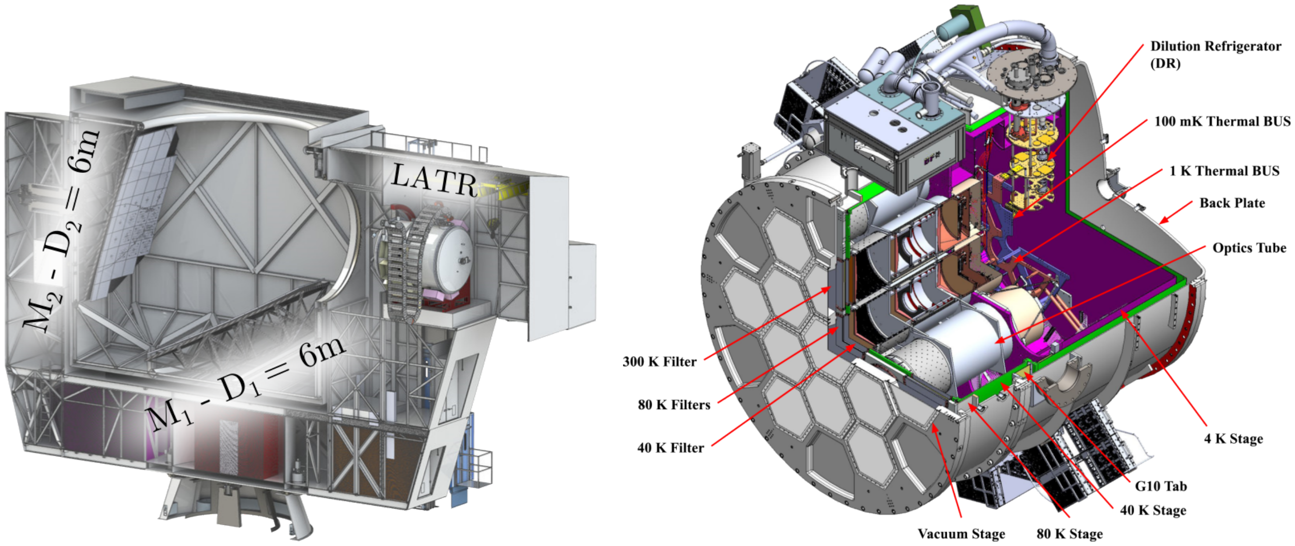

(a) *Receiver module* **(b)** *Low Frequency Telescope (LFT)*

Figure I.2.8: *(a) SO LAT telescope cutaway rendering with the Large Aperture Telescope Receiver (LATR) installed. (b) The receiver encloses 13 Optics Tubes (OTs), cooled down from* 300 K *to* 100 mK *at the detector plane for their good operation. As will be discussed further in Subsection I.2.2.3, filtering is applied to reject out of band signals as well as instrument thermal loading. Images reused from [78].*

tubes for medium and high frequencies. LiteBIRD LFT, Medium Frequency Telescope (MFT) and High Frequency Telescope (HFT) are shown in Fig.I.2.9, where images are reused from [79, 80, 81].

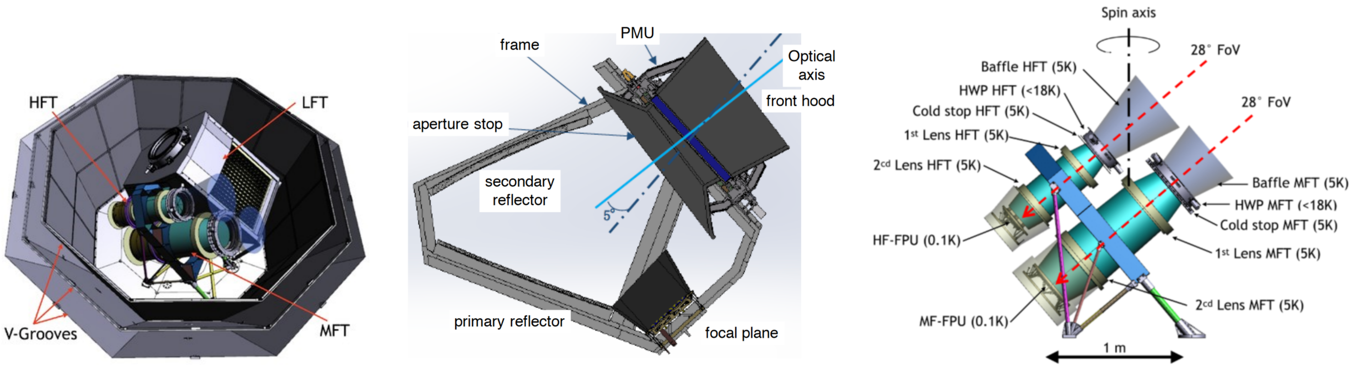

(a) *Receiver module* **(b)** *LFT* **(c)** *MFT & HFT*

Figure I.2.9: *LiteBIRD (a) receiver module, surrounded by V-grooves baffles, and containing (b) the fully reflective LFT. This instrument is constituted of the front hood, stopping the incoming light to avoid spillover on the primary mirror. The latter combines with the secondary mirror to focus the light onto the FPU. The fully refractive (c) MFT and HFT are also contained in the receiver module, both embedded in a cryostat. Similarly to the reflective alternative, the two lenses focus the incoming light, Lyot stopped, down to the FPU. Images reused from [79, 80, 81]*

The expected design characteristics of SO SATs and LATs [82, 83, 84, 85, 79, 78, 86] are summarised in Table I.2.1 and LiteBIRD LFTs, MFTs and HFTs [87, 88, 89, 80, 81] in Table I.2.2. A definition of the beam FWHM is given in Chapter II.3. It directly sets the pixel size, constrained by the fore-optics dimensions.

Table I.2.1: *Design characteristics of SO: operating frequency range* $f \pm \Delta f/2$*, beam FWHM, pixel size, number of detectors, array Noise Equivalent Temperature (NET) and temperature sensitivity* s_T*. The data are extracted from [82, 83, 84, 85, 79, 78, 86].*

FPU	f[GHz]	Δf[GHz] (Ratio)	θ_{FWHM}[arcmin]	Pixel size [mm]	# detectors	NET [µK$\sqrt{\text{Hz}}$]	s_T[µKarcmin]
LAT	27	6 (0.222)	8.4	13.4	222	28.6	52
	39	18 (0.462)	5.4	13.4	222	16.0	27
	93	35 (0.376)	2.0	5.3	10320	6.6	5.8
	145	40 (0.276)	1.2	5.3	10320	6.8	6.3
	225	60 (0.267)	0.9	4.0	5160	12.5	15
	280	45 (0.162)	0.8	4.0	5160	30.0	37
SAT	27	6 (0.222)	91	13.4	1050	10.00	35
	39	18 (0.462)	63	13.4	1050	6.24	21
	93	35 (0.376)	30	5.3	23000	15.17	2.6
	145	40 (0.276)	17	5.3	23000	38.73	3.3
	225	60 (0.267)	11	4.0	12000	130.4	6.3
	280	45 (0.162)	11	4.0	12000	176.07	16

Table I.2.2: *Design characteristics of LiteBIRD: operating frequency range* $f \pm \Delta f/2$*, beam FWHM, pixel size, number of detectors, array NET and temperature sensitivity* s_T*. The data are extracted from [87, 88, 89, 80, 81].*

FPU	f[GHz]	Δf[GHz] (Ratio)	θ_{FWHM}[arcmin]	Pixel size [mm]	# detectors	NET [µK$\sqrt{\text{Hz}}$]	s_T[µKarcmin]
LFT	40	12 (0.30)	70.5	32	48	18.50	53.4
	50	15 (0.30)	58.5	32	24	16.54	32.3
	60	14 (0.23)	51.1	32	48	10.54	25.1
	68	16 (0.23)	41.6	16	144	9.84	19.6
	68	16 (0.23)	47.1	32	24	15.70	19.6
	78	18 (0.23)	36.9	16	144	7.69	15.3
	78	18 (0.23)	43.8	32	48	9.46	15.3
	89	20 (0.23)	33.0	16	144	6.07	12.4
	89	20 (0.23)	41.5	32	24	14.22	12.4
	100	20 (0.23)	30.2	16	144	5.11	15.6
	119	20 (0.23)	26.3	16	144	3.80	12.6
	140	20 (0.23)	23.7	16	144	3.58	8.3
MFT	100	23 (0.23)	37.8	11.6	366	4.19	15.6
	119	36 (0.30)	33.6	11.6	488	2.82	12.6
	140	42 (0.30)	30.8	11.6	366	3.16	8.3
	166	50 (0.30)	28.9	11.6	488	2.75	8.7
	195	59 (0.30)	28.0	11.6	366	3.48	6.7
HFT	195	59 (0.30)	28.6	6.6	254	5.19	6.7
	235	71 (0.30)	24.7	6.6	254	5.34	8.6
	280	84 (0.30)	22.5	6.6	254	6.82	19.0
	337	101 (0.30)	20.9	6.6	254	10.85	21.9
	402	92 (0.23)	17.9	5.7	338	23.45	52.3

The interest in making both space and ground-based observations lies in the trade-off between aperture size versus mapping speed, atmospheric and ground contributions to the signal. Ground based experiments have the advantage of reaching very large aperture sizes, enabling the observation of small angular scales on sky, as can be gathered from comparing the FWHM reached by SO LATs against LiteBIRD telescopes. Space missions can however scan at high mapping speed by spinning fast and are free from ground pickup and atmospheric windowing.

I.2.4 Focal Plane Units

I.2.4.1 Detector coupling

The telescope angular response, polarisation properties, bandwidth and temperature sensitivity are of the highest importance to measure CMB signals accurately and are strongly defined by the FPU. It was previously mentioned in Section I.2.2.4 that instrumental systematic effects can induce spurious polarised signals on the detectors, which may result in contributions to the measured power spectrum, possibly pushing it off the cosmic-variance limit. Considering that the B-mode polarisation signals are of order $10^{-4}\,\mu\mathrm{K}$ for $r = 10^{-1}$, laid against the temperature anisotropies signal with an average temperature of $2.725\,\mathrm{K}$, it is clear that the detectors populating the FPU must have incredibly high sensitivity, thus high SNR, or low NET, where the NET is the temperature signal giving $\mathrm{SNR} = 1$ when integrated over $0.5\,\mathrm{s}$. These detectors would ideally be photon-noise-limited, suffering only from the noise induced by incident photons and not from the detector itself or other sources. Further definition of these characteristics will be given in Section V.1.2 but it is worth mentioning that current detector technologies for CMB observation, namely Transition Edge Sensors (TESs) bolometers and KIDs, are superconductor devices, photon-noise limited by design.

A TES bolometer is made of a superconducting thin film of critical temperature T_c sunk in a colder bath. When biased by the relevant voltage, the light sensor operates in its transitional state and small temperature variations are transcribed into a large change in the TES resistance. The detector stays stable in temperature as the technology relies on a strong electrothermal feedback that linearizes its response, expands its bandwidth, and ensures a direct relation between observed TES current and incident power [90]. The latter is monitored by a Time-Division Multiplexing (TDM) or Frequency-Division Multiplexing (FDM) readout technology relying on Superconducting Quantum Interference Devices (SQUIDs) [91].

KIDs are LC resonators incorporating akinetic inductance sensitive to photo-absorption [92, 93, 94, 95]. Incoming photons with energies greater than the superconducting gap of the break Cooper pairs change the density of quasiparticles in the device, modifying its kinetic inductance. Individual detectors are driven at their natural resonant frequency through a simple RF line. The changes in the amplitude and phase of such probe tone resulting from the modification of the film properties by the absorbed photons are monitored as resonant frequency shifts. Tens of thousands of these detectors can be packed in a single wafer, resulting in a multichroic array with a high Multiplexing (MUX) ratio.

The optical power drastically reduces through the telescope as the light is absorbed, diffracted or scattered away. The atmosphere and the constituents of the instrument load the detectors, raising the photon-noise level, overtaking the CMB levels. Observing time may be limited depending on the weather conditions on site, the cryostat cycles, the components calibrations, and so on. Considering a virtual instrument sensitive to $r < 10^{-3}$ scanning for $\ell < 50$, with a single photon-noise limited pixel mapping the sky [96], and considering the constraints mentioned above, its observation times would span ~ 5 years for a space mission to ~ 200 years for a ground based experiment. To reach the desired sensitivity in r at such large scales in a reasonable observational timescale

[57], such instrument would need hundreds of thousands of such pixels. Multichroic detectors can be employed to further improve the mapping speed. A large instrumental bandwidth, ideally of 10 : 1, is indeed necessary to remove fore-ground contribution of any kind, occurring at closer red-shifts, although current instruments can reach 3 : 1 ratios. Designing an array of highly sensitive, diffraction-limited multichroic pixels providing a suitable FOV necessitates the optimisation of two competing factors: detector count and aperture illumination efficiency, essentially function of the focal optics beam diameter.

I.2.4.2 Optics Tubes

In essence the optics tube consists of a set of fore-optics refractors gathering the incoming light onto the FPU, comprising tightly packed arrays of antenna-coupled detectors. Direct coupling is also an option. Superconducting detectors necessitates cooling down to sub-Kelvin temperatures. In order to avoid any excess noise on the detectors, the cryostats are staged at decreasing temperatures and each stage comes with a set of filters, rejecting the optical and thermal load out of band. A rotating HWP is a standard choice to select the CMB polarised signals by modulation over spurious signals added from foregrounds for instance. The SO OTs, typical of current and future CMB instruments, are shown in Fig.I.2.10 where images are reused from [78].

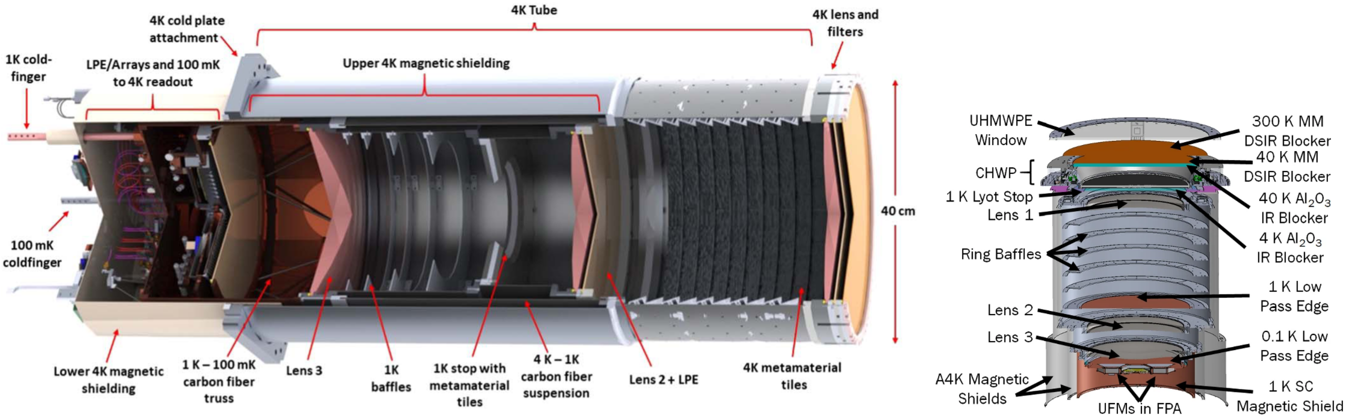

(a) *LAT optics tube* **(b)** *SAT optics tube*

Figure I.2.10: *Detailed view of the Computer Assisted Design (CAD) modelled SO (a) LAT and (b) SAT fully refractive optics tubes, using a 3 lens system.*

I.2.4.3 Focal Optics

Current technological developments are made to reach the desired precision, namely, directly coupled detectors [97, 98, 99], coherently summed hierarchical arrays [100, 101, 102], platelet horns [103] and antenna coupled lenslets [104, 105], which will now be discussed in details.

I.2.4.3.1 Filled array of directly coupled detectors

A filled array of directly coupled detectors advantageously occupies the focal plane area entirely. Immediate consequences of directly illuminating such arrays are that the focal plane effective area increases, the gathered power is not diluted by any focal optics, and the number of detectors is the largest reachable, resulting in a higher sensitivity and thus, high throughput. Another consequence is that the FOV is fully sampled since pixel size is minimised and spacing can thus reach the required $0.5\mathcal{F}\lambda$ Nyquist spatial sampling rate. This results in high mapping speed. Since no focal optics are required, the fabrication costs and complexity are kept low.

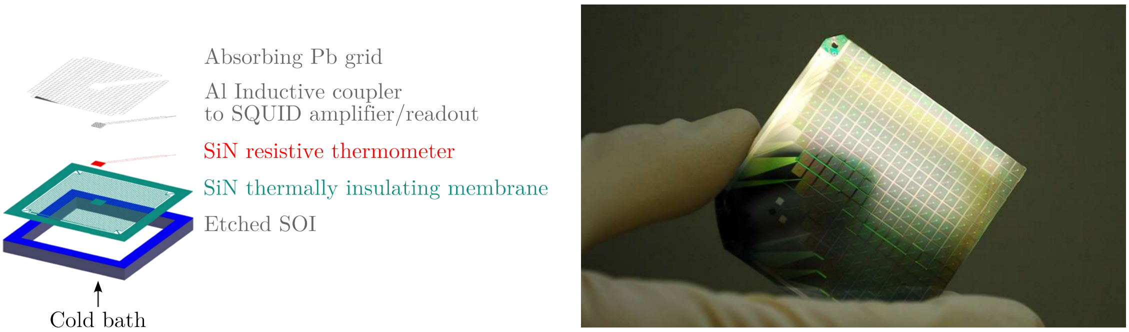

(a) **(b)**

Figure I.2.11: *(a) Exploded view of a single TES bolometer as designed for (b) the Q&U Bolometric Interferometer for Cosmology (QUBIC) focal plane array. The photon absorbing layer, made of Lead, couples thermally to the Silicon Nitride thermometer operating in its transitional state via a voltage bias. Any absorbed photon results in a change in the resistance of the thermometer, inductively coupled to the superconducting Aluminium line of the amplifier SQUID and further read out. Images are reused from [106, 107].*

However, the combination of smaller detectors and lower power shined upon them induces much lower SNRs, giving a factor of 2 drop in sensitivity compared to other FPUs alternatives [62]. The pixel beams are also inherently broader and the devices inevitably mix stray light with the CMB signals. Characterisation of the integrated Primordial Inflation Polarization Explorer (PIPER) Backshort Under Grid (BUG) kilopixel TESs arrays was recently conducted for the balloon-borne mission pre-flight validation [111]. The detectors shown sufficient Noise Equivalent Power (NEP) to map the CMB B-mode signals for $\ell < 300$ down to $r < 0.007$. On the ground, NIKA2 has been successfully deployed and commissioned, and realised a first successful science verification run in April 2017 [108]. Whilst PIPER aims at observing large angular scales, this instrument is concerned with high ℓ, relying on a total of 2900 KIDs distributed over four arrays scanning the 150 GHz and 260 GHz bands. The direct detection is accomplished via a Hilbert fractal inductive meander, sensitive to both polarisation by design. Both type of detectors offer a very similar NET response. The QUBIC instrument relies on directly illuminated arrays used in conjunction with re-imaging fore-optics, typical of interferometers [112]. The signal from the sky enters the cryo-

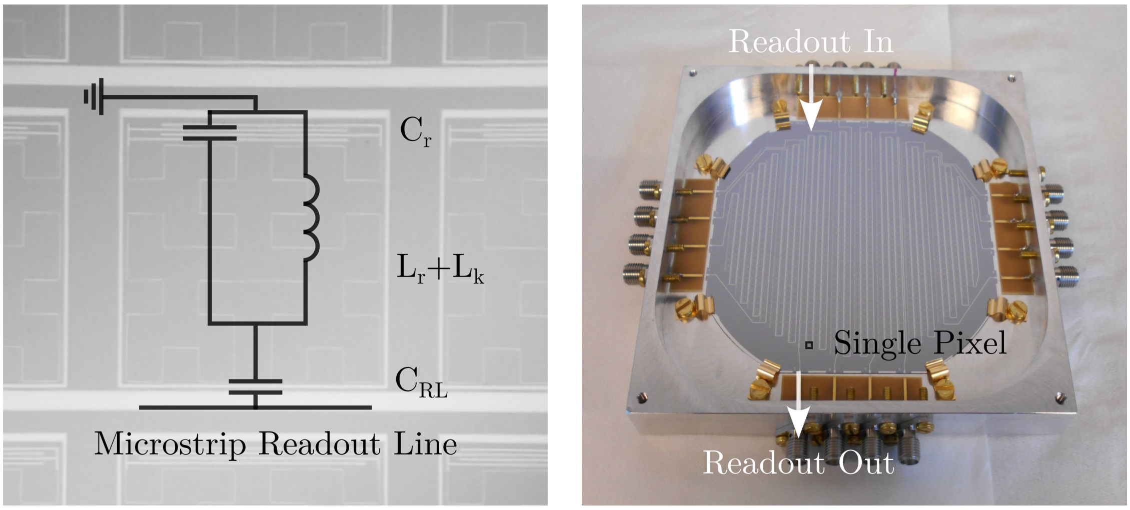

(a) **(b)**

Figure I.2.12: *(a) A single KID, part of (b) the Néel IRAM KIDs Array (NIKA2) focal plane array. The Hilbert pattern of the inductor allows for the detection of both polarisations. When it absorbs incoming photons, the natural frequency of the lithographed L_rC_r circuit, fed by the microstrip line at the bottom, is shifted off as the kinetic inductance L_k changes. This effect is fed through the microstrip line via a coupling capacitor C_{RL}. A simple comparison by demodulation of the input and output signals allows a high MUX readout. The photographs are reused from [108, 109, 110].*

stat through High Density Poly-Ethylene (HDPE) window, a rotating half-wave plate modulates the polarised CMB signals, and a polarizing grid selects one of the two linear polarization components. An array of back-to-back corrugated horns collects the radiation and re-images it onto a dual-mirror optical combiner that focuses the signal onto two orthogonal TESs bolometers focal planes, each constituted of 256 pixels adding up to 1064 in total. A dichroic filter placed between the optical combiner and the focal planes selects the two operating frequency bands, centred at 150 GHz and 260 GHz. The technical demonstrator was successfully tested and is currently being installed on the observation site [113].

I.2.4.3.2 Coherently summed hierarchical arrays of sub-wavelength antennas

Alternatively, the detectors can be coupled to a microstrip network architecture coherently combining the signals received from a phased antennas array. The focal planes of the Suborbital Polarimeter for Inflation Dust and the Epoch of Reionisation (SPIDER) balloon, which recently landed safely after its second flight, uses such coherently summed hierarchical arrays [100, 101, 102]. A similar FPU arrangement is also adopted at the BICEP2 and Keck array telescopes in the South pole [114]. This focal plane is operating as follows: the incoming optical power is coupled via two co-located, orthogonally polarised planar antenna arrays, namely slots patterned in a ground plane lithographed on a Silicon wafer, separated to spatially sample the acquired light. For a given polarisation orientation, the received signals are coherently combined through a microstrip summing architecture to synthesize a single equivalent antenna. The result is band-pass filtered before being acquired by the TES bolometer. The BICEP collaboration summarised the performances reached for BICEP2, the Keck array and the SPIDER instruments in a report, stating that the cameras are reaching 20% to 30% bandwidth at 95 GHz, 150 GHz and 230 GHz, the typical cross-polarisation is about 0.5% and the optical efficiency attains 35% at worst. There are roughly

2500 detectors populating the FPU of each instrument, with a higher limit on sensitivity reaching $\sim 300\,\mu\mathrm{K}\sqrt{\mathrm{Hz}}$, although $\sim 10\,\mu\mathrm{K}\sqrt{\mathrm{Hz}}$ sensitivities were consistently measured over the arrays at 150 GHz. The synthesized beam has -12 dB sidelobe levels, further cut down by the integration of a cold stop in the OTs. The antenna array chip is directly compatible with the detector plane as they both rely on lithography techniques applied to Silicon wafers for their fabrication, an inherently scalable and cost-effective manufacturing process. The free-space to dielectric mismatch is mitigated by a $\lambda/4$ Quartz Anti-Reflection Coating (ARC), resulting in an overall design immune to differential thermal contraction and misalignment. Stray light coupling remains a challenge, accounting for 3% to 4% of the total optical power received.

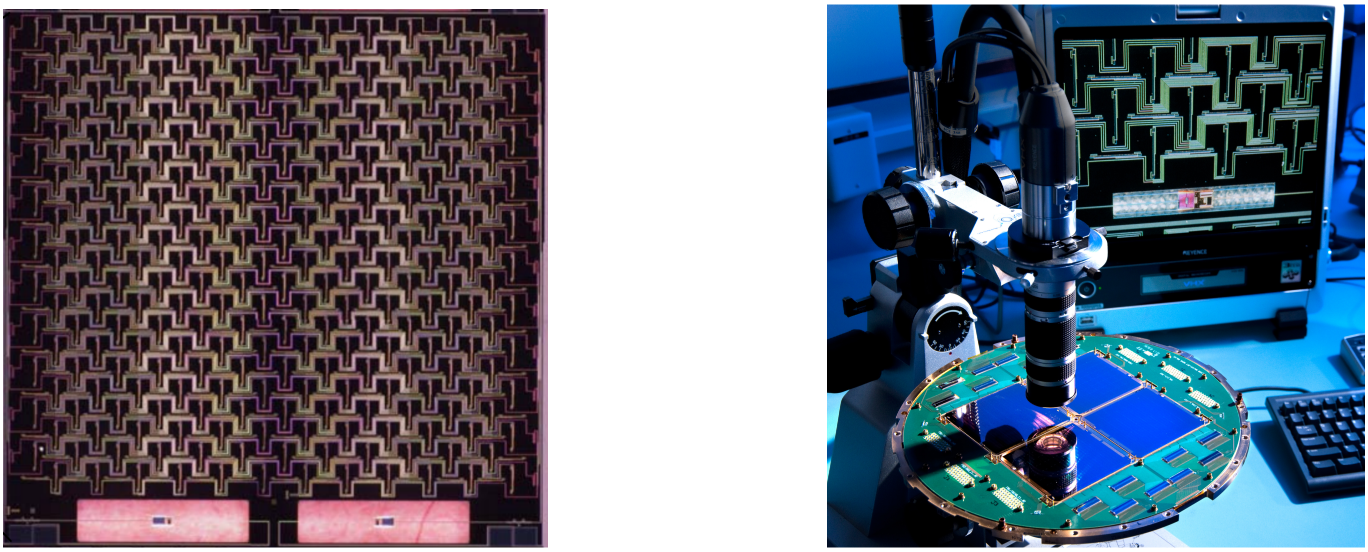
(a) **(b)**

Figure I.2.13: *(a) Photograph of one of the four BICEP2 arrays incorporated onto (b) a focal plane wafer, being scrutinised under the microscope [114, 115, 116]. The large pack of antennas is clearly visible on the top, with their combining lines weaved around. At the edges, the lines are running through microstrip filters selecting the bandwidth of observation of a given set of antennas. The bolometers are sitting in the bottom of the array.*

I.2.4.3.3 Horn antenna arrays

Instead of combining the beams of coherently summed hierarchical arrays of sub-wavelength receivers, larger antennas can be used. In particular, feedhorns have been widely employed in radio astronomy and are a well demonstrated technology. For instance, the various FPUs populating the constitutive instruments of the Planck satellite where based on directly illuminated bolometers coupled with corrugated horn antennas [61]. LiteBIRD MFT, HFT and SO FPUs will also rely on directly machined feed-horns coupled to TES bolometers [87].These devices defines the angular response of a pixel and in the current designs, the use of an Ortho-Mode Transducer (OMT) is preferred to separate both polarisations and subsequently couple the divided power to the detectors, placed at the end of a microwave circuit after on-chip signal processing. Corrugated horns allows high control of the beam profile and ensures low cross-polarisation levels but necessitates a larger aperture diameter than other type of horns by design [103]. An comparable alternative is the smooth-walled multi-flare angle horn [117]. This type of antenna can be more closely packed in an array, offering an elegant trade-off between beam coupling efficiency and beam systematics control. The Planck High Frequency Instrument (HFI) had 36 pixels in total, as CMB instruments require a number of detectors orders of magnitude above, the scalability of the horn arrays becomes a challenge. Machining the block in Aluminium 6601 and gold plating is the most straightforward and cost-effective approach but the manufacturing process present low tolerances. The thermal contraction differential between the metal and the Silicon detector wafer also becomes a concern at such large scales. Alloys could potentially be used as an alternative [118] although specialist tools are then required and the process becomes more time consuming. Alternatively, stacked platelets of metallised Silicon can be used, resulting in a direct compatibility with the detector plane. The consecutive apertures are either reactive ion or laser etched, then the metal is lithographed. The second option is a promising manufacturing method, still in development, as it largely reduces cost and machining time compared to the Reactive Ion Etch (RIE) [103]. As was mentioned in Section I.2.2.2, horn antenna arrays present optimal optical quality but inherently limit the mapping speed due to a lower $\mathcal{F}$ and a larger aperture size [62]. Whilst the band coverage of such antenna could reach 10 : 1 bandwidth or higher, the OMT is limited to a 2.3 : 1 ratio. Mismatch between the two elements may further result in cross-polarisation leakage, reduction of power efficiency and loss in bandwidth [119, 120]. The Atacama Cosmology Telescope (ACT)POL instrument comprises 2043 detectors [121] fed by OMT-coupled horns, operating with an optical efficiency of 50% to 70% over the 75 GHz – 110 GHz and 125 GHz – 175 GHz bands [121]. The LiteBIRD collaboration reported 70% optical efficiency on all four bands, narrowed down due to an OMT to horn block mismatch [122]. The SO collaboration also presented experimental characterisation of the focal planes giving an average optical efficiency of 77% for the 200 GHz – 240 GHz and 270 GHz – 320 GHz bands [120].

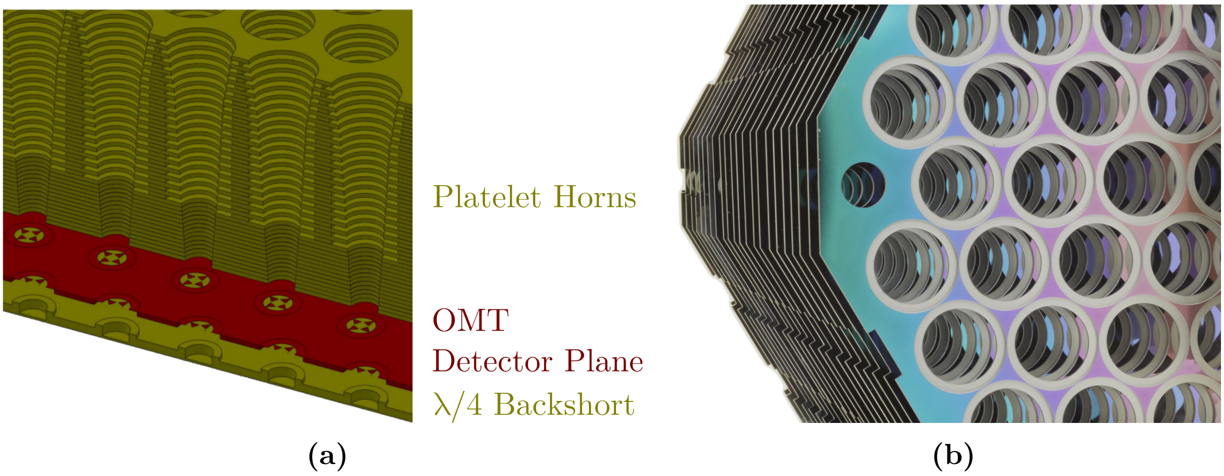

Figure I.2.14: *(a) CAD model of a corrugated platelet horn array and (b) the successive fabricated layers [123]. OMTs are stacked under the feedhorns, separating the polarisation signals and transferring the power to the detectors. A $\lambda/4$ backshort couples the power radiated on the back to the OMT.*

I.2.4.3.4 Planar antennas coupled to lenslet arrays

A final pixel design approach consists of coupling the detector pair to a dual-polarisation sensitive, broadband planar antenna fed by an hyper-hemispherical lenslet. Sinuous antennas are favoured for such application as they are log-periodic structures. Their operational frequency bandwidth is set by the radially evolving metal pattern: the largest and smallest features of the antenna respectively set the lowest and highest frequency accessible. The hyper-hemispherical lenslet going atop the antenna is constituted of an extended hemisphere made of Silicon or any other dielectric approaching its electrical characteristics. Such profile approximates an ellipse, which would fully focus an incoming plane wave [124, 125, 126]. The overall design is fully embedded in Silicon, ensuring a straightforward scalability and full compatibility with the detector plane. The antenna is suspended on a membrane so that the energy fully transits through the overlaid dielectric. The geometry of the overall focal optics scales down with the dielectric refractive index, and the lenslets have high $\mathcal{F}$ compared to horns. This result in an attractive trade-off between pixel spacing, $\mathcal{F}$ and optical efficiency allowing for high mapping speeds.

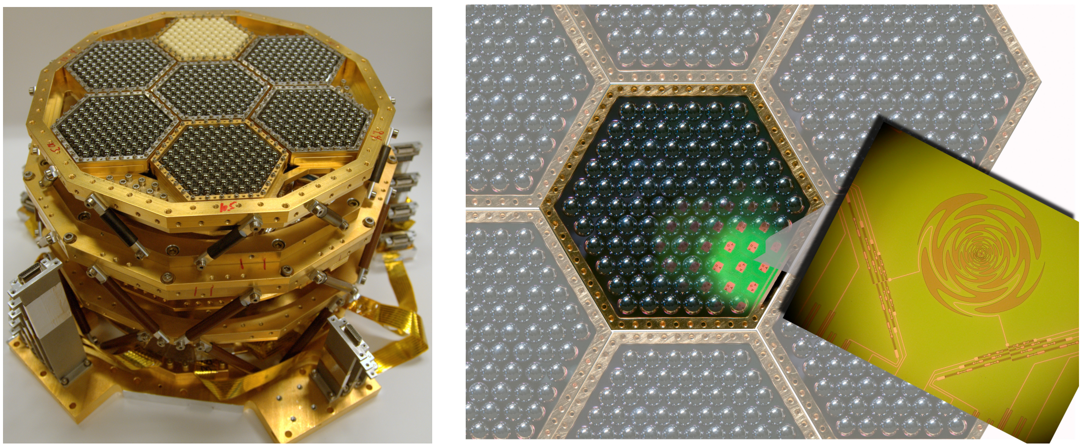
(a) **(b)**

Figure I.2.15: *(a) The complete Polarization of Background Radiation (POLARBEAR)2 focal plane, mounted on its cryogenic assembly structure. The full pack of hyper-hemispherical lenslets is clearly visible. (b) The focal optics are coupled to dual-polarised planar sinuous antennas feeding the subsequent detectors. As for the coherently summed hierarchical antennas, the broadband nature of the sinuous necessitates the use of microstrip filtering to select the band of interest before feeding the signal to the detectors, as shown on the insert. Both pictures are reused from [125].*

Based on the latter advantages, the LiteBIRD collaboration considers using sinuous antenna coupled lenslet arrays in conjunction with TESs bolometers to fully fill the LFT FPU [87], where 12 bands could be covered by 2 pixel sizes. However, the minimum feature size that can be patterned for the antenna, coupled with the need of and ARC to match the lenslet to free-space significantly limit the bandwidth attainable by such pixel design to ratios of order $1.2 : 1$ to $2 : 1$, comparable with other focal optics. On the larger wafer sizes required for the coming CMB experiments, the thermal contraction differential between the ARC layer and the lenslets coupled to their non-planar profiles could result in partial mismatches or even delamination. As for previous designs, since the detector plane is not encased, stray light is picked up by the lenslets. To mitigate this issue, an absorbing resistive layer can be added in between the chip and the lenslet array, but hinders hindering the detector performances [127]. The POLARBEAR2 collaboration implemented this type of focal optics array for 7588 pixels in the South Pole, and found cross-polarisation levels of 4.6% and 2.2% at the 77.5 GHz − 102.5 GHz and 130 GHz − 170 GHz operational bands, respectively. Simon´s array will expand on POLARBEAR with two more 3.5 meter telescopes to be deployed at the James Ax Observatory, each of which should incorporate ∼ 10000 detectors. The South Pole Telescope (SPT) was another experiment successfully deployed in the austral summer of 2016–2017 with a full focal plane of 2690 pixels covering the 80 GHz − 110 GHz, 135 GHz − 167 GHz and 190 GHz – 245 GHz bands on a 1 arcmin resolution on sky, with an optical efficiency of 25%, 44% and 26.5%, providing $\sim 9\,\mu\mathrm{K}\sqrt{\mathrm{Hz}}$, $\sim 8\,\mu\mathrm{K}\sqrt{\mathrm{Hz}}$ and $\sim 28\,\mu\mathrm{K}\sqrt{\mathrm{Hz}}$ NETs respectively.

I.2.5 MetaLs as a focal optics alternative

Inspired by the existing hyper-hemispherical lenslets, MetaL are a new technology under development [128, 129]. Metamaterials offer pristine control over the amplitude, phase and polarisation states of light waves [130, 131]. Additionally, the thin film fabrication techniques involved in their manufacturing enables scalability of the planar metamaterial-based surfaces, which can serve as a base for various quasi-optical designs [132, 133]. A lenslet design based on such technology, embedded in Silicon, should enable finer engineering of the sidelobe levels, cross-polarisation, and other beam properties of the focal optics whilst being directly transferable to the detector plane. A fully embedded option would scale down with the refractive index of Silicon, resulting in an attractive mix of compactness due to a low pixel spacing and high optical efficiency, increasing the mapping speed. Whilst ARC is still required on the image side, the device is flat and the incoming field is effectively a plane wave, allowing for an equally plane coating layer. Several ARC options are currently under development [134, 135, 136, 137] to be applied to hyper-hemispherical lenslets or the larger fore-optics. These can be made in a planar design and applied to a MetaL, relaxing the fabrication constraints and minimising the potential mismatches defects. Preliminary investigations are ongoing to prove the MetaL concept [138]. Inscribed in this effort, the present work thoroughly analyses the MetaL air-gapped prototype shown in Fig.I.2.16 by presenting a full beam characterisation conducted both in a set of electromagnetic simulations, and experimentally on a dedicated, systematics limited test bed, warm. To further prove the MetaL concept, the preliminary stages of a cold beam holography measurement are further drawn, in particular, the design and fabrication of a complete pixel, sensitive to a single polarisation and fully matched to free space, where a MetaL made in Cardiff University is coupled to a sinuous antenna feeding a set of KIDs.

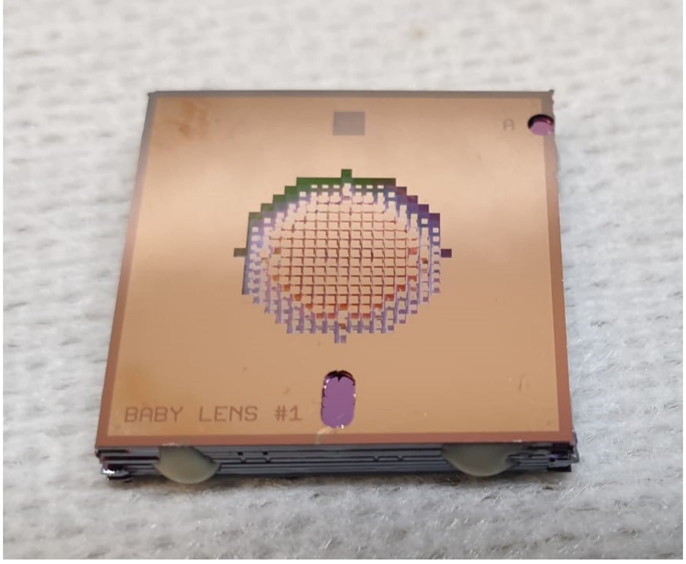

Figure I.2.16: *Photography of a phase-engineered, air-gapped MetaL prototype, taken by the author.*

II Optical Systematics

Part II Outline

To characterise the suitability of the proposed lenslet for CMB applications, it is necessary to define its inherent beam characteristics and explore its impact as if it was integrated in an instrument FPU. Various CMB analysis techniques are in preparation to process the data gathered by future instruments [72, 73, 74, 75]. Currently these tools can be used to predict the missions outcome relying on an end-to-end pipeline approach where each telescope constituents is integrated and its systematics considered throughout.

Whilst scanning, the CMB map is recorded as the overlapping combination of timed detector responses reorganised in TODs. A map making analysis [139, 140, 77, 72] is traditionally run to determine a maximum likelihood of what the sky map should be over the entire bandwidth, taking into account beam systematics, rotation on sky while scanning, pixel-to-pixel correlations and noise contributions. Future datasets are expected to be much larger and considering the sensitivities required, the community focuses on optimising the current methods. Amongst the main requirements lies the realistic characterisation and incorporation of beam systematics. Tools such as Fast Effective Beam Convolution in Pixel space (FEBeCoP), developed for Planck [141], estimates an effective beam for each pixels, reconstructed from input beam parameters, polarisation angles, cross-polar leakage, etc. The resulting beams are then combined and convolved with the desired regions of the sky at selected time spans, allowing for full sky convolution. This operation is computationally more efficient if done in Fourier space, where the beam may again be expressed as a window function decomposed in spin weighed spherical harmonics [142].

In this part, a review of the main characteristics of a beam will be conducted in Chapter II.3 and its systematics will be further described. These definitions will enable an deeper understanding of the beam profile, mentioned a number of times in the discussion on CMB instrumentation given in Part I. The characteristics presented here will further be inspected during the design and experimental study of the performances of the MetaL prototype lenslet in Part III and Part IV. An elementary map based analysis will then be presented in Chapter II.4 where the compiled C_ℓ^{BB} of a sky map will be convolved with an ideal Gaussian beam. This method will be of ulterior use in part IV, where the non-ideal beams of a hyper-hemispherical lenslet and the MetaL device will be compared.

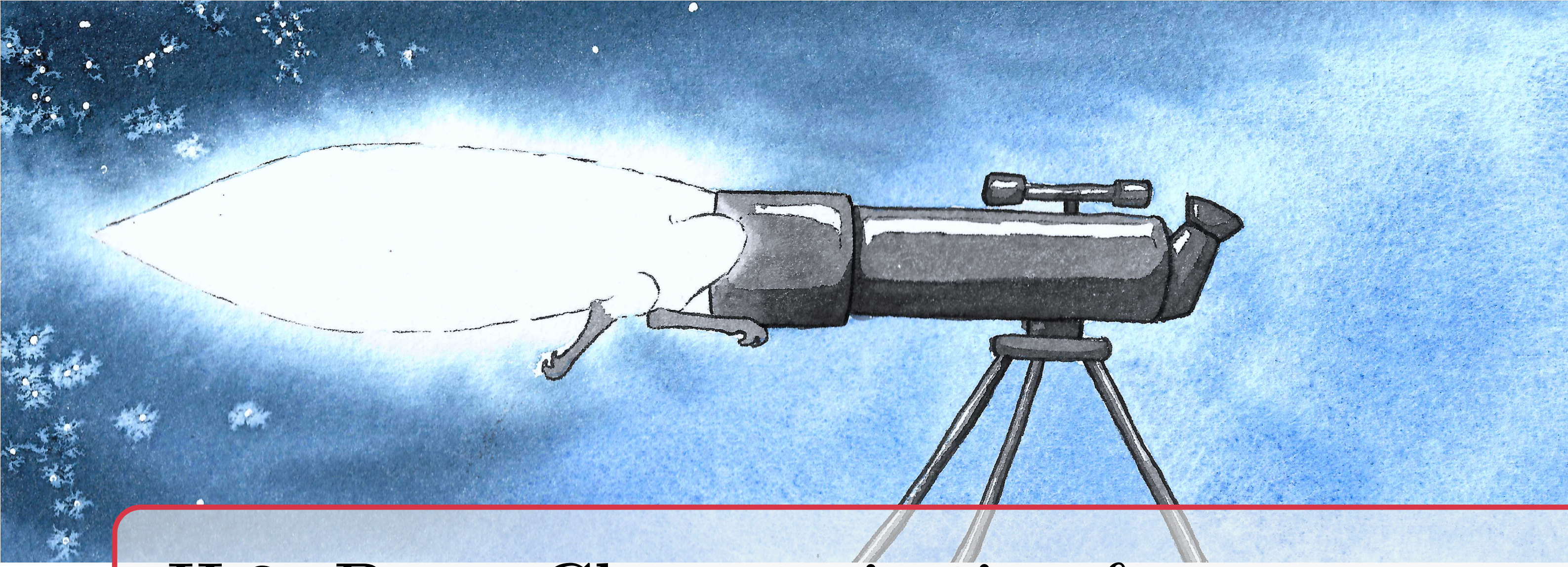

II.3. Beam Characterisation & Systematics

To prove the concept of MetaLs in the context of modern and future CMB experiments, a prototype device is analytically and experimentally characterised in the present work. Its beam will be simulated, then measured and compared against a simulated hyper-hemispherical lenslet counterpart. The comparison is extended to a benchmark analysis where the beam of both devices are projected on sky and their effect, compared. The preliminary design, fabrication and experimental plan of a pixel assembly resembling that of a CMB FPU, where the lenslet is coupled to a sinuous antenna feeding detectors will further be discussed. This chapter gives preliminary definitions which will be referred to throughout the rest of this work, starting by a few general characteristics and systematics of a beam.

II.3.1 Laguerre-Gaussian Beams

The aperture size of focal optics under consideration for CMB experiments is generally the same order of magnitude as the operating wavelengths, as can be seen in Table I.2.2 and Table I.2.1. It follows that the propagated field can be described as a Laguerre-Gaussian Beam (LGB) E_κ (II.3.7) [143], constituted of a superposition of Laguerre-Gaussian modes E_p (II.3.8). The MetaLs and hyper-hemispherical counterpart of concern for the present proof of concept are designed with a 5 mm radius and are therefore suited for such beam decomposition. The feeding elements they are coupled with similarly present wavelength sized apertures.

Classic characteristics for a beam propagating in free-space along an OA orientated in the z direction are shown in Fig.II.3.1a. In this figure, the source radiates a beam from the phase centre C_ϕ, which may be offset from the physical centre of the device and show a Gouy phase shift ϕ_0. At this origin, the beam has a waist w_0 (II.3.1), increasing along with the distance from the beam origin on the OA z (II.3.8), where it is noted w. At any given distance z, the normalised intensity decreases, ultimately falling down to $1/e^2$ where the beam reaches its limit extent, the beam width w_e (II.3.9).

$$w_0 = \frac{\lambda\sqrt{2\ln 2}}{2\pi\tan\theta_0} \tag{II.3.1}$$

$$w = w_0\sqrt{1+\left(\frac{\lambda z}{\pi w_0^2}\right)^2} \tag{II.3.2}$$

$$w_e = \frac{w}{\sqrt{2\ln 2}} \tag{II.3.3}$$

A radius of curvature R_b can be established at any given surface of constant phase, or equiphase. The beam will eventually diverge asymptotically along a cone defined by the angle Θ. The Rayleigh length (II.3.4) is the distance from the phase centre at which the beam waist is equal to $\sqrt{2}w_0$. It is a good approximation of the range of focus of the source. Going past the Rayleigh range, the wavefront curvature stabilises, thus the source radiates in the far field region.

$$z_R = \pi w_0^2/\lambda \tag{II.3.4}$$

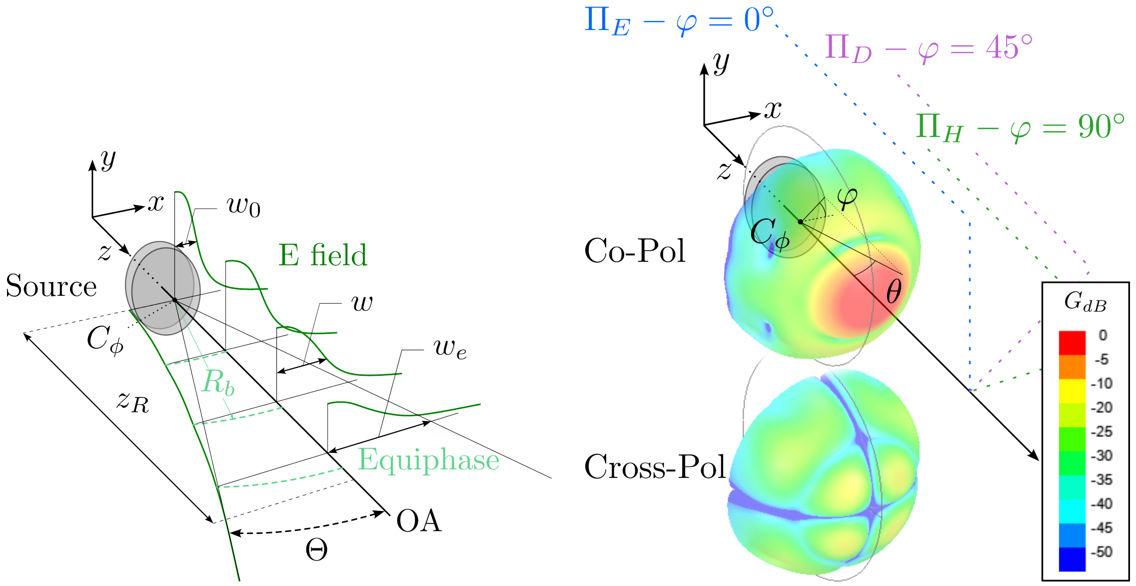

(a) **(b)**

Figure II.3.1: *(a) Gaussian beam propagating along z and its characteristics. The E-field intensity along a given equiphase is shown for cuts at various z projected on a plane parallel to the Gaussian source aperture for clarity. (b) Co and cross-polarisation far field patterns in* dB *originating at C_ϕ and the related spherical coordinates: elevation φ and azimuth θ. Figures made with Inkscape by the author.*

To a first order the far field intensity profile of a diffraction limited device of diameter D_c and operating at the wavelength λ is depicted by the Fourier transform of an Airy profile, integrated over its aperture (II.3.5) at the distance of observation z. In practice, a realistic antenna far field will incorporate diffraction contributions by design, as shown in Fig.II.3.6 for instance. This radiation profile corresponds to the near field pattern of the device, integrated as explained before [144, 145], where the near field itself is compiled from the local currents via Maxwell equations. Electromagnetic simulation software such as ANSYS High Frequency Structure Simulator (ANSYS-HFSS), extensively used in the present work, are relying on this approach to depict the currents and fields of a modelled optics.

$$I(z) = I_0 \left(\frac{2\mathcal{J}_1(z)}{z} \right)^2 \tag{II.3.5}$$

$$z = \frac{\pi D_c \sin\theta}{\lambda} \tag{II.3.6}$$

The far field can be summarised through the E, D and H-plane cuts, where the E and H-planes are containing the E and H-field directions respectively, whilst the D-plane is the median plane. Describing a beam radiated by a device in these three planes procures an immediate description of its properties, defined in Section II.3.2. This beam representation, also illustrated in Fig.II.3.6, will be used throughout the present work.

Comparatively to the integrated Airy pattern, a finer representation of a focal optics beam is given by a LGB decomposition. The normalised form of the κ^{th} order LGB is transcribed in cylindrical coordinates by (II.3.7). Each LGB mode is expressed by (II.3.8), where the $\mathcal{L}_p$ are the ordinary Laguerre polynomials. The complex amplitudes A_p of each mode have an analytical solution when the field at the aperture is known, as is the case for feed horns or simple apertures [146, 147]. This decomposition was encoded in Python for further use in Part IV and is available in Appendix B.

For situations where the field at the aperture cannot be derived, as is the case for lenses, they may be simply replaced by a generic complex number of amplitude α_p and phase ϕ_p (II.3.9). Figure II.3.2 presents the five first LGB modes normalised and three beam profiles for $\kappa = 0$, 2 and 5. Higher order modes, optically noticeable as they add a non-negligible amount of side lobes, as per shown in Fig.II.3.2b, are effectively contaminating the beam. The gaussicity, further defined in Section II.3.2, primarily defines the quality of the Gaussian beam radiated by a focal optics.

$$E_\kappa(r,z) = \sum_{p=0}^{\kappa} A_p E_p(r,z) \tag{II.3.7}$$

$$E_p(r,z) = \sqrt{\frac{2}{\pi w^2}} \mathcal{L}_p(u) \exp\left[-\frac{u}{2} - j\left(kz + \frac{\pi r^2}{\lambda r_b} - (2p+1)\phi_0 \right) \right] \tag{II.3.8}$$

$$A_p = \alpha_p e^{-j\phi_p} \tag{II.3.9}$$

$$u = \frac{2r^2}{w^2} \tag{II.3.10}$$

$$\eta_p = |A_p|^2 \tag{II.3.11}$$

$$\phi_0 = \arctan\left(\frac{\lambda z}{\pi w_0^2} \right) \tag{II.3.12}$$

II.3.2 Optical Properties & Systematics

As was depicted in Part I, within a given instrument, a source radiating a beam with a similar profile as the one shown in Fig.II.3.6 would be coupled to the fore-optics on one hand and the detector plane on the other hand. In a similar manner, the MetaL characterisations conducted in Part IV and Part V necessitate to combine the lenslet with a source probe, namely a waveguide

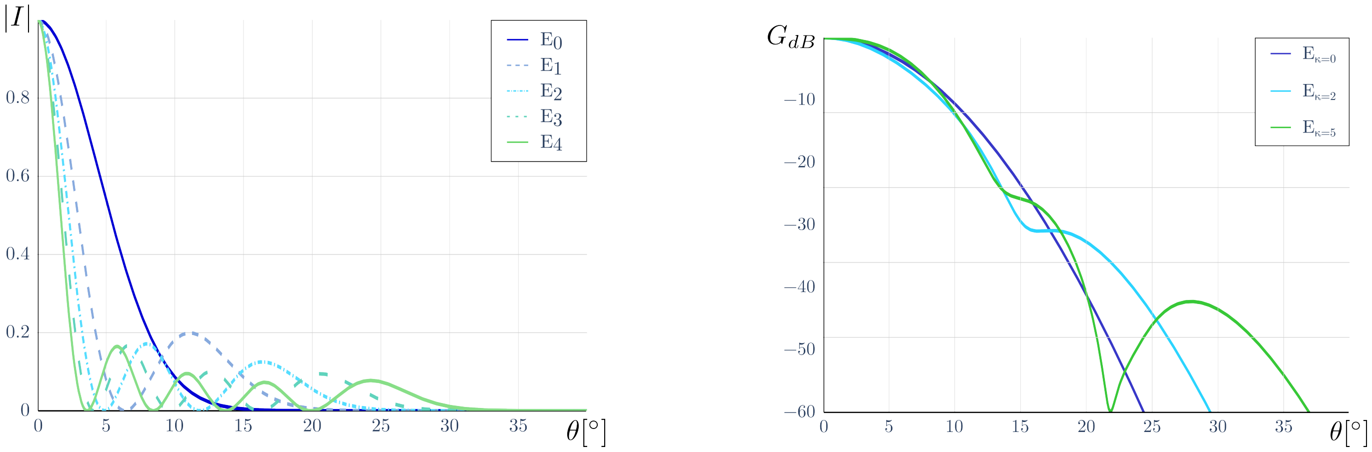

(a) **(b)**

Figure II.3.2: *(a) Normalised intensity $|I|$ of the $p = 0$ to 5 LGB modes. (b) LGB for $\kappa = 0$, 2 and 5, in* dB. *$\kappa = 0$ is a perfectly Gaussian beam. Figures made with Python and Inkscape by the author.*

transition and a sinuous antenna for the warm and cold measurements, respectively. To establish the efficiency of such coupling the following properties must be checked:

Gaussicity η_0

Fraction of the power contained in the beam main lobe corresponding to the 0^{th} order optical mode of a LGB beam decomposition. It is expressed as a percentage of power, obtained from (II.3.11) with $p = 0$. A low gaussicity implies losses to higher order modes which must be avoided when designing a focal optics. If only the main lobe of the beam of a CMB instrument is considered, then since at low ℓ, the cosmic variance is typically of order 5% (I.1.3), $\eta_0 > 95\%$ is a good first order approximation on the gaussicity requirement for a proper reconstruction of the power spectra.

Differential Gain Δg

The absolute value of the difference between the maximal peak directivity of the beam in the E and H-planes (II.3.13), g_E and g_H respectively, expected to be 1% or lower in typical CMB instruments [66, 148, 149] to avoid contaminations of the B-mode signal.

$$\Delta g = \frac{|g_H - g_E|}{(g_H + g_E)/2} \tag{II.3.13}$$

Beam Ellipticity $\mathcal{E}$

Square of the numerical eccentricity of the beam (II.3.14), where w_0^E and w_0^H are the beam waist in the E and H-planes. Elliptical beams [66, 150, 151] generates spurious spherical harmonics resulting in E to B leakage, but for $\mathcal{E} < 10\%$, this defect can be identified and removed post-processing.

$$\mathcal{E} = \frac{\left|w_0^H - w_0^E\right|}{w_0^H + w_0^E} \tag{II.3.14}$$

Cross-polarisation Beam Shapes

The cross-polarisation is defined as per [152] and effectively describes a leakage from one optical polarisation to the other. For axi-symmetrical optics radiating a linearly polarised wave, the cross-polarisation shapes presents a quadrupole symmetry near the optical axis, transforming to a dipole-like symmetry off axis which can be derived in the limit case of a circular aperture [153]. A deviation from this pattern transcribes into an E to B leakage. The maximal cross-polarisation level must be kept below 1% for CMB experiments [154, 151].

Coupling efficiency $\eta_\mathbf{C}$

Ratio P_t/P_i of the total power P_t transmitted through the optics, integrated above the aperture of the device in the sky direction, over the input power P_i contained in the section of the source beam illuminating the aperture of the device. If both beams are Gaussian and properly aligned, the efficiency calculation reduces to that of a power coupling coefficient for two axially aligned beams of width w_1 and w_2 (II.3.15). η_C is directly affecting the throughput of a given instrument as the fraction of source brightness observed at the detector plane. Namely, each optical components will have a given efficiency which can be factorised in (I.2.1). Coupling efficiency, or optical efficiency, is often used to depict the performances of any given FPU, and standard values were given for the focal optics options reviewed in Part I.

$$\eta_C = \frac{4}{\left(w_1/w_2 + w_2/w_1\right)^2} \tag{II.3.15}$$

Bandwidth BW

Frequency coverage for which the focal optics radiates a nearly Gaussian beam with sufficiently low cross-polarisation level and minimal attenuation at focus.

Strehl Ratio $\mathbf{S_R}$

Ratio materialising the phase centre offset and, in the case of focal optics, LGB higher order contributions to the beam when compared with a diffraction limited focusing system (II.3.16). This characteristic is often used for larger fore-optics components, where the Gaussian description of the beam is traditionally replaced by a combination of physical and geometrical optics. The Strehl ratio is effectively described as the exponential of the negative RMS difference between an ideal, diffraction limited optics of equivalent effective aperture size (II.3.5), and the field of the actual device (II.3.16) [53].

$$S_R = e^{-\left(\overline{\Delta\phi^2} - \overline{\Delta\phi}^2\right)^2} \tag{II.3.16}$$

A practical view of S_R is shown in Fig.II.3.3, where the ideal beam of a diffraction limited aperture of $R = 5\,\mathrm{mm}$ is plotted against two LGBs profiles. The wavefront offsets $\Delta\psi$ correspond to the area between the Airy profile, in red, and the near Gaussian or non-Gaussian beam, in green and purple respectively. Clearly, the Strehl ratio portrays optical deviations in a similar manner as gaussicity, both providing close results. The latter will be the criteria of choice through this work as it gives a quantified loss of power to higher order optical modes but it should be noted that the S_R can be more easily related to aberrations through an adequate wave decomposition [53, 155, 156].

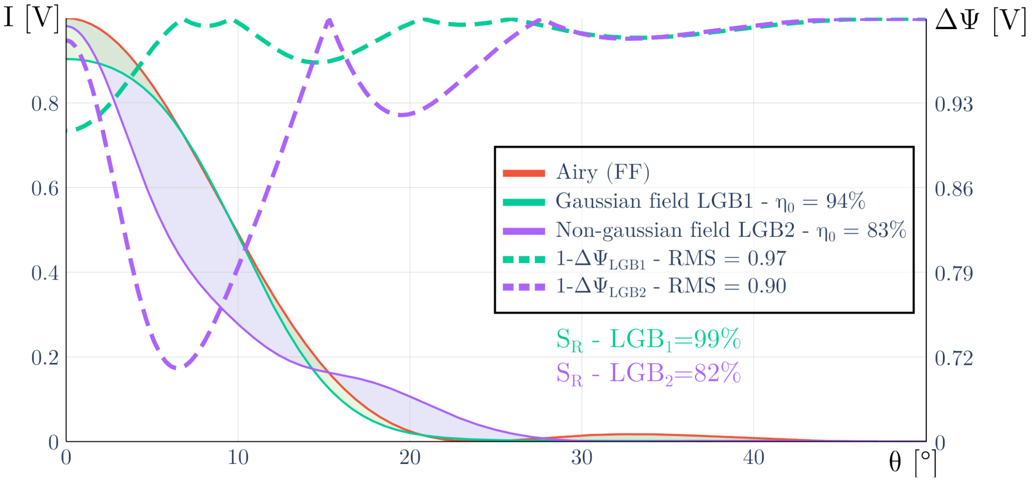

Figure II.3.3: *Description of the Strehl ratio by comparison of an An Airy profile, ideal far field radiation pattern of a* 5 mm*, plotted in red, with a nearly Gaussian beam and a non-Gaussian beam, in green and purple respectively. The wavefront offsets* $\Delta\psi$ *are given for both in dashed lines and corresponds to the areas underlined in matching colours. Figures made with Python and Inkscape by the author.*

Common Pointing σ_χ

Relative distance offset in the average position of the beam centroids of the A and B polarization at focus.

Differential Pointing $\sigma_{\chi_\mathbf{d}}$

Relative angular offset at focus, induced by the focal optics, between the E and H polarised beam centroids in units of the nominal beam width.

Polarisation Rotation $\theta_\mathbf{d}$

Non-orthogonality of the two polarization directions x and y within the focal optics.

Beam truncation T

Ratio of the beam width w_t (II.3.3) of the source probe at the truncating distance F_0 over the diameter of the coupled optics D_c (II.3.17). Fig.II.3.4 shows a truncation $T = 1$, where the width at the optics aperture matches its size, $w_t = D_c$.

$$T = \frac{w}{D_c} \tag{II.3.17}$$

The edge taper T_e describes the effect caused by a stop of diameter D_c on a beam of width w_t at a distance F_0 from its phase centre C_ϕ (II.3.18). The fractional power of a Gaussian beam that falls outside the aperture radius is effectively equal to the edge taper of the beam at that radius.

$$T_e = \exp\left[-2\left(\frac{R}{w_t}\right)^2\right] \qquad T_e^{dB} = -10\log T_e \tag{II.3.18}$$

When coupling a lenslet of thickness t_l to an antenna or a waveguide transition for instance, the truncating distance is the effective focal length F_0 (II.3.19), where the phase centre displacement from the aperture z_{δ_ϕ} is negative in the forward direction.

$$F_0 = z_{tl} + z_{\delta_\phi} + \frac{t_l}{2} \tag{II.3.19}$$

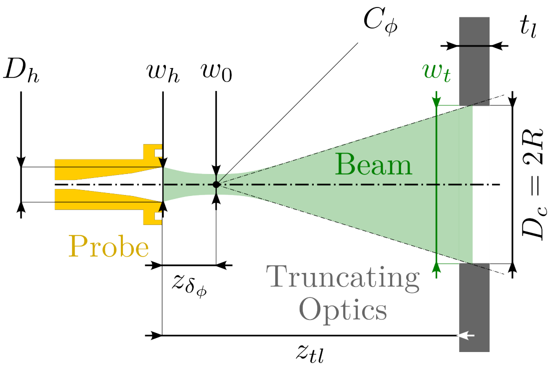

Figure II.3.4: *Truncation of the beam of a feed from a device at a distance* F_0 (II.3.19). *Figure made with Inkscape by the author.*

Truncating the beam may result in a drop of power, caused by clipping if the optics aperture is over illuminated, or through spillover from higher order optical mode contributions when under illuminated instead. The separating distance z_tl will also affect where maximal power is transmitted as the beam broadens out. Fig.II.3.5 shows that an efficient truncation corresponds to a trade off between the separation and the size stopping the incident beam.

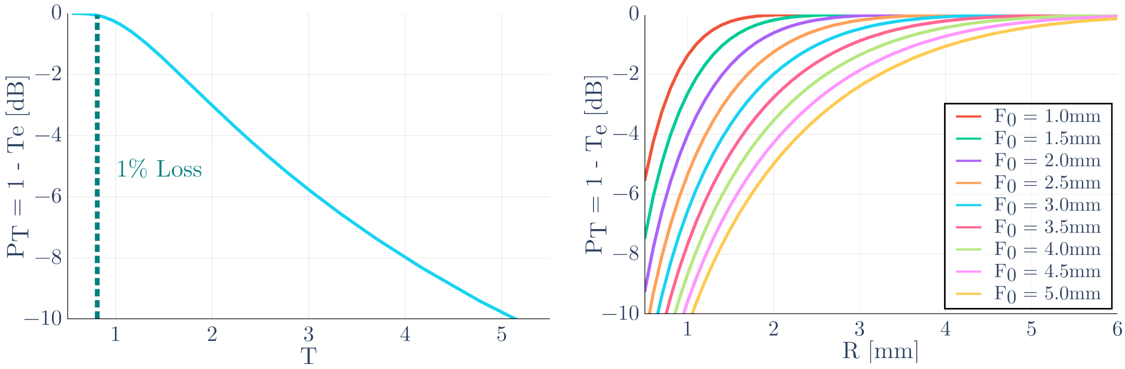

(a) **(b)**

Figure II.3.5: *(a) Normalised transmitted power* P_T *as a function of the truncation ratio* T (II.3.17). *The smaller and the closer the aperture, the more clipped the beam is, resulting in lower* P_T. *(b) Normalised transmitted power* P_T *as a function of truncation ratio* T *for a* $R = 5\,\mathrm{mm}$ *aperture. The optimal truncation is reached for* $T = 0.78$. *Figures made with Python and Inkscape by the author.*

The notations and definitions given above will be used extensively for the MetaL and feeding antennas analysis conducted in Part IV and Part V.

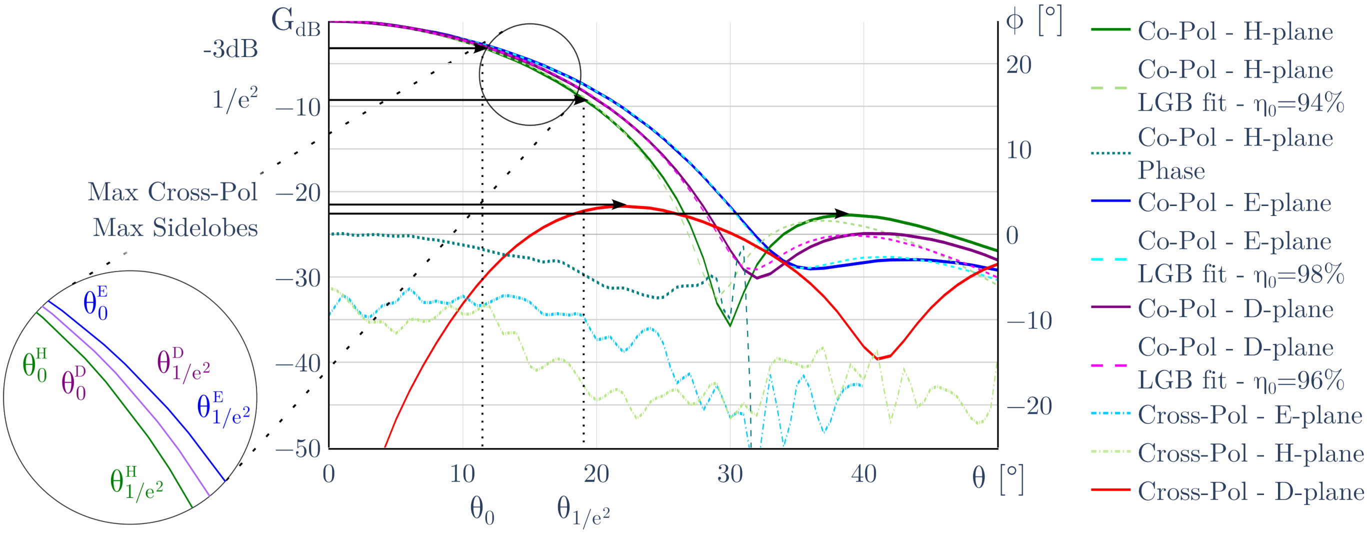

Figure II.3.6: *Beam characteristics depicted on the E, D and H-plane cuts. Figures made with Python and Inkscape by the author.*

Investigations are ongoing to identify and mitigate the impact of instrumental beam systematics based various end-to-end pipeline analysis. Within this effort, evaluating the performances of the multiple FPUs under development is of primary importance. Some of the systematics defined above may have a lesser impact on B-mode detection [41]. For instance, it was demonstrated that through adequate scanning strategies, suppression of spurious B modes generated by differential gain and pointing was possible. The impact on the reconstructed C_ℓ was further established for ellipticity and cross-polarisation, systematics that would still impede the measurements [157, 158, 159, 160, 148]. Non-Gaussian beams do not generate spurious B signals from the temperature or E-polarised counterparts, but a fraction of the power is lost to higher order LGB modes since they feed a portion of the power contained in the main lobe. With an adequate truncation of the beam by a Lyot stop and further baffling, the sidelobes are strongly limited. However, they couple directly with strong foreground emissions from diffuse galactic components, the ground signals, etc. producing a significant source of contamination [161]. Thus, it becomes clear that for a focal optics, a near-perfect Gaussian far field is desired.

With these considerations in mind, a comprehensive experimental characterisation of a focal optics component can be conducted by measuring its co-polarisation and cross-polarisation patterns in the E,H and D-planes and extracting the relevant optical properties from the previously established list, as will be done to prove the MetaL concept in Part IV. If integrated to an experiment, insights on the performances of a FPU for CMB applications could further be established by running a full instrument analysis. In the present work, a benchmark analysis will be conducted instead, based on map-making analysis techniques. The goal will be to compare the impact of the MetaL beam on C_ℓ^{BB} with that of a comparable hyper-hemispherical lenslet, using an ideal Gaussian beam as a reference.

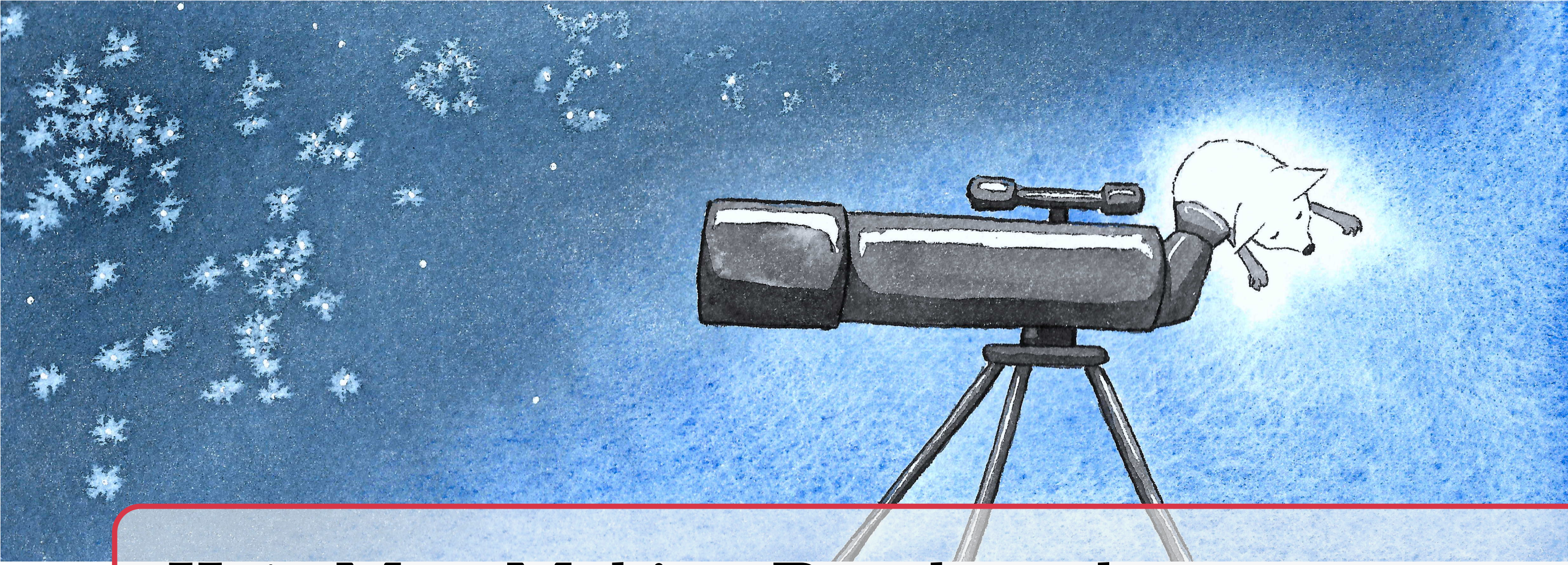

II.4. Map Making Benchmark

Precise characterisation of each systematic impact is necessary in the context of an instrument design. However, to prove the MetaL concept, it was instead chosen to benchmark the performances of a prototyped lenslet against a hyper-hemispherical equivalent. Relevant results that instrument designers can use will be given in Part IV, where the beam characteristics and their optical systematics will be compared. But the discussion can be extended to the sensitivity in r (I.1.8) in the context of a simplified experiment through a benchmark analysis. The latter is accomplished by convolving an ideal beam with the sky on one hand and the realistic beams of the optics components to be compared on the other. Then the resulting power spectra for each optics can be retrieved and compared against one-another. If their order of magnitude for a given r is maintained, their systematic impact is arguably similar. Hereafter, the method is presented for the reference beam only for simplicity and will be extended to the hyper-hemispherical lenslet and the MetaL in Part IV.

For the sake of simplicity and to keep the focus on the sensitivity in r, this implementation disregards a number of otherwise important elements. The rest of the instrument, its scanning strategy, the noise contributions and its inherent systematics are not considered, thus, it does not represent a realistic view of its optical performances. For instance, a Lyot stop would be installed in an instrument to cut-off sidelobes, the fore-optics would reshape the beam, scaling it up to reach the desired observing angular scale, possibly reducing its cross-polarisation level or extending the beam ellipticity, etc. The impact of foregrounds, astrophysical signals emitted between the CMB photon decoupling and the instrument, is also neglected. It comprises galactic foregrounds, namely thermal emission from galactic dust, synchrotron radiation, and so on, particularly relevant for B-modes science, as well as extragalactic signals, such as cosmic infrared background, SZ effects, radio and infrared point sources, and so on. Similarly, accurately modelling and decorrelating instrumental, atmospheric and photon noise is a difficult tasks [162], unnecessary for such benchmark analysis. To mimic a telescope FOV, the beams have been rescaled to the relevant FWHM. Whilst not being overly realistic, this benchmark approach should give a feel of the suitability of the MetaL technology by means of comparison with existing and already demonstrated focal optics.

In fact, with such simplifications, this method will provide dramatically bad result by incorporating spurious polarisation signals that would usually be compensated for by the scanning strategy, the use of baffles, stops, absorbers, polarisation modulators, and so on.

The techniques used for this approach are based from codes introduced during a map making analysis workshop in 2022 [163], with re-adaptations such as the incorporation of any input 2D beam maps in an array format and its scaling to any desired FWHM, the calculation of δC_ℓ for each spectra and the generation of input spectra with Code for Anisotropies in the Microwave Background (CAMB). The written code can be made available upon request to the author.

II.4.1 Producing CMB maps

The procedure is initiated by making CMB maps of N pixels along one direction using a set of input power spectra C_ℓ^{init} generated with CAMB [164] from a set of realistic cosmology parameters [165], with a given multipole step size $\delta\ell$ and a maximum multipole ℓ_{max}, effectively setting a lower limit on the angular pixel size ϑ_{pix}. Fig.II.4.1a presents a B-mode power spectrum for $r = 0.001$, where it can be seen that CAMB outputs D_ℓ spectra, which are effectively C_ℓ rescaled by $(\ell+1)\ell/2\pi$. D_ℓ are a standard in cosmology, independent of ℓ for scale invariant fluctuations. As the systematic effects considered are related to beams of widths on the degree or sub-degree scales, small compared to the observed areas at low ℓ, the flat sky approximation is used [166], in other terms, spatial deformation and homogeneous photo illumination is assumed in the FOV.

As illustrated in Fig.II.4.1b, the power spectra are rotated in Fourier space, where $\ell = 0$ is at the centre of rotation and a pixel is scaled to the size of a multipole in Fourier space (II.4.1), with the spatial pixel size ϑ_{pix} in arcmin.

$$\ell_{pix} = 2\pi/[(\vartheta_{pix}/60)(\pi/180°)] \tag{II.4.1}$$

The FFT of a random Gaussian density map of unit variance is then multiplied with the spectrum. It was previously explained in Part II that a Gaussian distribution closely fits the CMB brightness temperature and polarisation maps. The real component of the Inverse Fast Fourier Transform (IFFT) provides a CMB map corresponding to the spectrum of concern. Fig.II.4.2 provides an example of this procedure. A bias in amplitude is introduced but this will be corrected during the power spectrum reconstruction.

The final maps are obtained applying an IFFT on the resulting rotated spectra, producing realistic outputs as shown in Fig.II.4.3.

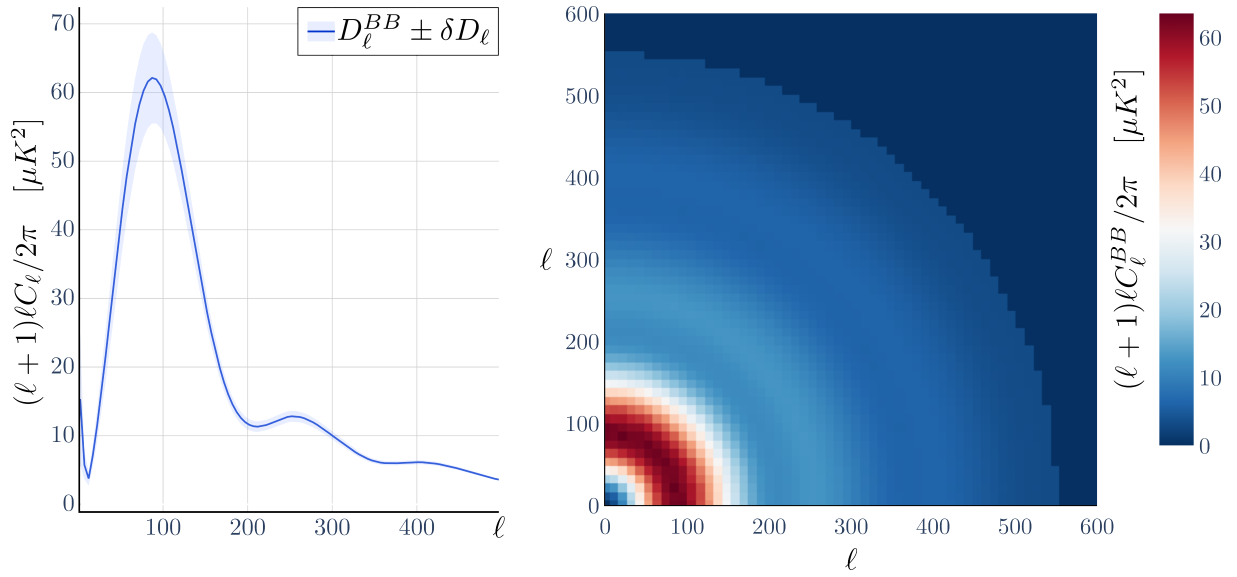

(a) **(b)**

Figure II.4.1: *(a) D_ℓ^{BB} spectrum (blue trace) generated with CAMB using the cosmology parameters derived by the Planck community [165] and the related cosmic variance δC_ℓ (light blue area of uncertainty). (b) Rotation of the spectrum in harmonic space. Figures made with Python and Inkscape by the author.*

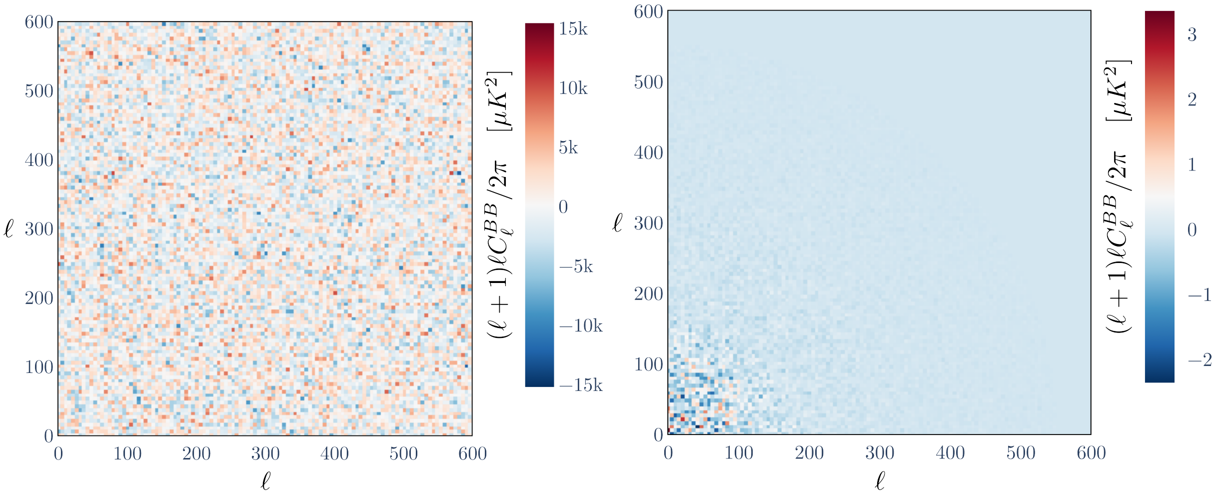

(a) **(b)**

Figure II.4.2: *(a) FFT of the random Gaussian field of normalised intensity in angular space. (b) The same field masked by the power spectrum input. Note that the power spectrum is not null at higher ℓ, causing a blue hue over the rest of the map. Figures made with Python and Inkscape by the author.*

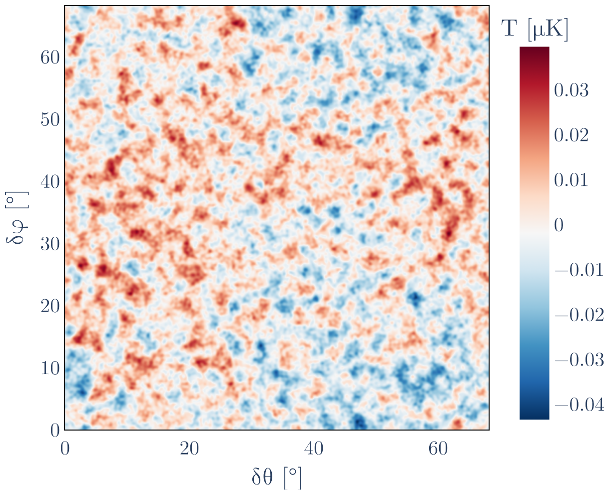

Figure II.4.3: *Realistic CMB B-mode sky map made from an input power spectrum generated with CAMB. Figure made with Python and Inkscape by the author.*

II.4.2 Beam convolution & apodization

As discussed in Section II.3, an idealised beam is perfectly Gaussian and, without adequate scanning in place, axi-symmetric. To easily compile such beam pattern, the 0th order mode (II.3.8) is reduced to a simpler form (II.4.2), where θ_{FWHM} is the beam FWHM. in Section I.1.2.2 and in Section I.2, it was underlined CMB observations require beams of angular waist $\theta_0 = 25'$, $3'$ and $1'$ to reach the large angular scales necessary to detect primordial gravitation on one hand, and the medium and high scales needed to acquire better knowledge of large scale structures on the other hand. A $\theta_{FWHM} = 25'$ beam is presented in Fig.II.4.4, where R is the spatial radius from $(0\text{ arcmin}, 0\text{ arcmin})$.

$$\begin{aligned} E_0(R) &= e^{-\frac{1}{2}\left(\frac{R}{\sigma}\right)^2} \\ \sigma &= \frac{\theta_{FWHM}}{2\sqrt{2\ln 2}} \end{aligned} \tag{II.4.2}$$

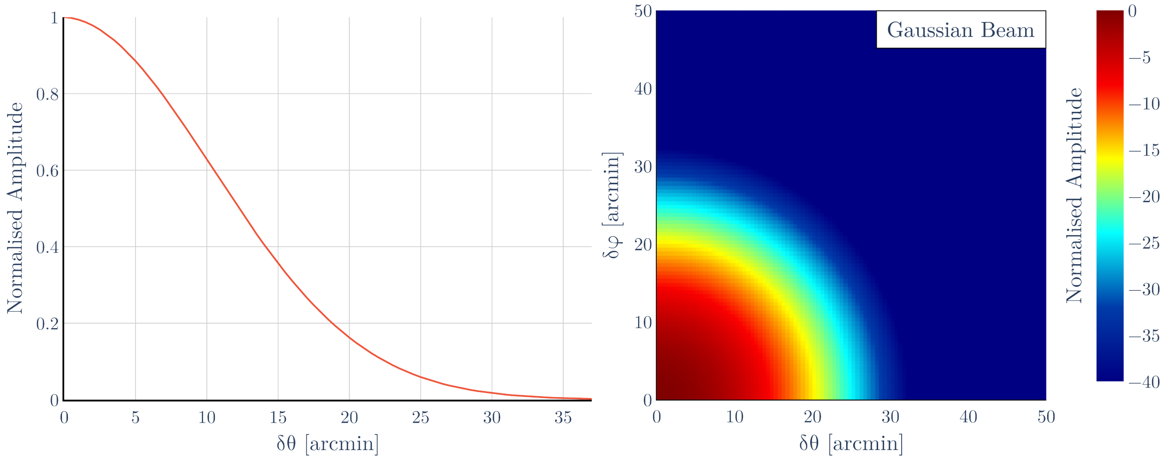

(a) **(b)**

Figure II.4.4: *(a) H-plane cut of the 0th order mode Gaussian beam normalised intensity. (b) Corresponding map in real space. Figures made with Python and Inkscape by the author.*

The convolution is then done by multiplying the CMB map with the beam in Fourier space and IFFT back in real space. This part is disregarding the scanning strategy that an instrument would otherwise conduct. Taking into account the latter would require to look at the TOD which is computationally expensive and out of the scope of this analysis. Fig.II.4.5 shows a raw map and its convolved result with the above beam. The corresponding Q and U maps are also given, directly aligned with the polarisation directions of the beam, $\theta = 0°$ and $\varphi = 0°$ respectively. It is worth noting that the mean temperature of the convolved map may drop by up to a few orders of magnitude, indicating a bias caused by the beam which will need to be corrected when reconstructing the power spectra. In the case of an instrument, rotations would be included as they could potentially impact E to B leakages [157, 158, 159, 160, 148]. As only the beam systematics are of concern in the present benchmark analysis, this is not considered.

The generated maps are defined in a limited angular space. FFTs are effectively integrations of the maps over an infinitely repeated real space, generating spurious effects from mismatch at the actual angular boundaries. To prevent this, an apodization with a window function is done,

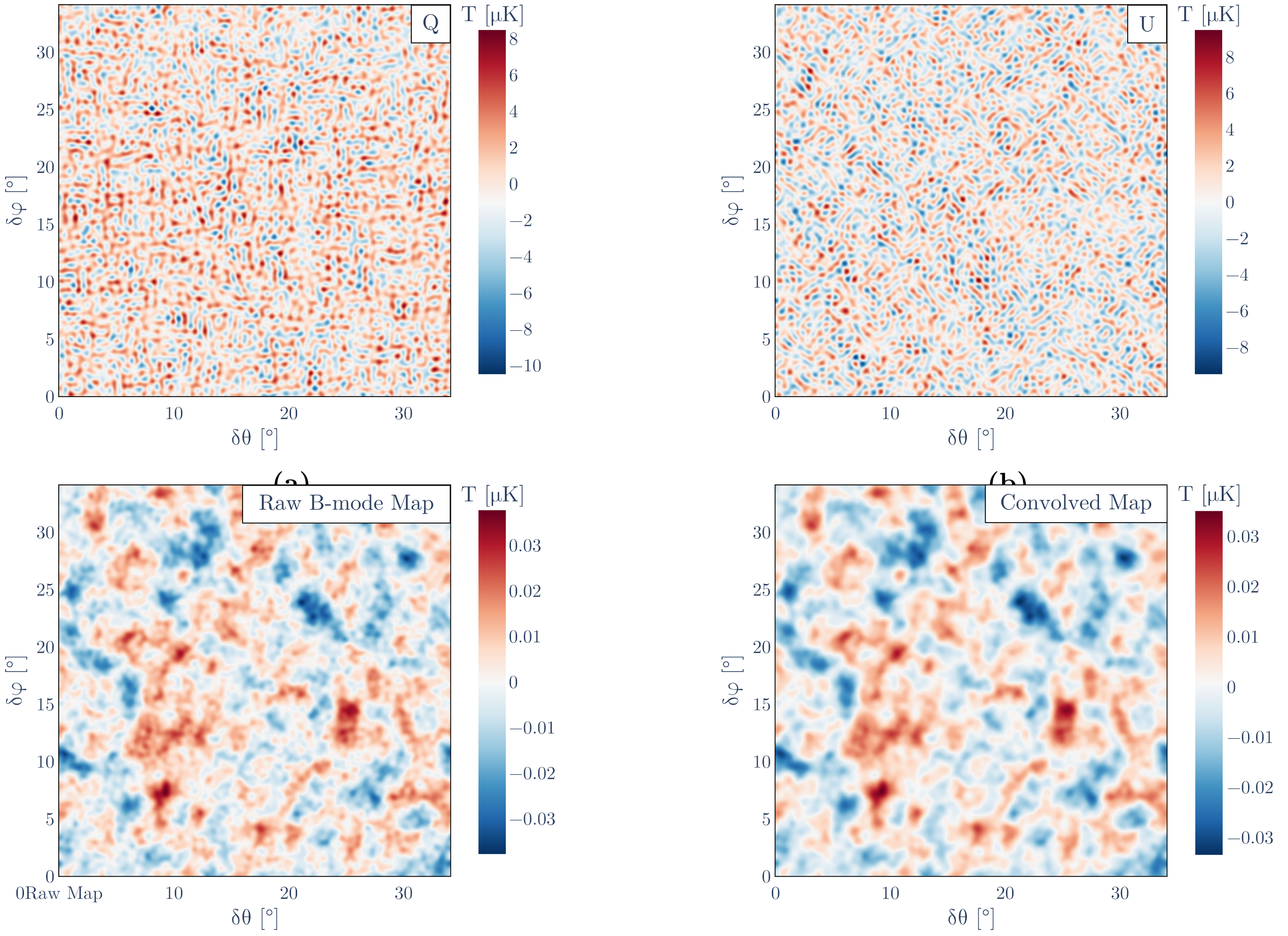

(a)

(b)

(c)

(d)

Figure II.4.5: *Convolved Q (a) and U (b) maps of the initially raw B-mode sky (c), convolved with a* $25'$ *beam (d). Such a broad beam clearly blurs the fine angular details but is sufficient to reach* $\ell < 500$. *Figures made with Python and Inkscape by the author.*

corrected to avoid E to B leakage [167] to the convolved map. Such apodization is illustrated in Fig.II.4.6.

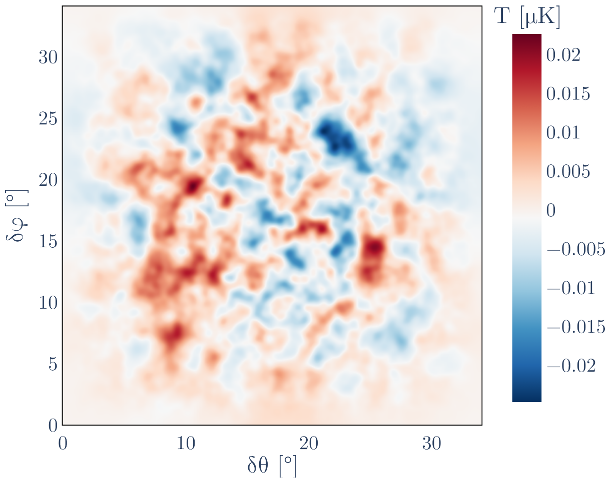

Figure II.4.6: *Apodized and convolved CMB B-mode sky map. Figure made with Python and Inkscape by the author.*

The power spectra are compiled by using an FFT on all convolved and apodized maps of a given signal, TT, EE, TE or BB, then taking the average of the square of the absolute value of each binned pixel in harmonics space and IFFT the result to the final spectra. This is equivalent to wrapping up a rotated spectrum that varies per angle along the radius, the reverse calculus than the one made to create the maps initially.

As stated above, the convolved and apodized signals have a reduced amplitude from the beam and the apodization, a defect corrected via the instrument transfer function T (II.4.3). The numerical error is finally given by calculation of the RMS. Fig.II.4.7 shows The input B-mode power spectrum for $r = 0.001$, alongside a reconstructed one compiled through the method depicted in this section, for 64 realisations of a sky mapped with a perfect Gaussian beam. $\delta\hat{D}_\ell^{BB}$ is the numerical dispersion of the binned maps around $\hat{D}_\ell^{BB}$ and $\delta D_{\ell,init}^{BB}$ is the square root of the cosmic variance as defined in (I.1.3).

$$\hat{C}_\ell = TC_{\ell,init} \tag{II.4.3}$$

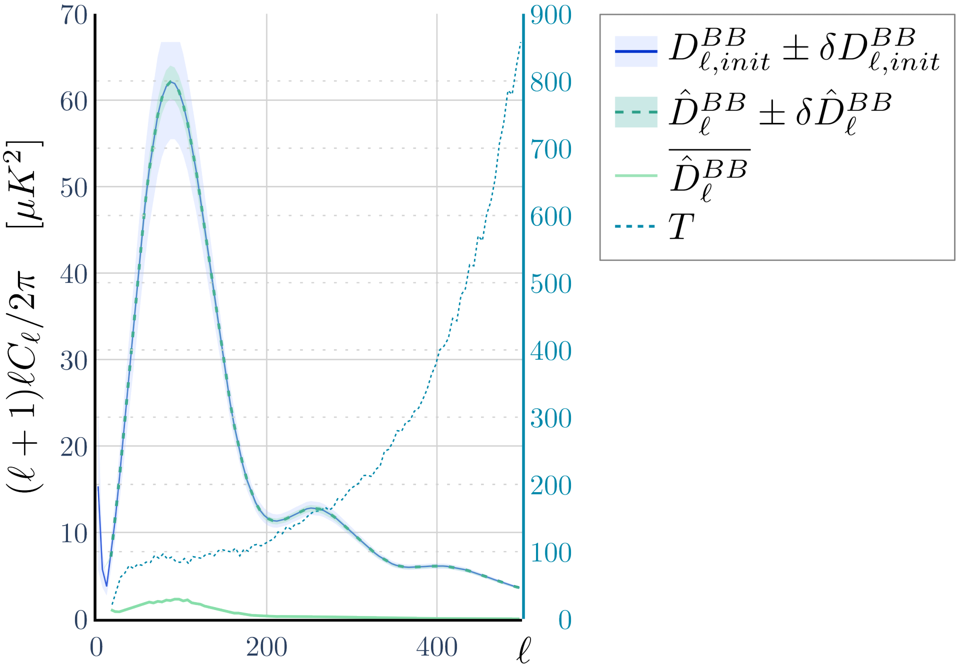

Figure II.4.7: *Reconstructed B-mode power spectrum* $\hat{D}_\ell^{BB}$*, corrected by* T *to account for signal reduction* $\overline{\hat{D}_\ell^{BB}}$ *while scanning a* $\sim 36°$ *square sky with a perfect Gaussian beam. The maps were generated from the initial power spectra* $D_{\ell,init}^{BB}$ *compiled with CAMB. Figure made with Python and Inkscape by the author.*

The transfer function T fully compensate any deviation caused by the Gaussian beam windowing from the input spectrum. This reference function will be applied for both the hyper-hemispherical lenslet and the MetaL in Part IV. The same set of 64 maps will also be used for this comparative benchmark analysis, opening the discussion that will be conducted at the end of Part IV with regards to the analytical and experimental study of the beam radiated by the prototype MetaL under scrutiny in the present work.

As was mentioned previously, this method is overly simplified. It was however primarily taken from the focal optics designer perspective. Indeed, the incorporation of additional optical components such as the fore-optics lenses, the mirrors, the HWP, etc. comes with the incorporation of their own systematics, which may overtake or amplify the ones caused by the optics of concern. Similarly, whilst a given scanning strategy may relax B-mode contamination by e-modes due to the beam ellipticity, its inclusion to such analysis also prevents the evaluation of a design requirement on the axi-symmetry of the beam. To summarise, optical requirements can only be produced from full end-to-end analysis and are thus completely determined by the concerned experiments. In the present work, a prototype device is studied, which is independent of any instrument. This coarse estimation in the sensitivity in r is thus simply a preliminary benchmark approach to estimate the suitability of the MetaL concept for CMB observation. A way forward may be to incorporate the lenslet beam in place of an existing, analysed FPU, in a more complete software, such as Time Ordered Astrophysics Scalable Tools (TOAST) [73] or BeamConv [72], and compare the performances in a relevant context.

III

Principle & Design of a Metamaterial-based Lenslet

Part III Outline

Instrumentalists are the ophthalmologists and optometrists who try to adjust for the currently blurry CMB picture. The MetaL development inscribes itself in the community's effort to decipher the details of the origin and evolution of the Universe. The said lenslet is made of metamaterials, a media consisting of an arrangement of wavelength or sub-wavelength patterns carved in, or printed on a selected dielectric to modify its intrinsic properties. The material permittivity and permeability is then tuned through the geometry of the constitutive shapes [168, 131]. Premises of the modern metamaterials were theorised in the late XIX$^{\text{th}}$ century, soon after James Clerk Maxwell unveiled the "Dynamical Theory of the Electromagnetic Field" [169]. Jagadish Chandra Bose then worked on the refraction of millimetre waves, notably in chiral media of his own design [170]. Such material eventually offered views on a wide range of applications, from identification of the presence of various polarisation dependant specimens of interest for medical purposes to electro-steerable beam of use in telecommunications. In the mid-XX$^{\text{th}}$ century, Winston Kock designed and realised a variety of lenses [171] based on periodic structures, noticing the optical properties of a media could be tuned using a variety of geometrically varying metallic shapes. Victor Veselago extended the concept to negative refractive index materials [168], eventually fabricated in the end of the century by John Pendry [172]. A super-lens design was proposed shortly after, a device at the surface of which the refracted sub-wavelength waves propagates with a positive refractive index, allowing the focus of an object in the near field, an attractive feature for microscopy. The XXI$^{\text{th}}$ century has seen a gradual interest in metamaterials, one can think of the famous optical invisibility cloak [173, 174]. With a device relying on such materials and their capability to modify the electrodynamics of a given dielectric, an optics designer can optimise the beam characteristics, depicted in Part II, to match the requirements set within the context of any given CMB experiment. In order to reach the required sensitivities, that is, the scalability needed to incorporate tens of thousands of detectors on the FPUs of modern and future instruments, a metamaterial based technology would ideally be embedded in Silicon. Preliminary developments in MetaLs are currently made to achieve this goal [138, 135]. The aspiration of the present work is to help in proving the concept of this promising technology. A fully embedded lenslet would indeed be compact whilst preserving optical efficiency. Inherently flat, its integration to FPUs would be straightforward, with little to none alignment defects. Whilst ARC is still required, it would be laid on a flat surface, simplifying its fabrication.

In this part the MetaL device is presented, relying on the use of metamaterials to shape the light in accordance the the contemporary needs for Cosmology. Primarily, the modelling of a dielectric medium is presented. A preliminary discussion on metamaterials, further illustrating their capability to modify the media they are embedded in. The focus is then made on a specific type of such materials, the Frequency Selective Surfaces (FSSs) at the heart of the MetaL design. Finally, the phase engineering procedure is depicted and applied to the design of an air-gapped prototype. Mention is then made of improvements and other routes to design similar lenslets.

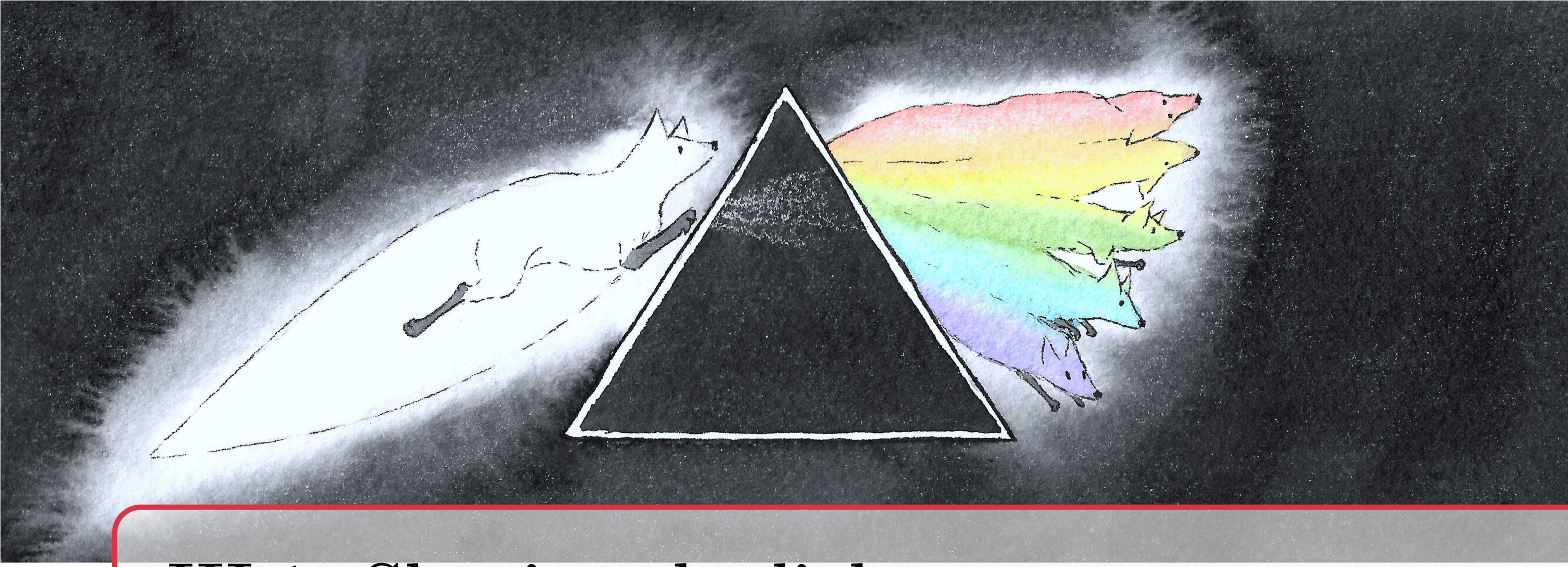

III.1. Shaping the light

III.1.1 Enhancing Dielectric Materials

III.1.1.1 Electromagnetic wave in a dielectric

III.1.1.1.1 Dielectric properties

Metamaterials are enhancing the properties of the dielectric they rely on. It is thus of interest to depict what constitutes a dielectric and what its characteristics are. Qualitatively, such media has electromagnetic properties sitting in between those of metals and gases. Whilst photons are travelling freely in vacuum, in a given material, they collide with electrons, bound or not to baryons. In particular, in metals, each atom of the crystalline structure has free unbound electrons. When sat in an applied electromagnetic field, this electronic lattice is instantly polarised. In a dielectric, some or all electrons are bound to the baryons, thus, when submitted to an electromagnetic field, several mechanisms are at play: bound electrons may drift from the baryons they are bound to, molecules will orientate themselves along the field direction in an orientational mechanism, ionic bounds will either compress or stretch and depending on the dielectric's constituents, some photons may be absorbed. Three principal electric properties are used to define the comportment of such material. Its conductivity σ essentially depicts a material capability to conduct electric current induced from an applied electric field. It is function of the electrical resistance of the material as defined by Ohm's Law, its volume and electronic density. The effective permittivity ϵ (III.1.1) describes how efficiently the electronic lattice of a material polarises under an applied electric field. ϵ', ϵ'' and $\epsilon'''(f) = \sigma(f)/f$ indicates how refractive, absorptive and conductive the material is, respectively.

$$\epsilon(f) = \epsilon'(f) - j\left(\epsilon''(f) + \epsilon'''(f)\right) \qquad \text{(III.1.1)}$$

Finally, the loss tangent $\tan\delta$ (III.1.2) determines the Ohmic losses due to conduction $\tan\delta_c$, typical of conductors, and refraction $\tan\delta_d$, typical of dielectrics, occurring in a given volume of material under an applied electric field.

$$\tan\delta(f) = \frac{\sigma(f) + f\epsilon''(f)}{f\epsilon'(f)} = \tan\delta_c + \tan\delta_d \tag{III.1.2}$$

For a metal σ will be large while $\epsilon' \to \epsilon_0$ and $\epsilon'' \to 0$, where ϵ_0 is the permittivity of free-space. This result in a virtually lossless material. Lossless dielectrics will have $\sigma = 0$ and will not absorb the electric field, leading to $\tan\delta = 0$. Another important dielectric property is the permeability of the material, characterising the capability to conduct magnetic currents induced from an applied magnetic field, and denoted μ. μ_0 is the permeability of free-space. Both permittivity and permeability are often expressed as relative to free-space.

III.1.1.1.2 Transmission Line Model for Wave Propagation

The MetaL design, further depicted in chapter III.3, relies on stacked metamaterials, which can be depicted as a succession of equivalent dielectric slabs. They are modelled accordingly by transcribing the effect of the permittivity and permeability of the media to a light wave refracted throughout. A standard approach is to consider the dielectrics as Transmission Line (TL) sections, a model encompassing the transmitted and reflected part of such wave. Stacking several layers of dielectrics then result in a succession of consecutive TLs. CMB electromagnetic waves are intrinsically TEM, the electric and magnetic fields are contained in the plane transverse to the propagation direction. The electric field can be depicted as running between a positively charged termination and a negatively charged one. A TEM wave propagating through a given architecture with M components can thus be decomposed into a succession of TL elements, as illustrated by Fig.III.1.1. Each is viewed as a 2 port network and the transmission and reflection occurring within are transcribed in an ABCD matrix (III.1.3), originally defined in terms of the voltages and

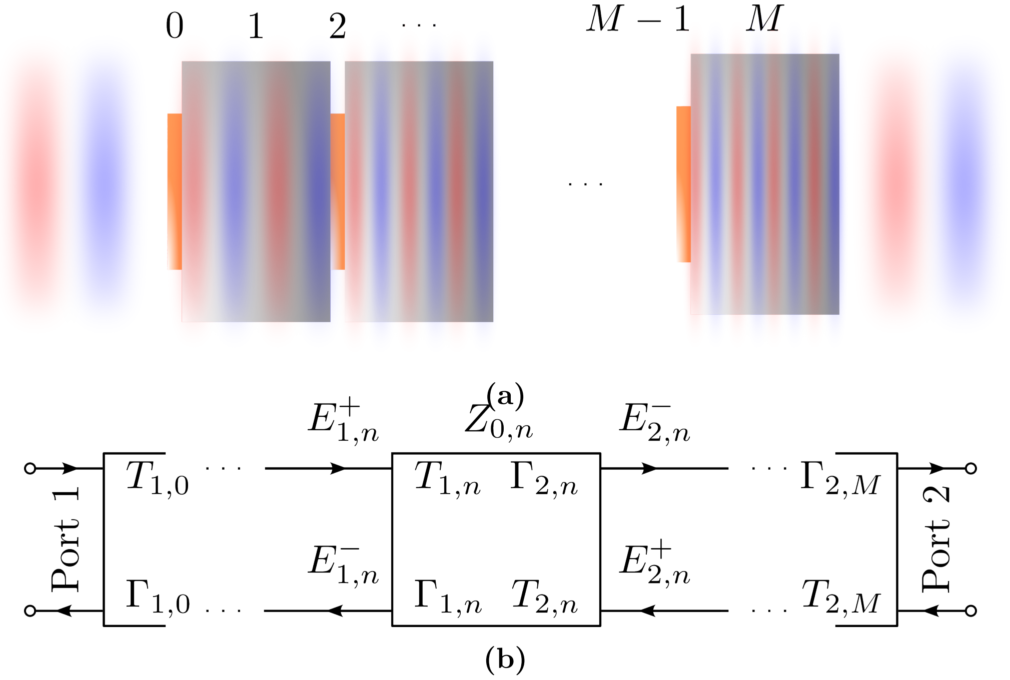

Figure III.1.1: *(a) Transverse Electro-Magnetic (TEM) wave going through a generic architecture, (b) decomposed as a succession of cascading 2-ports TL. Figures made with Inkscape by the author.*

currents going through the element of concern. The matrix entries may instead be expressed in terms of impedances Z, admittances $Y = 1/Z$ or scattering parameters S [175, 176]. The latter description is used to derive such matrix S_n (III.1.4) for an element at position n in the architecture as a function of its reflection Γ_n and transmission T_n parameters. The matrix of the complete architecture S_M is obtained by a simple reverse multiplication of the matrices of each constituents. In turn the overall transmission T_M and reflection R_M coefficients can be retrieved (III.1.5) [176, 177].

$$S_n = \begin{bmatrix} A & B \\ C & D \end{bmatrix} = \begin{bmatrix} T_n\left(1 - \frac{\Gamma_n^2}{T_n^2}\right) & \frac{\Gamma_n}{T_n} e^{j2kh_n} \\ -\frac{\Gamma_n}{T_n} e^{-j2kh_n} & \frac{1}{T_n} \end{bmatrix} \text{, where } h_n = l_1 + ... + l_{n-1} \tag{III.1.3}$$

$$S_M = S_N^p S_N^d S_{N-1}^p S_{N-1}^d ... S_2^p S_2^d S_1^p S_1^d = \begin{bmatrix} S_M^{11} & S_M^{12} \\ S_M^{21} & S_M^{22} \end{bmatrix} \tag{III.1.4}$$

$$T_M = S_M^{11} - (S_M^{12} S_M^{21} / S_M^{22}) \qquad R_M = -(S_M^{21}/S_M^{22}) \tag{III.1.5}$$

An infinitely extended dielectric slab of thickness l and relative permittivity ϵ_r (III.1.1) is depicted in Fig.III.1.2. The TEM wave propagates at normal incidence along the vector $\hat{k}$ in free space and $\hat{k}'$ in the dielectric, with $k' = k\sqrt{\epsilon_r}$. The related reflection and transmission coefficients are given by (III.1.6) and (III.1.7) respectively [176, 177]. Reflectionless responses of a single dielectric slab is obtained when its thickness equates a multiple of a quarter of half-wavelength. The overall transmission pattern is that of an interference filter.

$$T_n^d = \frac{(1 - r^2)\exp\left(j\left(k - k'\right)l\right)}{1 - r^2 \exp\left(-j2k'l\right)} \text{, where } r = \frac{1 - \sqrt{\epsilon_r}}{1 + \sqrt{\epsilon_r}} \tag{III.1.6}$$

$$\Gamma_n^d = \frac{r(1 - \exp\left(-j2k'l\right))\exp\left(j\left(k\right)l\right)}{1 - r^2 \exp\left(-j2k'l\right)} \tag{III.1.7}$$

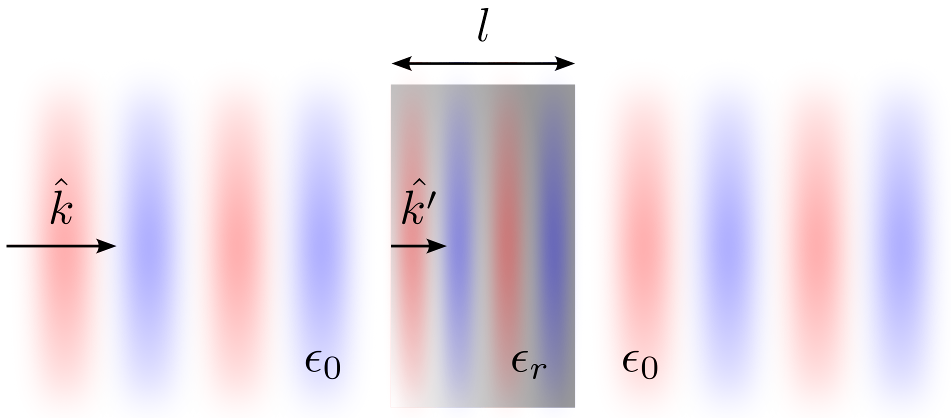

Figure III.1.2: *TEM wave passing through an infinitely extended slab of dielectric in free-space. Figure made with Inkscape by the author.*

When a stack of metamaterial is considered, each section of the equivalent TL is changed to account for the modified dielectric properties, which results in the modification of (III.1.6) and (III.1.7). The specific changes induced by the type of surfaces used in the lenslet design are depicted in Chapter III.2. The patterns in question are arrays of square patches lithographed onto Silicon Nitride membranes resting on back etched Silicon slabs, effectively resulting in vacuum embedded FSSs. This type of metamaterial will now be discussed further.

III.1.1.2 From dielectrics to metamaterials

A variety of metamaterials have been discovered and their use depends on the engineering requirements. The FSSs are single or stacked layers of thin metal films which homogeneously alter the overall optical properties of the underlying dielectric with the clear purpose of filtering a given set of frequency bands. Extensive use is made of the FSS in the MetaL design. The most common FSS shapes comes in two complementary sets, wire grid which acts optically as a High-Pass Filter (HPF), and Low-Pass Filter (LPF) patch grid, as the one shown in Fig.III.1.3. They can further be combined to design a Band-Pass Filter (BPF) [132]. An overview of the different filter types and their characteristics is given in Chapter III.2, with a focus on the square patch grids as they are the FSS at the base of the MetaL design concept. The same surface type is taken here as an example to emphasize how such shapes can be used to create a material with tunable electromagnetic characteristics. The unit cell of such FSS is shown in Fig.III.1.3.

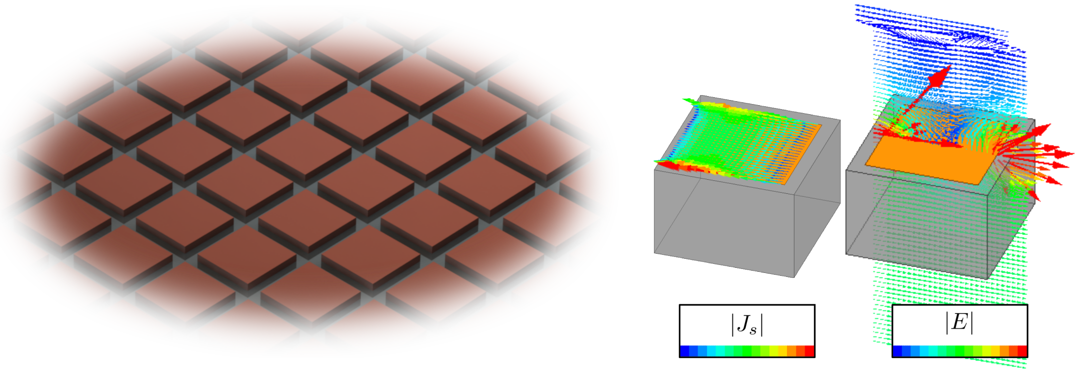

Figure III.1.3: *A single FSS meta-surface constituted of an infinite array of metal square patches. The Normalised surface current density J_s induced from an incoming TEM wave is shown for a single unit-cell, as are the overlaid incident and scattered waves. Figure made with ANSYS-HFSS and Inkscape by the author.*

A TEM wave incident on a patch induces a current density J_s depicted in Fig.III.1.3. The resulting potential between two patches then leads to the generation of a scattered wave that is superimposed to the initial field, also illustrated in Fig.III.1.3. This comportment is similar to that of a capacitance, where the anode and cathode would be the edges of two consecutive patches, and explains the LPF effect achievable with this FSS.

Huygens surfaces constitute another type of FSSs, scatterers which can be spatially modified to fine tune wavefronts locally. The Split-Ring Resonator (SRR), a resonating geometry popularised by John Pendry [172] on the research of negative refractive index materials, are a good example of Huygens surfaces. Investigations on their applicability to a lenslet design are mentioned in Chapter III.3. A single layer of SRRs is presented in Fig.III.1.4. Similarly to the gap between patches, the split couples the field capacitively to the neighbouring ring. The perpendicular sides are effectively wires with circulating currents, preventing the field to establish in this direction. The present SRR design is thus single-polarised.

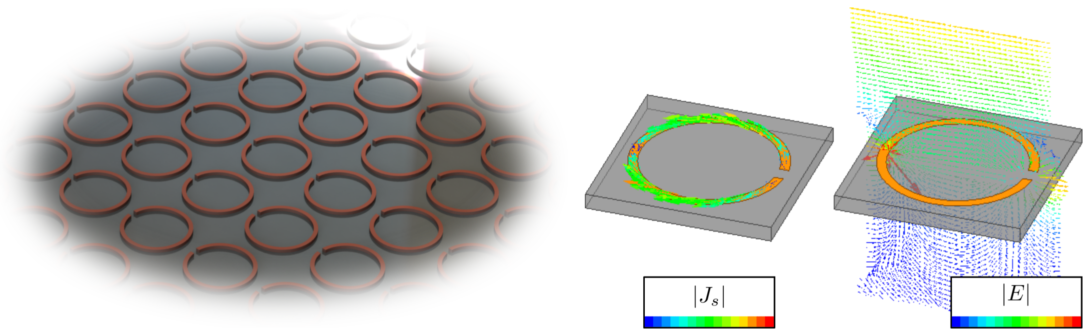

Figure III.1.4: *A SRR meta-surface and its unit-cell, over which the the E-field is overlaid at the central cut plane crossing with the split. The normalised surface current density J_s induced from an incoming TEM wave is also shown. Figure made with ANSYS-HFSS and Inkscape by the author.*

Fig.III.1.5 further illustrates the de-embedded transmission T, reflection Γ and phase shift $\Delta\phi$ response of three structures modelled in ANSYS-HFSS: a 100µm thick slab of Silicon enhanced with a square patch grid on one hand, and a SRR meta-surface on the other hand. De-embedding consists of removing the impact on Γ and $\Delta\phi$ of the media the element of concern is embedded in. A dielectric with tunable permittivity and with the same thickness was also analysed, showing a match with the patch grid for $\epsilon_r \simeq 19$, much higher than the relative permittivity of Silicon. The SRR exhibits a resonance at 55GHz, filtering out the TEM wave over a large bandwidth.

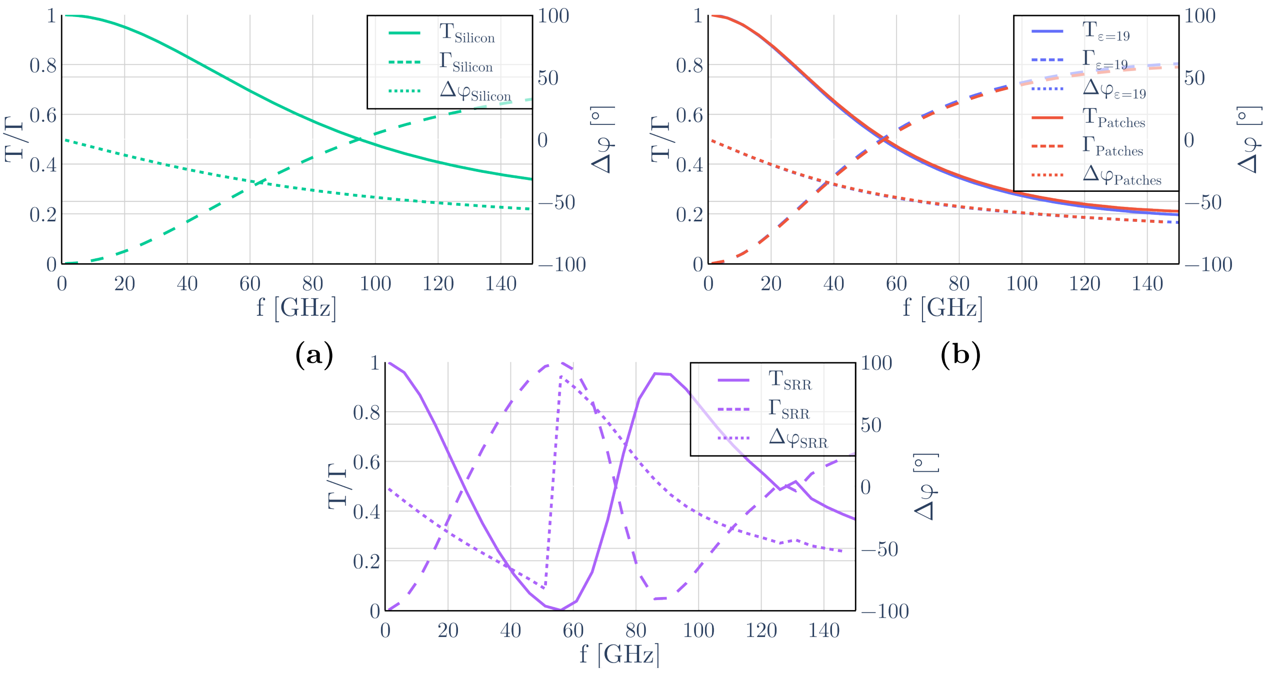

(a) **(b)**

(c)

Figure III.1.5: *T, Γ and $\Delta\phi$ responses of (a) a* 500µm *thick, semi-inifinite Silicon slab, (b) the same dielectric supporting the FSS array of square patches alongside an equivalent dielectric of permittivity $\epsilon_r = 19$, and (c) a SRR on a* 100 µm *Silicon layer. In (b), the transmission drops from* 100% *to* $\sim$ 20% *over the bandwidth plotted, illustrating how such surface type operates a frequency selection. Figures made with ANSYS-HFSS, Python and Inkscape by the author.*

By adding a metal surface to a dielectric, thus building a metamaterial, one can effectively tune its refractive index, block a tunable frequency range, play with the phase to "shape the light". This preliminary qualitative description allows to grasp the potential of such media for an optics design. FSSs, as their name indicates, enable the selection of a bandwidth of choice and causes a phase shift in the passing TEM wave. These features makes them an interesting candidate for a lens design. The latter essentially aims at transforming the phase of a wave in a quadratic manner, to a first order, whilst preserving the transmission at the maximum achievable. In the following chapter, the TL model given above for a dielectric stack will be revisited to encompass the FSSs, shapes at the base of the MetaL concept. The discussion will begin with the depiction of single layers and their comportment as filters [132]. Stacked assemblies will be detailed further, corresponding to the metal-mesh filters traditionally used in CMB. In the following Chapter, the MetaL design method will then be presented.

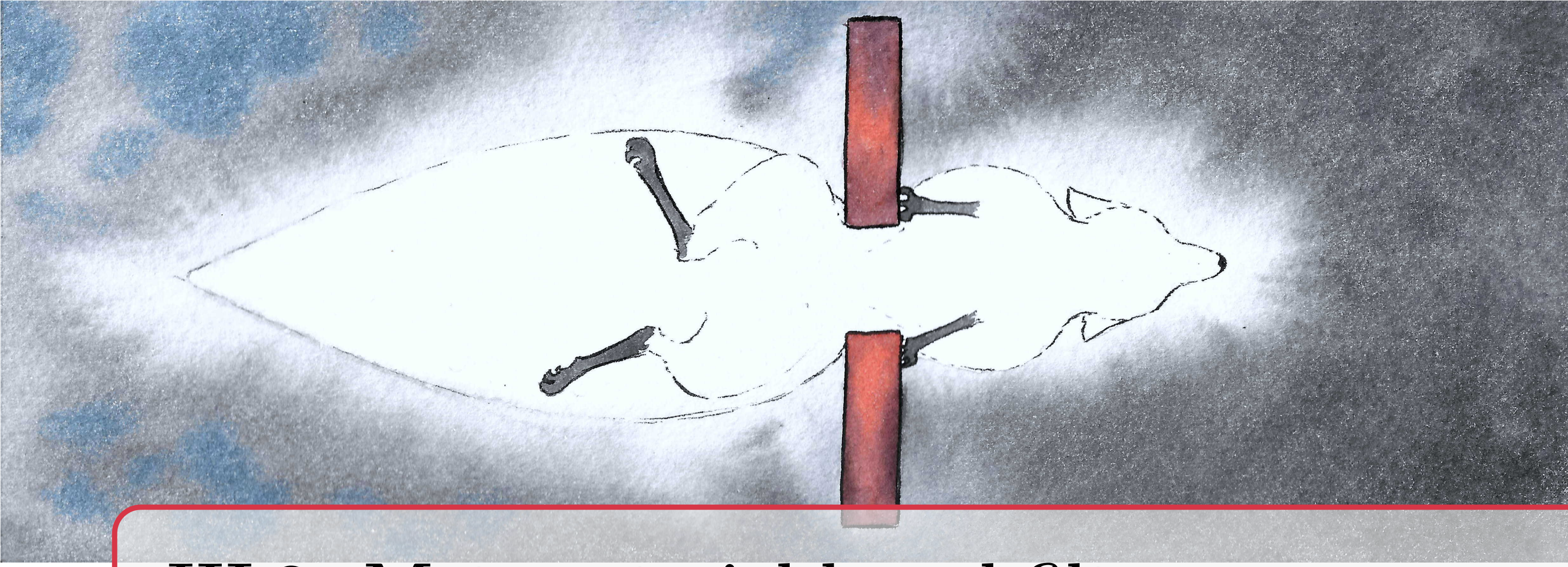

III.2. Metamaterial-based filters

III.2.1 Frequency Selective Surfaces

FSSs, an array of metal patterns lithographed onto a dielectric to alter its frequency response, are utilised for the MetaL design, as will be underlined in Chapter III.3. The characteristics of square patch and wire grid arrays will be discussed here, emphasising their filtering properties and demonstrating how this can provide a controllable phase shift whilst preserving transmission of a passing TEM wave. A comprehensive analytical description of infinitely periodic gratings [178, 179, 180] is out of the scope of this work as their depiction through the transmission line model [181, 182, 183, 184], discussed in the previous chapter, is sufficient to establish a MetaL design.

III.2.1.1 Preliminary considerations on polarisation

Amongst the possible FSSs, a term that encompasses any planar metal patterns that are frequency selective, wire and square patch arrays have specific polarisation properties that makes them inherently compatible with CMB observations. Indeed, detection of the E and B-modes of the CMB polarisation sky map is done through the detection of Q and U signals, as was discussed in Section I.1.2.2. For the benchmark method described in Chapter II.4 and undertaken in Part IV, it was underlined that the direct coordinates of observation for the mock instrument considered are directly matching those of the Q map. In other terms, the E and H-planes of the beam are aligned with the two orthogonal polarisation observed. A real instrument pipeline would rotate TODs back into the polarisation coordinates, accounting for the systematics mentioned in Chapter II.3 and the scanning strategy undertaken by the instrument. It was discussed that any mismatch between the two polarisations detected would lead to an undesirable leakage of the T or E to B signals. An optics design relying on FSSs thus needs to provide a polarisation independent response, which directly leads to constrain the pattern geometry, necessarily symmetrical on two orthogonal directions on the grid plane. Square patch and wire grid arrays respect this symmetry condition. It will be shown in the following section that the desired frequency range of a given FSS is preserved up to the normalised frequency of the feature $\omega = g/\lambda$, where g is the unit-cell size. Above this threshold, when g is above a wavelength, diffraction effects start appearing. The scattered field begins to include higher order components that adds in the wave, whereas for $\lambda \gg g$, the only propagating parts of the scattered fields are the 0^{th} order modes in both directions.

III.2.1.2 Inductive and Capacitive Grids

The Babinet principle shows that a wire and a square patch array sharing a complementary geometry will be counterparts of one another in their optical effect on the incident wave. Since the wire arrays are effectively made of virtually infinite metal lines, the incident wave will induce currents throughout at $\omega << 1$, which causes a full reflection, similarly to an inductance in an electronic circuit. Complementarily, as was briefly shown in Section III.1.1.2, the patches will be fully transmitting in the same regime, acting like a capacitance. Each type of grid is thus called inductive and capacitive, acting as HPF and LPF, respectively. Filters can be described with a few characteristics which will now be exposed.

A filter is operating a window function on the incident TEM wave, selecting the frequency regime carried through the structure. A LPF, HPF and BPF responses are depicted in Fig.III.2.2, and their characteristics are defined further hereafter. The cut-on/off frequencies $f_{c1/2}$ are reached at the -3dB transmission thresholds. They materialise the beginning of the edges of the filter, whilst the end is reached at the null frequencies $f_{\circ 1/2}$, further down at -20dB. The bandwith BW thus covered is the range allowed between the cut-on and cut-off frequencies. The in-band response of a filter may oscillate around an averaged amplitude $\bar{A}$, with a peak of oscillations δ_A, as illustrated in Fig.III.2.2. This inhomogeneous response is undesirable and $\left|\bar{A} - \delta\right| / \bar{A}$ is generally designed to be close to 0%. Finally, the null selectivity $S_{c1/2}$ is the power attenuation occurring through the transitional regime, at the edges. At cut-off, $S_c = A_{\text{dB}}(f_{\circ 1/2})/A_{\text{dB}}(f_{c1/2})$.

Wire grids effectively acts as HPF and patch grids as LPF with a null frequency $f_\circ$. Their unit-cell are shown in Fig.III.2.1b and Fig.III.2.1a, respectively. Such material can be modelled as a 2-port TL where the metal pattern is represented by a shunt admittance, and the dielectric is placed as an impedance in series [182].

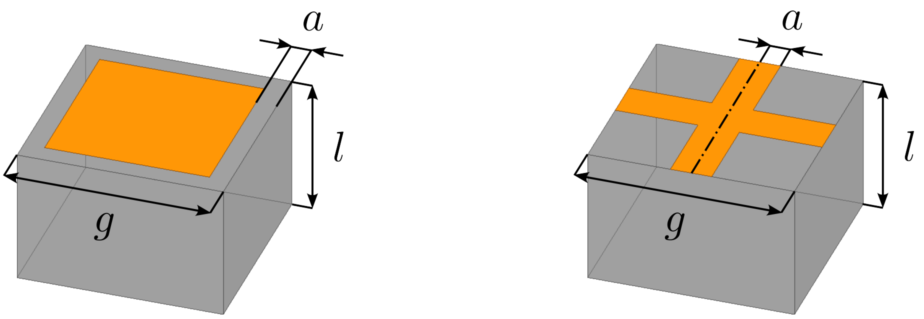

(a) (b)

Figure III.2.1: *Unit-cell of (a) a capacitive and (b) a wire grid. Figures made with Inkscape by the author.*

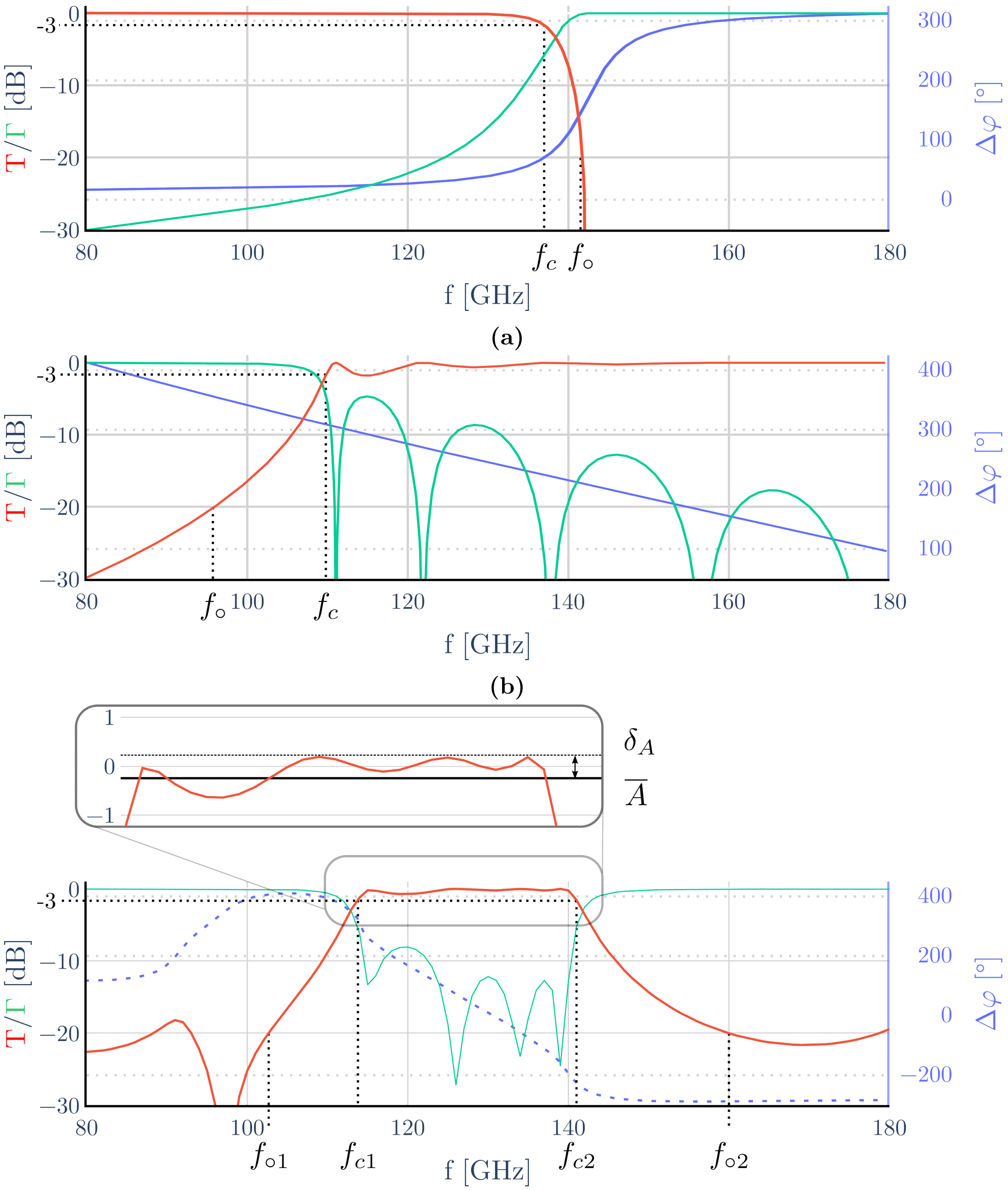

(a)

(b)

(c)

Figure III.2.2: *T, Γ and $\Delta\phi$ responses of (a) a LPF constituted of a succession of capacitive grids, (b) a HPF constituted of a succession of inductive grids and (c) a BPF combining both grids. For (c), the cut-off frequencies are $f_{c1} = 112$GHz and $f_{c1} = 142$GHz, thus the filter has a 40GHz bandwidth. It presents ripples with a ~ 0.1dB amplitude in band. The filter selectivity is $S_c = 20$dB. Figures made with Python and Inkscape by the author.*

The resulting analytical description of such model for a capacitive grid has a complex transmission T^p (III.2.1) and reflection R^p (III.2.2), providing a phase shift $\Delta\phi^p = arg(T)$. p will be used later as an identifier for the layer number when the discussion extends to stacked FSSs in Section III.2.1.3. Combining the shape and its underlying dielectric (III.1.6) (III.1.7) is done through the ABCD matrix method (III.1.3), (III.1.4), (III.1.5). A dedicated python code relying on these equations was written to produce the results plotted throughout this part. It is presented in Appendix C.

$$T^p = 1/(1+Y^p) \qquad R^p = \sqrt{1-|T^p|^2} \tag{III.2.1}$$

$$\begin{aligned} Y^p &= -j\frac{\beta}{(\beta^2-1)}\frac{\ln\left[\csc\left(\pi a/2g\right)\right]}{g/(g-a)+(g/\sqrt{2}\lambda)^2} \\ &\quad \text{where } \beta = (\lambda/g)\left[1-0.41(a/g)\right] \end{aligned} \tag{III.2.2}$$

The shift in $f_\circ$ as a function of the unit-cell size g is shown in Fig.III.2.3a and further illustrated by Fig.III.2.4. Modifying the feature geometry via the wire half-width, or indifferently, the half gap between patches a, enables fine tuning over $f_\circ$ (III.2.3) as demonstrated in Fig.III.2.3c [182].

$$\omega = \frac{g}{\lambda} = 1 - 0.41\frac{a}{g} \tag{III.2.3}$$

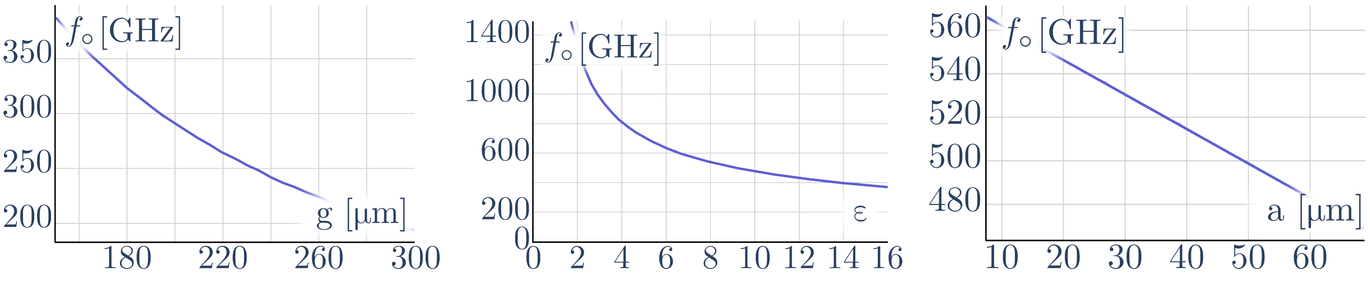

(a) **(b)** **(c)**

Figure III.2.3: *$f_\circ$ as a function of (a) g, (b) ϵ_r and (c) a for a* 100µm *thick substrate. Figures made with Python and Inkscape by the author.*

Increasing the underlying dielectric thickness reduces the amount of fringes near the edge, incidently improving the selectivity. Using a material with higher relative permittivity is reducing $f_\circ$ as shown in Fig.III.2.3b. It is worth noting that ϵ_r has a first order impact on this comportment. Using Silicon as a dielectric, an ideal option for coupling to the detector plane, will strongly impede the bandwidth of the filter considering the high dielectric constant $\epsilon_r = 11.9$ of this material.

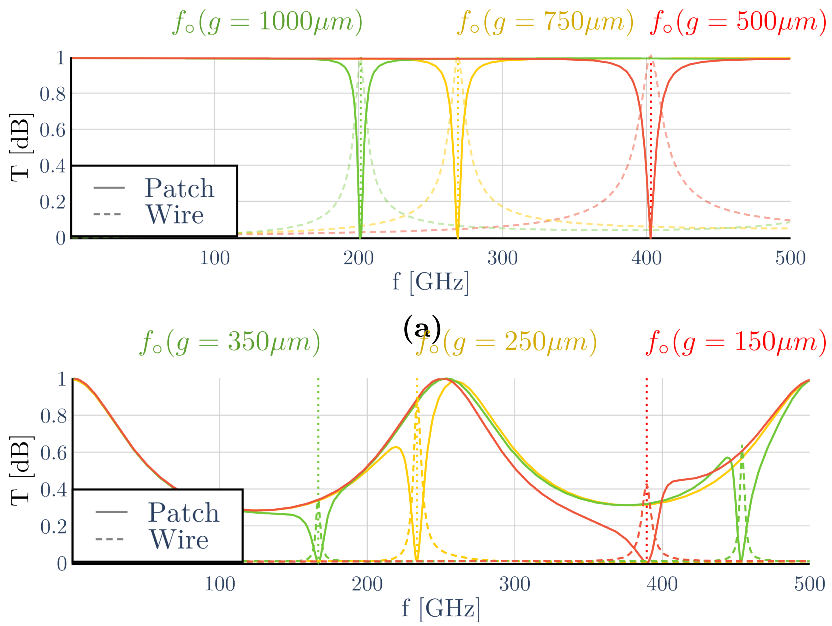

(a)

(b)

Figure III.2.4: *Transmission response of capacitive grids and wire grids complements with various unit-cell sizes, with* $a/g = 0.8$ *in (a) Vacuum and in (b) Silicon. Figures made with Python and Inkscape by the author.*

III.2.1.3 Multiple Layers

Stacking alternate layers of inductive and capacitive grids result in a band-pass response, as was shown in Fig.III.2.2c. An overlap in BW must be defined, designing the feature sizes of the square patches and wires accordingly. Oppositely, stacking the same grid multiple times will amplify the selectivity of the LPF or HPF. It was mentioned in Section I.2 that instruments need to cover multiple octaves of bandwidth in order to remove foreground contributions efficiently. The LPF resulting from capacitive square patch arrays can be designed to span a broad frequency range whilst imprinting a phase shift. As such, they are selected for the MetaL design. It will be discussed in Part V that detectors have a lower limit in frequency, below which the photo-energy is insufficient to enable the breaking of Cooper pairs. Waves at lower frequencies transmitted to the detector plane would add up noise. A focal optics design composed as a BPF could be of interest to solve this issue, but in practice, these can pre-emptively be filtered out throughout the optics tube of the instrument. The MetaL is thus designed over a capacitive grid stack where the geometrical parameters of the patches are fine-tuned. Sensitivity in transmission and phase shift is given for a LPF made of air-gapped or Silicon embedded grids. Its baseline geometry is expressed in Table III.2.1. The impact of each geometrical parameter is similar to what was depicted for a single layer, with additional subtleties. The stack is modelled via the cascading matrix (III.1.4), also integrated to the code in Appendix C.

Fig.III.2.5 illustrates the sensitivity of the LPF in the number of layers. Increasing N also increses the number of ripples and the associated δ_A but improves drastically the filter selectivity. $\Delta\phi$ scales linearly with N as the increased path length adds up with the phase shift caused by the patches.

The impact of the feature size is shown in Fig.III.2.6. The capacitive effect dominates for small

Table III.2.1: *Design characteristics of a LPF with* $f_\circ \simeq 300\text{GHz}$ *in Vacuum and* $f_\circ \simeq 180\text{GHz}$ *Silicon.*

Dielectric	ϵ_r	g[μm]	a[μm]	l[μm]
Vacuum	1.0	400	125	400
Silicon	11.9	90	40	30

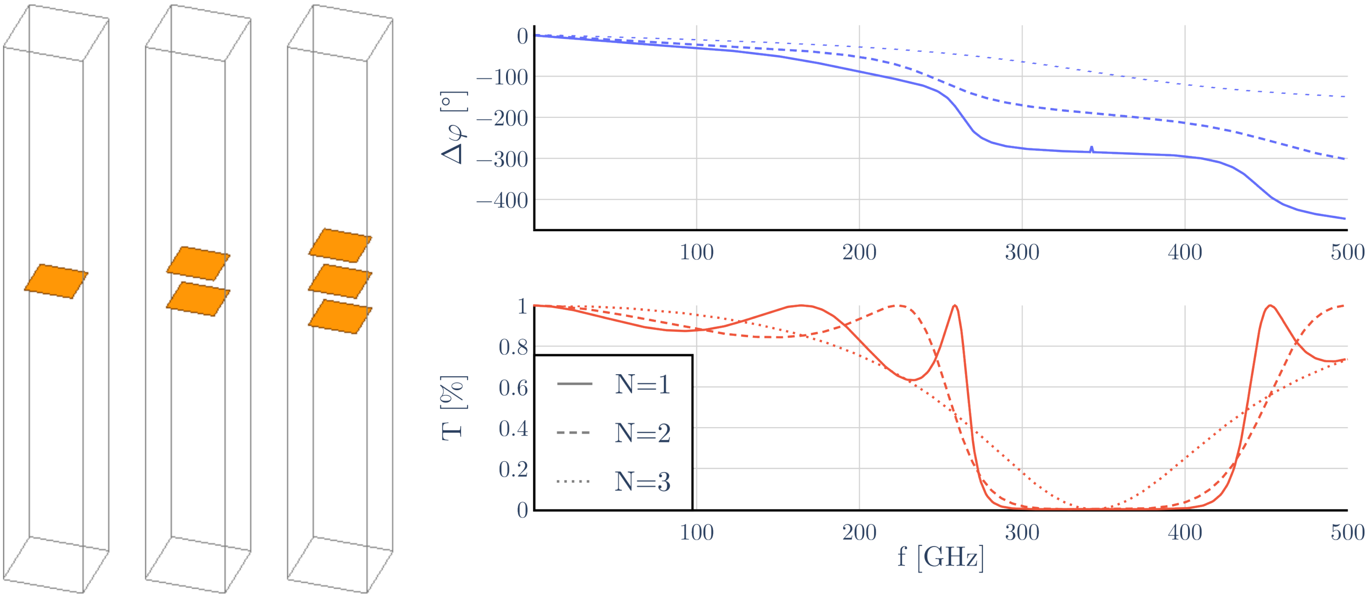

Figure III.2.5: *Sensitivity of* T *and* $\Delta\phi$ *in* N *for a LPF constituted of a succession of capacitive grids suspended in Vacuum. Figure made with Python and Inkscape by the author.*

gaps, ensuring low δ_A as well as improving S_c. The phase shift is strongly related to the feature size.

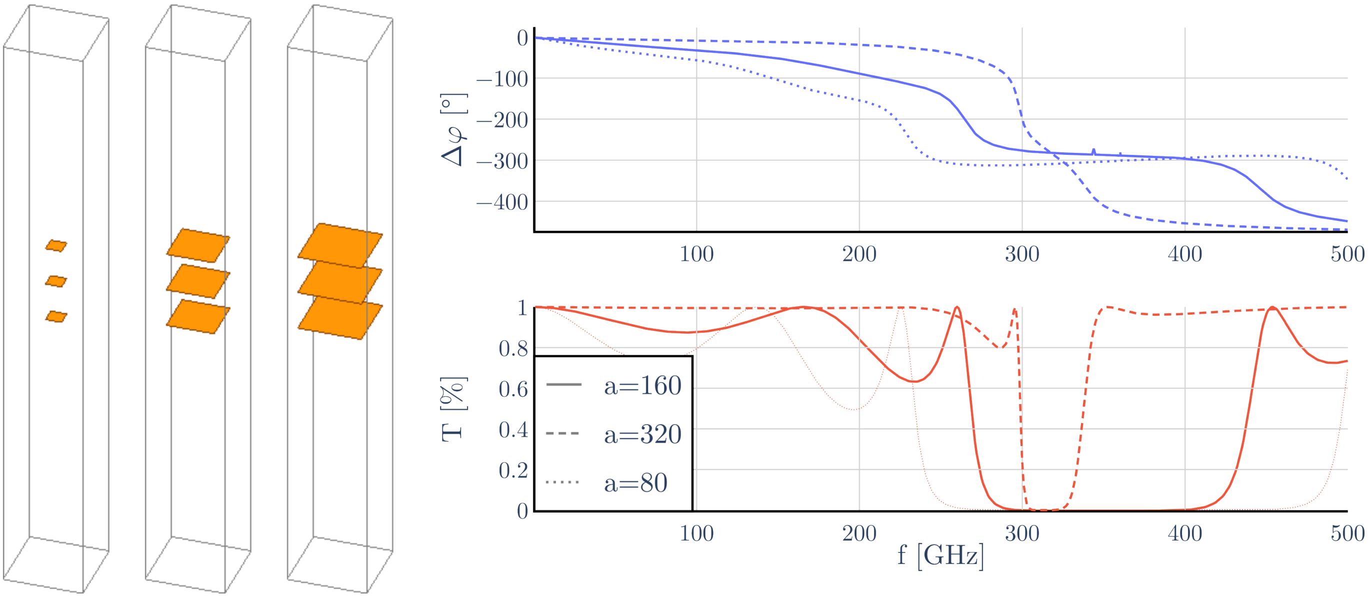

Figure III.2.6: *Sensitivity of* T *and* $\Delta\phi$ *in* a *for a LPF constituted of a succession of capacitive grids suspended in Vacuum. Figure made with Python and Inkscape by the author.*

A thinner dielectric offers a more stable response over an extended bandwidth at the cost of selectivity. For a design embedded in Silicon, as shown in Fig.III.2.7, despite a design relying on small a_n and l_n, the fringing effect inherent to the dielectric dominates. The higher order bands transmitted and, to some extent, the diffraction patterns can be removed with by changing the a/g ratio of the consecutive layers. At present, devices have been made with 100µm Silicon substrates at best. Thinner wafers become difficult to handle and integrate to FPUs.

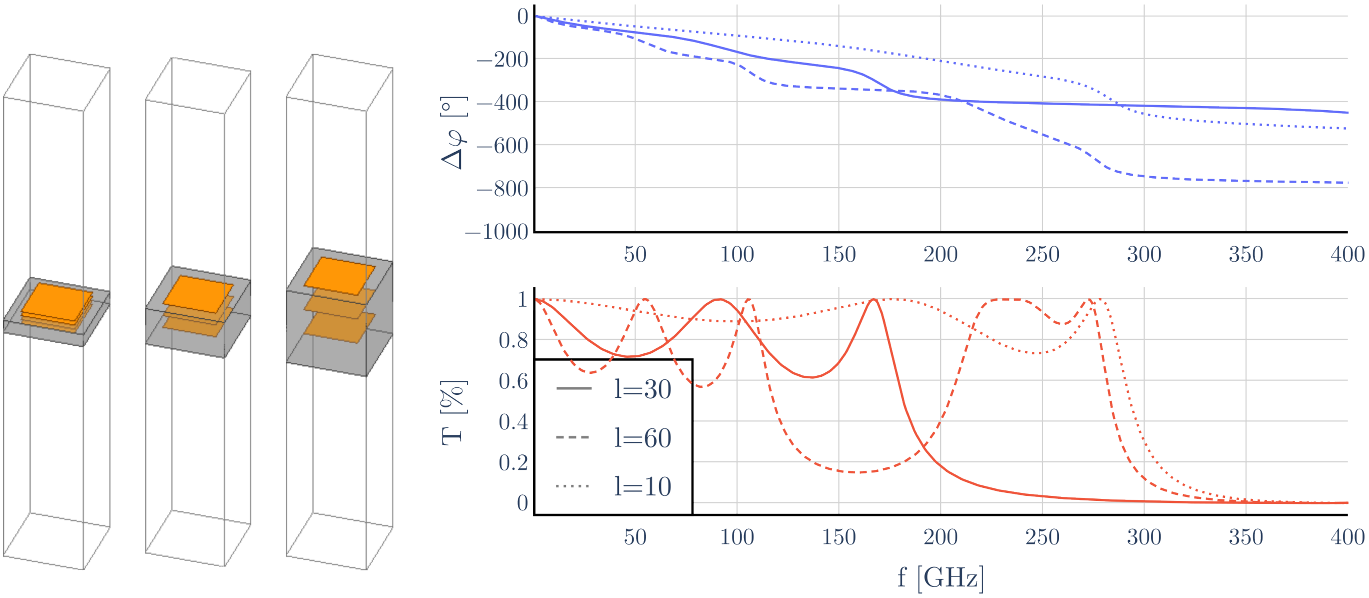

Figure III.2.7: *Sensitivity of T and $\Delta\phi$ in l for a LPF constituted of a succession of capacitive grids suspended in Silicon. Figure made with Python and Inkscape by the author.*

III.2.1.4 Limits and comments

The ohmic losses occurring in the metal shapes of a square patch array are proportional to $\eta\sqrt{c/\lambda\sigma}$, where σ is the metal skin depth, 0.21µm at 90GHz for a fairly impure Copper with a 99% Cu content, and a form factor $\eta = l/(1-2a/g)$ for the capacitive grid, and $\eta = g/2a$ for the inductive one is introduced. Even with degraded conductivity due to fabrication defects such as surface roughness or metal impurities that may occur during deposition, the losses will be negligible [184]. The impact of the dielectric may be limited by choosing a sufficiently thin substrate of low loss material, a trait that may be difficult to obtain in a focal optics technology, ideally embedded in Silicon for a direct compatibility with the detector plane.

The TL method previously discussed in Section III.1.1.1 and applied here to design filters has inherent limitations. Dielectric losses are not encompassed, non-normal incident wave cannot be treated and behaviour over the diffraction limit is not predictable through this method. Fig.III.2.8 illustrates the accuracy achieved by the TL method encoded in python, compared against a Finite Element Method (FEM) approach conducted in ANSYS-HFSS for a given filter design response. The simulated transmission and phase shift are obtained with ANSYS-HFSS, where the structure is solved using a 2-port Floquet-Bloch mode approach [185]. A single column of the filter stack is simulated, where the patches are set up as perfect conductors, repeated infinitely using the primary-replica (master-slave in the software terminology) boundaries. The Floquet-Bloch modes, namely the waves scattered on the transverse direction with respect to the patches, are taken into account in the model. On top of that, a fine meshing of the geometry can help simulating diffraction effect near the stop frequency. The TL model is a fast and accurate tool for preliminary designs of FSS based filters. For increasing number of layers, whilst the transmission response provided by the TL model near matches the simulated one, a slight deviation in phase shift is observed. For instance, for $N = 5$, $\delta\phi \leq 10°$ is obtained at 90GHz. Further validation of the results thus produced must be conducted with higher precision, for instance on ANSYS-HFSS, especially at high N.

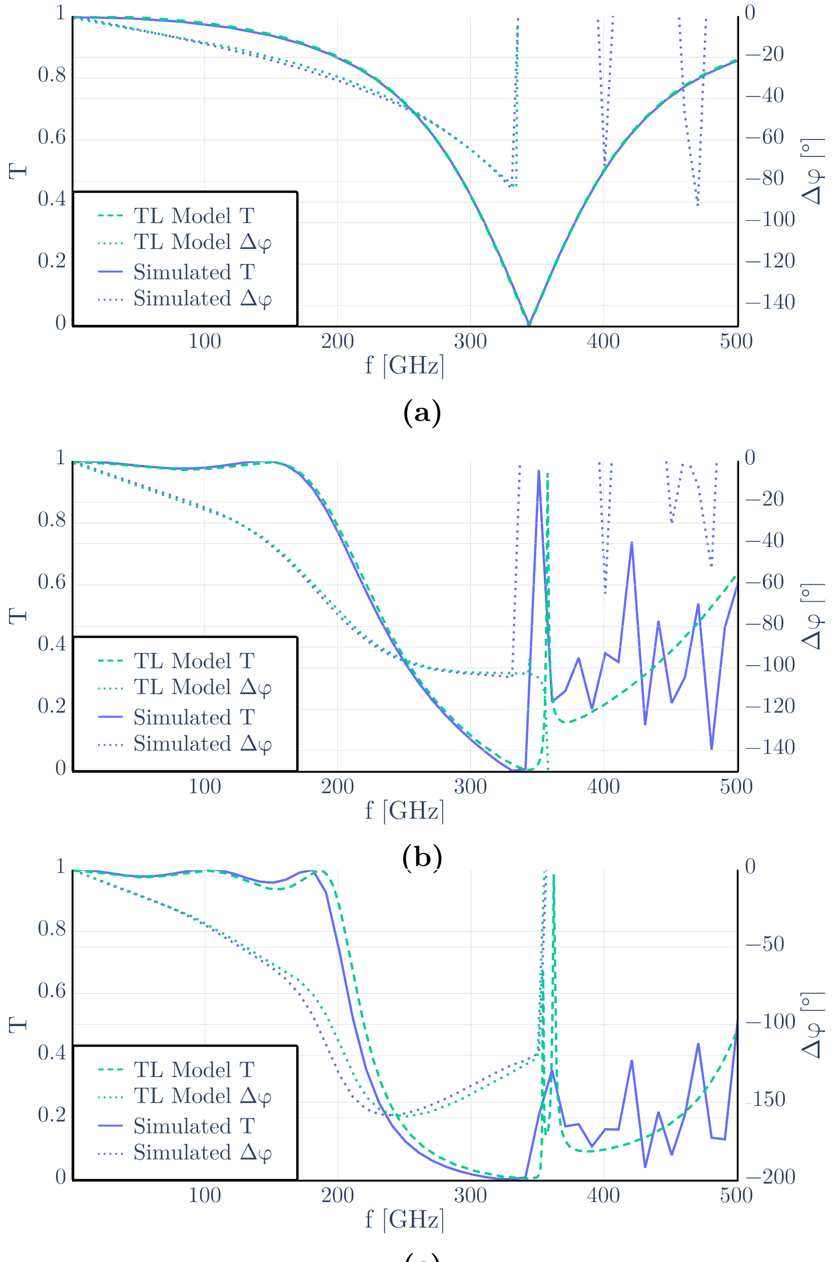

(a)

(b)

(c)

Figure III.2.8: *Comparison of the TL generated transmission and phase shift response, encoded in python, with those obtained in ANSYS-HFSS, produced by a LPF in Vacuum for (a) $N = 1$, (b) $N = 2$ and (c) $N = 3$. Figures made with ANSYS-HFSS, Python and Inkscape by the author.*

LPFs constituted of stacked arrays of square patches can provide a full transmission response over a large bandwidth with a tunable phase shift, linear with frequency in the pass-band. The design of these metamaterials can be conducted with an encoded TL model and validated through an FEM approach on a dedicated simulation software, such as ANSYS-HFSS. The MetaL concept relies on these techniques and will now be discussed further.

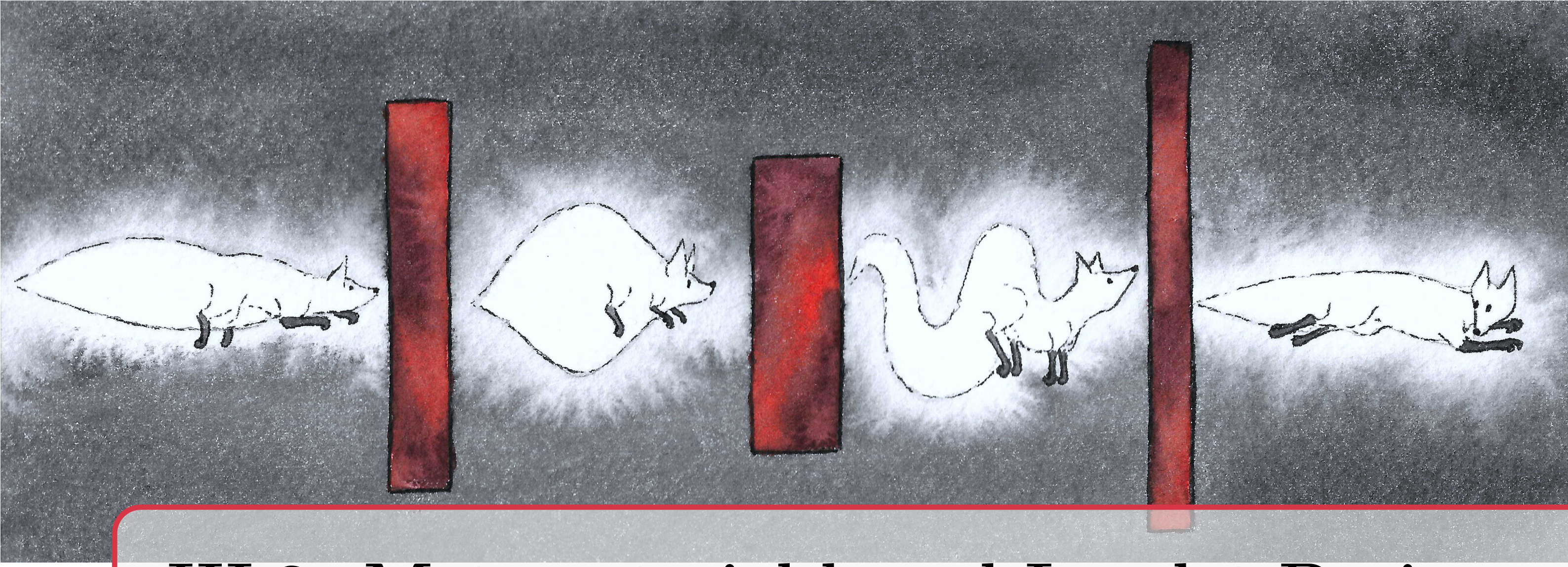

III.3. Metamaterial-based Lenslet Design

III.3.1 Phase-engineering Procedure

A wave incident on the top side of stacked layers of capacitive or inductive grids experiences a phase shift, as shown in Section III.2.1.2. As a lenslet aims at focusing the light onto a detector by implementing a phase transformation, such control over the wavefront and the allowable frequencies becomes a useful tool for the optics designer who can now match the incoming TEM wave to the coupled receiver. The Stokes - Helmholtz reciprocity principle [186, 187] is often used to take the reversed perspective on such coupling, where the quasi-spherical wave emitted by the detecting element is now the incident wave on the bottom side of the lenslet, which operates the phase transformation onto a plane wave. In the design of FPUs, the focal optics diameter D is the principal constraint and depends on the instrument fore-optics design and the frequency of interest. It is in fact imposing the pixel size, thus constraining the filling factor of the available focal plane, in turn affecting the instrument angular resolution and mapping speed. For the next generation of CMB experiments, $D = 10\text{mm}$ is a suitable pixel size for W-band observations, $[75\text{GHz}; 110\text{GHz}]$, as illustrated by Table I.2.2 and I.2.1.

The befitting phase transformation is traditionally achieved using ray tracing techniques, as is the case for the hyper-hemispherical lenslet, discussed below. The MetaL relies solely on a phase engineering procedure, inspired from the filter design techniques presented in Section III.2.1.2. Polypropylene embedded lenses and arrays have recently been made and characterised successfully [188, 128]. As discussed in Part I, transferring the technology to a Silicon embedded version is highly desirable for immediate matching with the detector plane and various options are currently under investigation, including the prototype characterised in the present work [189]. Promising results were demonstrated in the design of such lenslets [105, 135]. A proof of concept needs to be established through a comprehensive experimental analysis. Namely, the first steps, undertaken in the present work, are the full warm characterisation of the far field of a single MetaL prototype, validating the simulated response, which will serve as a reference for a follow up cold measurement of the lenslet beam when coupled to a detector, constituting a pixel. This work accomplishes the first item and offers some advances on the second. Accompanying the community's efforts in the realisation and demonstration of this promising technology, an air-gapped prototype MetaL operating in the W-band was developed at the National Institute of Science & Technology (NIST) institute, and the following parts focus on the activities taken in Cardiff through this work: a review of its design, a comprehensive experimental characterisation and a coupling architecture with KIDs as a proof-of-concept demonstration of the technology capabilities. The present chapter focuses on the MetaL design concept. A modelled hyper-hemispherical lenslet is discussed at first, simulated on ANSYS-HFSS in order to extract its far field response for further comparison with the MetaL. The design procedure of the latter is then depicted, starting from the extraction and discretisation of the phase profile of the element at focus, then moving on to how such discretised pattern is match by a pixel-column design constituted of stacked square patch arrays, and finally how the succession of columns realises the phase transformation required. The full lenslet is then simulated on ANSYS-HFSS although the model and results are reported further in Part IV.

III.3.1.1 A comparable hyper-hemispherical lenslet

Hyper-hemispherical lenslets consists of an anti-reflection coated extended hemisphere, patterned in a dielectric, where the extension length is chosen so that its focus matches the farthest geometrical focus of a synthesised reciprocal elliptical lenslet. As was discussed in part I, they have demonstrated good performances for CMB observation and as such, offers a relevant point of comparison with our device. A model is established [190, 191, 124] and shown in Fig.III.3.1 with a radius $R_h = 5$mm, extension length $l = 0.29R_h = 1450$µm, positioning the device optical focus as close as possible to the effective hemisphere geometrical focus. A $\lambda/4$ thick ARC made of PolyEtherImide (PEI) is added to match the Silicon lenslet to free-space. To draw a suitable comparison, the waveguide transition used for the MetaL experimental characterisation, discussed further in Part IV, was modelled scaled down and embedded in Silicon to feed the lenslet.

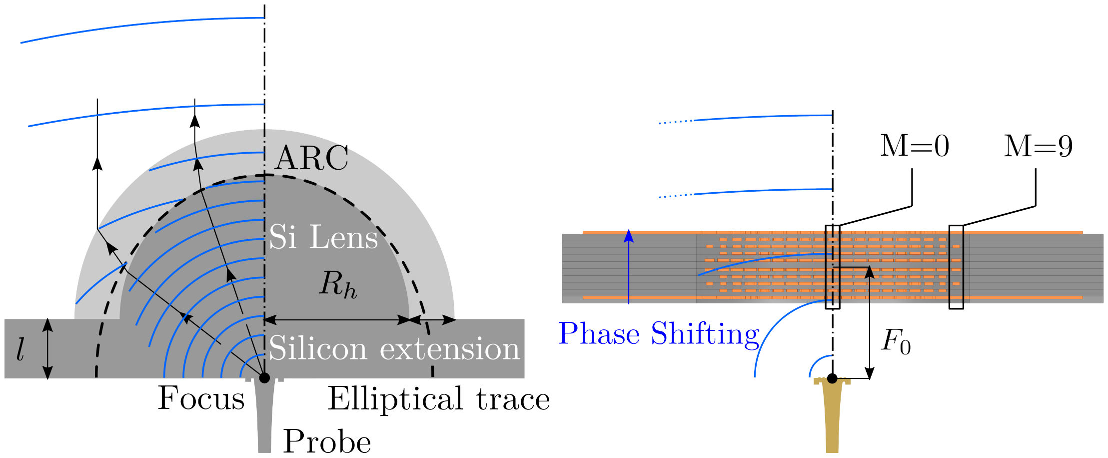

(a) **(b)**

Figure III.3.1: *(a) Cross-section view of the hemispherical lenslet coupled with the rectangular-to-circular waveguide transition positioned at the lenslet effective focal point, coincident with the upmost geometrical focus of the approximated ellipse. The probe considered is fully embedded in Silicon and scaled accordingly, matching the material constituting the lenslet. (b) Cross-section view of the MetaL coupled with the rectangular-to-circular waveguide transition in free space. The phase transformation occurs along the radius by M unit columns. Figures made with Python and Inkscape by the author.*

The hyper-hemispherical lenslet coupled to the waveguide transition is modelled in ANSYS-HFSS and its far field extracted further. In the model, shown in Fig.III.3.2, the waveguide transition walls are simulated as perfect electric conductors and symmetries are used to reduce computation load. Integration surfaces $\mathcal{S}_I$ surround the lenslet upper surface. They incorporated the radiation boundaries and are used to compute the radiated field and its power. The lenslet and inner volume of the transition are made of Silicon, whilst the ARC is defined as Alumina. The surrounding box is free-space. The field is computed at the source port and extended to the rest of the structure using FEM. The radiated far field, also shown in Fig. III.3.2, is integrated directly at the dedicated boundaries in ANSYS-HFSS. Its optical characteristics will be detailed in Part IV and compared against the MetaL response. The design of the latter will now be discussed in details.

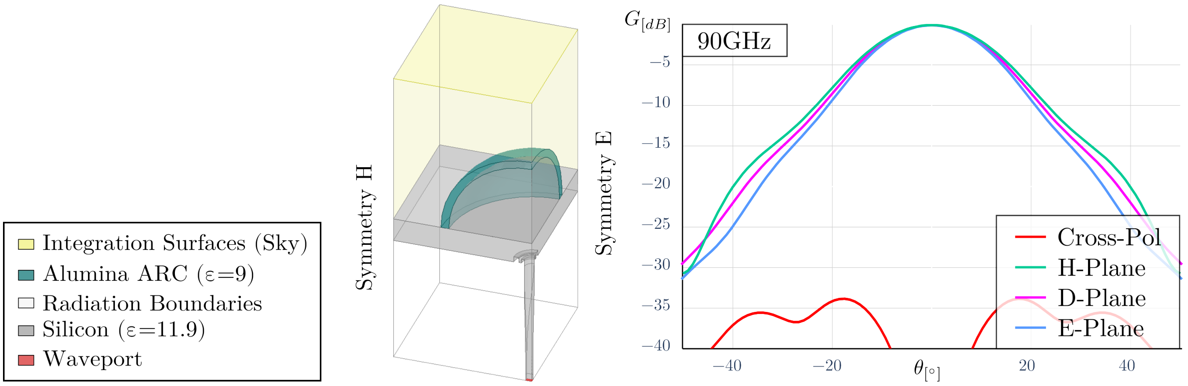

(a) **(b)**

Figure III.3.2: *(a) ANSYS-HFSS model of the Alumina coated Silicon hyper-hemispherical lenslet coupled to the rectangular-to-circular waveguide transition. The source port, materials and boundary conditions are highlighted. (b) Resulting far field pattern, to be characterised and compared with that of the MetaL in Part IV. Figures made with ANSYS-HFSS, Python and Inkscape by the author.*

III.3.1.2 Phase Pattern & Discretisation

For a given radiating source, the lenslet must operate a phase transformation radially whilst maintaining maximal transmission of the incident wave. The feed considered for the MetaL prototype is a stepped horn, further chocked to improve ellipticity of the beam and to reduce cross-polarisation [153]. The phase-engineering procedure consists of a radial discretisation of the phase profile of the feed for a chosen f-number, noted $f\#$. The probe is shown in Fig.III.3.3a along with the E-field it radiates, overlaid with the related phase cuts in the E, D and H-planes. A lenslet applying a phase shift matching this profile will ensure that the outgoing wave is planar. To perform the procedure, the feed phase patterns Φ needs to be determined at the predetermined focal length F_0. They are extracted for $f = 75\text{GHz}, 90\text{GHz}, 110\text{GHz}$ from a finite-element analysis model of the probe. The desired radial phase shift $\overline{\Delta\phi}$ to be imparted by the lenslet corresponds to the averaged $\Delta\Phi = \Phi - \Phi_{r=0}$ at the azimuth angles $\varphi = 0°, 45°$ and $90°$, fitted to a third degree polynomial with coefficients c_i, as per (III.3.1). This decomposition is further illustrated by Fig.III.3.3b for $f = 90\text{GHz}$. As previously stated, such averaging is necessary so that the lens response is symmetrical for both polarisations.

$$\overline{\Delta\phi}(r,f) = c_3(f)r^3 + c_2(f)r^2 + c_1(f)r = \overline{\Delta\Phi}(r,f)|_{\varphi=0°,45°,90°} \tag{III.3.1}$$

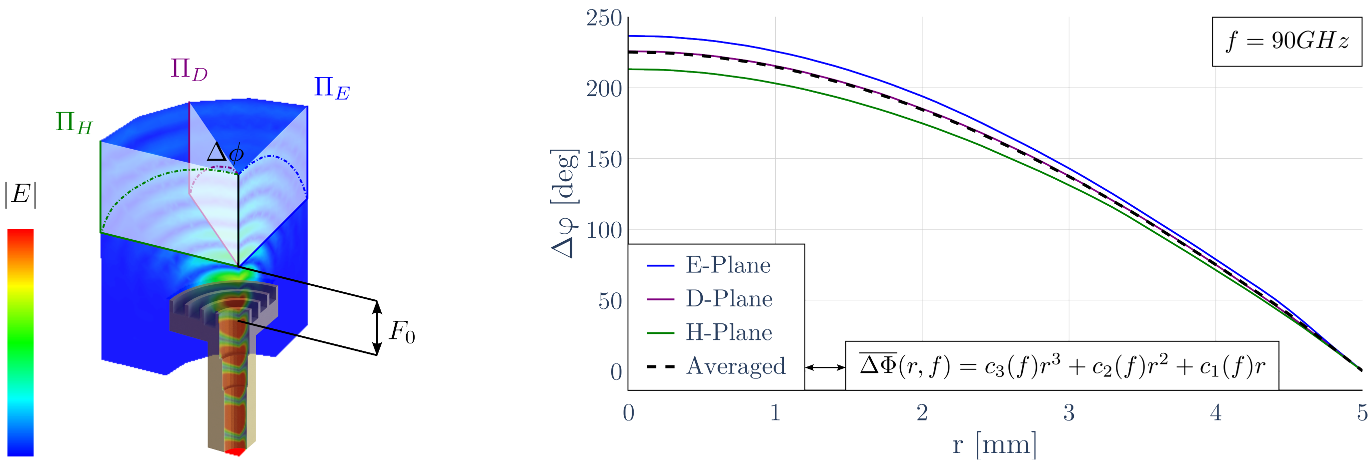

(a) **(b)**

Figure III.3.3: *(a) A visualisation of the probe, sectioned in a quarter and its phase cuts in the E, D and H-planes, at* F_0*, baseline of the calculation of the phase transformation the lenslet must operate. (b) Averaging of the phase cuts, as described by* (III.3.1)*. Figures made with ANSYS-HFSS, Python and Inkscape by the author.*

To realise the desired $\overline{\Delta\phi}$, the lenslet is radially decomposed into a subset of M pixels, each of which comprises a column of N stacked metallic square patches separated by an air-gap or any dielectric of choice, modelled as a TL equivalent lumped element circuit. The descretisation procedure of the desired $\overline{\Delta\Phi}$ is illustrated in Fig.III.3.4 for a unit-cell size $g = 500\mu\text{m}$, a value set by constraints described below. It is effectively a spatial averaging of the phases contained within a g^2 pixel operated on each pixel over the entire surface of the lenslet. In the case of the air-gapped prototype, it represents a total of 262 columns. The design procedure has two main constraints: the layer spacing l_n and the number of layers N. For each column, achieving the desired $\Delta\phi_M$ whilst maintaining high transmission $|T_M|$ is accomplished by tuning the unit-cell size g for the entire column, and the half-gaps a_n for each layer within.

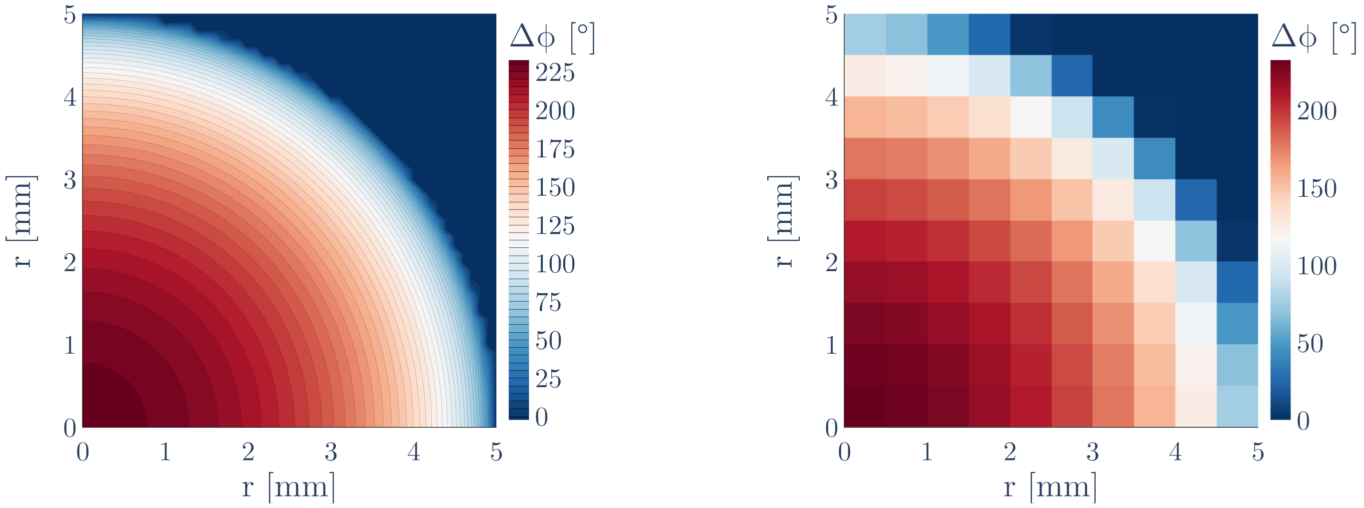

(a) **(b)**

Figure III.3.4: *(a) Contour view of the phase transformation to be made for* $f = 90\text{GHz}$*, and (b) its descretised version for* $g = 500\mu\text{m}$*. Figures made with ANSYS-HFSS, Python and Inkscape by the author.*

An immediate constraint lies in the layer spacing l_n as wafer thicknesses available commercially have fixed values for a given diameter. For instance, 150 mm diameter wafers may be available with 100 µm, 150 µm, 200 µm, ... thicknesses. Working with 100µm thick wafers, or thinner, for diameters reaching at least 100mm is a delicate task. Besides, its was previously mentioned in Section III.2.1.2 that metamaterial filters are diffraction limited (III.2.3). For a stable response, away from any diffraction effects, and an accurate modelling of the filter stack, it is necessary to set the spatial resonant frequency fairly low. As can be gathered from Fig.III.2.8 and Fig.III.2.3, a range of optimal ω may be determined through a pre-analysis on the stability on transmission vs achievable phase shift of the TL model, further conditioned by available wafer thicknesses. In the present case, the layers are air-gapped. As will be discussed in Chapter IV.1, this is obtained by suspending the patches onto 2 µm thin Silicon Nitride membranes, effectively optically transparent. The columns of the prototyped lenslet are designed with $\omega = 0.15$, giving $g = 500$µm and $l = 250$µm, a thickness conveniently available from wafer suppliers. The number of layers N needed is established by the highest desirable phase shift, provided by the central column, which is thus designed first.

III.3.1.3 Pixel-Column Design

The computation of a given pixel-column is dictated by the amount of phase shift desired at that pixel over the operating bandwidth of concern and a threshold on the transmission response, here set at a minimum of $\tau = 98\%$. The phase transformation versus frequency relationship can be fitted with a low order polynomial using the phase patterns of the probe sampled at the band edges and the central frequency, providing the phase shift $\Delta\phi_{M,pix}$ to be operated by the column at position M along the discretised lenslet radius. The following steps are then taken, starting by the central column:

1. Beginning with a single layer n, the feature size a_n is tuned to maximise the phase shift while maintaining the transmission over the desired limit.
2. If $\Delta\phi_M < \Delta\phi_{M,pix}$, keep all a_n that respected the threshold τ and increment N.
3. For each combinations of $(a_{n-1}, ...a_1)$, tune a_n and check if $\Delta\phi_{M,pix}$ is reached and if $T \geq \tau$.
4. Repeat until both conditions are met.
5. Each obtained column is then simulated in ANSYS-HFSS where the a_n are adjusted where needed via an optimisation protocol readily available in the software.

Accomplishing these operations for the first column, which necessitates the highest phase shift, will provide the number of layers N. For the air-gapped prototype, the inherent matching to free-space allows for a transverse symmetry at the lenslet central plane. Axial symmetry is also necessary for equal treatment of both CMB polarisation directions. Those combined conditions allows for the resolution of an half-octant of the lenslet, encompassing 37 columns instead of the 262 previously determined. Fig.III.3.5 presents an example of column design reaching $\Delta\phi_{0,pix} = 220°$ for a somewhat relaxed transmission at $\tau = 0.9$.

The optimisation procedure to tune the feature sizes may be conducted using various methods. For instance, genetic algorithms [135] could be adapted to this TL model. For the air-gapped prototype, a Markov Chain Monte Carlo (MCMC) procedure was used [128], which implies new steps:

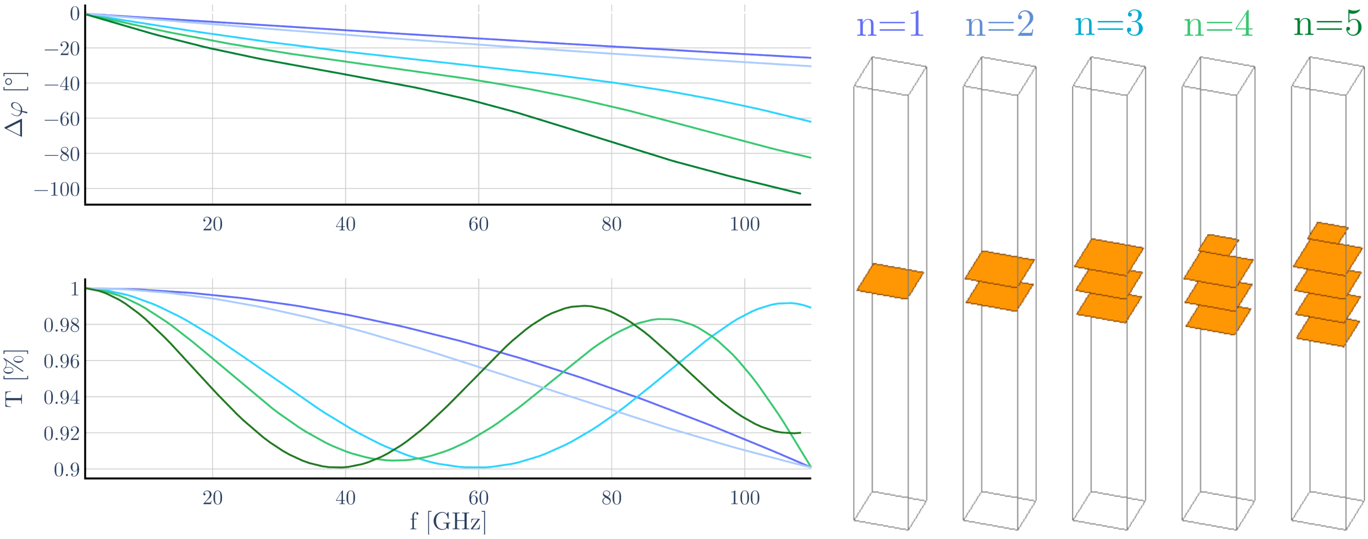

Figure III.3.5: *T and $\Delta\phi$ responses of a column built by consecutive increment of n and subsequent tuning of the related a_n. Figure made with Python and Inkscape by the author.*

1. Beginning with a single layer n, a set of a_n are randomly generated. Those of the patches matching the threshold τ and maximising phase shift are saved as first layers for potentially successful columns.
2. If $\Delta\phi_M < \Delta\phi_{M,pix}$, increment N.
3. A new random set of a_n is generated and all combinations are tried with the $a_{n-1}, ..., a_1$ already saved. The potential candidate to be saved must again maximise the criteria on $\Delta\phi_M$ and T.
4. If $\Delta\phi_M < \Delta\phi_{M,pix}$, repeat.
5. As before fine tuning is conducted in ANSYS-HFSS.

The lenslet prototype designed via this MCMC method is constituted of $N = 10$ layers for 185 optimised patches distributed through the 37 columns. The discretised transmissivity and phase shift are checked on ANSYS-HFSS using a model where each column of patches is analysed separately using a 2-port Floquet-Bloch mode approach. A given column is a stack of planar periodic patches, simulated as perfect conductors, repeated infinitely using the primary-replica (master-slave in the software terminology) boundaries. The resulting phase shift is shown in Fig.III.3.6 as a function of device radius.

III.3.1.4 Notes on Silicon-embedding

Embedding a design initially in free-space requires scaling down the geometry as an inverse relation with ϵ_r. Unfortunately, scaling means a required wafer thickness of $\simeq$ 75µm for 100mm diameter at least to reach the FPU size desired for CMB experiments. Handling a single layer would be extremely delicate and the process, difficult to repeat. On top of this, it was described in Section III.2.1.3 that high dielectric constant implies a strong fringing effect which dissipates by reducing the wafer thickness even further, or, to a second order, by adding a few extra layers. An added ARC layer is also necessary to ensure matching to free-space, a task with an added difficulty as the discretised phase transformation needs to be preserved while the enhanced artificial dielectric exhibits refractive indices higher than that of the Silicon $n_{Si} \simeq 3.5$. These may be integrated

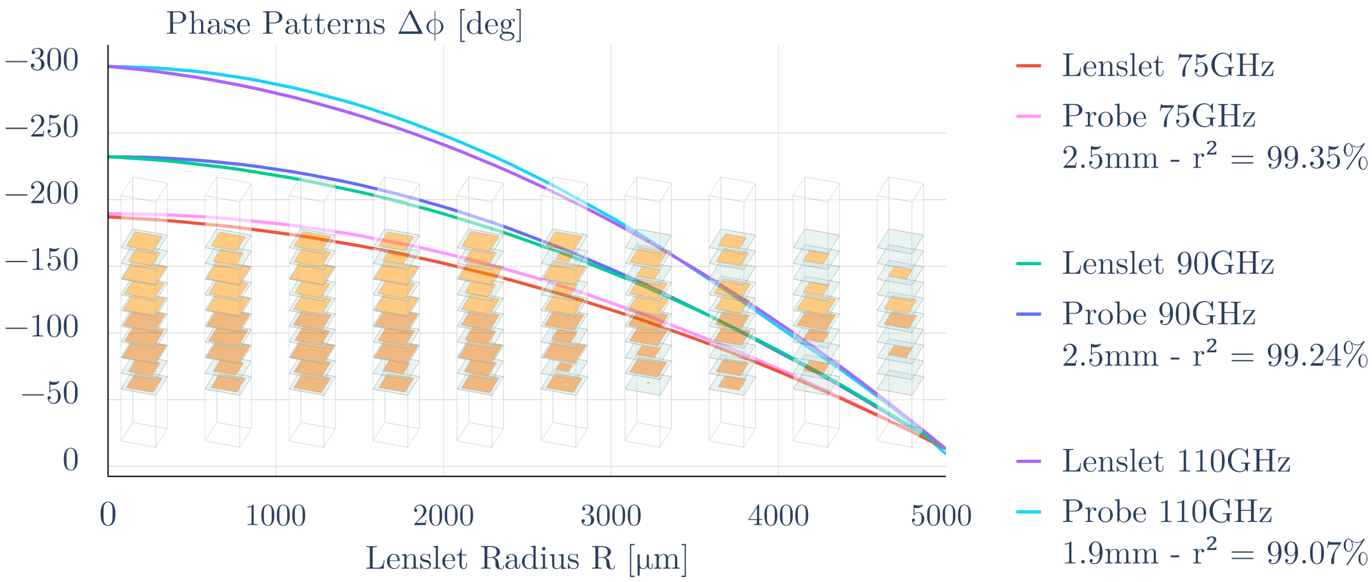

Figure III.3.6: *Phase transformation operated by the air-gapped prototype lenslet along its radius R. The matching phase profiles of the probe used to measure the lenslet beam pattern are also indicated for further discussion in Chapter IV.3. Figure made with ANSYS-HFSS, Python and Inkscape by the author.*

to the design [192, 135], but will again add extra layers. Suffering a 2dB loss, designs with 100µm thick wafers are possible with around 40 layers [135] but realistically difficult to fabricate.

To reduce the number of layers, alternative metamaterial surfaces could be applied instead. For instance lenses relying on SRRs or their complementary slots have been investigated [193, 194, 195], either building unit-columns constituted of patterns tuned to generate the desired discretised phase shift, or using twist-symmetries [196] to vary the Pancharatnam–Berry phase along the lenslet radius. For the present work, preliminary simulations were conducted on SRRs and their complementary shapes in ANSYS-HFSS but the results are not reported here as such patterns are relatively narrow band and their unit cell size is much larger than that of the square patches, resulting in a poor discretisation of the wavefront, thus a low gaussicity beam difficult to couple any instrument fore-optics.

Lenses embedded in polypropylene have been fabricated and preliminary experimental characterisation conducted [138]. However such material is unsuitable for temperatures below 1 K, where the shrinkage over a full array of 100 mm diameter or more will result in strong misalignments and warping, potentially causing delamination.

IV

MetaL Prototype Experimental Characterisation

Part IV Outline

An air-gapped, phase engineered MetaL prototype was fabricated at the NIST institute following the design method exposed in Chapter III.3. Preliminary experimental checks have been conducted [189] to rapidly validate the phase-engineering method and move on to investigations of devices fully-embedded in Silicon, including designs . Despite the heavy fabrication challenges and the high costs involved by the number of thin layers needed for their realisation, Silicon based devices are yet straightforwardly scalable and compatible with the FPUs. A full array can be fabricated using lithography techniques and stacking the resulting wafers together using simple alignment methods, a set of dowel pins for instance. As was underlined in Part III, using metamaterials enables some control over the sidelobe levels, cross-polarisation response, and other beam properties of the focal optics whilst being directly transferable to the detector plane. The array would be filled with MetaLs tightly packed whilst preserving a high optical efficiency, increasing the mapping speed.

The air-gapped prototype is a demonstrator technology and this work focuses on proving the MetaL concept by establishing a comprehensive and thorough analytical and experimental characterisation. The phase-engineering principle was described in the previous part and preliminary measurements were taken on this prototype and a Polypropylene array [138, 189], but it is proposed here to conduct a full beam description of the device over its entire operating bandwidth, both warm as a primary validation step and cold, integrated as part of a pixel design, demonstrating that the concept can indeed be applied to a FPU design.

A copy of the NIST prototype was made in the Institute for Compound Semiconductors (ICS) clean room at Cardiff University, with added vents and checks on the bounding method for cryo-compatibility. The fabrication process, devised and carried on at Cardiff University independently from the NIST institute is given in Chapter IV.1. It resulted in the successful production of a second device made of stacked layers of Silicon, etched back to obtain membranes on which the constitutive metal patterns are suspended, showing the the process is repeatable.

in Chapter IV.3, the required setup to conduct high quality measurements of the devices far field pattern is given. The sensitivity in misalignments, tilts and mismatches is devised through preliminary simulations, and stabilising solutions are established where necessary. The scanning principle and experimental setup is then presented to finally show the results in Chapter V.2, where these are exposed in the context of benchmark CMB scan, as per devised in Chapter II.4.

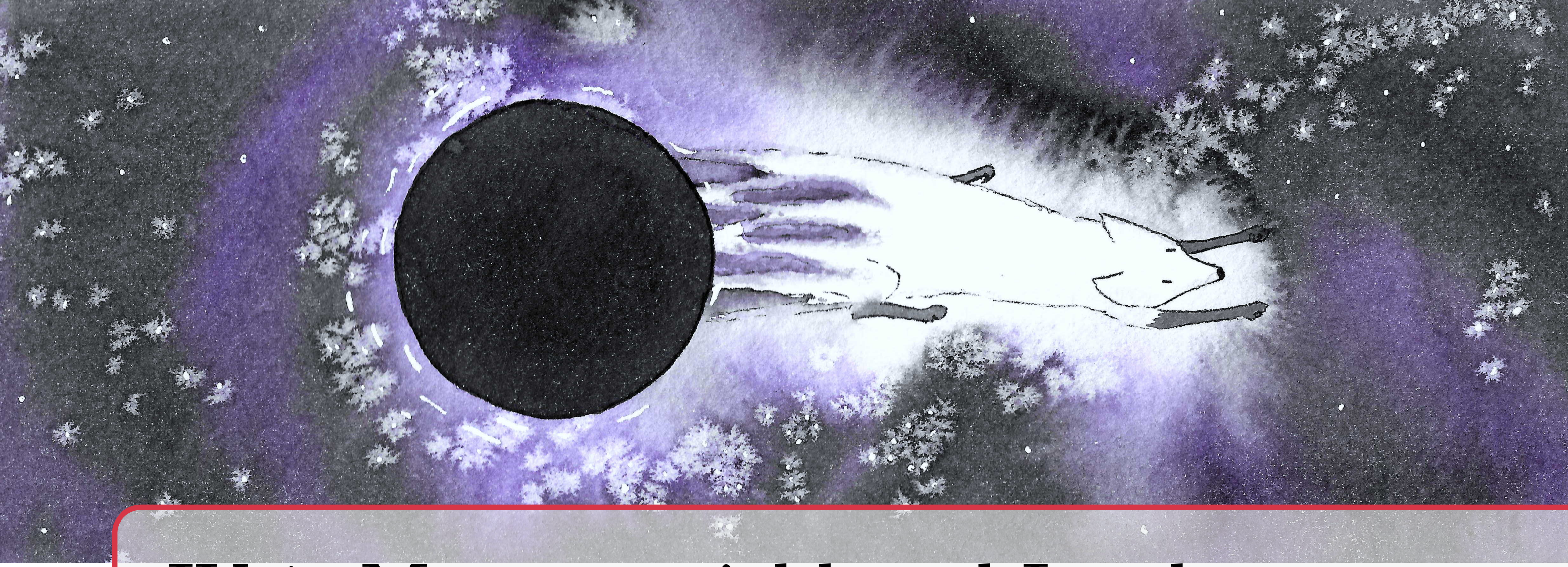

IV.1. Metamaterial-based Lenslet Fabrication

IV.1.1 Mask Layout & Processes

The MetaL consists of an assembly of stacked Silicon layers where the effective part of the lenslet, the FSSs, is lithographed at the centre on a 10 mm diameter Silicon Nitride membrane. The fabrication of the prototype made at NIST is briefly summarised in [189] but this device needed adaptations in order to couple it to a detector plane and carry cold measurements. Namely, ensuring that the bonding method used to keep layers together is suitable in a cryogenic environment and that air can evacuate properly during pumping. A second device is thus made at Cardiff University using a single 100mm diameter, 250µm thick, Silicon wafer. Pin holes were added to the layout, that would help with layer alignment during stacking. Vents were also included for the air to evacuate when the device would be put in the cryostat. At the edges, through lines were etched to help separating the layers from one-another by snapping them delicately. It was necessary to adapt the repartition of the different layers as to avoid a clash with supporting posts needed in the etch kit. Fig.IV.1.1 shows the layout used during the fabrication in details, with the three said posts at the centre in purple.

The full fabrication process, carried in Cardiff ICS clean rooms, except for the RIE done in Edimburgh Scottish Microelectronics Centre (SMC), is depicted in Fig.IV.1.2 and consisted of the following steps:

- **Wafer preparation**

  1 An etch stop made of 1500Å wet thermal oxide is grown on the upper side.

  2 A 2µm thick stoichiometric Silicon Nitride is deposited by Low Pressure Chemical Vapour Deposition (LPCVD) with a tensile stress below 250MPa to ensure the integrity of the membranes.
- **Metal layer**

  3 A 400nm layer of Copper is evaporated atop.

  4 The wafer is spin-coated with positive resist and the photomask of the metal patterns is then developed with a direct writer. The latent image in the resist is developed to form the

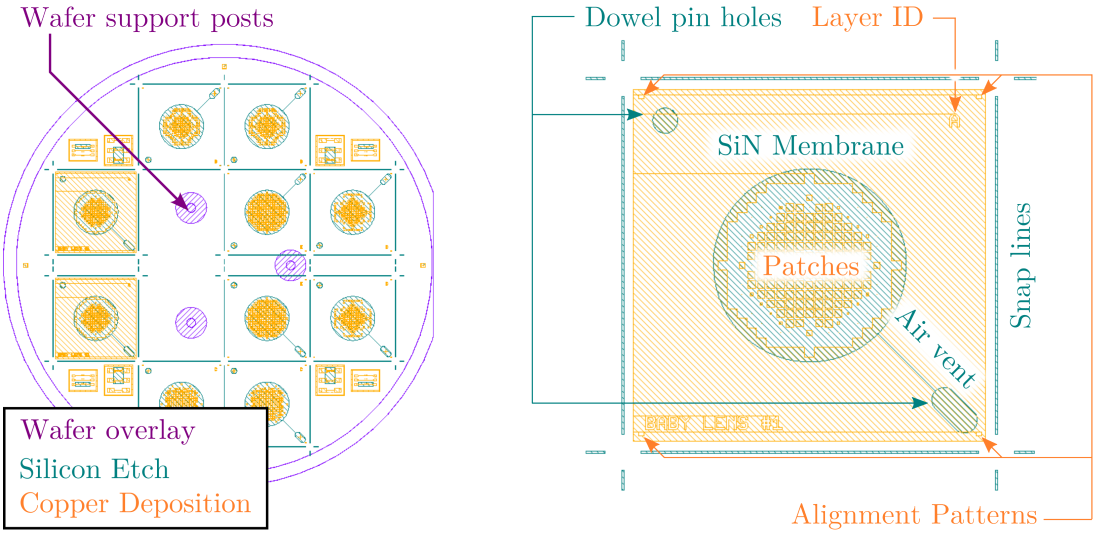

Figure IV.1.1: *Layout of the lenslet fabricated in Cardiff University clean rooms. All 10 layers constituting the prototype lenslet are included on a* 100mm *wafer. Figure made with KLayout and Inkscape by the author.*

required pattern.

5 The FSS are etched with Ammonium Persulphate. An attempt was initially made to lift-off the metal, which resulted in a lack of adherence of the patterns.

- **Backside etch for the membranes**

6 A 10XT positive photoresist is developed on both sides in the AZ developer with a 3:1 ratio. On the frontside, it protects the realised features. The backside mask for the Silicon etch is photolithographed afterwards.

7 The rims are plasma etched for the most part, and finished with a softer Xenon Hexafluoride etch. The latter procedure was added as the timing of the plasma etch was difficult to establish with regard to its rate and spatial distribution. Preliminary attempts resulted in pierced membranes if stopped too late, as shown on the left picture of Fig.IV.1.4, or leftover Silicon otherwise. The lengths of the snap lines were also reduced after layers separated. The last batch, finished with the softer Xenon Hexafluoride etch, resulted in an 80% yield.

8 Realisation of 8 layers of patterned metal patches on suspended Silicon Nitride membranes, completed with leftover layers from previous batches.

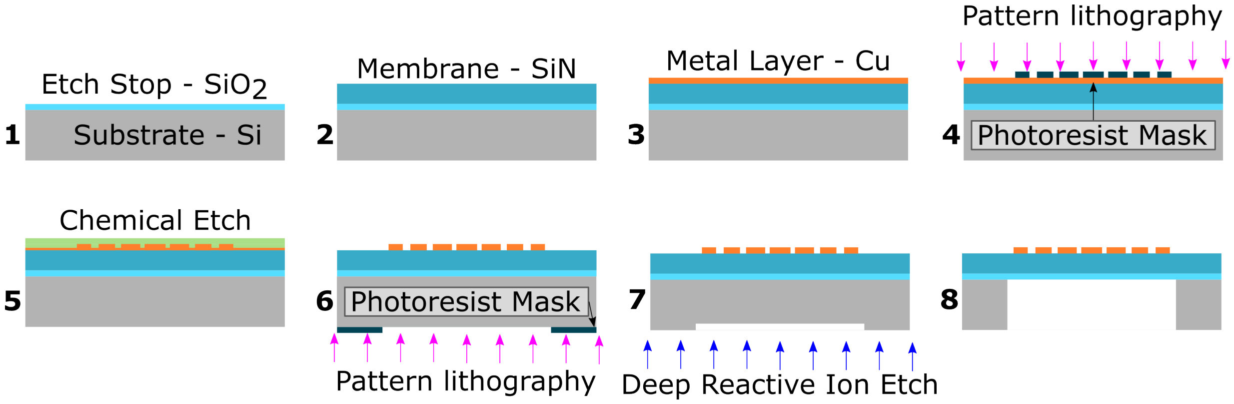

Figure IV.1.2: *Fabrication process flow showing the deposition, lithography and etching steps to realise a single layer of square patches suspended on thin membranes. Figure made with Inkscape by the author.*

Cryo-compatibility was checked for two types of glue: Stycast 1266 and Epotech 120. Glass temperature might be reached while cooling, or shrinkage and expansion might occur with the temperature gradients, risking delamination or stress on the membranes. The right photograph of Fig.IV.1.4 shows the glue penetrating between layers by capillarity, changing the effective layer thickness l. The photograph was taken after two glued layers were snapped off. The Epotech 120 has a much lower penetration and a more permissive curing time. The NIST prototype had a measured $\simeq$ 10µm averaged increase in the air-gaps.

The complete set of layers is shown in Fig.IV.1.3. For the fabrication of a single lenslet, stacking them together necessitated suitable accuracy on their transverse alignment. The tolerance in displacement for a layer at the mth position on the stack was established at $\delta p_m^{x/y} = 50\mu m$, as will be discussed further in Section IV.2.1. The integrated pin holes would have been sufficient for that purpose but couldn't be used as they were in a different position for the layers from previous batches. A dedicated assembly jig was designed, where large holes were opened on the top and bottom parts so the membranes would stay untouched and an angle bracket was added to align the layers together. Stacking was done in a clean environment under a binocular microscope. Fig.IV.1.5 illustrates the assembly procedure on the left photograph, and the alignment accomplished within tolerances on the next two pictures. Layers were cautiously installed one by one in the relevant order. Each layer was gently pushed against the L-bracket with a pair of soft tweezers whilst its position was checked under the microscope. Anisotropy in the alignment of the full stack was similarly done, looking both at the front and the backside, where more than 5 layers were visible providing the microscope focus was adjusted through the process.

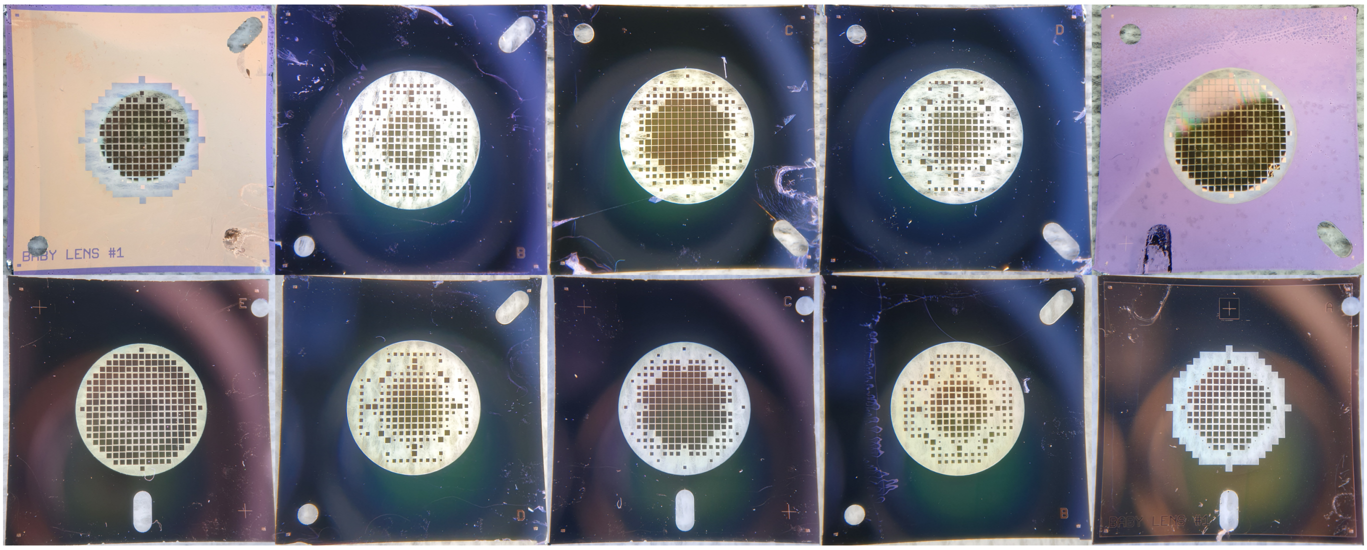

Figure IV.1.3: *Photography, taken by the author before assembling, of the ten layers constituting the prototype lenslet fabricated in the ICS cleanroom in Cardiff University and etched in Edinburgh SMC.*

Figure IV.1.4: *Photographies, taken by the author, of (Left) Broken layers from an over-etched* 100 mm *Silicon wafer. Each layer is a* 20 mm *by* 20 mm *square. The snap side lines were too long, causing high stress on the Silicon Nitride membranes which were pierced near the end of the etching process. (Center)* 130 µm *wide pin hole opened manually, before cleaning the pierced SiN. A few leftover Silicon Nitride shards can be seen, which were blown off afterwards. (Right) Tests of the penetration of two types of glue: Stycast 1266 (top) and Epotech 120 (bottom). The latter clearly penetrates less between layers and was preferred for this prototype final assembly.*

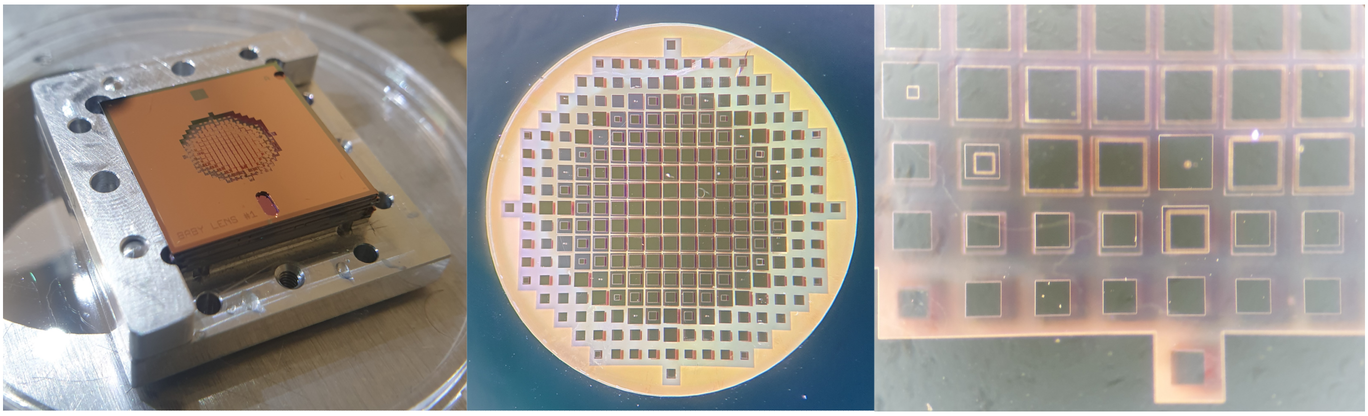

Figure IV.1.5: *Photographies, taken by the author, of (Left) Assembly jig with stacked and aligned* 20 mm *by* 20 mm *layers ready for clamping and gluing. (Center) Global view of the alignment of the two first layers, observed through the microscope. The aperture diameter is* 10 mm *(Right) View of all 10 layers, aligned below the desired tolerance. A single unit-column has a* 500 µm *cell size the leftover gap at the top is about the same as the tolerance limit* $\delta p_m^{x/y} = 50\,\mu\mathrm{m}$. *Displacements are clearly at least an order of magnitude below.*

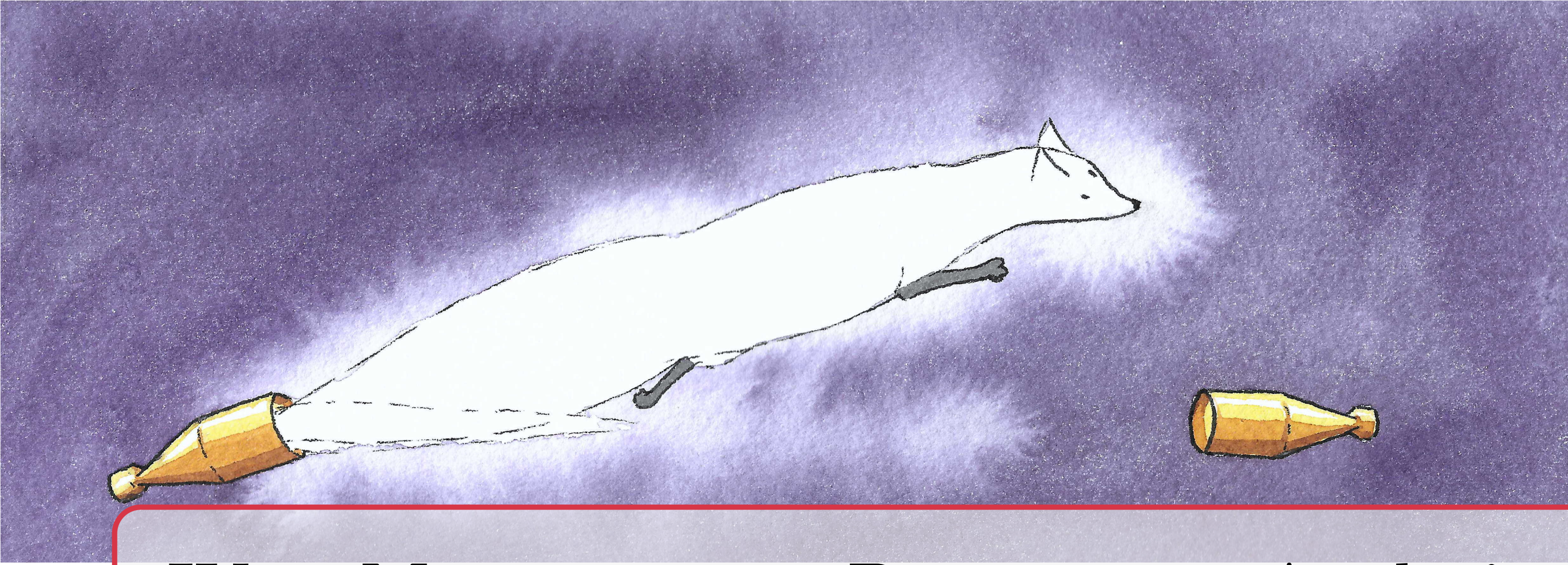

IV.2. Measurements Preparatory Analysis

The first step in proving the MetaL concept is to demonstrate the good optical quality of the fabricated prototypes, made at NIST and in Cardiff. The latter was made at a later time for the pixel design devised in Part V and its simulated and measured beam is discussed there. In this chapter, the analytical and experimental characterisation of the lenslet made at NIST is presented. The device beam pattern is first simulated in ANSYS-HFSS when coupled with the probe available in Cardiff. After preliminary measurements are conducted, the potential requirements necessary to avoid any systematic contribution of a refined optical test bench are derived from the model, where critical elements, previously identified, are integrated. For clarity, the entire set of simulations is fully covered by Section IV.2.1 whilst details regarding the probe are given in Section IV.2.2. The measurement setup, depicted in the next chapter, is then assembled in the anechoic chamber in Cardiff, with procedures in place to ensure the specified tolerances are respected.

IV.2.1 Preliminary Simulations

To validate the fabricated prototypes, an analysis of their radiated beam at the selected focal length is required. The model presented in Fig.IV.2.1a, simulated in ANSYS-HFSS, allowed to obtain the device response at a distance z_{tl} separating the waveguide transition aperture and the surface of the lenslet directly facing it. The probe initially used as a baseline for the lenslet design was not available in the laboratory and was therefore replaced by a waveguide transition of similar performances, further analysed in Section IV.2.2. Comparing its phase profile against that of the previous feed revealed a decrease in the focal length by $\sim$ 500µm, averaged over the bandwidth. This is determined considering the path length difference caused by an increase in phase shift at the initial F_0 (IV.2.1).

$$\delta z_{\delta\phi} = \delta\phi\lambda/2\pi \tag{IV.2.1}$$

In the model, the constitutive metallic patches and the waveguide transition walls are simulated as perfect electric conductors and symmetries are used to reduce computation load. Integration surfaces $\mathcal{S}_I$ placed in front of the lenslet upper surface are incorporated in the radiation boundaries in order to compute the radiated field and its power. A second set of integration surfaces, on the sides of the lenslet, allowed to check that the power leakage due to transversal mismatches between columns was negligible. The Silicon rims, sidewalls surrounding the lenslet aperture in each layer and effectively structurally supporting the membranes, have thus not been incorporated in the model to reduce the computing load. The Silicon Nitride layers have not been included either, since they are an order of magnitude below the wavelengths of concern, making them difficult to mesh for a full lenslet model. The metal thickness was disregarded for the reasons explained in Section III.2.1.4. Important mesh size variations were constrained using manual mesh definitions around fine features. The optimal probe to lens coupling is chosen by analysing the simulated far field that maximises the power efficiency $\eta_C > 80\%$, the gaussicity $\eta_0 > 90\%$ while minimising the ellipticity $\mathcal{E} < 5\%$. These thresholds are set in line with existing mission constraints [116, 197, 151], reviewed in Part II. Such an optimal beam response is depicted in Fig.IV.2.1b at $f = 90$GHz. Similar performances are observed at the bandwidth edges. The simulated field presents excellent beam characteristics over the range of focus $F_0 \pm z_R = 3.5\text{mm} \pm 1\text{mm}$. For all simulated z_{tl}, the ellipticity is below the 5% threshold whilst the gaussicity (II.3.11) is above 80% across the bandwidth of interest. The selection criteria is then the power efficiency η_C, consistently above 95% for $z_{tl} \in [1.9\text{mm}; 2.5\text{mm}]$ and maximised for the distance $z_{tl} = 2.3$mm.

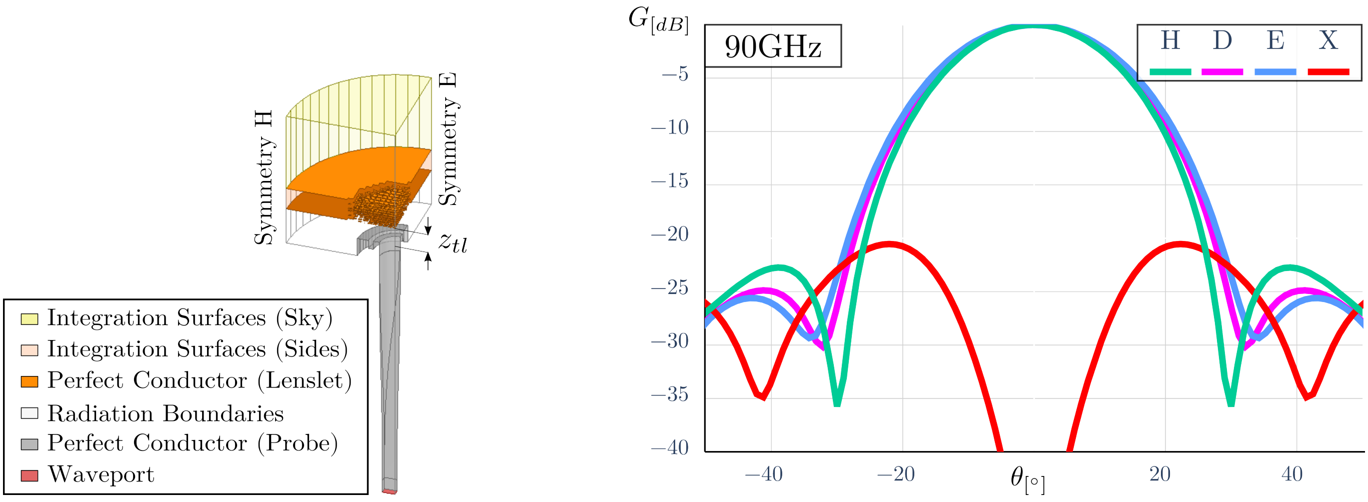

(a) **(b)**

Figure IV.2.1: *(a) Model of the probe-coupled lenslet simulated in ANSYS-HFSS, allowing an analytical validation of the design and a comparison point for the measured field. (b) E, D and H-plane cuts of the simulated co and cross-polarisation response of the device at $f = 90$GHz. Figures made with ANSYS-HFSS, Python and Inkscape by the author.*

The phase transformation accomplished by the lenslet is modelled via the radial distribution of columns described in Section III.3.1.3. The response is further compared with the probe phase patterns at different distances along the optical axis and through the operating bandwidth, as presented in Fig.III.3.6. Using the coefficient of determination criteria $r^2 > 99\%$ pointed to a range of distances $z_{tl} \in [1.9\text{mm}; 2.5\text{mm}]$, validating the 2.3mm obtained with the previous model. On top of this, noting that the probe has a $w_0 \simeq 1$ mm beam waist, averaged over the E, D and H-planes, the resulting ratio of the 5 mm radius truncating aperture of the lenslet is $T \simeq 0.76$, very close to the optimal 0.78. The shorter distance at high frequency also suggests a near zero achromatism $\Delta F_0 = F_0(110\text{GHz}) - F_0(75\text{GHz})/F_0(90\text{GHz}) = 0.13$.

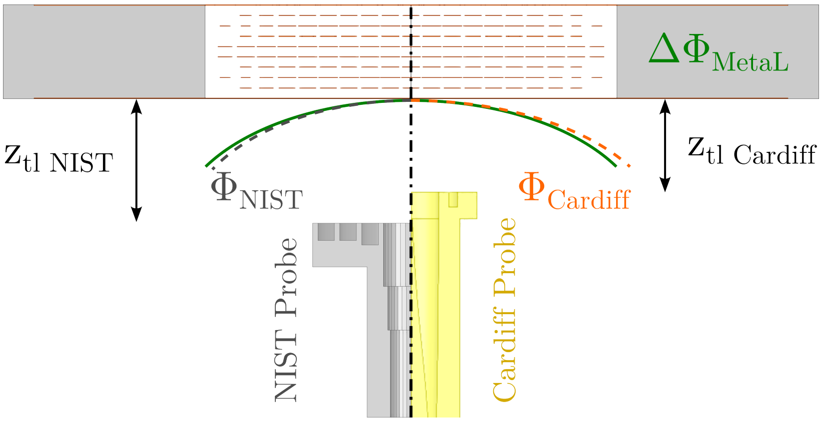

Figure IV.2.2: *Repositioning of the lenslet in accordance with the phase profile of the waveguide transition, showing a narrower beam waist compared to the initial probe. Figures made with ANSYS-HFSS and Inkscape by the author.*

The 10µm increase in air-gaps introduced during the fabrication, as discussed in Chapter IV.1, was modelled and found to have a negligible effect on the lenslet performances. It was possible to include the Silicon Nitride layers to the column models, where they could be resolved using suitable meshing. An additional phase shift of $\delta\phi_{SiN}(75\text{GHz}) = 18°$, $\delta\phi_{SiN}(90\text{GHz}) = 23°$ and $\delta\phi_{SiN}(110\text{GHz}) = 34°$ was observed, giving an averaged reduction in distance $\delta z_{tl} = 230$µm. Considering the lenslet thickness $t_l = 2.52$mm the resulting optimum focus is $F_0 = z_{tl} + t_l/2 = 3.55$mm. The 450µm deviation from the designed $F_0 = 4$mm is explained by the added phase shift introduced both by the Silicon Nitride layers and the mismatch with the waveguide transition.

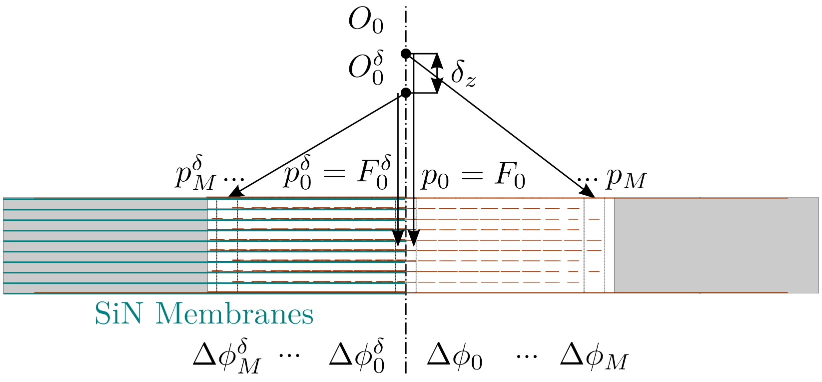

Figure IV.2.3: *Impact of the ten Silicon Nitride membranes on F_0. The dielectric extends the optical path length, resulting in an additional phase shift pulling the focus closer. Figures made with ANSYS-HFSS and Inkscape by the author.*

IV.2.2 Alternative Probe

The frequency converters used in the measurements depicted in Chapter IV.3 are equipped with WR10 rectangular waveguides whilst the original probe is a circular horn. A transition was thus designed by intersection of three blocks, illustrated in Fig.IV.2.4, where x is the rectangular waveguide transversal dimensions b, $a = 2b$ and the waveguide diameter d. The transmission is optimised by tuning the slope ff and length ll. The ellipticity is further improved by refining the geometry of the choke.

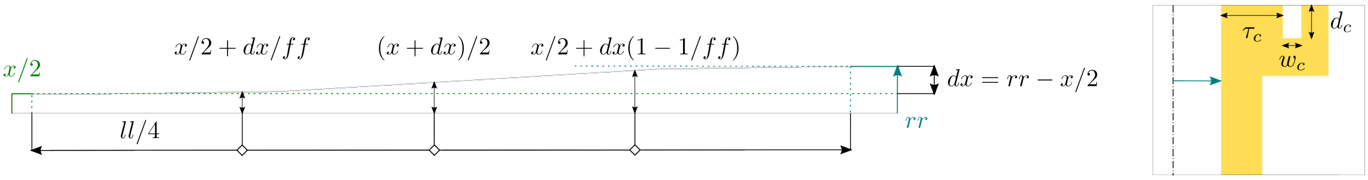

Figure IV.2.4: *Longitudinal section of the waveguide transition and its choke, showing their geometry parameters. Figures made with Inkscape by the author.*

The probe thus obtained is modelled in ANSYS-HFSS, its phase patterns are extracted at various z_{tl} and compared with the feed used for the lenslet design. Validating this probe experimentally is required as a deviation from the simulated radiated field would need to be incorporated further in the lenslet coupled model, or alternatively, modifications of the probe could be necessary. A potential shift from focus may be introduced by a displacement of the phase centre from the probe aperture. Its position was checked with the ANSYS-HFSS model by analysing the phase peak to peak variation along a wavefront, found to be a few tens of microns, further validated experimentally. Fig.IV.2.5 depicts the measured and simulated beam patterns of the probe at 90GHz in the E, D and H-plane cuts. Experimental characterisation of the probe is part of the measurement procedure of the lenslet. The related experimental setup will be discussed in Chapter IV.3. The broader shapes observed in the E and D-planes are due to a coarse alignment in those configurations. The bumps at the centre of the cross-polarisation pattern result from reflections off the grooves at the transition aperture. There is otherwise a reasonable match between the measured and simulated fields, also observed at 75GHz and 110GHz, sufficient to further investigate the probe to lenslet coupling.

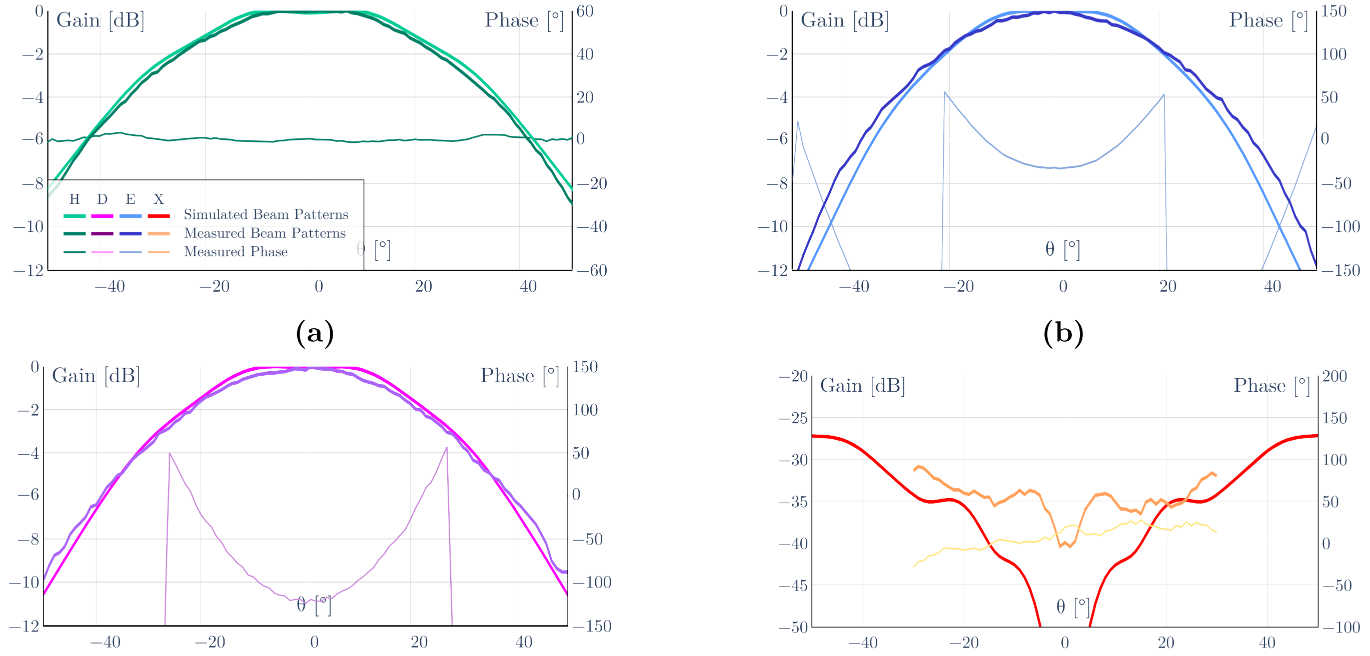

(a)

(b)

(c)

(d)

Figure IV.2.5: *Beam cuts in the (a) H, (b) E and (c) D-planes, and (d) cross-polarisation at* 90GHz. *Data simulated in ANSYS-HFSS and further measured, then compiled in Python by the author.*

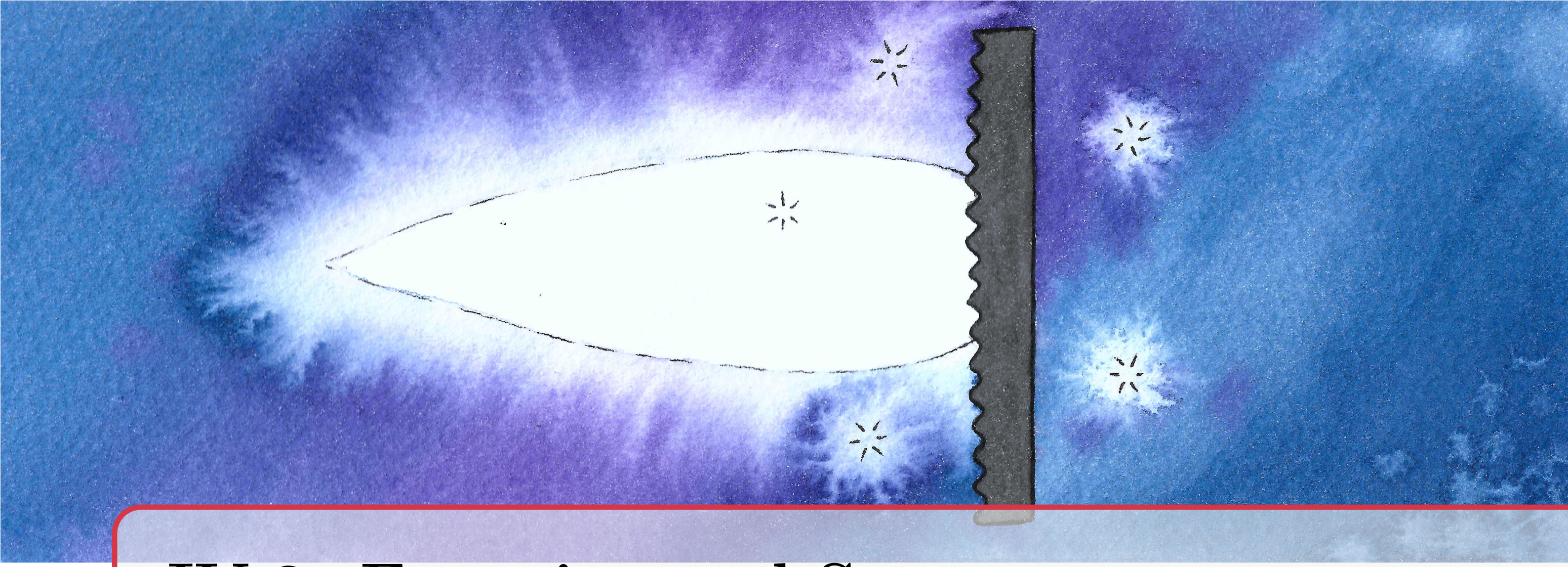

IV.3. Experimental Setup

The device was simulated in ANSYS-HFSS, coupled to the waveguide transition for which the adequate focus was found. Its far field profile was determined analytically at the frequency limits of the operating bandwidth and the central frequency. With this information, a setup can be designed to measure the beam experimentally and compare it with the simulated results. The measurement principle behind the acquisition of the far field pattern of the MetaL will be discussed first. Then, a thorough characterisation of alignment tolerances is presented, resulting from the experience acquired through a preliminary experiment. Finally, the assembly and related alignment procedures ensuring that the measurements are taken within those tolerances will be given. The MetaL far field thus mapped will then be shown and analysed in the following chapter.

IV.3.1 Measurement Principle

Realising a complete experimental characterisation of the lenslet implies mapping its co-polarisation and cross-polarisation response in the E, H and D plane cuts throughout the operating bandwidth, comparing the obtained beam to the simulation results and checking that the optical quality is within the requirements, further depicted in Section IV.3.2. The experimental principle is presented in Fig.IV.3.1, where a Receiver (Rx) scans the beam emitted by the device of concern, as it is rotated about its phase centre C_ϕ in a given plane. The device is coupled to a Transmitter (Tx) using a custom-engineered mount. Both the Rx and the Tx-Device Under Test (DUT) subassembly can be rotated by an angle φ around the OA. Its position can further be finely tuned in the longitudinal and transversal directions using a manual vernier 2-axis linear stage. A set of frequency converters is used to reach the desired bandwidth, onto which the waveguide transitions are mounted. The Rx and Tx stages are further connected to a Vector Network Analyser (VNA). The dynamic range was of order 90dB, covering the simulated -50dB first-null level of the device beam pattern. A dedicated software, coded by Dr Rashmikant Sudiwala in NI-Labview, was used for the test automation.

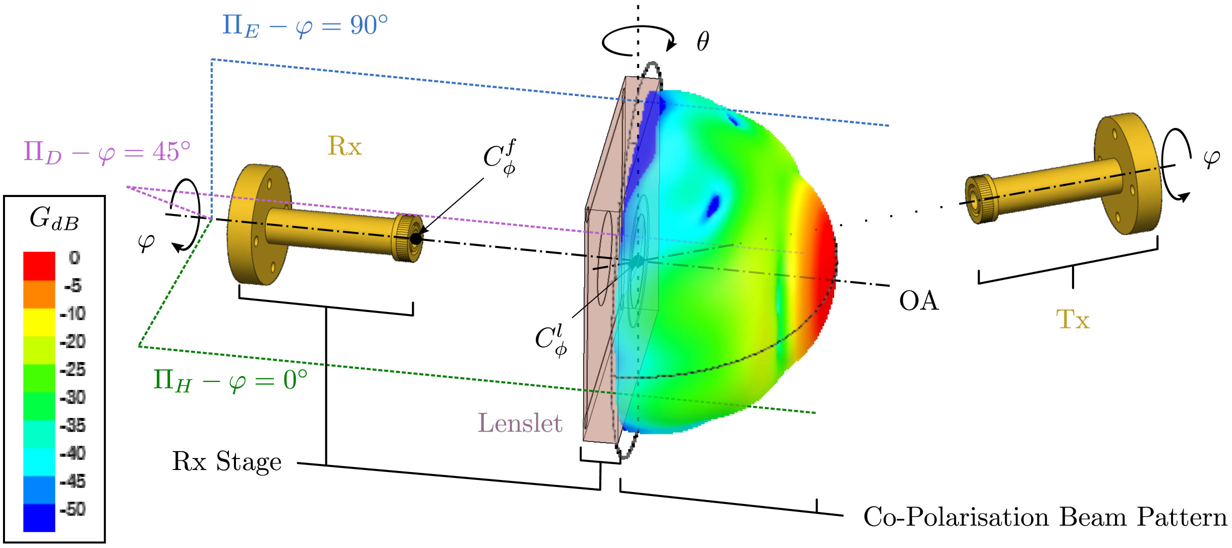

Figure IV.3.1: *Layout of the 2-port measurement setup, allowing beam scans in the E, H and D-planes, in a co and cross-polarisation configurations. The phase centre of the device C_ϕ^l is positioned at the centre of rotation. Scanning is done on a selected range of azimuth angle θ. The normalised co-polarisation beam pattern G_{dB} is superimposed onto the DUT. Figures made with ANSYS-HFSS and Inkscape by the author.*

IV.3.2 Systematics Control

Preliminary tests are conducted first, relying on the experimental principle described in Section IV.3.1 and shown in Fig.IV.3.2. It was then established that an accurate positioning of the probe and the lenslet along the optical axis was necessary and that a thorough identification of the tolerances needed to be conducted. The mounting strategy adopted to assemble the lenslet with the probe, positioned at focus, did not allow for fine tuning of F_0. The lenslet had to be adjusted by hand, tightening two nuts on the bolts supporting the optics and verifying the separation with calipers at a distance. The device was tilted with respect to the probe aperture plane, and this could not be mitigated. Identifying the systematics causing deviations of the observed beam from the simulated data, or if the simulation was at fault, proved difficult with this preliminary setup. A comprehensive analysis of the tolerances is thus carried out in order to devise a suitable mounting strategy and ensure proper alignment of the components constituting the test bench. To establish the constraints, the model of the probe-coupled lenslet discussed in Section IV.2.1 is modified by introducing longitudinal and transverse displacements and tilts of the lenslet with respect to the probe on one hand, and to the far field reference coordinates on the other, mimicking the Tx. The aforementioned displacements are transcribed in Fig.IV.3.3. Each displacement and rotation or tilt angles are iteratively spanned separately in ANSYS-HFSS, the resulting simulated far field is then compared with the reference one obtained when all devices are fully aligned along the OA. The comparison is made via an $r^2 = 90\%$ criterion and an additional check of the gaussicity threshold $\eta_0 > 90\%$. Limits were thus found on the longitudinal displacement between the lenslet and the probe, of $\delta z_{tl} = 100\mu\text{m}$, transversal misalignment of the lens with the OA, of $\delta x_l = 100\mu\text{m}$, transversal misalignment of Rx from the OA, of $\delta x_{TR} = 300\mu\text{m}$ in co-polarisation setup, and of $\delta x_{TR} = 10\mu\text{m}$ in cross-polarisation configuration with a tilt limit of $\delta\alpha_{TR} = \delta\beta_{TR} = \delta\beta_l = 3°$.

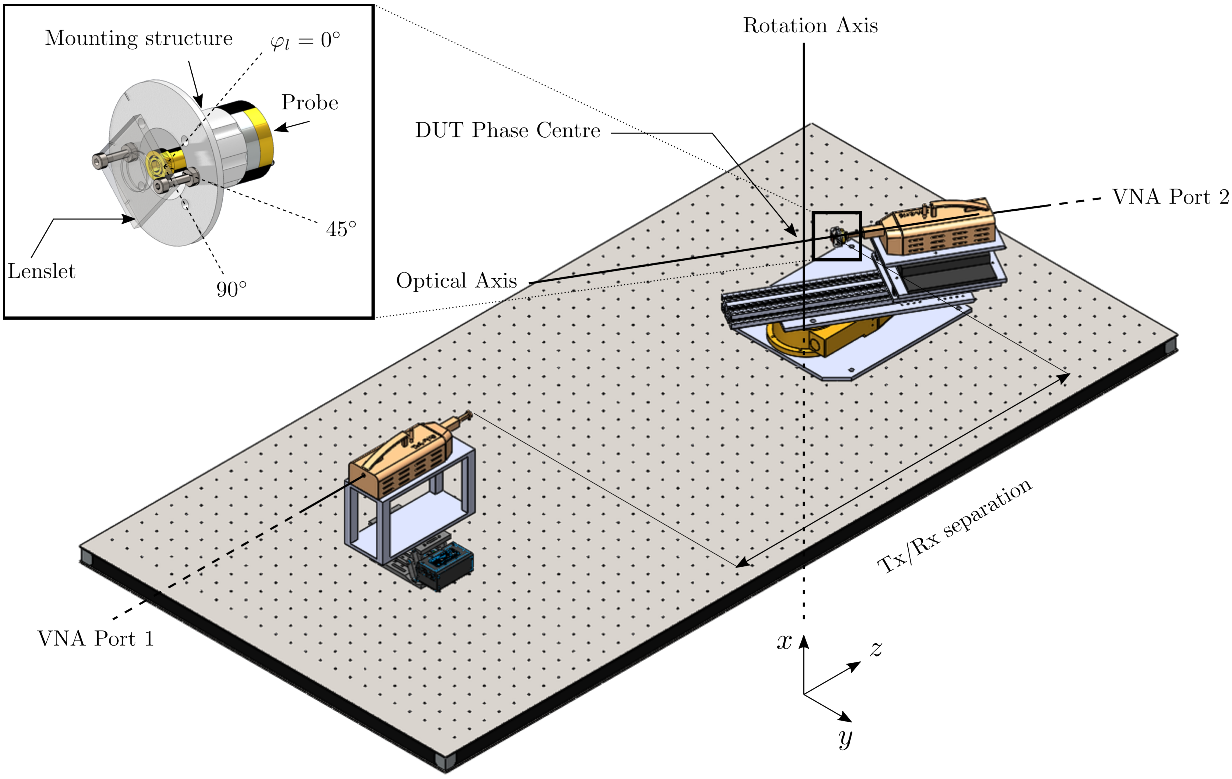

Figure IV.3.2: *Preliminary experimental setup, designed in Solidworks, implementing a 2D beam scan through the azimuth interval* $[-50°; 50°]$*, here in the H-plane. The plane cut is selected by rotating the Tx and Rx at the desired angles with respect to the OA. The mounting assembly did neither allow for a controllable* F_0 *positioning nor for a tunable tilt orientation of the lenslet with respect to the probe. Figure made with Solidowrks and Inkscape by the author.*

The simulations shown no tight constraints on the tilt angle for a co-polarisation measurement. Separating each component is giving an optimistic evaluation, but conducting a simulation of the interdependence of all parameters would require an unreasonably high computing power. In practice, these limits were sufficient guidelines to carry the precision measurements required.

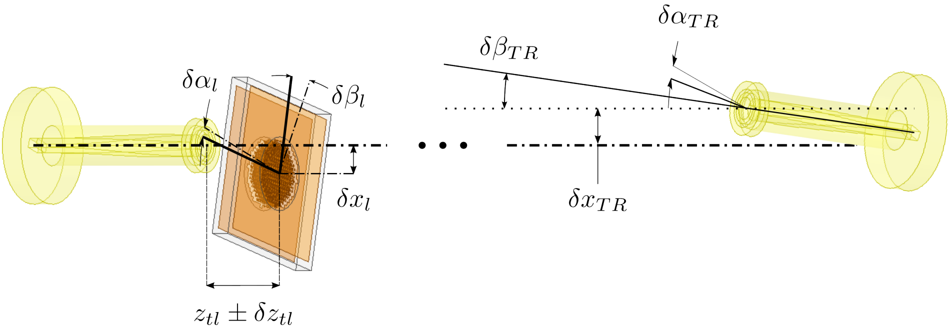

Figure IV.3.3: *Description of the longitudinal displacement between the lenslet and the probe, of* δz_{tl}*, transversal misalignment of the lens with the OA* δx_l*, transversal misalignment of Rx from the OA* δx_{TR}*, the tip angle* $\delta\alpha_{TR}$*, and tilt angles* $\delta\beta_{TR}$ *and* $\delta\beta_l$*. Figure made with ANSYS-HFSS and Inkscape by the author.*

A dedicated mount, shown in Fig.IV.3.4, is engineered in Cardiff by Mr Julian House, Mr Chris Dodd and the author to ensure the previously determined tight constraints are met. It further enables the longitudinal positioning of the lenslet with micrometric precision by rotation of the adjuster ring for which an 8th of a turn provides 100µm displacement. The fingers are machined from a single block of Stainless Steel, avoiding variations between the resulting parts. A set of holes and a recess ensures they are fixed and offer a flat surface for the lenslet to rest upon. In order for the lens and frame to be assembled, a measured 50µm provision is taken, that stays below the 100µm tolerance. A G10 clamp maintains the lenslet against the finger base while the frame ensures its installation with a very low tilt, given at 0.03° on the CAD model.

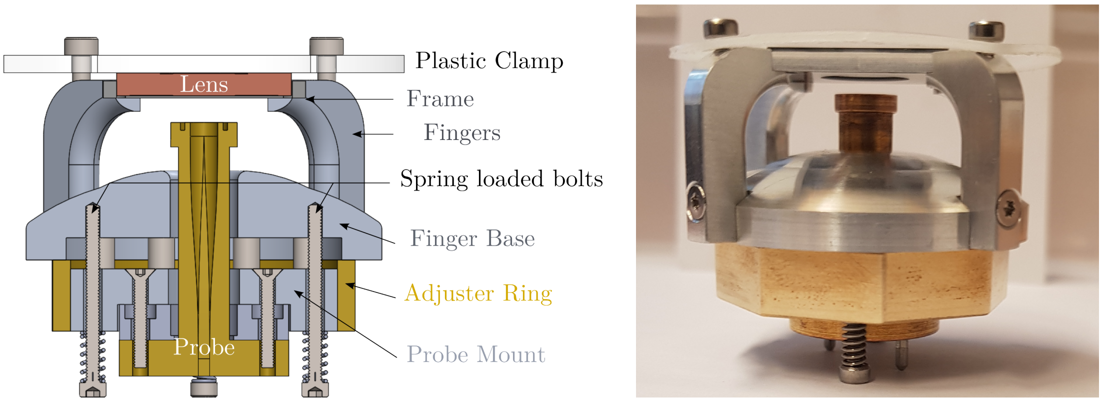

(a) **(b)**

Figure IV.3.4: *(a) Cross-section view and (b) photograph, taken by the author, of the engineered mount ensuring suitable alignment of the lenslet with respect to the probe. Figure made with Solidwokrs and Inkscape by the author.*

The mount was also integrated to the ANSYS-HFSS model, as shown in Fig.IV.3.5. The comparison method stays the same as the one described in the previous paragraph. A first run shown a strong deterioration of the far field profile due to the generation of standing waves caused by the highly reflective surface of the mount standing close to the lenslet bottom face. A absorbing boundary layer was thus added to the model and resulted in the retrieval of the desired beam profile. To mitigate this issue, a Thomas Keating (TK) tessellating RAM tile was machined specifically to be incorporated to the mount. The Aluminium frame shown no significant impact on the lenslet far field in these simulations.

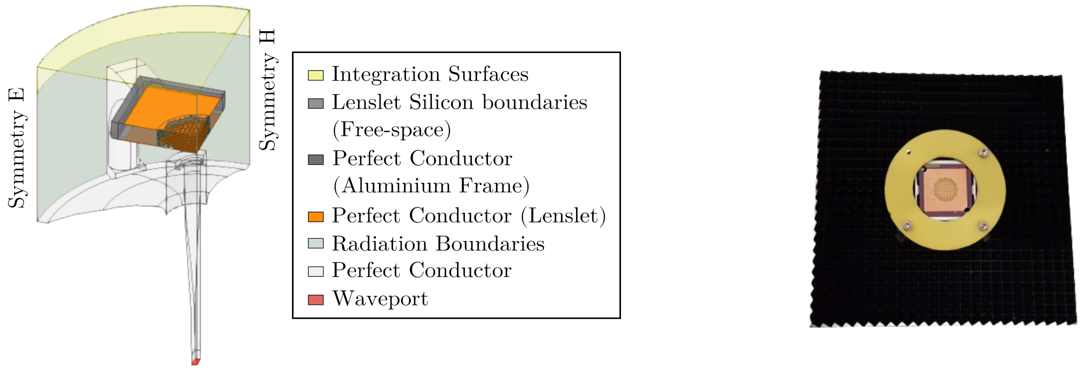

(a) **(b)**

Figure IV.3.5: *(a) ANSYS-HFSS model of the lenslet and waveguide transition assembled together with the re-engineered mounting assembly. The simulated far field thus compiled shown that the mount interferes with the field scattered between the probe and the lenslet, and contributes to the far field. (b) To mitigate this issue, a TK RAM tile was machined specifically to be incorporated to the mount, bolted between the lenslet and the probe.*

IV.3.3 Optical Bench Setup & Measurement Procedure

IV.3.3.1 Setup overview

Based on the preliminary setup depicted in in Section IV.3.2 and shown in Fig.IV.3.2, and with the alignment tolerances devised, an optical test-bench design is modelled in Solidworks, a CAD software. The experimental setup thus established is shown in Fig.IV.3.6. The MetaL is mounted on the Rx together with the waveguide transition and the TKRAM tile using the re-engineered mounting assembly previously discussed. The bulky Aluminium profile shown in Fig.IV.3.2 is replaced by a set of rails and a matching carrier. Full front panels made of TK RAM tiles and surrounding pyramidal absorbers are added to reduce background noise, as further explained later in this section. The principle is otherwise the same as the one depicted in Section IV.3.1.

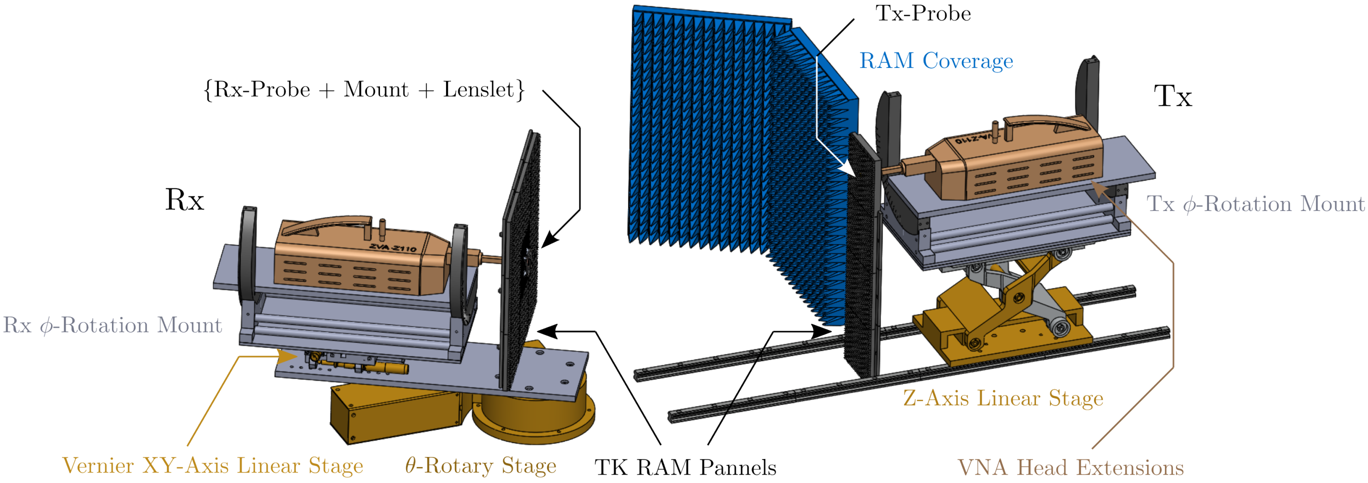

Figure IV.3.6: *CAD design, made in Solidworks by the author, of the optical bench setup, showing the various components required. As for the preliminary experiment, a 2D beam scan is conducted through the azimuth interval* $[-50°; 50°]$. *The plane cut is selected via the same rotation of the Tx and Rx. The new mount allows for precise separation between the waveguide transition and the lenslet while mounted on the frequency extender and ensure the MetaL sits flat in front of the probe.*

The test-bench is built up by adding the various constitutive parts in the order depicted in Fig.IV.3.7 onto the optics bench. This table weighs about 300 kg and set on passive vibration dampening legs. Its rigid surface is machined with a 100 µm tolerance to ensure minimal deflection from the horizontal plane when opticals elements are set up. The installation and measurement procedure consists of the following steps:

1 Levelling
2 OA materialisation
3 Rx assembly installation and alignment
4 Tx assembly installation and alignment
5 Elevation rotation preliminary centring
6 Tip and tilt mitigation
7 Waveguide transition final centring
8 Background measurements
9 MetaL integration & measurements

Notwithstanding, each of these component still needs to be levelled and aligned onto the optical axis both in the longitudinal and transversal directions. The setup is installed in an anechoic chamber, a large room isolated from any outside electromagnetic interferences. Its walls are indeed covered with Aluminium sheets, constituting an imperfect Faraday cage, and pyramidal RAM panels are fixed atop, filling the entire surface of the floor, walls and roof.

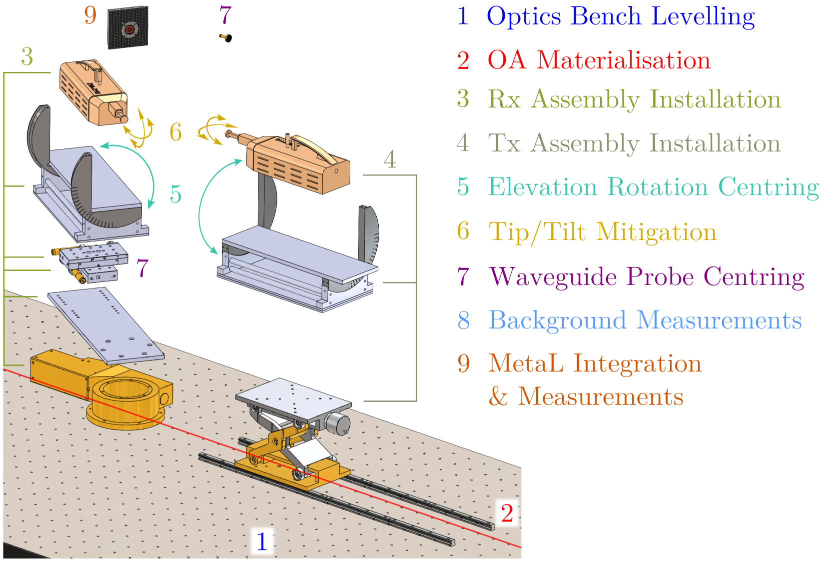

Figure IV.3.7: *Overview of the experimental setup procedure through an exploded view of the different parts constituting the Rx and Tx assemblies. Figure made with Solidworks and Inkscape by the author.*

IV.3.3.2 Notes on the hardware and software

The azimuthal range is covered by a motorised rotary stage actioned by a remote controller commended from the dedicated software developed by Dr Rashmikant Sudiwala in Cardiff. The frequency sweep and resulting measurement of the reflection and transmission parameters of this 2-port setup is conducted by a VNA. Essentially, this apparatus generates an Intermediate Frequency (IF) signal by means of Local Oscillator (LO) modulation and Digital-to-Analogue Conversion (DAC), swept in frequency by tuning the LO via a Phase-Locked Loop (PLL). The analogue tone is then up converted by the Tx frequency multiplier and sent to the Rx. The DUT affects the passing wave, which then reach the Rx. The received signal goes through the reversed chain until it passes a DAC. The VNA then finally operates a comparison between the sent and received signals, transcribed in terms of phase and S-parameters.

In the software, made in Cardiff by Dr Rashmikant Sudiwala in NI-Labview, used to establish the communication with the rotary stage controller and the VNA, the user could tune several parameters:

- Azimuthal range and step size: Operated scans were limited to $\theta_{max} = 50°$ by the cable tension and supporting posts, with 1° steps as to match the simulated data.
- Settling time: Accounts for mechanical vibrations which may need to be dissipated away before sweeping, thus preventing phase contamination [198]. The system was stable so 10ms proved to be sufficient.
- Averaging: First order electronic noise is smoothed out for an averaging set at 16 or higher.
- IF bandwidth: Defined the frequency span and the gain input of the VNA. Quick checks were done with 10kHz bandwidth, whereas final scans were conducted with 2kHz bandwidth.

Furthermore, this software is designed to run a forward and a backward scan, differences in the beams would demonstrate a backlash error affecting bi-directional repeatability of the rotary stage and one would then check for undesirably moving parts. Each averaged frequency point is taken twice, enabling the detection of standing waves for which the noise pattern would stay the same.

IV.3.3.3 Levelling

The horizontal plane set by the optics bench serves as a reference for the rest of the setup and must be set accurately. The horizontal levelling of the table is thus checked by using a 3-axis laser level. These devices offer an excellent accuracy with 1 mm vertical deviation at 30 m distance from the source, or 0.12 arcsec offset angle. The laser level is positioned off the bench whilst a reference, here a mounting cube is placed at one corner of the table. The latter is marked where the laser line crosses it, then moved onto the next corner and the underlying feet of the optics bench is raised so that the mark matches with the line again, as illustrated in Fig.IV.3.8.

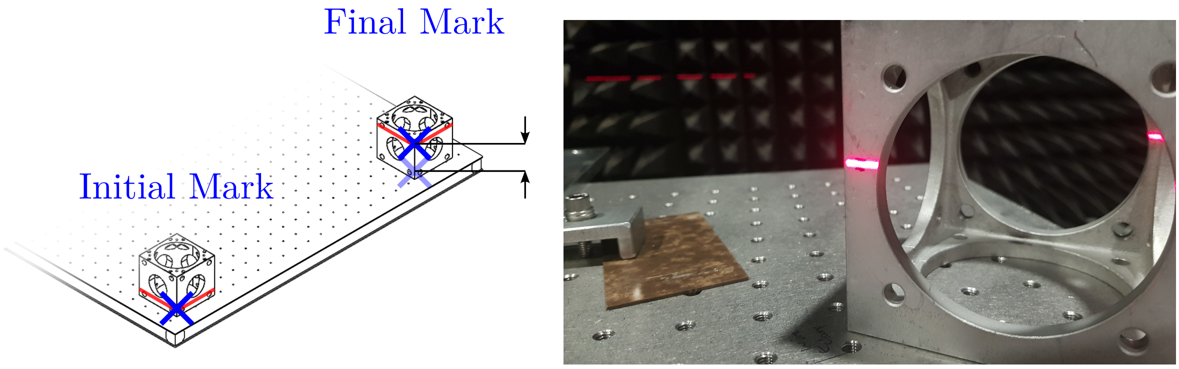

(a) **(b)**

Figure IV.3.8: *(a) A 3-axis laser level sets the horizontal plane. An initial mark is made on a reference screen. When displaced at the next corner, the vertical displacement from that mark gives the adjustment to make on the table height. The procedure is repeated until the line matches with the same mark on all four corners. (b) Photography, taken by the author, of the mounting cube used as the reference with pen marks made on each side of the laser line. Figure made with Solidworks and Inkscape by the author.*

IV.3.3.4 Optical axis materialisation

The OA must then be set as shown in Fig.IV.3.9. This is accomplished by first setting the laser away, roughly centred with respect to the desired axis, identifying the row of bolt holes on the table that are aligned with the OA and set the laser line along it iteratively, using a transversal linear stage and a rotary stage with fine pitch, plus a reference screen with a pen mark at each end of the table. Once the OA is set, the laser materialising the line will be kept in place for the rest of the assembling procedure.

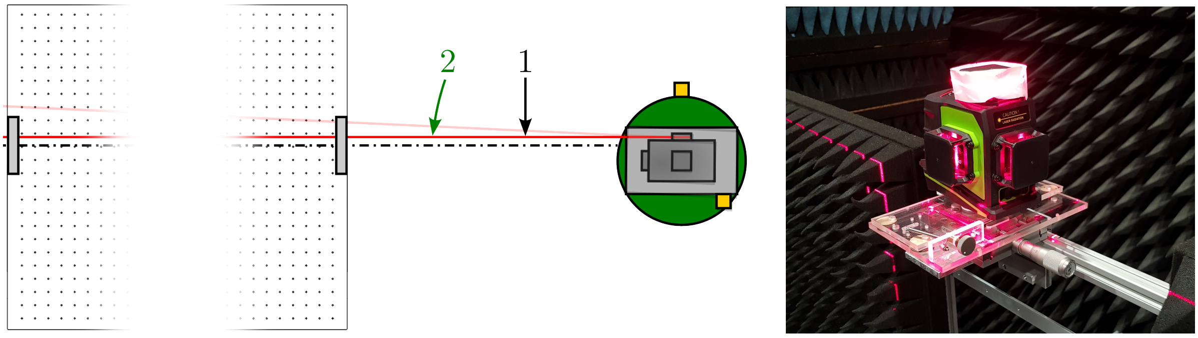

(a) **(b)**

Figure IV.3.9: *(a) First the laser line is translated so that it matches with the closest reference mark, then it is rotated so that it now matches the furthest mark. This process is repeated until the line matches both marks. (b) Photography, taken by the author, of the laser level, setup at a distance of the optics table on a set of stages. Figure made with Solidworks and Inkscape by the author.*

IV.3.3.5 Rx assembly installation and alignment

Once the OA materialised, The Rx side can be set up. The rotary stage support plate and other mounting plates are engraved or marked with centrelines to help with their alignment along the OA, as illustrated in the photograph in Fig.IV.3.10. Base plates are fixed using a set of clamps.

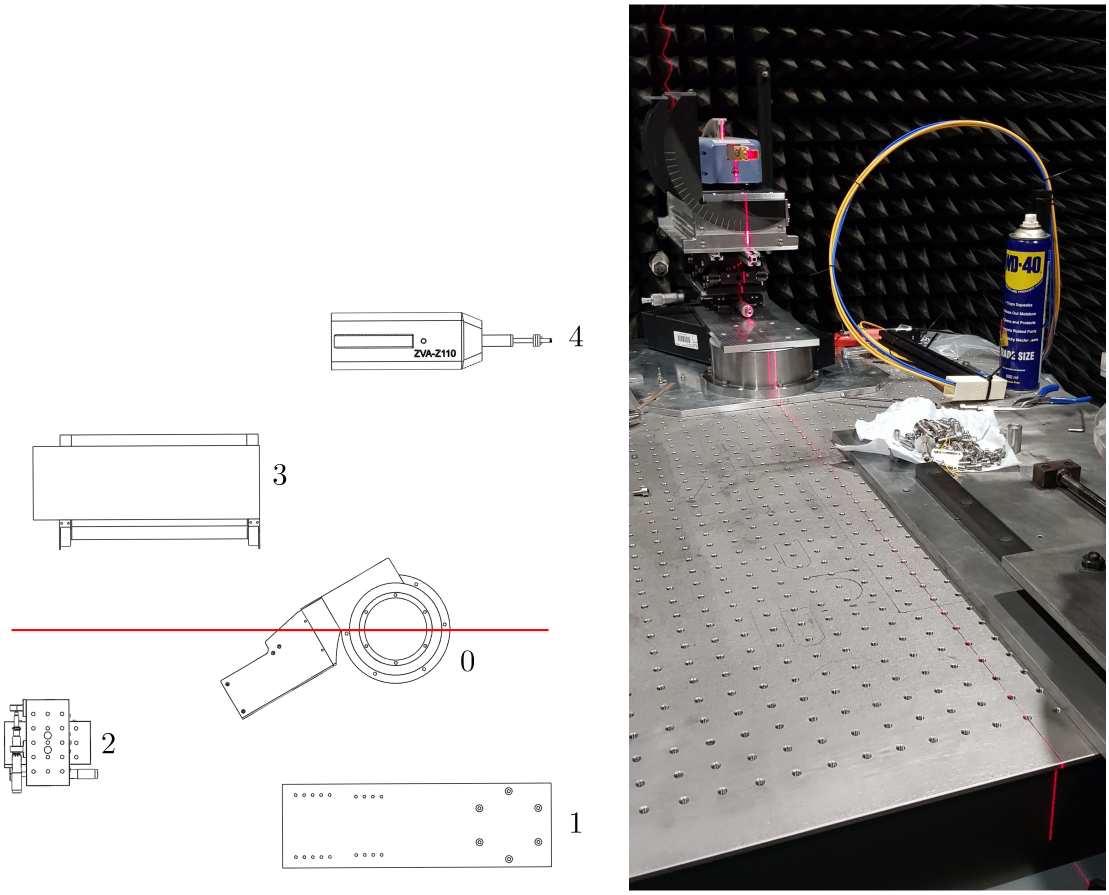

(a) **(b)**

Figure IV.3.10: *(a) Each constitutive elements of the Rx assembly is mounted onto the optics bench following the order depicted. Alignment marks are matched with the OA, materialised with the laser line preliminarily established. (b) The Rx assembly is shown fully assembled and aligned alongside the OA. Figure made with Solidworks and Inkscape, and photography taken by the author.*

IV.3.3.6 Tx assembly installation and alignment

The Tx side is subsequently assembled in the same manner. This side is set on rails to allow for a wide range of positions along the OA, should standing waves be of concern. The initial distance between the Tx and Rx at apertures is set at 500mm $\simeq 170\lambda$, far above the near field region and sufficiently away to allow potential reflected waves to dissipate in free-space. To check that the carrier travels alongside the OA, it is moved on each end of the path range. A first mark is made at one end and the deviation is checked at the other as per shown in Fig.IV.3.11, and corrected accordingly. Once the Tx assembly is completed, both sides are brought to the same height using the vertical stage.

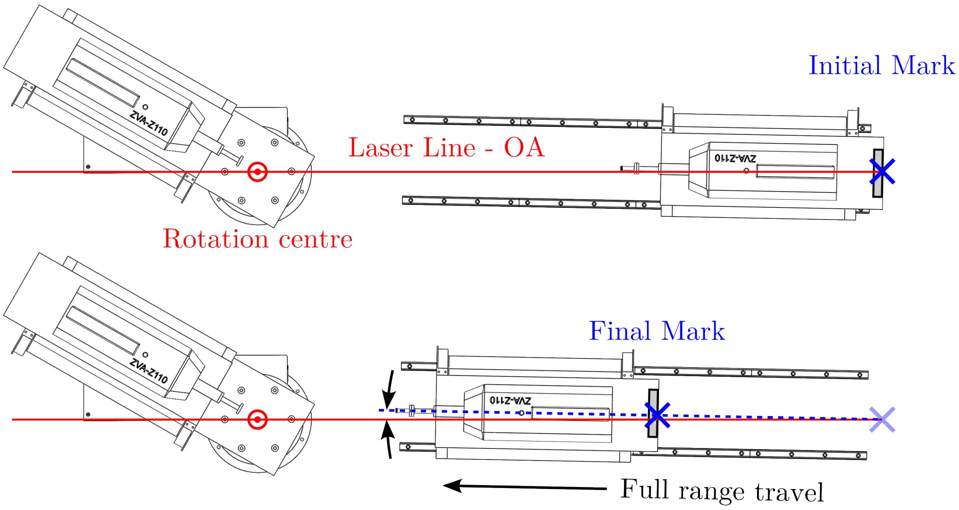

Figure IV.3.11: *Alignment procedure setting up the railing assembly on axis. A reference mark is made at one end of the rail course, the carrier is then moved to the other end where the displacement can be measured and corrected. Figure made with Solidworks and Inkscape by the author.*

IV.3.3.7 Elevation rotation preliminary centring

To verify that the rotary head mounts are centred in rotation around the optical axis, a USB HD-camera fixed into an aluminium profile rail bolted on a lab jack is placed in front of the probe apertures, live-feeding an image capture software where a cross-hair pattern is added. The camera is then moved along an the rail so that the cross-hair matches the centre of the aperture. The lab jack is previously aligned on the optical bench using a set of bolts along the transverse direction. It is then roughly centred and clamped on. The frequency converters are then be rotated and fixed in the E and H-planes whilst checking for a shift of the probe centre off the OA, as shown in Fig.IV.3.12. Such deviation is directly measured on the data acquisition software and the VNA heads are shimmed accordingly. The level is then readjusted if necessary.

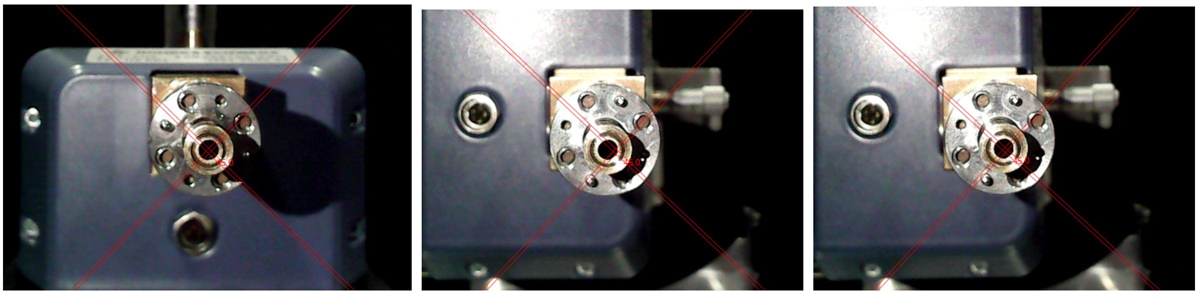
(a) (b) (c)

Figure IV.3.12: *Photographies, taken by the author, relating the procedure to centre the frequency extensions in rotation. (a) Initial position of Rx in the Tx H-plane. (b) The frequency extension is rotated to the Tx E-plane orientation and a shift appears on the horizontal axis, indicating that the centre of the aperture is not at the centre of rotation. (c) The resulting offset is compensated by adding shims raising up the frequency extender in the proper position. The process is repeated and it is checked that the aperture is now centred in rotation.*

IV.3.3.8 Tip and tilt mitigation

A tilt can be identified using a laser pointer and the combined refraction of the probe and waveguide apertures, and the reflected point coming off a flat mirror bolted onto the waveguide, as shown in Fig.IV.3.13. Any identified deviation is compensated by shimming the feet on the backside of the frequency head converters accordingly. Once set, accurate positioning of the probe at the centre of rotation is done using a set of micrometric linear stages.

(a) (b) (c)

Figure IV.3.13: *(a) & (b) A flat mirror is installed on the waveguide of the frequency extender and the angle at which the reflected ray hits back the laser source can be measured on a screen and corrected by adding shims under the front or back feet of the extender accordingly. (c) A final check is made by looking on a screen at the characteristic diffraction pattern of the open waveguide, necessarily symmetrical if centred and in a plane perpendicular to the OA. Figure made with Solidworks and Inkscape, and photographies taken by the author.*

IV.3.3.9 Waveguide transition final centring

At this stage, the motorised rotary stage controller, the frequency extenders and the VNA are connected. It was mentioned in Section IV.3.2 that a misalignment or a tip/tilt of Tx or Rx would cause a displacement along and transversally to the OA and result in a beam asymmetry. Such displacements are taken care of by repositioning the phase centre at the centre of rotation using the micrometric stage. The software provided a direct reading of the phase at Rx. If the latter is not flat, then the DUT is not at the centre of rotation and needs adjusting. An inward or outward bend of the phase would indicate that a forward or backward translation is necessary, whilst an asymmetry in the phase profile implies a left or right transversal shift from centre. A flat phase response is obtained by iterating on the position of Rx with the micrometric XY translation stage. Once suitably centred, the background measurements of the waveguide transition mounted without the MetaL can be conducted. The results were already presented in Chapter IV.2.

IV.3.3.10 MetaL integration & measurements

The mounted MetaL is then integrated to the Rx and centred using the 3-axis laser level. Its position is refined using the phase profile technique depicted above. These precautions will limit potential deviations, although the 300µm tolerance in transversal displacement will likely not be reached. The laser line may cause up to 0.5mm error at worst, which ensures an angular deviation from optical axis at phase centre of order 0.1°. The mounts for the frequency head converters are engraved with circular graduations of 5 degree steps. The tolerance in rotation is thus respected. Contributions from stray light were reduced using RAM extensively to cover reflective areas contributing to the device far field on one hand, and the beam transmitted and scattered by the lens on the other. Rx and Tx were positioned so that the optical height was 300λ, where most scattered waves were reflected off the bench. Analysing the probe far field response with an iterative RAM coverage shown that the regions immediately near the apertures were critical. The lens mount, the frequency converters and their rotating mounts caused scattering and added spurious patterns to the field. Contributions of the lenslet mount to the probe beam were successfully cancelled by the RAM tile installed. Comparing the measured beam pattern of the probe with and without this RAM protection shown the successful cancellation of the standing waves of concern. The precautions and careful analysis conducted throughout resulted in the assembly of the low systematics optical test bench shown in Fig.IV.3.14, which enabled accurate measurements of the lenslet beam patterns over the entire operating bandwidth.

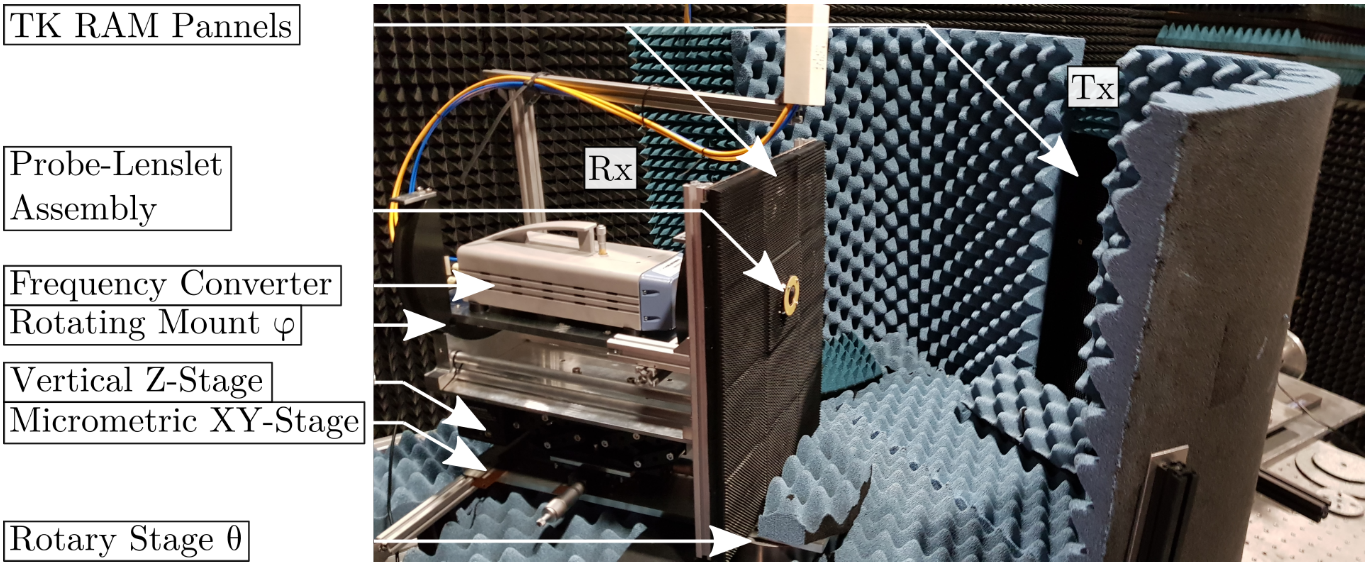

Figure IV.3.14: *Photography, taken by the author, of the fully assembled experimental setup allowing for the full characterisation of the lenslet beam patterns.*

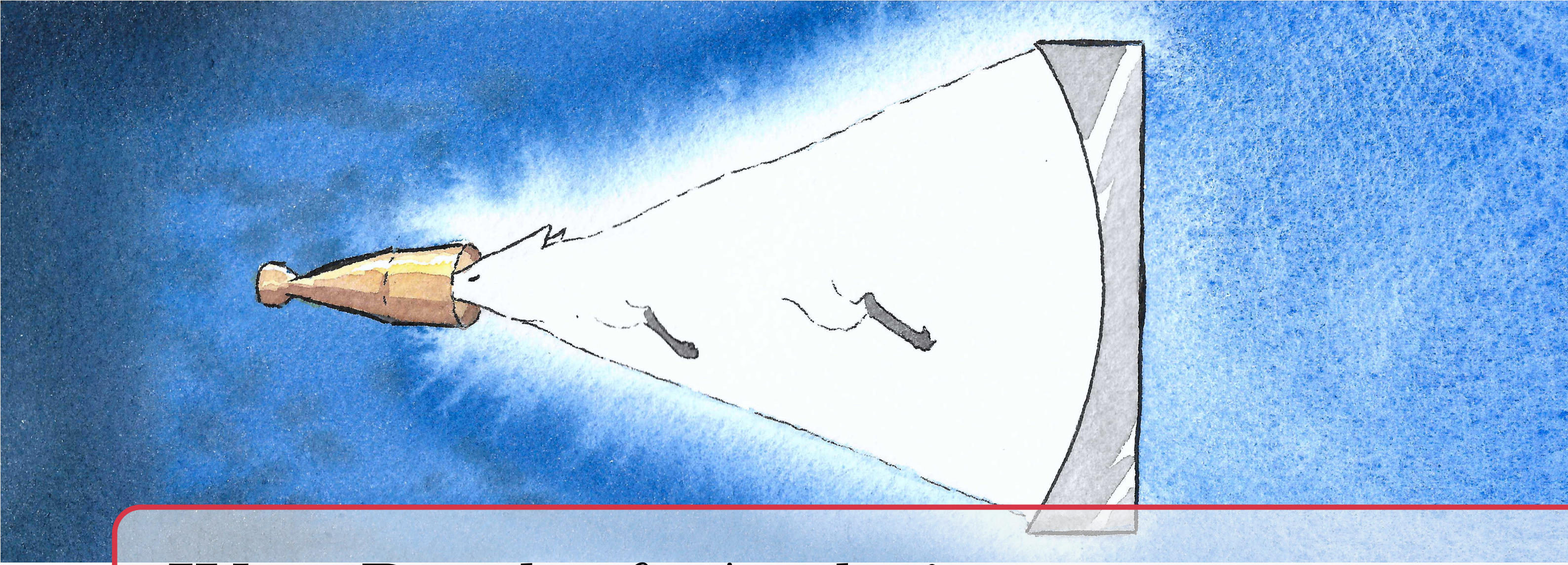

IV.4. Results & Analysis

IV.4.1 Beam profile of the MetaL

The normalised co-polarisation and cross-polarisation beam patterns for $F_0 = 3.15$mm in the E, H and D-planes are presented in Fig.IV.4.1, with their related phase response and LGB fits. Table IV.4.1 is summarising the extracted beam gaussicity η_0, ellipticity $\mathcal{E}$, waist w_0, width $w_{1/e}$ and the coupling efficiency η_C. The E and H leakages are the cross-polarisation cuts in E-plane and H-plane. The lenslet optical performances are consistent across the operating bandwidth.

Misalignments or tips/tilts of Tx or Rx were mitigated by repositioning the phase centre at the centre of rotation using the micrometric stage, leaving only the error on θ. Numerical corrections were applied to recentre the beam accordingly. Considering the level of precision obtained on the setup as per discussed in Chapter IV.3, such error has been estimated as $\delta\theta = 0.25°$ on a worst case scenario. This was propagated to derive the errors on w_0 and $w_{1/e}$, giving in turn errors on $\mathcal{E}$ and η_C using partial derivatives.

The LGB fit is conducted using w and R as parameters to match the fundamental mode to the beam whilst keeping $w_0 = \lambda\sqrt{2\ln 2}/2\pi\tan\theta_{HWHM}$, where $\tan\theta_{HWHM}$ is the angle at full-width half-maximum. The encoded method is shown in Appendix B. The resulting values are fixed and used to weight the fundamental mode $p = 0$ and higher order modes up to $p = 5$. The procedure is conducted for a given θ range, where the power of the beam E_f to be fitted is calculated as $\eta_f = \int_r |E(r,z)|^2 r dr$ with $r = R\sin\theta$. The resulting error on the gaussicity was estimated as the standard deviation of a set of η_0 calculated using the best LGB fit for various maximal azimuth values in the range $[40°; 50°]$ with steps of $1°$.

The simulated beam patterns of the hyper-hemispherical lenslet fed by a Silicon embedded version of the waveguide transition are commensurable to the prototyped planar lenslet response, as their characteristics emphasise further in Table IV.4.1, where the definitions given in Part II were used. The MetaL measured data were used for the computation of the results presented in this table.

Table IV.4.1: *Summary of the measured optical performance of the MetaL compared with its hyper-hemispherical simulated equivalent.*

Device	f [GHz]	$\overline{\eta_0}$[%]	$\mathcal{E}$[%]	w_0[mm]	η_C[%]	η_α[%]
MetaL	75	98±0.5	1.0±1.1	2.4±0.05	99±0.8	81±1.5
MetaL	90	98±0.5	8.8±1.4	2.5±0.07	99±1.0	79±1.5
MetaL	110	97±0.9	4.0±1.6	2.5±0.08	95±1.1	69±1.5
Hyper-hemispherical Lenslet	75	98±0.5	11.5	2.6	99	68±1.0
Hyper-hemispherical Lenslet	90	93±0.5	4.5	2.6	97	77±1.0
Hyper-hemispherical Lenslet	110	93±0.8	0.0	2.4	95	82±1.0

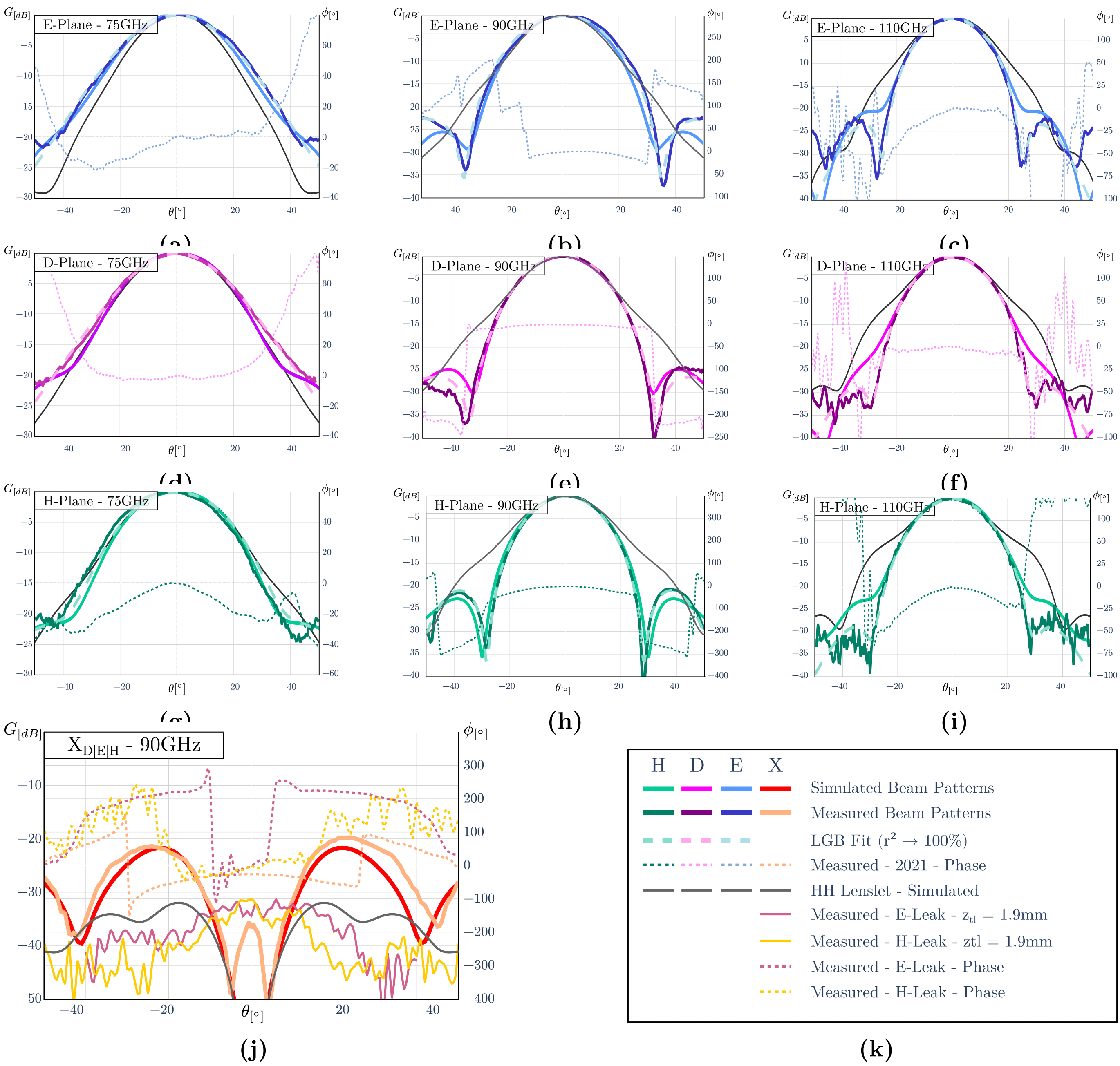

(a) (b) (c)

(d) (e) (f)

(g) (h) (i)

(j) (k)

Figure IV.4.1: *Phase-engineered lenslet (a) - (i) co and (j) cross-polarisation beam patterns measured and simulated at (a), (d), (g) 75GHz, (b), (e), (h), (j) 90GHz and (c), (f), (i) 110GHz in the (blue) E, (co-pol = purple, cross-pol = red) D and (green) H-planes. The beam response of the hyper-hemispherical lens (dark grey) is included to establish the desired comparison. Figures made with ANSYS-HFSS and Python by the author.*

IV.4.2 Discussion

Two identical metamaterial-based lenslets were measured, showing indistinguishable beam patterns in all three planes, indicating excellent repeatability in the fabrication. The measured beam shows a minor and occasional discrepancy in the beam width when compared with the simulated one, as is the case in the E-plane at 90GHz for example. At 110GHz, merging sidelobes were expected but the measured beam shows a clear separation from the main lobe, likely due to an inaccurate meshing in the model described in Section IV.2.1. Overall, there is a reasonable match of the sidelobes and a near perfect correspondence of the main lobe with the simulations throughout the operating bandwidth. The measured cross-polarisation pattern presents a central lobe shape at 90GHz, characteristic of tilt and misalignment between Rx and Tx, which the phase profile underlines further. As discussed in Section IV.3, such measurement is extremely sensitive to these variations [199], for instance a transversal deviation from the optical axis needs to be under a fraction of the operating wavelengths. Despite the efforts taken to limit such systematics, the cross-polarisation patterns could not be obtained at 75GHz and 110GHz. However, the level measured was consistently below the -21dB threshold. The prototype device further demonstrates a beam response comparable to that of the hyper-hemispherical lenslet down to -10dB.

The MetaL radiates a Gaussian beam of low ellipticity, presenting no merging sidelobes whilst maintaining a cross-polarisation level below -21dB and a differential gain of $\Delta g = 0.2\%$. The optical characteristics of this lenslet, tantamount to its hyper-hemispherical counterpart, demonstrates its potential suitability as a focal optics for future CMB experiments.

IV.4.3 Map Making Benchmark Comparative Analysis

To investigate further the quality of the MetaL, the map making analysis presented in Chapter II.4 is used to establish and compare the reconstructed B-mode power spectra obtained by scanning the sky with the simulated beam profiles of both lenslets. A requirement for low ℓ scanning is that the beam width should be 25arcmin, as devised in Section I.2. The simulated fields are rescaled accordingly, as shown in Fig.IV.4.2.

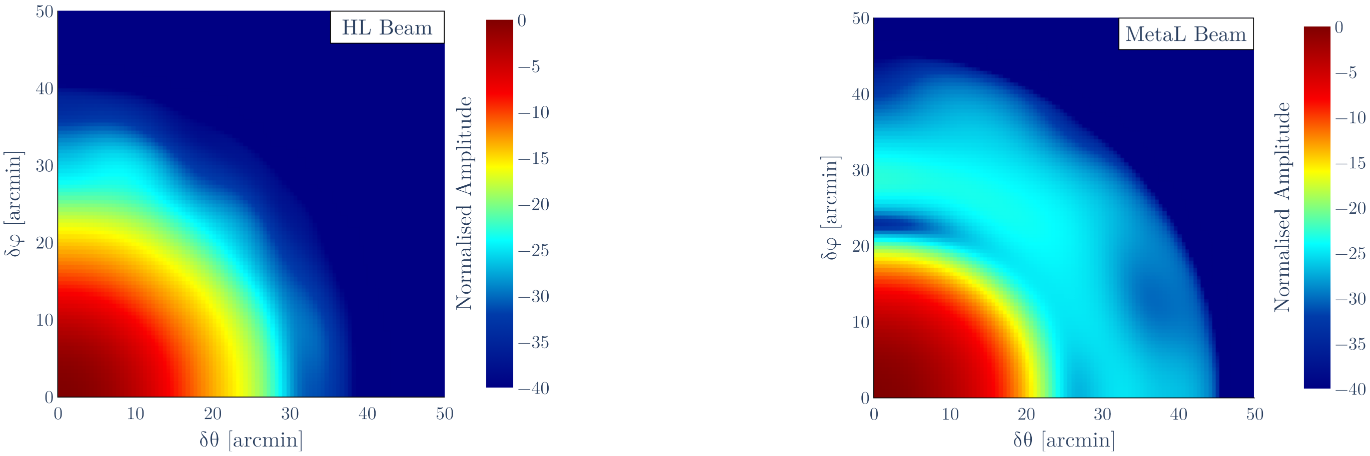

(a) (b)

Figure IV.4.2: *Simulated beam patterns of (a) the hyper-hemispherical lenslet and (b) the MetaL. Figures made with ANSYS-HFSS, Python and Inkscape by the author.*

As per depicted in Chapter II.3, in an ideal situation, the beam of an instrument is perfectly Gaussian, thus, the correction applied to the $\hat{C}_\ell^{BB}$ associated with each beam is that of the Gaussian beam. The resulting power spectra are shown in Fig.IV.4.3 alongside the C_ℓ^{BB} for $r = 10^{-3}$ and $r = 10^{-4}$. The case $r = 10^{-2}$ is not included for clarity as its amplitude is order of magnitudes above. Within the benchmark approach used, both lenses offer similar sensitivity on the tensor-to-scalar ratio. Besides the limitations related to the simplifications taken for this map-making analysis, the biases in the reconstructed spectrum cannot be directly related to a given systematics. In this benchmark context, the hyper-hemispherical lenslet and the MetaL beams of have a noticeably similar effect on the power spectrum reconstruction, further underlining that the MetaL offers comparable optical performances. A further analysis of interest could be to conduct a similar procedure in an instrument pipeline [73, 70].

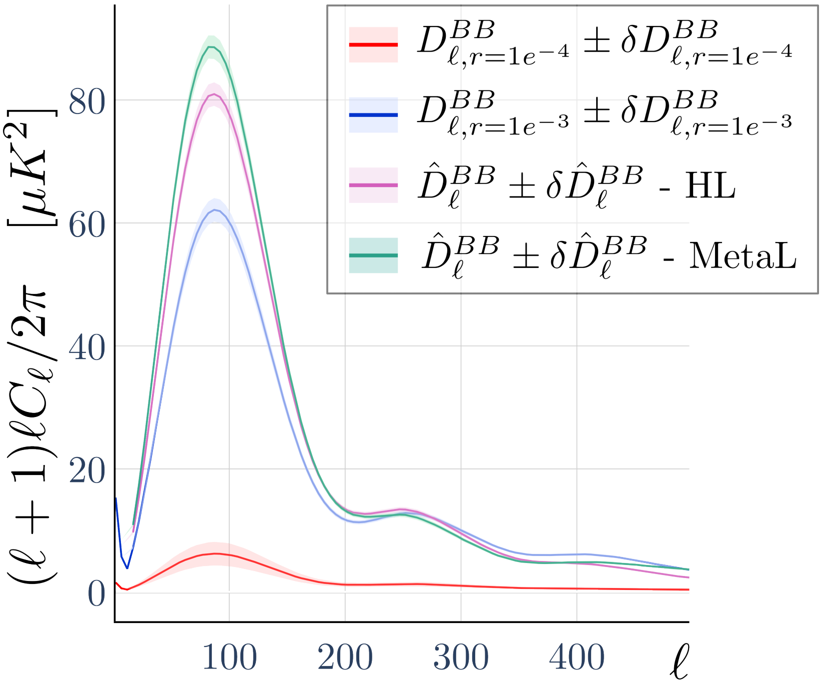

Figure IV.4.3: *Reconstructed B-mode power spectra obtained from scanning the sky with the hyper-hemispherical lenslet (HL) and the MetaL and corrected with the transfer function of their ideal Gaussian beam counterpart. Figures made with Python and Inkscape by the author.*

A comprehensive analytical and experimental characterisation of the air-gapped prototype MetaL was demonstrated in this part. The measured beam was analysed side-by-side with that of a simulated hyper-hemispherical lenslet counterpart, demonstrating comparable optical performances, confirmed further through a coded benchmark method projecting both beams on sky. With the beam characteristics of an isolated lenslet characterised, the next validating step is to couple the device with a detector in a pixel design relevant for CMB experiments, a task that we investigate further in the next part. The present MetaL radiates a near symmetrical Gaussian beam with cross-polarisation levels below -21dB and a differential gain of $\Delta g = 0.2\%$, demonstrating the potential suitability of the MetaL concept as a focal optics for future CMB experiments, should the design be successfully ported to a fully embedded alternative. As mentioned in previous parts, this would allow for a simplified ARC compared to the hyper-hemispherical lenslet, and bring compatibility with the detector plane whilst permitting a large number of pixels on the FPU.

V Detector Coupling

Part V Outline

Experimental validation of the MetaL has been established with an accurate measurement of its beam profile. Its optical quality and the related systematics were underlined and a benchmark analysis allowed to compare the prototype device with its hyper-hemispherical lenslet counterpart. As depicted in Section I.2.4, a pixel constituted of a lenslet-coupled broadband planar antenna, transferring the optical power to a set of detectors, offers attractive characteristics for CMB experiments.

The LiteBIRD LFT focal plane design is indeed based on such configuration, where a single pixel contains 6 sinuous antenna coupled, hyper-hemispherical Silicon lenslet fed, TESs that measure 3 bands with 2 orthogonal linear polarization states simultaneously, resulting in [40 GHz; 235 GHz] of instrument bandwidth [87]. Similarly, SO will populate some of their universal focal plane modules with lenslet coupled sinuous antennas feeding TESs for both the LAT and the SAT [84].

In this context, proposing a similar coupling constitutes the next step devised to prove the concept of the MetaL. A relevant sensor for the coming instruments is the KID, an ultra-sensitive superconducting technology with a high multiplexing ratio. Relying on lithography techniques, they can be easily manufactured in a cost effective manner. An end-to-end analysis of a full pixel is conducted in this part via a set of simulations of its constituents, namely, the detectors, the microstrip architecture and the antenna coupled lenslet. The pixel is constituted of the prototyped MetaL, coupled to a 4-branch planar sinuous antenna transferring the incoming power to a KID via a microstrip line through a combination of matching filters with a phase coupler. This design is inherently broadband, impedance matched and dual-polarised. It further offers excellent optical performances throughout the operating bandwidth.

The overall pixel design is depicted in Chapter V.1. First, elements of the operating principle and the design of a set of KIDs will be conducted. Secondly, the antenna selection is discussed, established by dressing a comparative analysis on various options. The microstrip architecture ensuring the end-to-end transmission of the optical signal is further depicted. Lastly, the current status on the fabrication of the detector chip, warm measurements of the beam of a copy of the prototype MetaL, readapted for cryo-compatibility and a plan forward to replicate those measurements cold are presented in Chapter V.2. With such pixel design and a characterised lenslet at the ready, the stage is set for further demonstration of the concept of MetaLs as a relevant technology for CMB applications which could possibly be extended to millimetre, sub-millimetre and FIR astronomy.

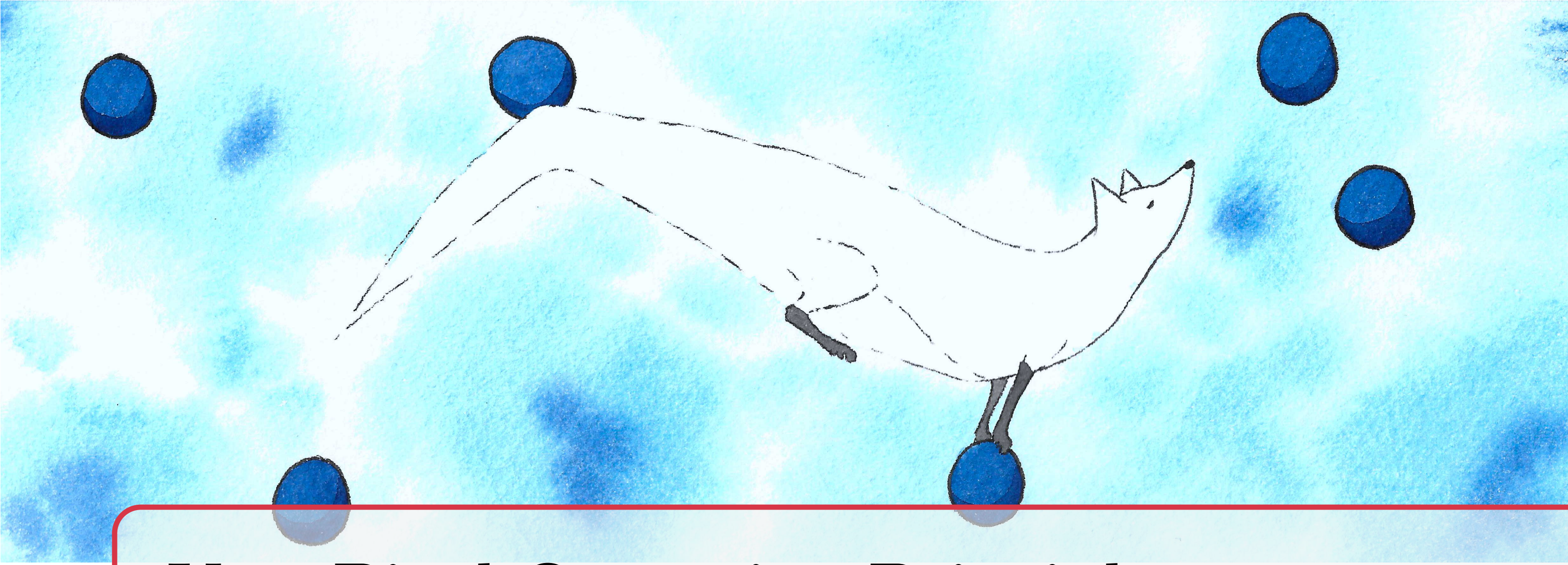

V.1. Pixel Operating Principle

V.1.1 Overview

The microstrip architecture of the detector plane for this prototyped dual-polarised pixel design is detailed in Fig.V.1.1. The polarisation separation is realised by coupling a 4-branch self-complementary log-periodic broadband sinuous antenna to two pairs of microstrip lines, one per polarisation. A filter operates the adequate impedance matching necessary for the lines joining at the centre of the antenna to couple to the branches. The microstrips are further combined out of phase with a rat-race coupler and the merged output transfers the received polarisation to a single KID in the same manner as for a CMB imager pixel [200]. A blind detectors are placed around the chip to pick up and monitor any stray light in a future experimental characterisation. It is worth noting that an on-chip spectrometer can be realised instead by feeding each detector with the optical line, adequately filtered at the desired frequency [201].

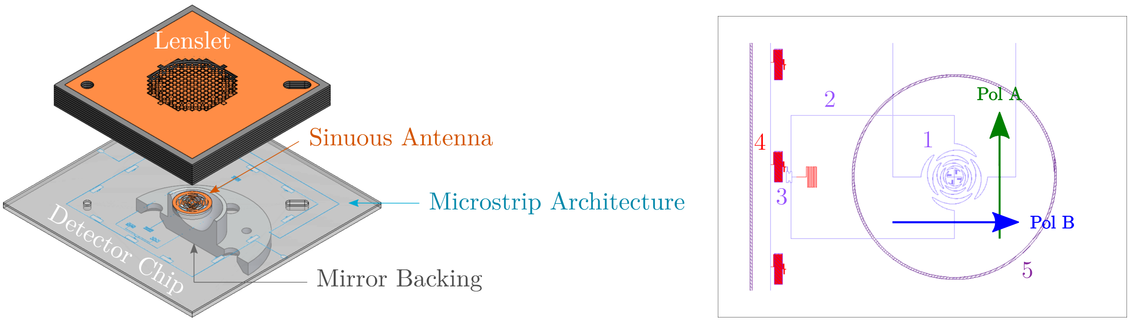

(a) **(b)**

Figure V.1.1: *(a) Full pixel layout constituted of the MetaL prototype focusing the incoming light onto a broadband dual-polarised sinuous antenna backed with a spherical mirror and coupled to a microstrip architecture tuned to match two KIDs. For clarity, the ground plane surrounding the antenna has been removed and a cross-section of the mirror is shown. (b) Detector plane layout depicting the transmission of the polarisation A received by the sinuous antenna (1) from the lenslet (5) to a KID (4) down the microstrip architecture. The latter is constituted of 2 branches (2) running under the sinuous antenna and combined via a rat race hybrid coupler (3). Figure made with Solidworks, KLayout and Inkscape by the author.*

V.1.2 Kinetic Inductance Detectors

V.1.2.1 Superconducting detector

Consider a photon with energy $h\nu => 2\Delta$, where Δ is the binding energy of the Cooper pairs (V.1.1), an electron coupling mechanism inherent to superconductors operating below their critical temperature T_c. Upon absorption of this photon in a superconducting film, pairs break, resulting in a modification of the kinetic inductance of the film. Should it be patterned in a set of resonators, each with a resonant frequency f_r and intrinsic quality factor Q_r, the change in inductance will also shift their resonances [92, 93, 95].

$$2\Delta = 3.5 k_B T_c \tag{V.1.1}$$

Sensing an optical input is then done by probing the detectors with a comb of microwave signals set to the resonant frequencies and by further monitoring the difference in the transmission response with the shifted signals. A view of two combs at position n and $n+1$ of the detector set, and their counterparts, shifted under optical load is presented in Fig. V.1.2. The frequency domain thus accessed enables large multiplexing ratios, elegantly read out on a single set of coaxial cables, a simple and cost effective solution to large format arrays desired for CMB experiments. This kind of detectors are sensitive to any incoming input, including stray light leaking into the FPU, which have a significant effect on the detector responses. A coupled focal optics impermeable to stray light is therefore necessary for the proper operation of the detector plane, a concern of importance for the MetaL technology proposed.

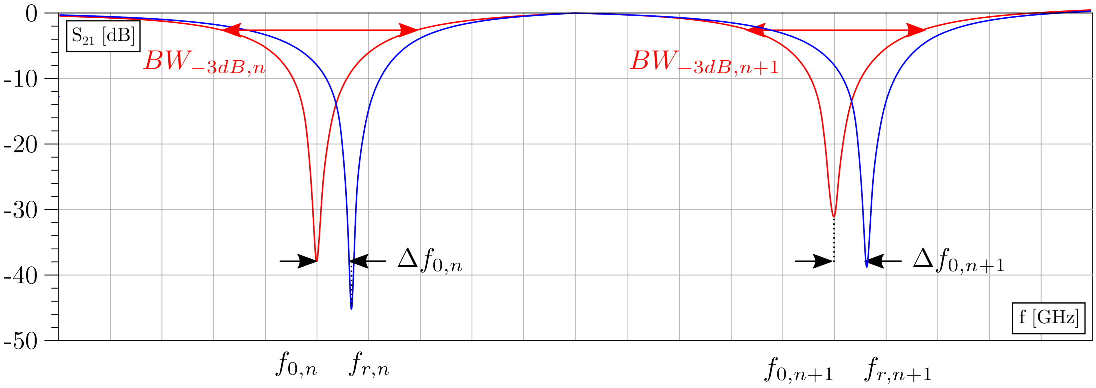

Figure V.1.2: *Example of two Lumped-element Kinetic Inductance Detectors (LeKIDs) transmission response S_{21} swept in readout frequencies, with $BW_{3\,\mathrm{dB}}$ the $-3\,\mathrm{dB}$ bandwidth. The blue curve is obtained for a low optical load and is called the "dark" response, whereas the red curve is the loaded one. Figure made with Python and Inkscape by the author.*

A LeKID, resonator for which light is coupled by energy dissipation through an inductive meander, can be described as an LC circuit, as shown in Fig. V.1.3. A modification of the kinetic inductance, encompassed by L_k, shifts down the resonant frequency of the detector (V.1.2). An added capacitor inserted in series provides coupling to the Radio Frequency (RF) readout line. Optimal coupling with the readout signal is obtained for $Q_i = Q_c$ [202], while optical coupling occurs at the junction between the Niobium feedline and the Aluminium inductor, impedance matched together. Given that Niobium has a critical temperature, below which superconductivity occurs, of $T_c = 9.3\text{K}$, the related binding energy gap is $\Delta \simeq 4.49 \times 10^{-22}\text{J}$. Similarly, Aluminium has $T_c = 1.2\text{K}$, giving $\Delta \simeq 5.80 \times 10^{-23}\text{J}$. To break pairs off the latter, a photon would need to be at a frequency above $f \simeq 87.5\text{GHz}$, against $f = \simeq 680\text{GHz}$ for the latter, far above the optical bandwidth of concern.

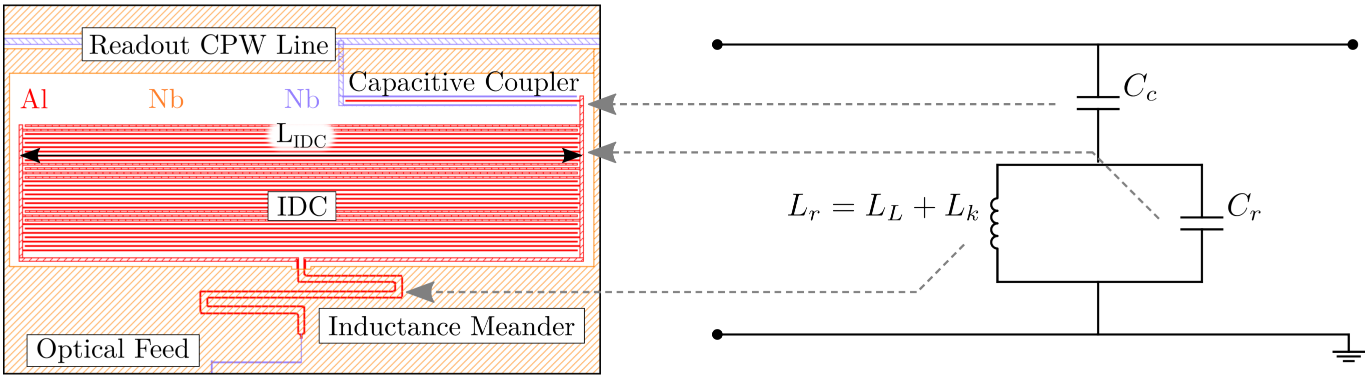

Figure V.1.3: *KID fed by a Niobium line transitioning to the Aluminium inductive meander where Cooper pairs are broken and power is subsequently sensed. The Inter-Digital Capacitor (IDC) and capacitive coupler lay within the etched area of the surrounding Niobium ground plane. Tuning their geometry allows for control of the detector* f_r *and* Q_r *respectively. The shift in resonance resulting from the breaking of the paired electrons is read out via a Co-Planar Waveguide (CPW) line. The RL equivalent circuit representation of a KID is shown on the right, coupled capacitively to the RF readout line via the capacitor* C_c*. Figure made with KLayout and Inkscape by the author.*

Under optical load, the detector Q_r (V.1.3) [202] reduces along with the shift in frequency from f_r to f_0. To properly readout the devices when implemented in the prototype pixel, determination of their f_r and Q_r measured dark, and assessment of their sensitivity, namely the Δf_0 per detector as a function of optical power input, is desirable. Such characterisation requires a careful analysis of their transmission response, where the combs with the native f_r are identified through a fitting procedure using a Lorentzian (V.1.4) centred around f_r with half-width bandwidth $f_r/2Q_r$ [202]. Verification of the behaviour of each detector under optical load would further be carried to check that the expected shift is reached, replacing f_r by f_0 in the Lorentzian parametrisation.

$$\omega_r = \sqrt{\frac{1}{L_r C_t}} \text{ , where } L_r = L_g + L_k \text{ and } C_t = C_r + C_c \tag{V.1.2}$$

$$Q_r = \left(\frac{1}{Q_i} + \frac{1}{Q_c}\right)^{-1} \text{, where } Q_i = \frac{2\pi f_0^2 L_r C_r}{\tan\delta} \simeq f_0/BW_{3_{dB}} \tag{V.1.3}$$

$$S_{21} = \left(1 - \frac{Q_r}{Q_c}\right) \frac{1}{1 + 2jQ_r \Delta f_r} \tag{V.1.4}$$

Q_i is expressed in (V.1.3) for the limiting case of IDCs patterned on a lossy dielectric, of loss tangent $\tan\delta$, which is the case for the designed detector sets, as is depicted further in Section V.1.2.3.

V.1.2.2 LeKID sensitivity

The sensitivity of a KID is limited by its Generation-Recombination (GR) noise. This superconducting device has inherent quasi-particle fluctuations as, in a continuous manner, the breaking of Cooper pairs resulting from thermal contributions generates electrons, which then recombines. These quasi-particles have an average lifetime τ_{qp}. The overall number of quasi particle n_{qp} thus sees a fluctuation δn_{qp} associated with a power P_{qp}. The temporal evolution of n_{qp} is depicted as a power spectrum $\mathcal{S}_{gr}$ (V.1.6). To express the detector sensitivity, the latter is transcribed into a NEP, defined as the signal power required to achieve a unity signal-to-noise ratio measured in a 1Hz post-detection bandwidth (V.1.7). N_{qp} is the number of quasi-particles generated by a GR equivalent optical load (V.1.5) [203], dependant of N_0, the single spin density of states at the Fermi level, a material dependant value of $1.7 \times 10^{-10}\mu\text{m}^{-3}$ for Aluminium; and of V_L, the inductor volume [95].

$$N_{qp} = n_{qp}V_L = 2N_0\sqrt{2\pi k_B T\Delta}\exp\left(-\frac{\Delta}{k_B T}\right)V_L \tag{V.1.5}$$

$$\mathcal{S}_{gr} = \frac{4n_{qp}\tau_{qp}}{1+(2\pi f\tau_{qp})^2} \tag{V.1.6}$$

$$NEP_{gr} = \sqrt{S_{gr}}\left(\frac{dP_{qp}}{dN_{qp}}\right) = 2\Delta\sqrt{\frac{N_{qp}}{\tau_{qp}}} \tag{V.1.7}$$

An incident photon stream of power P_{ph}, with an optical bandwidth $\Delta\nu$, result in a photon noise contribution which translates into a NEP_{ph} (V.1.9). It decomposes into a shot noise associated with the Poisson statistics of photon arrival, and a Bose noise ancillary to the wave nature of light, transcribed as NEP_{shot} and NEP_{bose} respectively [204, 203].

$$P_{ph} = 2k_B T\Delta\nu \tag{V.1.8}$$

$$NEP_{ph} = \sqrt{NEP_{shot}^2 + NEP_{bose}^2} = \sqrt{2P_{ph}h\nu + P_{ph}^2/\Delta\nu} \tag{V.1.9}$$

V.1.2.3 Design of the Detector Set

The KID design used in the optical coupling with the MetaL prototype is presented in Fig.V.1.3 and was built upon previous developments [205, 95]. An underlying Silicon Nitride membrane is present, required as a dielectric for the coupling microstrip architecture and as to support the antenna structure. Ideally this layer should be removed from underneath the IDC but this would require a step down of the Aluminium line in the fabrication, a difficult process. KIDs on amorphous dielectrics see their Q_i factor dominated by losses in the media, namely, $Q_i \simeq 1/\tan\delta$. The dielectric gives rise to an additional noise contribution know as Two Level System (TLS), typically present at low frequencies [206]. This would be problematic for a realistic detector plane but may be sufficient in the present prototype. The intent is to measure this noise source and modulate the optical signal at a higher frequency, where TLS does not dominate the power spectrum.

In order to design a set of KID with given f_r and suitable Q_r, a linear parametrisation of the IDC length is conducted first for a fixed inductance geometry (V.1.3) in SONNET. The variation in f_r

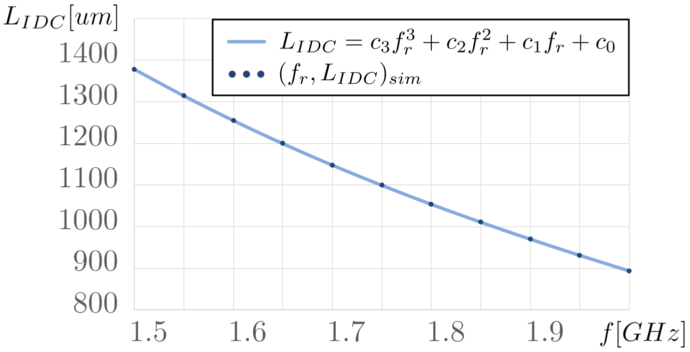

Figure V.1.4: *L_{IDC} vs. f_0 fitted from a set of equally spaced IDC lengths and corresponding resonances. Figure made with SONNET, Python and Inkscape by the author.*

is plotted against L_{IDC} and fitted with a polynomial, as shown in Fig.V.1.4, whilst maintaining Q_r above $\sim$ 6000.

The coupling capacitor geometry is fixed, with finger lengths of 500µm and the inductive meander is designed so that minimal reflection occurs at the junction with the Niobium feedline, with a volume $V_L \simeq 130\mu m^3$. A set of 10 KIDs operating in the readout bandwidth [1.8 GHz; 2.6 GHz], spaced by steps of $\sim$ 100 MHz and showing Q_i between 5k and 10k have been designed to be fabricated on Silicon wafers. A separate model of the inductor coupled to a microstrip line allowed the determination of the Niobium to Aluminium transition input impedance $Z_{kid} = 29.5\Omega$. The design parameters and simulated response properties, obtained from SONNET, are summarised in Table V.1.1.

Table V.1.1: *Summary of the designed KIDs. The characteristics of the optically coupled detector are written in bold. The superscript m indicates measured results, following the experimental method described in Section V.2.2.*

KID #	1	2	3	4	5	**0**	6	7	8	9	10
f_r[GHz]	1.85	1.92	1.99	2.05	2.12	**2.19**	2.26	2.33	2.40	2.47	2.55
f_r^m[GHz]	1.95	2.04	2.09	2.18	2.21	**2.24**	2.25	2.30	2.40	2.44	2.59
L_{IDC}[µm]	1377	1314	1254	1199	1147	**1099**	1053	1010	970	931	893
Q_i	6500	6400	6600	6400	5900	**7800**	8000	7800	7500	7500	7300

The KIDs are a highly sensitive technology, inherently broadband, relying on readily scalable thin film fabrication methods and allowing for high multiplexing ratio. They are fully suited to match the constraints established for future CMB experiments and as such, came as a natural choice for the pixel design of concern to further prove the concept of the MetaL. The present set of detectors, sitting on amorphous Silicon Nitride, is not optimised for sensitivity but allowed for simplicity in fabrication.

V.1.3 Antenna Coupling

The lenslet prototype is not limited to 110GHz and may be coupled to any feed with a phase pattern matching that of the probe it was initially designed for. It was discussed in Section I.2.4 that due to their broadband and frequency independent field pattern [207], planar antenna coupled lenslets were an attractive pixel design for CMB [104, 105, 87, 208]. A dual twin-slot [209], 4-branch bow-tie[210], sinuous [211] and log-periodic toothed antennas [212] are shown in Fig.V.1.5. Each option is modelled in ANSYS-HFSS and the resulting phase profiles and beam patterns are compared in order to select an optimal solution. Table V.1.2 summarises their optical performances, as defined in Chapter II.3.

V.1.3.1 Antennas Comparative Analysis

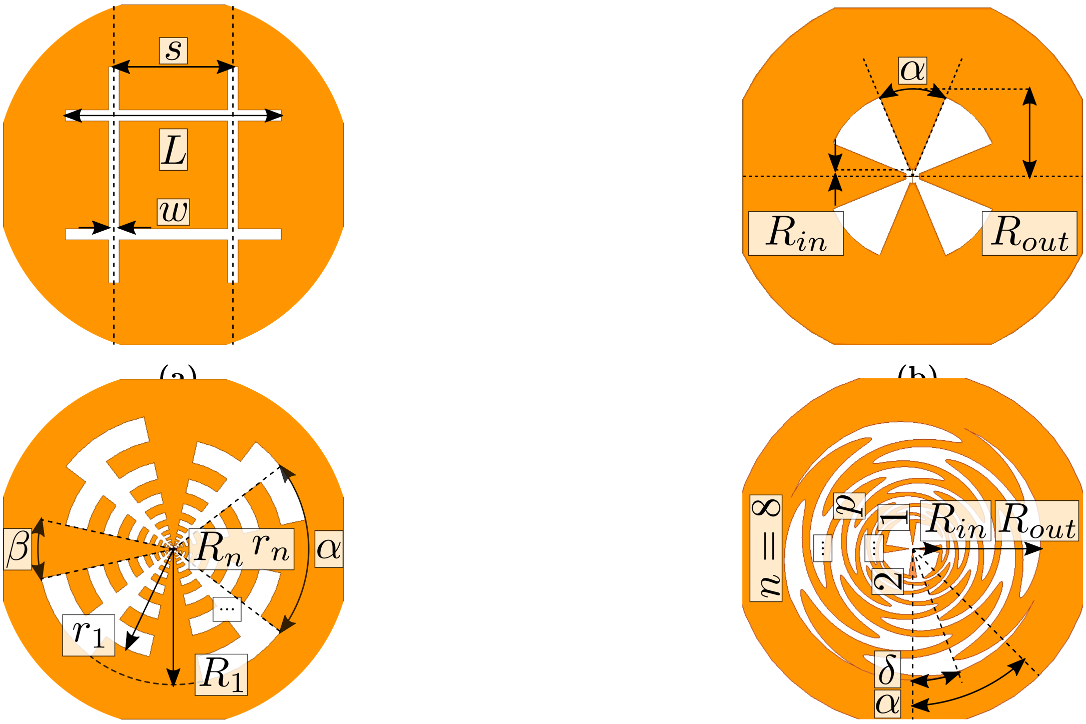

(c) **(d)**

Figure V.1.5: *Geometry parameters of (a) the dual-twin slot, (b) the bow-tie, (c) the log-periodic toothed and (d) the sinuous antennas. A parametric analysis was conducted on the geometry to identify the critical dimensions and their impact on the antenna beam response, cross-polarisation peak level, central frequency and bandwidth. The selected antenna was further optimised in ANSYS-HFSS using a Quasi-Newton method. Figures made with ANSYS-HFSS and Inkscape by the author.*

Each antenna is modelled as a perfect electric conductor, contained in a vacuum box surrounded with radiation boundaries, as per Fig.V.1.6. The input signal is implemented via a pair of lumped ports per polarisation, driven out-of-phase, connected on one end to a cross shaped microstrip at the centre of the antenna, acting as the common ground, and to the arm at the other end. Each port impedance was parametrised with a common variable and the effective value was obtained using an iterative process until minimal reflection was reached. To validate the use of lumped ports as a suitable replacement for the microstrip lines, the latter have been modelled but its dimensions, small compared to the rest of the model, prevented proper convergence of the FEM analysis. The far-field radiation was extracted from the boundaries of the air box situated above the antenna S_{FF}, and the phase profile was calculated along lines contained in the E, D and H plane cuts and situated at a vertical distance d_ϕ from the antenna centre. The acceptable mismatch is determined via the parametrised port impedance, decreased towards the detectors optical line impedance Z_{kid}

while the reflection response is checked. The largest mismatch is then defined as $\Delta Z_0 = Z_0 - Z_0''$, where Z_0'' is the port impedance at which $S11 < -10\,\mathrm{dB}$ for a 20 GHz bandwidth, sufficient to showcase the lenslet coupling to KID.

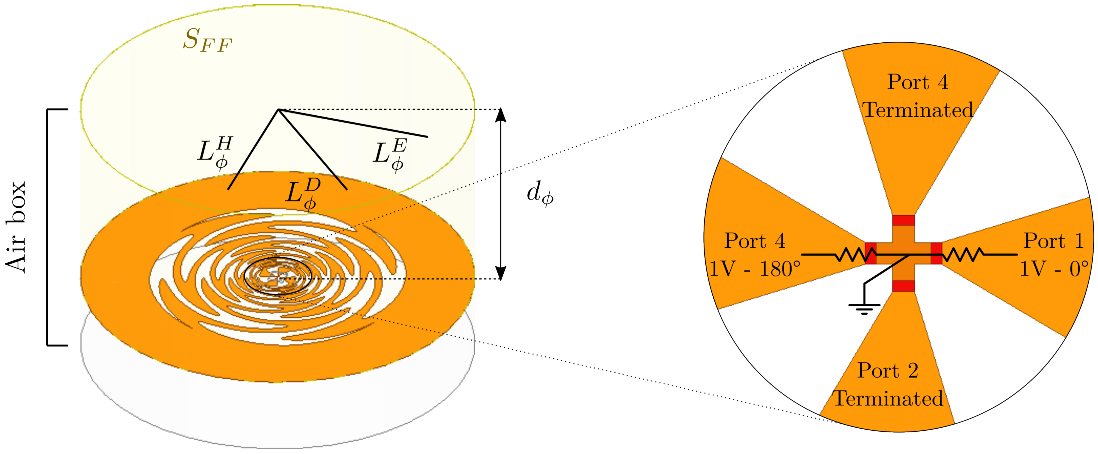

Figure V.1.6: *ANSYS-HFSS model of the sinuous antenna showing the far-field integration surfaces* S_{FF}*, the linear phase cuts* $L_\phi^{E,D,H}$ *at a variable distance* d_ϕ *and zooming on the lumped port feeding. The sinuous is driven in a single polarisation state, with a couple of lumped ports driven* 180° *and the other, terminated. Figures made with ANSYS-HFSS and Inkscape by the author.*

All antennas were designed to radiate a beam of $\theta_{HWHM} \simeq 30°$ half-width at half-maximum angle, matching that of the waveguide probe originally feeding the MetaL prototype. Each are showing excellent gaussicity, low ellipticity and similar directivity. The sinuous antenna stands out as a suitable option [125], already in use at the SPT [200], and selected for SO and LiteBIRD FPUs, as it is offering a large operational bandwidth with continuous low cross-polarisation peak level. The impedance difference with the detectors optical line is high but the antenna can be operated efficiently over a broad impedance range, easily matched with a suitable microstrip architecture which will be discussed further in Section V.1.4. It is worth noting that the toothed log-periodic alternative offered interesting performances but was not tunable to provide the necessary beam width to match the prototyped lenslet.

Table V.1.2: *Summary of the antennas performances: Characteristic impedance* Z_0*, admissible impedance deviation* ΔZ_0*, central frequency of operation* f_c*, bandwidth* BW*, half-width at half-maximum angle* θ_{HWHM}*, gaussicity* η_0*, ellipticity* ϵ*, directivity* D *and peak cross-polarisation level* X_{pk}*.*

Antenna Type	$Z_0[\Omega]$	$\Delta Z_0[\Omega]$	f_c[GHz]	BW[GHz]	$\theta_{HWHM}[°]$	$\eta_0[\%]$	$\epsilon[\%]$	D[dB]	X_{pk}[dB]
Dual Twin-slot (a.)	50	20	85	30	28.6	95	0.0	7.15	-17.8
Bow-tie (b.)	120	70	90	40	30	85	6.1	7.65	-10.5
Toothed Log-periodic (c.)	220	40	110	60	22.8	98	2.7	8.13	-14.5
Sinuous (d.)	200	100	110	60	30	88	7.4	8.92	-23.5

V.1.3.2 Sinuous Antenna Design

V.1.3.3 Antenna Backing

Planar antennas show a preferred radiative direction into the substrate when fabricated on high dielectric constant dielectrics such as Silicon, with $\epsilon_r = 11.7$. However, when patterned on a membrane approximating free space, the antenna will radiate on either side, leading to a 50% drop in efficiency if not compensated for. As per discussed in Chapter III.3, efforts are ongoing to embedded the MetaL technology in Silicon and the current prototype device is inherently matched with free-space. To refocus the power at the centre of the antenna, one option is to use a spherical backshort matching the phase pattern at an optimal distance d_m, as shown in Fig.V.1.7. The mirror radius and vertical origin offset from the antenna centre are defined fitting its radial cut to the antenna frequency and cut averaged phase pattern at d_m. A ball nosed cutter is used to machine the spherical backshort, restricting the available radii to a limited set.

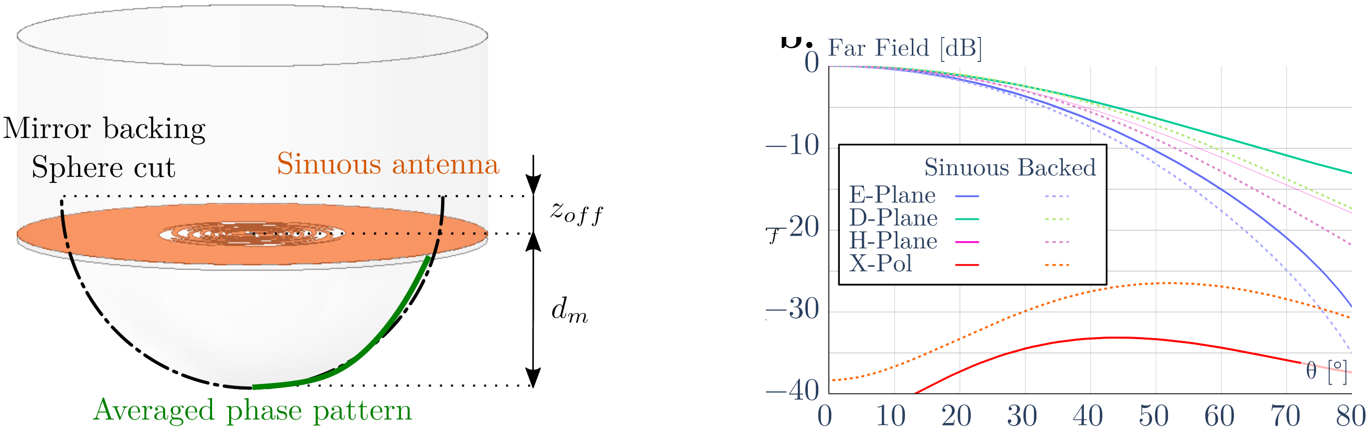

(a) **(b)**

Figure V.1.7: *(a) View of the spherical mirror-backed antenna showing the sinuous frequency and cut-averaged phase pattern (green) at* d_m *and the overlaying sphere cut of the matching mirror. To fit the pattern, the sphere centre is displaced vertically by* z_{off}*. (b) Far-field response of the sinuous alone (plain) and the backed version (dashed) in the E, D and H plane cuts at* 90 GHz*. Whilst preserving the ellipticity and the beam width, the backing result in 5% increase in gaussicity but raises* X_{pk} *to* −26 dB*, still below the* −21 dB *limit. As checked in the simulations, the peak gain sees a* 3 dB *increase as expected. Figures made with ANSYS-HFSS, Python and Inkscape by the author.*

V.1.4 Microstrip Network

V.1.4.1 Network design

The KIDs are optically fed by a 2 µm wide Niobium microstrip line of characteristic impedance 29.5 Ω, on top of which a 500 nm thick dielectric layer of Silicon Dioxide and a 200 nm thick Niobium ground plane are deposited. The matching Microstrip (MS) architecture devised further is modelled on Advanced Design System (ADS), where default material characteristics are used. Namely, Silicon Dioxide has a permittivity of 3.9 and loss tangent of 0.02. On the opposite end of the line, the self-complementary planar antenna is matched to free-space with a theoretical input impedance of 188Ω[207]. Illustrated in Fig.V.1.8 are simulated design of an N-patch and a dual-stub filters optimised in ADS as to adequately provide the desired impedance match of the microstrip line at the antenna centre over a relatively large bandwidth [80 GHz; 130 GHz]. The supporting membrane, Silicon or Silicon Nitride, had no major impact on the simulated responses and was subsequently discarded from the model. The stub solution is preferred to the bulkier geometry of the optimal 3-patch filter, clashing with the antenna shape itself.

In addition, for the antenna to provide a linearly polarised beam, its opposite pair of arms must

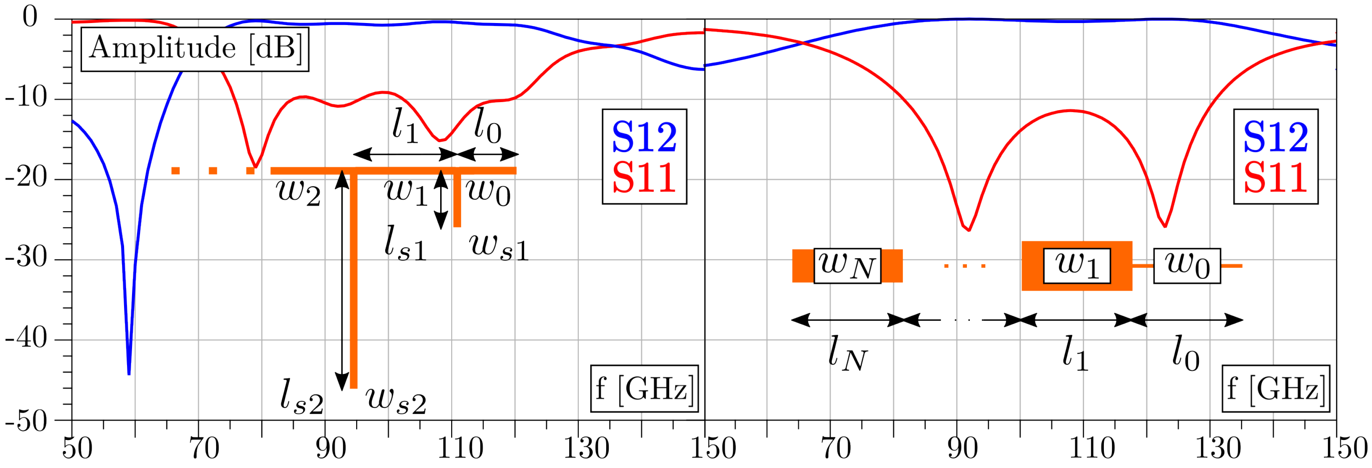

Figure V.1.8: *Transmission* $S12_{\mathrm{dB}}$ *and reflection* $S11_{\mathrm{dB}}$ *response of the optimised dual-stub (left) and (right) 3-patch filters. The dual-stub is parametrised by the widths* $w_{0,1,2}$ *and lengths* $l_{0,1}$ *of the successive microstrip lines starting at the antenna centre, and by the stubs widths* $w_{s1,2}$ *and lengths* $l_{s1,2}$*. The N-patch filter is a modified quarter-wave filter where the* $\lambda/4$ *condition is relaxed. The* i^{th} *patch is parametrised by its width* w_i *and length* l_i*.*

be driven 180° out-of-phase, necessitating the matched line to be split through a rat-race coupler further away from the antenna. A transition occurs where the bulk Silicon is etched which causes an additional mismatch, compensated by a step in microstrip width at the interface. The latter impacted the filter performances and it was found that a single stub operated better in this context. An end-to-end simulation of the readjusted filtering, the dielectric transition and the coupler was conducted in ADS, as presented in Fig.V.1.9 along with the transmission response from the signal branches to the combined branch and the phase difference stability between the signal branches. As can be seen from the response, to cover a large bandwidth through the entire architecture whilst ensuring an out-of-phase driving of the antenna set of opposite arms, the different elements involved are ultimately interacting, introducing resonance between the branches resulting in an interfering pattern. The transmission of each antenna arm is found to average around 45%, giving a combined efficient averaging around 90% across the optical band of interest. The phase difference between the two arms across the band is 180° ± 10°.

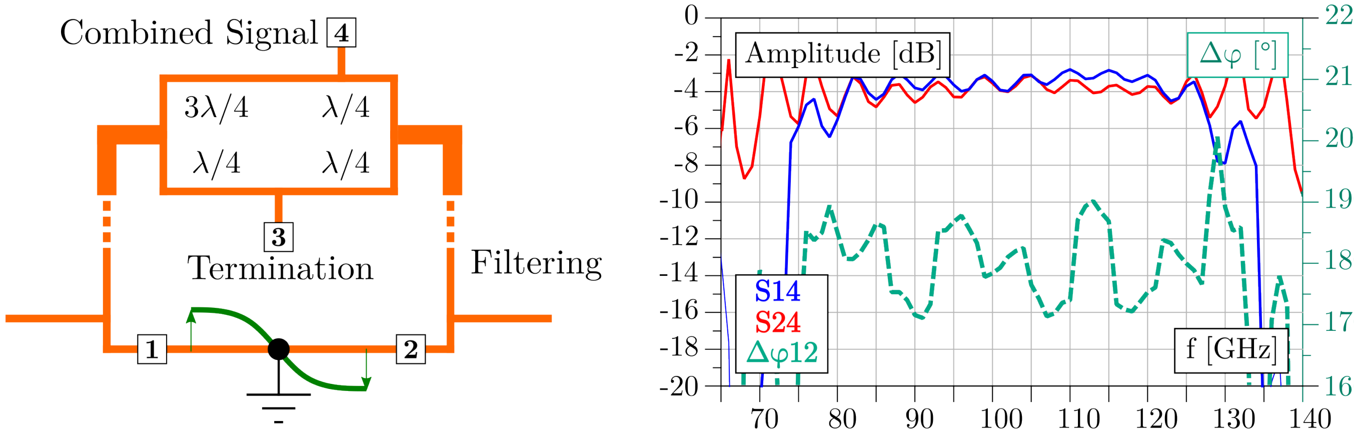

Figure V.1.9: *Schematics of the optimised microstrip architecture constituted of the branches (1) and (2) filtered with a stub and step in width, further combined (4) by a hybrid junction adequately terminated (3). The transmission responses of branches (1) and (2) of the architecture and their phase difference* $\Delta\varphi$ *is plotted aside. Figure made with SONNET, Python and Inkscape by the author.*

Considering the inherent sensitivity of the detectors, a 10% loss in power induced by the difficult impedance transformation and phase coupling operation necessary for the free-space pixel design concerned by the present work is expected. As dielectric are modelled lossless, metal lines as ideal conductors, and considering the microstrip lengths involved the effective loss will be much higher. Considering the KIDs inherent sensitivity and the power of the source used for the cold experimental characterisation of the pixel beam, as will be discussed in Section V.2, the losses are deemed acceptable.

V.1.4.2 Simulated Antenna Coupled MetaL

The resulting far-field pattern of the antenna-coupled lenslet is presented in Fig.V.1.10 at 90 GHz in the E, H and D planes, simulated in ANSYS-HFSS and fitted with a 5th order Laguerre-Gaussian. The gaussicity is 99%, the ellipticity is at a net 0% and the directivity is at 17.67 dBi with no gain differential. The cross-polarisation and sidelobe levels are below −20 dB, ensuring minimal polarisation leakage and spillover respectively. Measurements in the laboratory shown the phase centre was about 200 µm in front of the lenslet, with less than 50 µm variation with frequency, resulting in a Strehl ratio close to 1, in line with analytically estimated ratios reported [213]. The preliminary simulations carried on the sinuous antenna-coupled MetaL presents promising performances for the devised pixel design, in line with CMB applications.

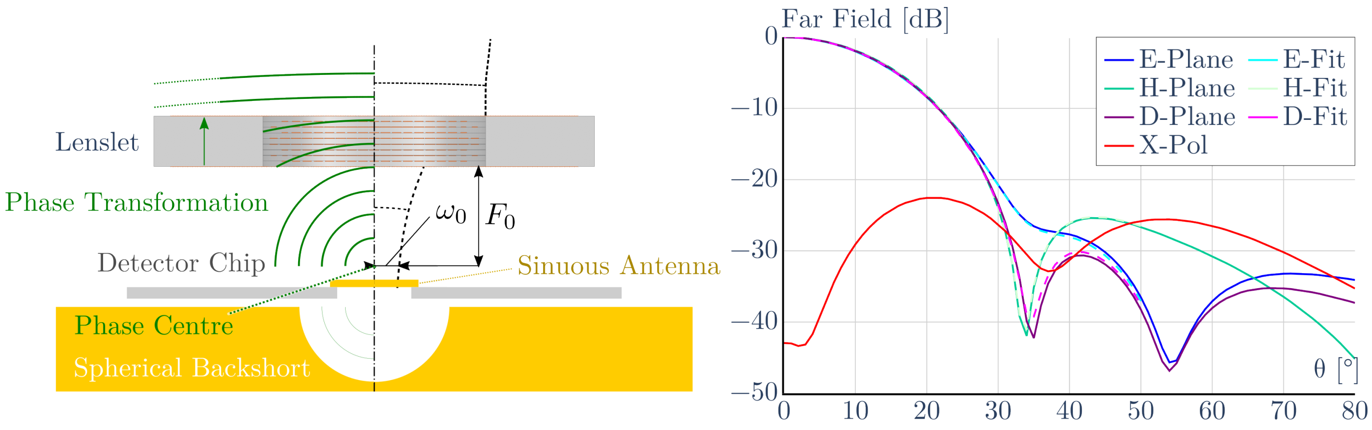

Figure V.1.10: *Sinuous antenna-coupled air-gap phase-engineered metamaterial-based lenslet far-field response in the E, D and H cut planes and cross-polarisation at* 90 GHz*. Figure made with ANSYS-HFSS, Python and Inkscape by the author.*

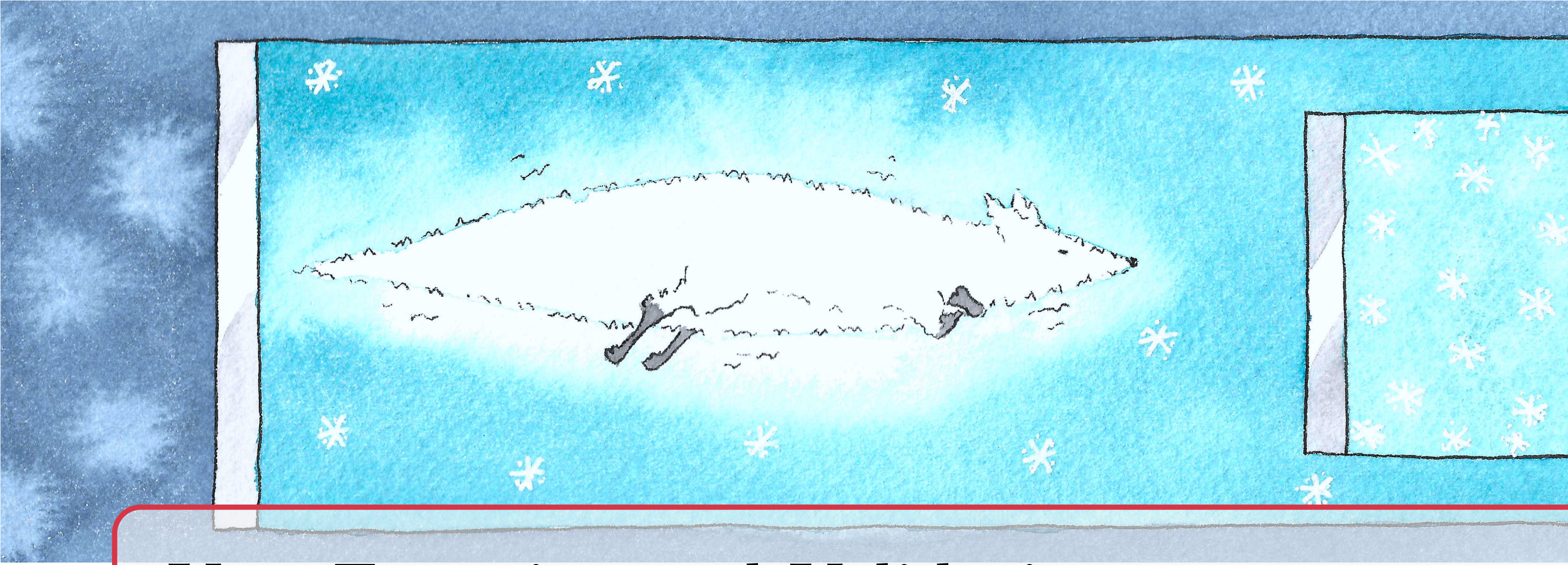

V.2. Experimental Validation

V.2.1 Pixel Fabrication

Four prototype detector chips are laid out, illustrated in Fig. V.2.1. The Silicon Dioxide substrate required for the MS line does not support stress well. In previous tests, coatings over the full area of the wafer broke during cool down. Partial coating is investigated here instead, with deposited slices of Silicon Dioxide on chips 1 and 3 and etched gaps on chips 2 and 4. In order to identify potential problems with the MS architecture, dark KID 1 is connected to the optical line of the second polarisation on chips 2 and 3. The choice was made to keep the detectors on Silicon Nitride to avoid fabrication complexity at the cost of higher noise contributions [206, 214]. Dual-polarisation capability necessitates two optical lines running 90° from one another and crossing over, as shown in Fig. V.1.1. Stepping down and bridging are two difficult processes, especially considering the narrow lines required to match the high impedance at the antenna centre to the low impedance of the KIDs. As the aim consists of proving the concept of the MetaL, a variation of the pixel for

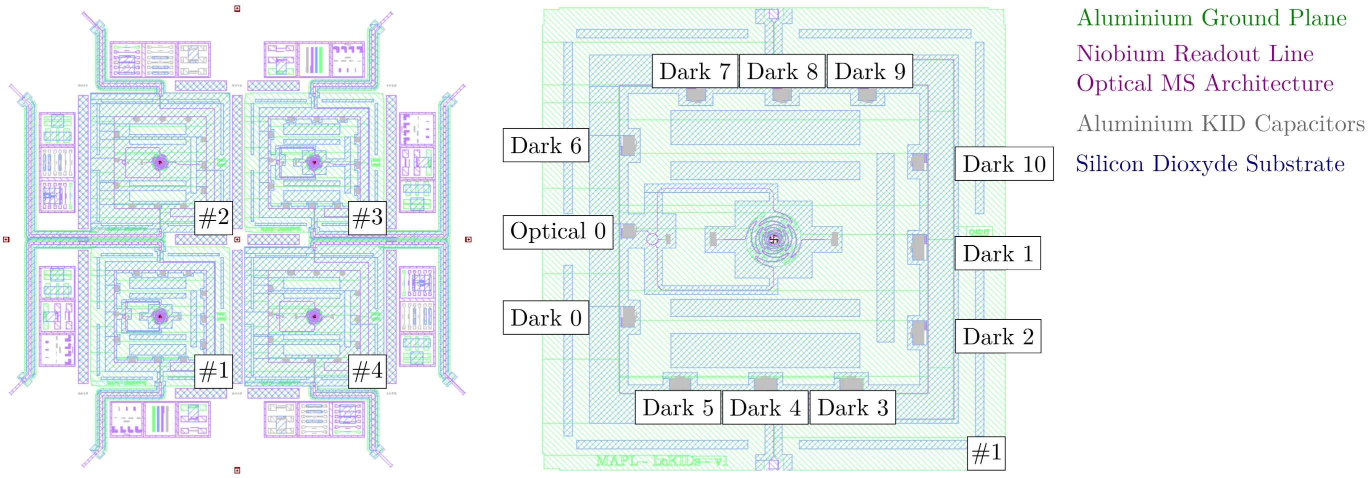

Figure V.2.1: *Layout of the four prototyped chips to demonstrate the MetaL coupling capabilities. Long RF readout tracks run to the edge of the wafer for dark measurement of all four chips simultaneously, further discussed in Section V.2.2. Test patterns surrounds the four chips for future qualification of the detectors. Figure made with KLayout and Inkscape by the author.*

a single polarisation is considered instead. The layout of the microstrip architecture discussed in Section V.1.4 is shown in Fig. V.2.2.

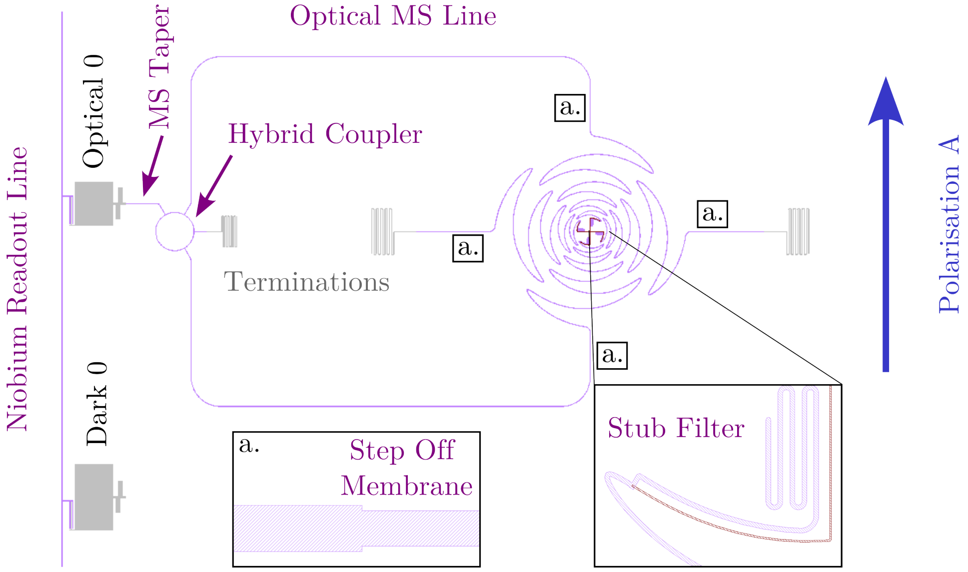

Figure V.2.2: *Detailed layout of the single polarisation variation, illustrating the different matching strategies optimised in ADS. Figure made with KLayout and Inkscape by the author.*

The fabrication rundown presented in Fig. V.2.3 was conducted in the Cardiff ICS clean rooms by Dr Christopher Dunscombe, and in Edinburgh SMC for the RIE. It consisted of the following steps:

- **Wafer preparation**

  The 111 float zone high resistivity ($> 10,000\Omega$cm) Silicon wafer is coated in a furnace with **1** a 300nm Silicon Dioxide etch stop.

  This is followed by **2** a 400nm stoichiometric Silicon Nitride LPCVD with a tensile stress below 250MPa to ensure the integrity of the membranes.
- **KID Aluminium layer**

  The KID layer comes first. **3** A 50nm layer of high purity Aluminium is Electron-Beam Physical Vapor Deposition (EBPVD) with a deposition rate of $2\text{Å}s^{-1}$.

  4 The wafer is spin-coated with positive resist, further photolithographed with a direct writer.

  5 The KIDs are then chemically etched with phosphoric acid, nitric acid and water. After the photoresist is removed using solvents: N-Methyl-2-Pyrrolidone (NMP), then Acetone and Isopropyl-Alcohol (IPA), **6** the finished KIDs are obtained.
- **Microstrip architecture Niobium layer**

  Next comes the microstrip architecture layer, involving sensitive 1µm patterns, for which the following lift-off method was devised through trials and errors. **7** A S1805 positive resist is grown using an AZ developer on a 1:1 ratio of sodium and deionised water to avoid Aluminium etching at connections.

  8 A 75nm Niobium layer is then sputter deposited.

  9 The resist is removed using the same solvents as previously, lifting-off the undesired sections of Niobium.

- **Silicon Dioxide dielectric substrate**
  The underlying Silicon Dioxide, dielectric layer of the microstrip architecture, is formed using a lift-off process. **10** A coating of AZ2020 negative resist is developed in the AZ developer as previously.
  11 A 500nm of Silicon Dioxide is then EBPVD.
  12 Again the underlying resist is dissolved, leaving only the desired patterns.
- **Niobium ground plane**
  A lift-off procedure is used again for this layer. **13** The resist process is the same as in step **10**.
  14 the Niobium deposition is conducted as per step **8**.
  15 As above, the resist is finally dissolved to finish the ground plane.
- **Backside etch for the membranes**
  Following the Inductively Coupled Plasma (ICP) etch of the Silicon Nitride and the dissolution of the primary photoresist, **16** a 10XT positive photoresist is developed on both sides in the AZ developer with a 3:1 ratio. On the frontside, it protects the realised features.
  17 It is photolithographed on the backside to define where the bulk silicon will be removed.
  18 The Silicon is Deep Reactive Ion Etch (DRIE) in Edinburgh using Sulphur Hexafluoride/Octafluorocyclobutane Bosch process.
  19 The leftover resist is dissolved, leaving the finished wafer.

V.2.2 Dark Measurements

V.2.2.1 Experimental Setup

Preliminary dark measurements are carried out to validate the f_r and Q_r of the designed KIDs and assess the good operation of the readout line. When detector characterisation is required, those measurements are carried out with a homodyne setup to investigate the shift in Q_r and f_r of the resonators as a function of temperature. The detectors are then operated at their optimal readout power, that which maximises the SNR.

The homodyne setup, depicted in Fig. V.2.4, operates a comparison between the input signal comb sent to the detectors and the received readout output coming from the chip, as follows. The base tone is generated with a low noise synthesizer. This LO signal is further split between:

- The cryostat - Upstream the cryostat RF input, a variable attenuator enables tuning of the power driving the detectors. Additional attenuators are present, here providing −20dB at 50K and −10dB at 4K, necessary to compensate for electronic temperature noise contributions. The readout signal thus reaches power levels that the KIDs can handle. Once passed the detectors, the shifted signal passes through a Low Noise Amplifier (LNA). A LPF may be used in the 50K stage to filter out amplifier noise due to saturation. The readout power level is reached back and the signal is sent to the In-phase/Quadrature (IQ) mixer.
- IQ mixer - The base tone and the shifted signals are compared together. The IQ mixer effectively outputs analogue time-streams proportional to the real and imaginary part of the

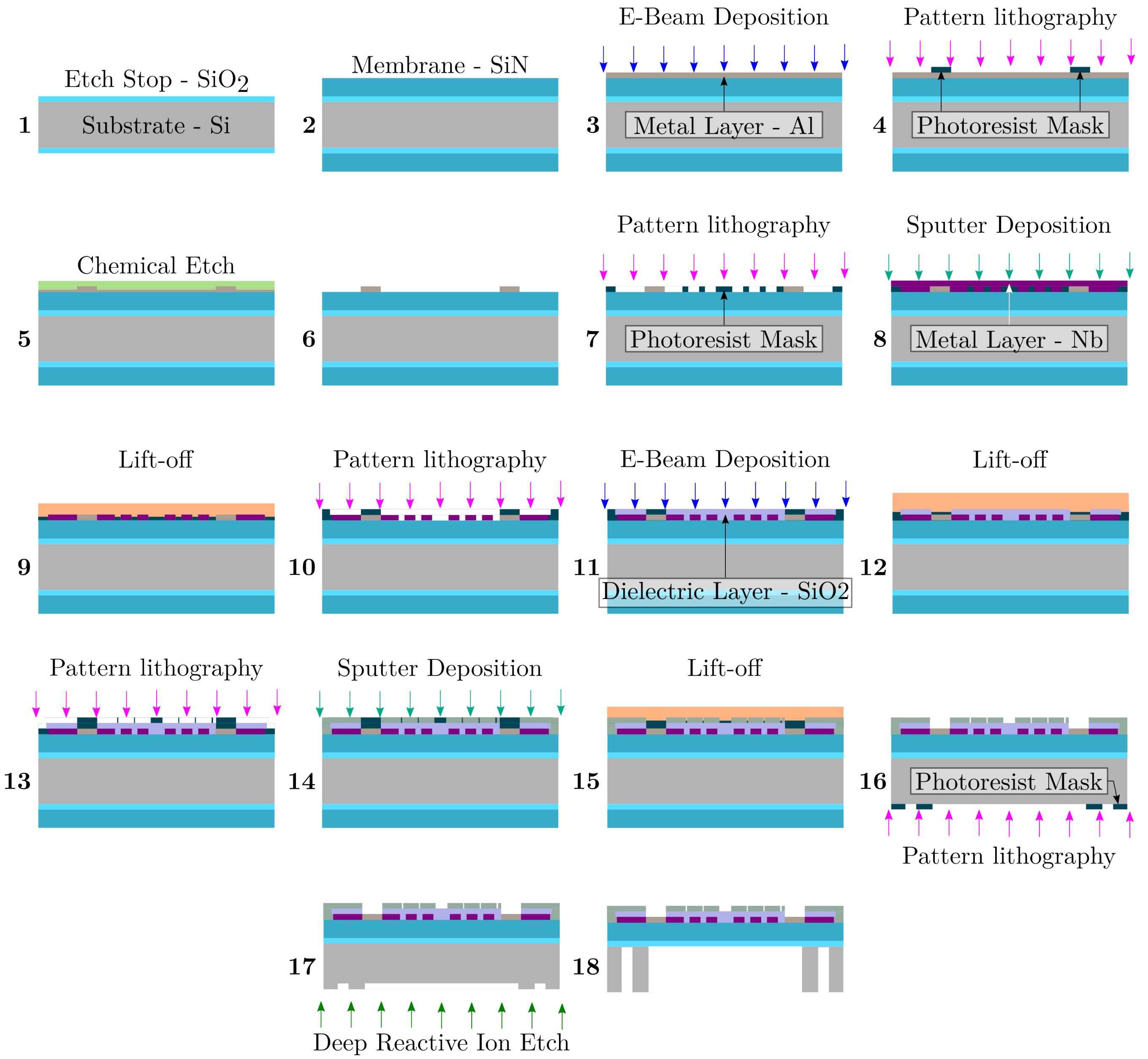

Figure V.2.3: *Fabrication rundown of the prototype detector chips. Figure made with Inkscape by the author.*

transmission response s_{21}, I and Q respectively, which are then low-pass filtered to prevent aliasing of high frequency signals before reading by the data acquisition system, digitized and saved for further processing.

In the present scenario, validation of the LeKIDs f_r is desired. Potential detectors are initially identified with a VNA sweep and further characterised with the homodyne setup. All four chips are packed together and read out cold in a dark environment as to identify potential defects. A photograph of the sample ready for such test is shown in Fig. V.2.4. Once the LeKIDs are identified, the wafer is diced into individual elements, schematised in the centre of Fig. V.2.1.

V.2.2.2 Detectors f_r and Q_i Validation

The sweeps are laid out in Fig. V.2.5 for a base temperature at 83mK. The obtained f_r are mentioned in Table V.1.1. Several spurious resonances and their overtones can be observed, associated

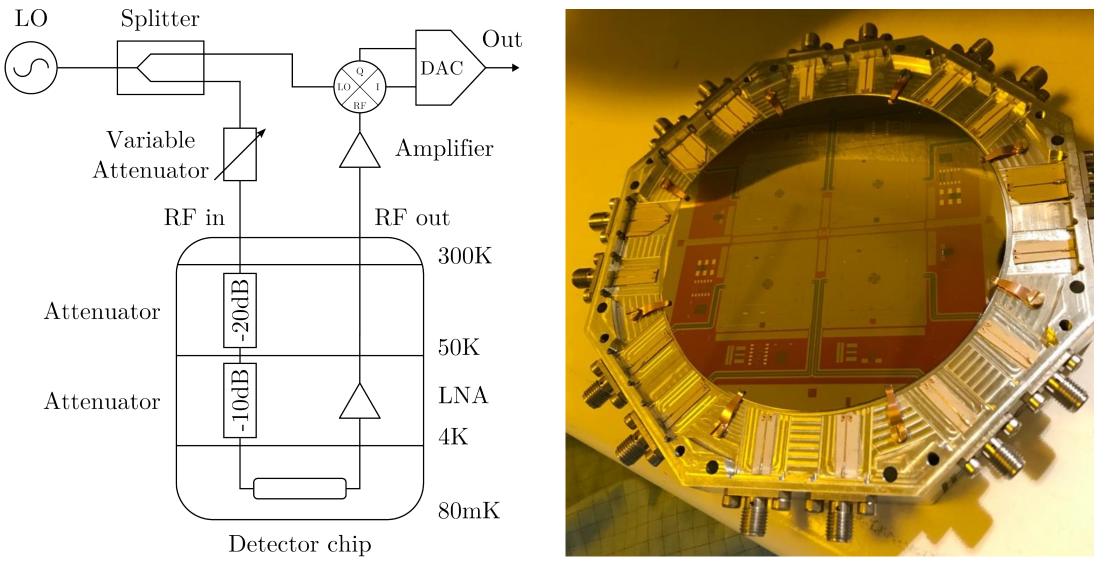

Figure V.2.4: *Homodyne setup diagram and sample in the dedicated holder, enabling testing of multiple chips on a single* 100mm *wafer. Figure made with Inkscape and photography taken by Dr Christopher Dunscombe.*

with parasitic effects on the chip or its packaging, and will be removed from further analysis. They are not associated with the designed detectors as these are identifiable by noting they do not vary with a change in temperature. Identification of the detectors is conducted by isolating the characteristic peaks in the S_{21} response and their shift with temperature.

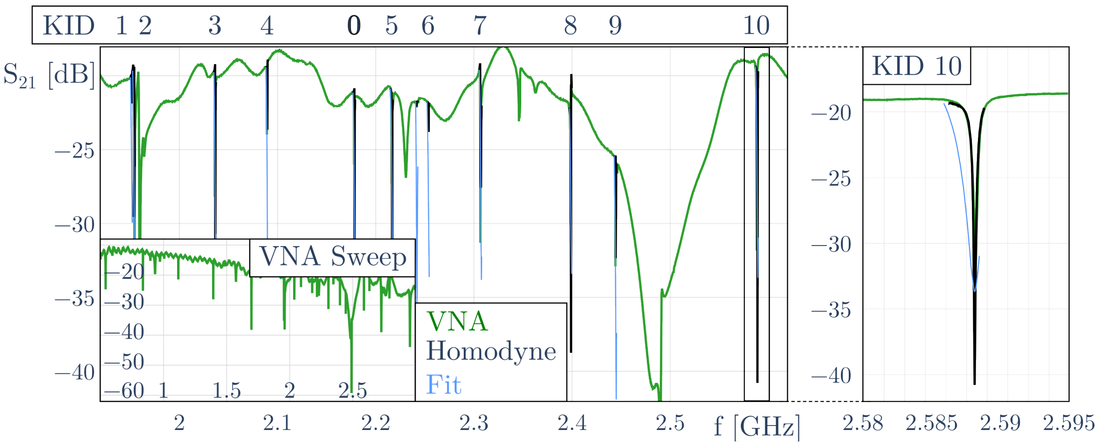

Figure V.2.5: *Frequency sweep for KIDs identification. The VNA scan is conducted first with varying base temperatures to roughly check the detector positions. The homodyne system is then run on all potential candidates. A proper characterisation of the quality factors is made by tuning the attenuation level. Figure made with Python and Inkscape by the author.*

V.2.2.3 Power Spectrum Density of the Optical KID

Power Spectral Density (PSD) extraction is done through noise measurements, carried in Cardiff with the help of Dr Tom Brien, where each point in the homodyne sweep consists of an average of a user defined number of samples, typically of order of several thousands, taken at an adjustable rate. The overall PSD, in units of $\mathrm{Hz}^2\,\mathrm{Hz}^{-1}$, is the combined result of acquired short time streams sampled at the maximum rate on one hand, and larger samples at a slower rate on the other. The optical KID PSD obtained at a base temperature of 82mK with an attenuation of 38dB is given in

Fig. V.2.6. The on resonance GR area is the effective frequency range of operation of the detector, characteristic of its sensitivity. This band stops where the roll-off region begins, indicative of the quasi-particle life time dependence of the GR. $\tau_{qp} \simeq 100\mu s$ is estimated by fitting the PSD with the analytical expression for the GR contribution (V.1.6) [203]. The local peaks observed are pickup noises caused by the Pulse Tube Cryocooler (PTC) and the main power supply, which operates at 50Hz. An off-resonance comparison is necessary to distinguish contributions from the system, such as RF electronics, from detector related noises. The synthesizer generating the LO signal becomes noisy in the region near its carrier frequency. At low frequencies, TLS noise dominates. Namely, the amorphous structure of the underlying dielectric supporting the superconducting film gives rise to a potential energy distribution that allows groups of atoms or molecules to transition between multiple potential energy minima. Macroscopically, this transcribes into time varying changes in the dielectric constant, increasing the uncertainty on f_r at low modulation frequencies. Despite a lack of sensitivity in the low frequency range, mostly due to the underlying Silicon Nitride contributions [206], the KIDs are operating close to the GR limit at modulation frequencies above 10Hz.

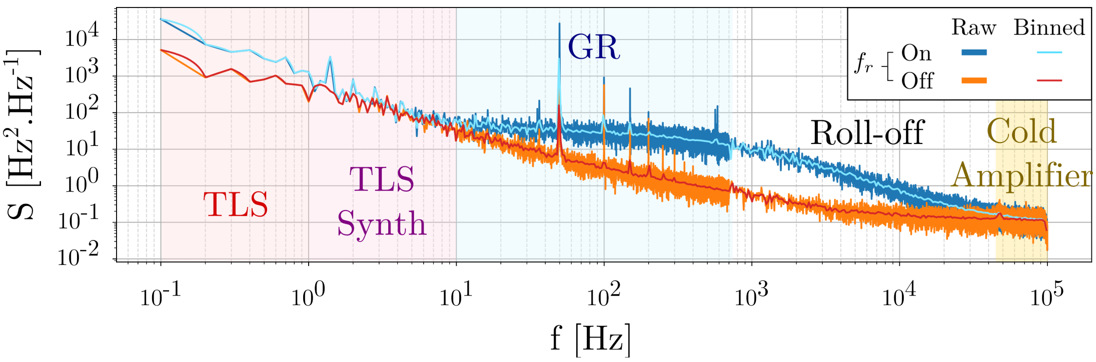

Figure V.2.6: *PSD of the optical KID at* 82mK *with an attenuation of* 38dB*, with noise contributions from the TLS, synthesizer, GR and LNA underlined. Figure made with Python by the author, relying on data acquired with the help of Dr Tom Brien.*

V.2.3 Cardiff-made Lenslet

The prototype chip is currently still under development. A cryo-compatible lenslet was fabricated in parallel, as previously mentioned in Chapter IV.1. The mount was adapted with longer fingers to further enable measurement at $F_0 = 4.5\text{mm}$, optimal focal length at which the sinuous antenna is coupled. Notably, a permanent frame was added to safely swap the lenslet from warm to cold mountings. Simulations were carried in ANSYS-HFSS to check that the frame does not contribute to the lenslet far field. It is worth noting that whilst the probe beam profile does not match that of the antenna at this distance, warm measurements were still required as a validation step for the newly fabricated device. Fig. V.2.7 shows the measured beam profile of the cryo-compatible variation of the prototype lenslet at 75GHz, 90GHz and 110GHz in the E, D and H-planes, against its beam response simulated in ANSYS-HFSS. Measurements were carried on the setup previously described in Chapter IV.3.

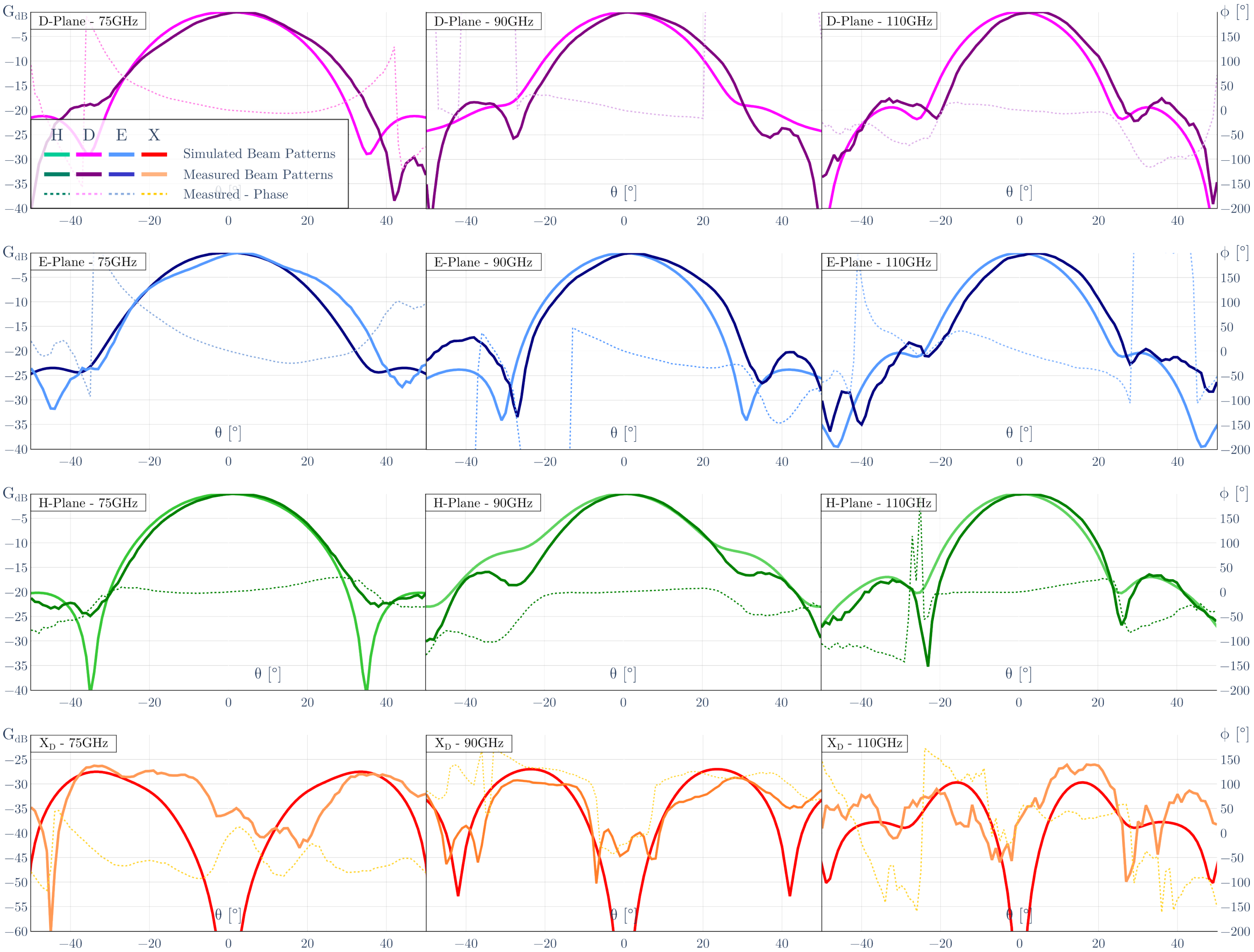

Figure V.2.7: *Cardiff made, cryo-compatible variation of the prototype lenslet co and cross-polarisation beam patterns measured and simulated at 75GHz, 90GHz and 110GHz in the E, D and H-planes.*

V.2.4 Cold Measurements Plans

V.2.4.1 Cryogenic Setup

To encase the chip and ensure suitable alignment between the lenslet and the sinuous antenna, a dedicated holder is made which maintains constraints close to those derived in Section IV.2.1. Details of its design are given in Fig. V.2.8. The lenslet, sat in its frame, is slid in a slot 200µm larger. The potential transversal mismatch due to this provision can be compensated using a gauge feeler or shims on the sides of the lenslet casing to ensure adequate centring.

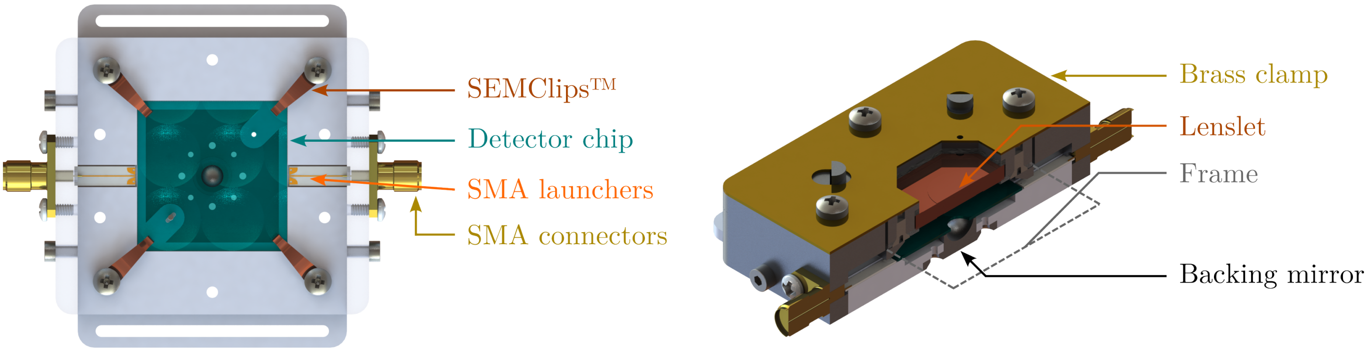

Figure V.2.8: *CAD model of the detector chip holder, with depicted constituents. Figure made with Solidworks and Inkscape by the author.*

The sample is then installed on the cold plate of a test cryostat, which can reach a base temperature of 250mK. Each cryogenic stage is equipped with large optical windows. Out of band, each window will act as a blackbody source on a given stage, adding up to the temperature load. To mitigate their impact, a set of metamaterial filters is added where relevant [132, 215], designed in the same manner as discussed in Chapter III.2. The cryogenic setup is shown in Fig. V.2.9.

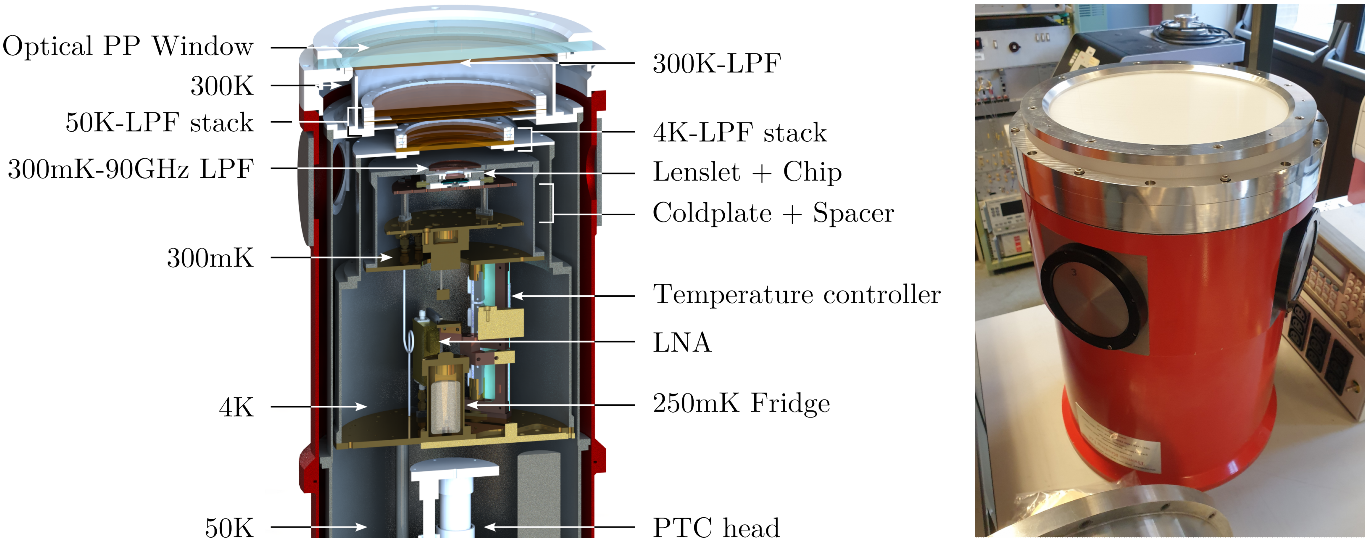

Figure V.2.9: *CAD rendering of the cryostat, underlying the different temperature stages, associated filters and sample position. The fabricated window was recently installed and can be seen on the photograph, on the right hand side. Figure made with Solidworks and Inkscape by the author.*

Beam mapping of the MetaL prototype will be carried in the near future in Cardiff by Prof Simon Doyle, Dr Tom Brien, Dr Ian Veenendaal and the author. Fig. V.2.10 shows the beam scanner experimental setup designed alongside a photograph of the latest status of its installation in the laboratory. Mapping will be done scanning an optical source in front of the cryostat window on multiple planes normal to the OA. Adequate RAM coverage will surround the scan area. The source considered may either be a blackbody or a Toptica coherent emitter [216] covering the full bandwidth, chopped at a selected frequency. In both cases, the resulting difference between the optical and the background power, modulated at the chopping frequency, is proportional to the power transmitted (V.1.9) and the beam can thus be reconstructed.

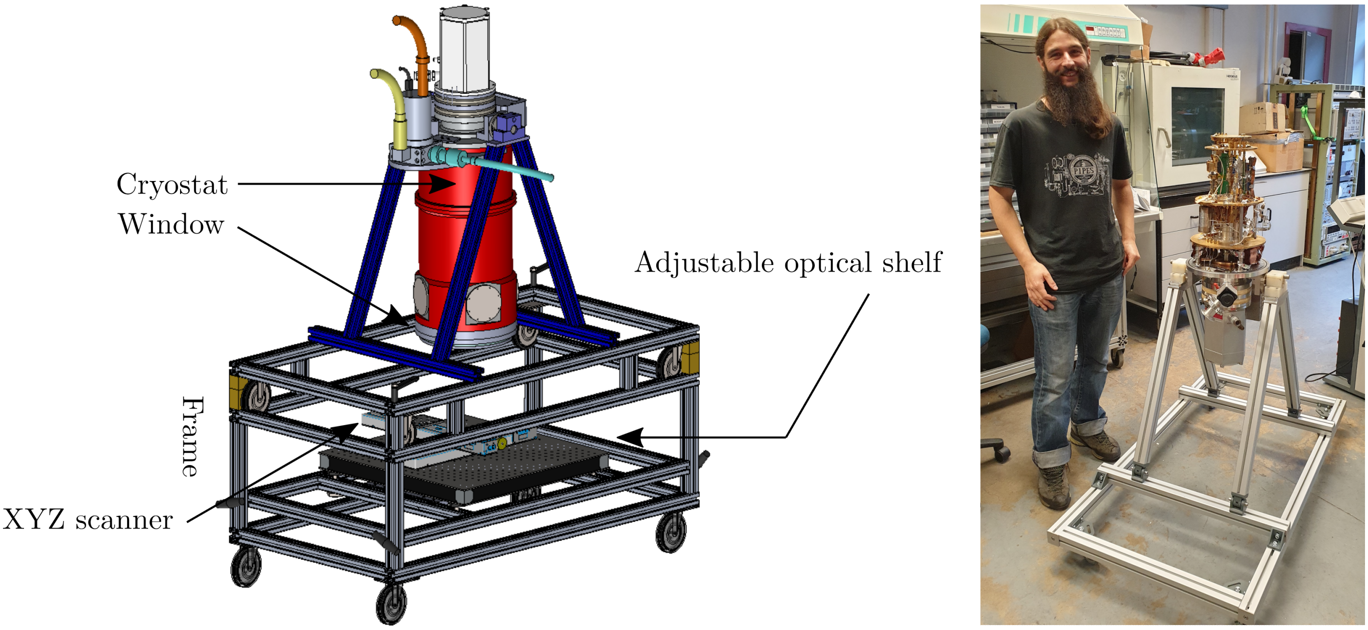

Figure V.2.10: *CAD model of the cold beam map setup, partially installed in the lab. Figure made with Solidworks and Inkscape, and photography taken by Mr Gethin Robson.*

V.2.4.2 Optical Sensitivity

The GR limit sensitivity of the optical detector $NEP_{gr} = 2.30\text{aW}$ (V.1.7) is calculated at 250mK, the base temperature of the setup. Within the GR noise dominated region, the measured sensitivity will drop as background photon noise adds in (V.1.9) (V.2.1), with the associated NEP_{bg}.

$$NEP_{meas} = \sqrt{NEP_{gr}^2 + NEP_{ph}^2} \tag{V.2.1}$$

Considering that the laboratory is at room temperature $T = 300\text{K}$, that the pixel is fully illuminated by the background light, of power $P_{bg} = 414\text{pW}$ (V.1.8), and disregarding optical mismatch for the current estimate, $NEP_{bg} = 1.87\text{fW} \gg NEP_{gr}$ is obtained (V.1.9) at the central frequency $\nu = 90\text{GHz}$ for $\Delta\nu = 50\text{GHz}$, the operating bandwidth of the pixel, as discussed in Section V.1.4. NEP_{bg} dominates the detector sensitivity. It is known as the photon noise limit, effective maximal sensitivity the detector can reach in the context of the experimental setup.

The Toptica source provides 2µW of power [216], corresponding to a shot noise limit of $NEP_{src} =$

155pW far above the photon noise limit. The detectors would in fact be saturated by such amount of power so a Neutral Density (ND) filter or a LPF with a slow cut-off will be used to reduce the optical power thus coupled. This short analysis illustrates that the detectors designed will be photon-noise limited and can indeed be used for the beam scan devised in Section V.2.4.1.

The prototype pixel proposed, constituted of the MetaL coupled to a 4-branch planar sinuous antenna transferring the incoming power to an optical KID via a matching microstrip network architecture, is simulated end-to-end. The present analysis indicates that such design is broadband and offers excellent optical performances. With the lenslet at hand and the detector chip currently being fabricated, the experimental characterisation discussed above will constitute a decisive step in proving the MetaL concept for CMB applications.

Conclusion

To look as far as the technology can reach, to push the capabilities of the instruments further and in doing so, catch the faintest of primordial photons, grasp the precise details of the very first picture of the Universe.

A humble contribution to advance the FPUs design of modern and future instruments aiming at mapping the CMB was presented in this thesis, inscribed within the community broader effort too catch the B-mode polarisation faint signals and characterise the contaminating foregrounds to clear out the dynamics of the creation and early evolution of the Universe.

Through a review of the current depiction of the CMB, it was underlined that the cosmological parameters of the ΛCDM model, the contemporary framework for Cosmology depicting the Universe constituents and dynamics, at the base of the Big Bang paradigm, are fully constrained by the power spectra C_ℓ of the temperature and polarisation signals. After decades of investigations, dated back from COBE, the TT, EE and TE power spectra are presently well defined over a large ℓ span, resulting in an estimation of most of the cosmology parameters with around 1% error. Amongst a few other parameters, the tensor to scalar ratio r of the density versus primordial gravitational wave fluctuations is not yet constrained but currently set to a higher limit at $r < 10^{-2}$. This ratio sets the conditions of an inflationary scenario in the early Universe. However, the B-mode polarisation signals, signature of the primordial gravitational waves, are very faint, orders of magnitude below that of the temperature map. Modern and future experiments aim at observing these signals at low ℓ with a matching sensitivity to set a new constraint, at least an order of magnitude below. Furthermore, the opposite end of the angular scales, over $\ell = 1100$, lays information on the late time Universe constituents and evolution, large scale structures seeding and formation. Galactic and extra-galactic foregrounds overlay the already faint signals, and must be accurately accounted for. To validate the ΛCDM model, or improve the current uncertainties it is set at, precision measurements of the CMB polarisation signals at high sensitivities for both $\ell < 200$ and $\ell > 1100$ are required.

These objectives call for considerable technological advances in instrumentation. Modern and coming experiments must provide high throughput in the bandwidths of interest, calling for pristine optics offering optimal power coupling from the sky to the FPU whilst ensuring efficient out of band rejection on one hand, and for a large number of densely packed, highly sensitive detectors on the other hand. A telescope angular response, polarisation properties, bandwidth and temperature sensitivity are of the highest importance to measure CMB signals accurately and are strongly defined by the FPU. Reviewing the current technological developments made in this area, various options were discussed. Directly coupled detectors offer the largest number of packable detectors, is easily scalable, and provides high throughput and fast mapping at a low cost. However, as the detectors are directly illuminated, their beam is poorly constrained, their sensitivities is hindered and stray light becomes a problem. Coherently summed hierarchical arrays result in the lowest illuminated focal area and still suffers from stray light. Yet, the technology improves the sensitivity of the instrument by efficiently coupling power through the antennas and is embedded in Silicon. The fabrication techniques are thus scalable and straightforwardly compatible with the detector plane with no shrinkage, thus no differential shifts of the optics with respect to the detectors in a cold environment. A more traditional approach is to use Silicon platelet horn antennas, where the smooth conical walls are etched through a number of wafers, stacked together. This alternative offers an elegant trade-off between beam coupling efficiency and beam systematics control in an array directly compatible with the detector plane. However, the fabrication process is more involved both in terms of time and costs and may be harder to scale up. A final alternative are the planar antennas coupled to lenslet arrays, where a pair of detectors is coupled to a dual-polarisation sensitive, broadband planar sinuous antenna, fed by an hyper-hemispherical lenslet. The latter consists of an extended hemisphere made of Silicon, covered with an ARC dome either sputtered or glued upon. The antenna coupled lenslets constitutes an attractive trade-off between pixel spacing, $\mathcal{F}$ and optical efficiency, still permitting high mapping speeds. If the fabrication is simpler than that of platelet horns, obtaining a smooth hemispherical surface stays challenging and not cost effective. They also suffer from stray light and there is a differential thermal shrinkage of the ARC.

Of the various candidate discussed, SO and LiteBIRD decided to keep traditional horn antenna arrays and implement a few antenna-coupled lenslet array based FPUs to push forward the development of this technology, now demonstrated in POLARBEAR2 and other recent instruments. The MetaL concept, inspired from the hyper-hemispherical lenslet, is based on metamaterials, a technology offering pristine control over the amplitude, phase and polarisation states of light waves. A MetaL array would consist of an assembly of stacked Silicon wafers where the effective part of the lenslets would be lithographed FSSs, reminiscent of Cardiff metal-mesh filters, a well proven technology. This solution would be cost effective, scalable, planar and could integrate Silicon based ARCs, tackling the challenges suffered by their hyper-hemispherical counterpart.

The MetaL concept requires various demonstrating steps before the technology reaches maturity. The latest developments shown that a fully embedded lenslet array would require tens of $\simeq 75$µm thick wafers of 100mm diameter, at best. Such array would be difficult to fabricate. While research is ongoing to suitably design fully embedded devices, the present work proposed to analytically and experimentally characterise a prototype device, matched to free-space instead of Silicon by design. A full beam characterisation was conducted both in a set of electromagnetic simulations, and experimentally, on a systematics limited optical test bed, warm. The measured beam was compared to a simulated hyper-hemispherical counterpart, both in terms of optical characteristics and via a benchmark CMB map convolution based analysis. Preliminary stages of a cold beam holography measurement were further depicted, in particular, the design and fabrication of a complete pixel, sensitive to a single polarisation and fully matched to free space, where a MetaL made in Cardiff University is coupled to a sinuous antenna feeding a set of KIDs, resembling the pixel design for SO and LiteBIRD.

The optical requirements for CMB instruments may vary for a given experiment. The beam map of an integrated FPU should be put through an end-to-end pipeline to verify its performances adequately. Nonetheless, estimated limits can be built upon existing specifications. It was thus devised that the required gaussicity, namely the amount of power carried by the main lobe, should be $\eta_0 > 95\%$; the differential gain between the two polarisation directions should be $\Delta g < 1\%$; the beam asymmetry is given by its ellipticity, limited at $\mathcal{E} < 10\%$; and the amount of one polari-

sation leaking to the other should be less than 1%. The warm beam measurements carried in the present work shown that the MetaL prototype radiates a near symmetrical Gaussian beam with cross-polarisation levels below -21dB and a differential gain of $\Delta g = 0.2\%$, in line with the CMB instrumental requirements, and comparable to its hyper-hemispherical lenslet counterpart, demonstrating the potential suitability of the MetaL concept as a focal optics for future experiments.
In this context, a pixel design coupling the lenslet to a detector set in a similar manner as is done for SO and LiteBIRD constitutes the next step devised to prove the MetaL concept. KIDs were chosen for such coupling as they are an ultra-sensitive superconducting technology with a high multiplexing ratio, fully suited for the large scale focal planes required for CMB experiments. The pixel is constituted of the prototyped MetaL, coupled to a 4-branch planar sinuous antenna transferring the incoming power to a KID via a microstrip line through a combination of matching filters with a phase coupler. This design is inherently broadband, impedance matched and dual-polarised. Throughout the operating bandwidth, the simulated far-field pattern of the antenna-coupled lenslet offers excellent optical performances. Its gaussicity is 99%, the ellipticity is at a net 0% and the directivity is at 17.67 dBi with no gain differential. The cross-polarisation and side-lobe levels are below -20 dB, ensuring minimal polarisation leakage and spillover respectively. The preparatory steps for a cold beam holography measurement procedure were laid out in this work, which should confirm the simulated performance of this pixel design. Upon demonstrated coupling, such pixel could be readapted to conduct on-chip spectroscopy.
Hopes and efforts are directed towards taking a glimpse at the large scale mechanisms and the finer details of the CMB polarisation. To this end, a number of new instruments are currently being deployed or under development, such as SO and LiteBIRD, which requires pristine optical quality. Accent is made on systematics limited, cost-effective and compact solutions. Standing amongst other technology developments, this thesis presented a proof of concept for the MetaL. It was shown that this focal optics offers adequate optical performances for CMB instruments and other potential millimetre, sub-millimetre and far infra-red applications, in a comparable manner to the existing and demonstrated hyper-hemispherical lenslet. Progress is made on the adaptation of the MetaLs concept to transfer the technology to a Silicon-embedded variation, which would offer immediate scalability and efficient direct coupling with detector planes. To further demonstrate this lenslet capability, an air-gapped prototype was readapted and fabricated for coupling with KIDs through a dedicated antenna and matching network architecture. Whilst the design was finalised, the fabrication of the pixel thus devised is still ongoing. Future plan for the experimental characterisation of the optical coupling capabilities of the MetaL were overlaid.
Through the present comprehensive depiction and characterisation of the MetaL concept, it is the author's hope that the answer of the Scholar was given, whilst that of the Poet was the reader's companion through subtle accompanying sparkles of not so imaginary tales...
... to reach a deeper focus on the primordial Universe.

Back Matter

Acronyms

ΛCDM Λ Cold Dark Matter.

ACT Atacama Cosmology Telescope.
ADS Advanced Design System.
ANSYS-HFSS ANSYS High Frequency Structure Simulator.
ARC Anti-Reflection Coating.
ATRAN Atmospheric TRANsmission.

BAO Baryonic Acoustic Oscillations.
BICEP Background Imaging of Cosmic Extragalactic Polarization.
BPF Band-Pass Filter.
BUG Backshort Under Grid.

CAD Computer Assisted Design.
CAMB Code for Anisotropies in the Microwave Background.
CMB Cosmic Microwave Background.
COBE COsmic Background Explorer.
CPW Co-Planar Waveguide.

DAC Digital-to-Analogue Conversion.
DES Dark Energy Survey.
DLFOV Diffraction-Limited Field Of View.
DRIE Deep Reactive Ion Etch.
DUT Device Under Test.

EBPVD Electron-Beam Physical Vapor Deposition.

FDM Frequency-Division Multiplexing.
FEBeCoP Fast Effective Beam Convolution in Pixel space.
FEM Finite Element Method.

FFT	Fast Fourier Transform.
FIR	Far Infra-Red.
FOV	Field Of View.
FPU	Focal Plane Unit.
FSS	Frequency Selective Surface.
FWHM	Full Width Half Maximum.
GR	Generation-Recombination.
GUT	Grand Unified Theory.
HDPE	High Density Poly-Ethylene.
HFI	High Frequency Instrument.
HFT	High Frequency Telescope.
HPF	High-Pass Filter.
HWP	Half-Wave Plate.
ICP	Inductively Coupled Plasma.
ICS	Institute for Compound Semiconductors.
IDC	Inter-Digital Capacitor.
IF	Intermediate Frequency.
IFFT	Inverse Fast Fourier Transform.
IPA	Isopropyl-Alcohol.
IQ	In-phase/Quadrature.
JAXA	Japan Aerospace Exploration Agency.
KID	Kinetic Inductance Detector.
LAT	Large Aperture Telescope.
LATR	Large Aperture Telescope Receiver.
LeKID	Lumped-element Kinetic Inductance Detector.
LFT	Low Frequency Telescope.
LGB	Laguerre-Gaussian Beam.
LiteBIRD	Lite satellite for the study of B-mode polarization and Inflation from cosmic background Radiation Detection.
LNA	Low Noise Amplifier.
LO	Local Oscillator.
LOS	Line Of Sight.
LPCVD	Low Pressure Chemical Vapour Deposition.
LPF	Low-Pass Filter.
MCMC	Markov Chain Monte Carlo.
MetaL	Metamaterial-based Lenslet.
MFT	Medium Frequency Telescope.

MS Microstrip.
MUX Multiplexing.

ND Neutral Density.
NEP Noise Equivalent Power.
NET Noise Equivalent Temperature.
NIKA2 Néel IRAM KIDs Array.
NIST National Institute of Science & Technology.
NMP N-Methyl-2-Pyrrolidone.

OA Optical Axis.
OMT Ortho-Mode Transducer.
OT Optics Tube.

PEI PolyEtherImide.
PIPER Primordial Inflation Polarization Explorer.
PLL Phase-Locked Loop.
POLARBEAR Polarization of Background Radiation.
PSD Power Spectral Density.
PTC Pulse Tube Cryocooler.

QUBIC Q&U Bolometric Interferometer for Cosmology.

RAM Radiation Absorbent Material.
RF Radio Frequency.
RIE Reactive Ion Etch.
RMS Root Mean Square.
Rx Receiver.

SAT Small Aperture Telescope.
SMC Scottish Microelectronics Centre.
SNR Signal-to-Noise Ratio.
SO Simons Observatory.
SPIDER Suborbital Polarimeter for Inflation Dust and the Epoch of Reionisation.
SPT South Pole Telescope.
SQUID Superconducting Quantum Interference Device.
SRR Split-Ring Resonator.
SZ Sunyaev-Zeldovich.

TDM Time-Division Multiplexing.
TEM Transverse Electro-Magnetic.
TES Transition Edge Sensor.
TK Thomas Keating.
TL Transmission Line.

TLS	Two Level System.
TOAST	Time Ordered Astrophysics Scalable Tools.
TOD	Time Ordered Data.
Tx	Transmitter.
VNA	Vector Network Analyser.
VPM	Variable-delay Polarization Modulator.
WMAP	Wilkinson Microwave Anisotropy Probe.

Bibliography

[1] Peter Coles and Francesco Lucchin. *Cosmology: the origin and evolution of cosmic structure.* 2nd ed. Chichester, Eng: John Wiley, 2002. ISBN: 978-0-471-48909-2 (cited on page 6).

[2] Ya. B. Zel'dovich. "Gravitational instability: An approximate theory for large density perturbations." In: *Astronomy and Astrophysics* 5 (Mar. 1970). ADS Bibcode: 1970A&A.....5...84Z, pages 84–89. ISSN: 0004-6361. URL: `https://ui.adsabs.harvard.edu/abs/1970A&A.....5...84Z` (visited on 09/07/2023) (cited on page 6).

[3] David Lindley. "COBE starts its search for galactic fingerprints". en. In: *Nature* 342.6248 (Nov. 1989). Number: 6248 Publisher: Nature Publishing Group, pages 329–329. ISSN: 1476-4687. DOI: `10.1038/342329a0`. URL: `https://www.nature.com/articles/342329a0` (visited on 09/07/2023) (cited on page 6).

[4] C. L. Bennett et al. "Nine-year Wilkinson Microwave Anisotropy Probe (WMAP) Observations: Final Maps and Results". In: *The Astrophysical Journal Supplement Series* 208 (Oct. 2013). ADS Bibcode: 2013ApJS..208...20B, page 20. ISSN: 0067-0049. DOI: `10.1088/0067-0049/208/2/20`. URL: `https://ui.adsabs.harvard.edu/abs/2013ApJS..208...20B` (visited on 09/07/2023) (cited on page 6).

[5] G. Hinshaw et al. "Nine-year Wilkinson Microwave Anisotropy Probe (WMAP) Observations: Cosmological Parameter Results". en. In: *The Astrophysical Journal Supplement Series* 208.2 (Sept. 2013). Publisher: The American Astronomical Society, page 19. ISSN: 0067-0049. DOI: `10.1088/0067-0049/208/2/19`. URL: `https://dx.doi.org/10.1088/0067-0049/208/2/19` (visited on 09/07/2023) (cited on page 6).

[6] James Imamura. *Planck Era.* en. 2019. URL: `https://pages.uoregon.edu/imamura/123cs/lecture-6/planck.html` (visited on 01/06/2023) (cited on page 6).

[7] Barry Madore, Eric Gawiser, and J Silk. *Extragalactic Articles.* en. 1997. URL: `http://ned.ipac.caltech.edu/level5/index.html` (visited on 11/07/2022) (cited on page 9).

[8] Wayne Hu and Martin White. “The Cosmic Symphony”. In: *Scientific American* 290.2 (Feb. 2004), pages 44–53. ISSN: 0036-8733. DOI: `10.1038/scientificamerican0204-44`. URL: `https://www.scientificamerican.com/article/the-cosmic-symphony` (visited on 02/13/2023) (cited on page 9).

[9] D.J. Eisenstein. *Baryon Acoustic Oscillations*. en. URL: `https://scholar.harvard.edu/deisenstein/book/baryon-acoustic-oscillations` (visited on 01/09/2023) (cited on page 9).

[10] Rafael Guzman. *Observationnal Cosmology*. en. 2016. URL: `https://users.astro.ufl.edu/~guzman/ast6415/` (visited on 11/07/2022) (cited on page 9).

[11] D.J. Eisenstein. “Dark energy and cosmic sound”. en. In: *New Astronomy Reviews* 49.7-9 (Nov. 2005), pages 360–365. ISSN: 13876473. DOI: `10.1016/j.newar.2005.08.005`. URL: `https://linkinghub.elsevier.com/retrieve/pii/S1387647305000850` (visited on 01/09/2023) (cited on page 9).

[12] Planck Collaboration et al. “Planck 2015 results. I. Overview of products and scientific results”. In: *Astronomy & Astrophysics* 594 (Oct. 2016). arXiv:1502.01582 [astro-ph], A1. ISSN: 0004-6361, 1432-0746. DOI: `10.1051/0004-6361/201527101`. URL: `http://arxiv.org/abs/1502.01582` (visited on 01/09/2023) (cited on pages 9, 18, 21).

[13] J. N. Goldberg et al. “Spin- s Spherical Harmonics and ð”. en. In: *Journal of Mathematical Physics* 8.11 (Nov. 1967), pages 2155–2161. ISSN: 0022-2488, 1089-7658. DOI: `10.1063/1.1705135`. URL: `http://aip.scitation.org/doi/10.1063/1.1705135` (visited on 02/13/2023) (cited on page 10).

[14] Martin White. *Cosmic Rosetta Stone*. 1997. URL: `https://w.astro.berkeley.edu/~mwhite/rosetta/` (visited on 02/13/2023) (cited on page 10).

[15] P. D. Naselsky and D. I. Novikov. “General Statistical Properties of the Cosmic Microwave Background Polarization Field”. en. In: *The Astrophysical Journal* 507.1 (Nov. 1998). Publisher: IOP Publishing, page 31. ISSN: 0004-637X. DOI: `10.1086/306294`. URL: `https://iopscience.iop.org/article/10.1086/306294/meta` (visited on 09/17/2023) (cited on page 10).

[16] Matias Zaldarriaga and Uros Seljak. “An All-Sky Analysis of Polarization in the Microwave Background”. In: *Physical Review D* 55.4 (Feb. 1997). arXiv:astro-ph/9609170, pages 1830–1840. ISSN: 0556-2821, 1089-4918. DOI: `10.1103/PhysRevD.55.1830`. URL: `http://arxiv.org/abs/astro-ph/9609170` (visited on 02/09/2023) (cited on pages 10, 22).

[17] Wayne Hu. *CMB Introduction*. en. 2001. URL: `http://background.uchicago.edu/~whu/beginners/introduction.html` (visited on 11/07/2022) (cited on page 10).

[18] Wayne Hu and Martin White. “A CMB Polarization Primer”. In: *New Astronomy* 2.4 (Oct. 1997). arXiv:astro-ph/9706147, pages 323–344. ISSN: 13841076. DOI: `10.1016/S1384-1076(97)00022-5`. URL: `http://arxiv.org/abs/astro-ph/9706147` (visited on 01/11/2023) (cited on page 11).

[19] William R. Coulton, Kazuyuki Akitsu, and Masahiro Takada. *Constraining cosmological vorticity modes with CMB secondary anisotropies.* en. arXiv:2301.11344 [astro-ph]. Jan. 2023. URL: `http://arxiv.org/abs/2301.11344` (visited on 01/30/2023) (cited on page 11).

[20] Uros Seljak and Matias Zaldarriaga. “Signature of Gravity Waves in Polarization of the Microwave Background”. In: *Physical Review Letters* 78.11 (Mar. 1997). arXiv:astro-ph/9609169, pages 2054–2057. ISSN: 0031-9007, 1079-7114. DOI: `10.1103/PhysRevLett.78.2054`. URL: `http://arxiv.org/abs/astro-ph/9609169` (visited on 02/03/2023) (cited on page 12).

[21] Jacques Delabrouille. “Measuring CMB polarisation with the Planck mission”. en. In: *Astrophysics and Space Science* 290.1 (Feb. 2004), pages 87–103. ISSN: 1572-946X. DOI: `10.1023/B:ASTR.0000022166.34602.c7`. URL: `https://doi.org/10.1023/B:ASTR.0000022166.34602.c7` (visited on 02/13/2023) (cited on pages 12, 22).

[22] Edward Collett. *Field guide to polarization.* SPIE field guides v. FG05. OCLC: ocm58456547. Bellingham, Wash: SPIE Press, 2005. ISBN: 978-0-8194-5868-1 (cited on page 12).

[23] Planck Collaboration et al. “Planck 2015 results. XIII. Cosmological parameters”. In: *Astronomy & Astrophysics* 594 (Oct. 2016). arXiv:1502.01589 [astro-ph], A13. ISSN: 0004-6361, 1432-0746. DOI: `10.1051/0004-6361/201525830`. URL: `http://arxiv.org/abs/1502.01589` (visited on 01/09/2023) (cited on page 12).

[24] Planck Collaboration et al. “Planck 2018 results. VI. Cosmological parameters”. In: *Astronomy & Astrophysics* 641 (Sept. 2020). arXiv:1807.06209 [astro-ph], A6. ISSN: 0004-6361, 1432-0746. DOI: `10.1051/0004-6361/201833910`. URL: `http://arxiv.org/abs/1807.06209` (visited on 01/09/2023) (cited on page 12).

[25] Olaf Schmidt, Karl-Heinz Wilms, and Bernd Lingelbach. “The Visby Lenses”. en-US. In: *Optometry and Vision Science* 76.9 (Sept. 1999), page 624. ISSN: 1538-9235. URL: `https://journals.lww.com/optvissci/abstract/1999/09000/the_visby_lenses.19.aspx` (visited on 10/17/2023) (cited on page 14).

[26] J. Enoch. “First known lenses originating in Egypt about 4600 years ago!” eng. In: *Hindsight (Saint Louis, Mo.)* 31.2 (Apr. 2000), pages 9–17. ISSN: 2374-3263 (cited on page 14).

[27] Jay M. Enoch. “History of mirrors dating back 8000 years”. eng. In: *Optometry and Vision Science: Official Publication of the American Academy of Optometry* 83.10 (Oct. 2006), pages 775–781. ISSN: 1040-5488. DOI: `10.1097/01.opx.0000237925.65901.c0` (cited on page 14).

[28] A. Mark Smith. *Ptolemy and the foundations of ancient mathematical optics: a source based guided study.* Transactions of the American Philosophical Society vol. 89, pt. 3. Philadelphia: American Philosophical Society, 1999. ISBN: 978-0-87169-893-3 (cited on page 14).

[29] Harry Edwin Burton. “The Optics of Euclid”. EN. In: *JOSA* 35.5 (May 1945). Publisher: Optica Publishing Group, pages 357–372. DOI: `10.1364/JOSA.35.000357`. URL: `https://opg.optica.org/josa/abstract.cfm?uri=josa-35-5-357` (visited on 10/17/2023) (cited on page 14).

[30] Alhazen and A. I. Sabra. *The Optics of Ibn al-Haytham. Books I-III: On direct vision.* eng. Studies of the Warburg Institute v. 40. OCLC: ocm24910015. London: Warburg Institute, University of London, 1989. ISBN: 978-0-85481-072-7 (cited on page 14).

[31] A. I. Sabra. *The Optics of Ibn al-Haytham. Books IV-V: On Reflection and Images Seen by Reflection.* eng. Edited by Jan P. Hogendijk. Studies of the Warburg Institute v. 40. OCLC: ocm24910015. London: Warburg Institute, University of London, 1989. ISBN: 978-1-908590-58-9 (cited on page 14).

[32] Eric Sidebottom. “Roger Bacon and the beginnings of experimental science in Britain”. In: *Journal of the Royal Society of Medicine* 106.6 (June 2013), pages 243–245. ISSN: 0141-0768. DOI: `10.1177/0141076813488482`. URL: `https://www.ncbi.nlm.nih.gov/pmc/articles/PMC3705416/` (visited on 10/17/2023) (cited on page 14).

[33] René Descartes and Laurence Renault. *Discours de la Méthode.* fre. GF 1091. Paris: Flammarion, 2000. ISBN: 978-2-08-071091-8 (cited on page 14).

[34] Christiaan Huygens. *Traité de la lumière : Où sont expliquées les causes de ce qui lui arrive dans la reflexion, & dans la refraction et particulièrement dans l’étrange réfraction du cristal d’Islande.* en. A Leide: Chez Pierre vander Aa, marchand libraire, 1690. DOI: `10.5479/sil.294285.39088000545160`. URL: `https://library.si.edu/digital-library/book/traiteydelalumi00huyg` (visited on 10/17/2023) (cited on page 14).

[35] Isaac Newton and Duane H. D. Roller. *Opticks: or, a treatise of the reflections, refractions, inflections, & colours of light.* Dover edition, [English edition]. Mineola, New York: Dover Publications, Inc, 2012. ISBN: 978-0-486-60205-9 (cited on page 14).

[36] W. Doberck. “The inventor of the telescope”. In: *The Observatory* 2 (Mar. 1879). ADS Bibcode: 1879Obs.....2..364D, pages 364–370. ISSN: 0029-7704. URL: `https://ui.adsabs.harvard.edu/abs/1879Obs.....2..364D` (visited on 10/17/2023) (cited on page 14).

[37] Galileo Galilei and Carlo Manolessi. *Opere di Galileo Galilei.* Bologna: per gli hh del Dozza, 1655 (cited on page 14).

[38] James R. Voelkel and James Robert Voelkel. *Johannes Kepler and the new astronomy.* eng. Oxford portraits in science. New York: Oxford University Press, 1999. ISBN: 978-0-19-515021-6 978-0-19-511680-9 (cited on pages 14, 15).

[39] James Gregory. *Abdita radiorum reflexorum & refractorum mysteria, geometrice enucleata …* la. Google-Books-ID: W2U_AAAAcAAJ. Thomson, 1663 (cited on pages 14, 15).

[40] André Baranne and Françoise Launay. “Cassegrain: a famous unknown of instrumental astronomy”. In: *Journal of Optics* 28.4 (Aug. 1997), pages 158–172. ISSN: 0150-536X. DOI: `10.1088/0150-536X/28/4/004`. URL: `https://iopscience.iop.org/article/10.1088/0150-536X/28/4/004` (visited on 10/17/2023) (cited on page 14).

[41] Shaul Hanany, Michael D. Niemack, and Lyman Page. “CMB Telescopes and Optical Systems”. en. In: *Planets, Stars and Stellar Systems: Volume 1: Telescopes and Instrumentation*. Edited by Terry D. Oswalt and Ian S. McLean. Dordrecht: Springer Netherlands, 2013, pages 431–480. ISBN: 978-94-007-5621-2. DOI: `10.1007/978-94-007-5621-2_10`. URL: `https://doi.org/10.1007/978-94-007-5621-2_10` (visited on 01/10/2023) (cited on pages 15, 16, 18, 21, 42).

[42] J. A. Bennett. “William Herschel’s Large Twenty-Foot Telescope”. In: *Quarterly Journal of the Royal Astronomical Society* 17 (Sept. 1976). ADS Bibcode: 1976QJRAS..17..303B, page 303. ISSN: 0035-8738. URL: `https://ui.adsabs.harvard.edu/abs/1976QJRAS..17..303B` (visited on 10/17/2023) (cited on page 15).

[43] J. P. C Southall. “The Principles and Methods of Geometrical Optics, especially as Applied to the Theory of Optical Instruments”. en. In: *Nature* 85.2155 (Feb. 1911). Number: 2155 Publisher: Nature Publishing Group, pages 499–500. ISSN: 1476-4687. DOI: `10.1038/085499a0`. URL: `https://www.nature.com/articles/085499a0` (visited on 10/17/2023) (cited on pages 15, 16).

[44] Henri Chrétien. “Le téléscope de Newton et le télescope aplanétique”. In: *Revue d’optique théorique et instrumentale* 2 (1922) (cited on page 15).

[45] Seunghyuk Chang and Aluizio Prata. “Geometrical theory of aberrations near the axis in classical off-axis reflecting telescopes”. EN. In: *JOSA A* 22.11 (Nov. 2005). Publisher: Optica Publishing Group, pages 2454–2464. ISSN: 1520-8532. DOI: `10.1364/JOSAA.22.002454`. URL: `https://opg.optica.org/josaa/abstract.cfm?uri=josaa-22-11-2454` (visited on 10/05/2023) (cited on page 16).

[46] C. Dragone. “Offset multireflector antennas with perfect pattern symmetry and polarization discrimination”. In: *The Bell System Technical Journal* 57.7 (Sept. 1978). Conference Name: The Bell System Technical Journal, pages 2663–2684. ISSN: 0005-8580. DOI: `10.1002/j.1538-7305.1978.tb02171.x`. URL: `https://ieeexplore.ieee.org/document/6773968` (visited on 10/17/2023) (cited on pages 16, 17).

[47] T.-S. Chu. “Polarization properties of offset dual-reflector antennas”. In: *IEEE Transactions on Antennas and Propagation* 39.12 (Dec. 1991). Conference Name: IEEE Transactions on Antennas and Propagation, pages 1753–1756. ISSN: 1558-2221. DOI: `10.1109/8.121596`. URL: `https://ieeexplore.ieee.org/document/121596` (visited on 10/16/2023) (cited on page 16).

[48] S. Chang and A. Prata. “A design procedure for classical offset Dragonian antennas with circular apertures”. In: *IEEE Antennas and Propagation Society International Symposium. 1999 Digest. Held in conjunction with: USNC/URSI National Radio Science Meeting (Cat. No.99CH37010)*. Volume 2. July 1999, 1140–1143 vol.2. DOI: `10.1109/APS.1999.789514`. URL: `https://ieeexplore.ieee.org/document/789514` (visited on 10/17/2023) (cited on page 16).

[49] Y. Mizugutch, M. Akagawa, and H. Yokoi. “Offset dual reflector antenna”. In: *1976 Antennas and Propagation Society International Symposium*. Volume 14. Oct. 1976, pages 2–5. DOI: `10.1109/APS.1976.1147539`. URL: `https://ieeexplore.ieee.org/document/1147539` (visited on 10/17/2023) (cited on page 16).

[50] Shaul Hanany and Daniel P. Marrone. “A comparison of designs of off-axis Gregorian telescopes for mm-wave large focal plane arrays”. In: (June 2002). arXiv:astro-ph/0206211. DOI: `10.48550/arXiv.astro-ph/0206211`. URL: `http://arxiv.org/abs/astro-ph/0206211` (visited on 10/01/2023) (cited on page 16).

[51] Eugene Hecht. *Optics*. eng. 5 ed/fifth edition, global edition. Boston Columbus Indianapolis New York San Francisco Amsterdam Cape Town Dubai London Madrid Milan Munich: Pearson, 2017. ISBN: 978-0-13-397722-6 978-1-292-09693-3 (cited on pages 16, 17).

[52] Michael D. Niemack. “Designs for a large-aperture telescope to map the CMB 10× faster”. EN. In: *Applied Optics* 55.7 (Mar. 2016). Publisher: Optica Publishing Group, pages 1688–1696. ISSN: 2155-3165. DOI: `10.1364/AO.55.001688`. URL: `https://opg.optica.org/ao/abstract.cfm?uri=ao-55-7-1688` (visited on 10/17/2023) (cited on pages 16, 18).

[53] Max Born and Emil Wolf. *Principles of optics*. eng. Seventh anniversary edition, 60th anniversary of first edition, 20th anniversary of seventh edition. Cambridge, United Kingdom: Cambridge University Press, 2019. ISBN: 978-1-108-47743-7 (cited on pages 16, 39, 40).

[54] G. B. Airy. “On the Diffraction of an Object-glass with Circular Aperture”. In: *Transactions of the Cambridge Philosophical Society* 5 (Jan. 1835). ADS Bibcode: 1835TCaPS...5..283A, page 283. URL: `https://ui.adsabs.harvard.edu/abs/1835TCaPS...5..283A` (visited on 10/17/2023) (cited on page 16).

[55] null Rayleigh. “XXXI. Investigations in optics, with special reference to the spectroscope”. In: *The London, Edinburgh, and Dublin Philosophical Magazine and Journal of Science* 8.49 (Oct. 1879). Publisher: Taylor & Francis _eprint: https://doi.org/10.1080/14786447908639684, pages 261–274. ISSN: 1941-5982. DOI: `10.1080/14786447908639684`. URL: `https://doi.org/10.1080/14786447908639684` (visited on 10/17/2023) (cited on page 16).

[56] Bernard Lyot. “The Study of the Solar Corona and Prominences without Eclipses (George Darwin Lecture, delivered by M. Bernard Lyot, Assoc.R.A.S., on 1939 May 12)”. In: *Monthly Notices of the Royal Astronomical Society* 99.8 (June 1939), pages 580–594. ISSN: 0035-8711. DOI: `10.1093/mnras/99.8.580`. URL: `https://doi.org/10.1093/mnras/99.8.580` (visited on 10/16/2023) (cited on page 17).

[57] Kevork N. Abazajian and CMB-S4 Collaboration. *CMB-S4 Science Book, First Edition*. en. Technical report arXiv:1610.02743, FERMILAB-FN-1024-A-AE, 1352047. Oct. 2016, arXiv:1610.02743, FERMILAB–FN–1024–A–AE, 1352047. DOI: `10.2172/1352047`. URL: `http://www.osti.gov/servlets/purl/1352047/` (visited on 02/15/2023) (cited on pages 18, 26).

[58] M. Remazeilles et al. “Exploring cosmic origins with CORE: B-mode component separation”. en. In: *Journal of Cosmology and Astroparticle Physics* 2018.04 (Apr. 2018), page 023. ISSN: 1475-7516. DOI: `10.1088/1475-7516/2018/04/023`. URL: `https://dx.doi.org/10.1088/1475-7516/2018/04/023` (visited on 10/16/2023) (cited on pages 18, 21).

[59] H. Nyquist. “Certain Topics in Telegraph Transmission Theory”. In: *Transactions of the American Institute of Electrical Engineers* 47.2 (Apr. 1928). Conference Name: Transactions of the American Institute of Electrical Engineers, pages 617–644. ISSN: 2330-9431. DOI: `10.1109/T-AIEE.1928.5055024`. URL: `https://ieeexplore.ieee.org/document/5055024` (visited on 10/17/2023) (cited on page 18).

[60] Claude Elwood Shannon and Warren Weaver. *The mathematical theory of communication.* eng. 21. print. Urbana: Univ. of Illinois Press, 1998. ISBN: 978-0-252-72548-7 (cited on page 18).

[61] Bruno Maffei et al. “Planck-HFI focal plane concept”. In: *Optical, Infrared, and Millimeter Space Telescopes.* Volume 5487. SPIE, Oct. 2004, pages 523–531. DOI: `10.1117/12.552577`. URL: `https://www.spiedigitallibrary.org/conference-proceedings-of-spie/5487/0000/Planck-HFI-focal-plane-concept/10.1117/12.552577.full` (visited on 10/16/2023) (cited on pages 18, 29).

[62] Matthew J. Griffin, James J. Bock, and Walter K. Gear. “Relative performance of filled and feedhorn-coupled focal-plane architectures”. EN. In: *Applied Optics* 41.31 (Nov. 2002). Publisher: Optica Publishing Group, pages 6543–6554. ISSN: 2155-3165. DOI: `10.1364/AO.41.006543`. URL: `https://opg.optica.org/ao/abstract.cfm?uri=ao-41-31-6543` (visited on 10/17/2023) (cited on pages 19, 27, 30).

[63] Steven D. Lord. *ATRAN.* 1992. URL: `https://atran.arc.nasa.gov/cgi-bin/atran/atran.cgi` (visited on 01/10/2023) (cited on page 20).

[64] Steven D. Lord. *A new software tool for computing Earth’s atmospheric transmission of near- and far-infrared radiation.* en. Technical report. Number: A-92154. NASA Ames Research Center Moffett Field, CA, United States, Jan. 1992. URL: `https://ntrs.nasa.gov/citations/19930010877` (visited on 01/10/2023) (cited on page 20).

[65] Alexandre E. Adler, Adriaan J. Duivenvoorden, and Jon E. Gudmundsson. *Modelling ground pickup for microwave telescopes.* arXiv:2207.05662 [astro-ph]. July 2022. DOI: `10.48550/arXiv.2207.05662`. URL: `http://arxiv.org/abs/2207.05662` (visited on 10/16/2023) (cited on page 20).

[66] P. A. R. Ade et al. “Bicep2. III. Instrumental Systematics”. en. In: *The Astrophysical Journal* 814.2 (Nov. 2015). Publisher: American Astronomical Society, page 110. ISSN: 0004-637X. DOI: `10.1088/0004-637X/814/2/110`. URL: `https://doi.org/10.1088/0004-637x/814/2/110` (visited on 10/17/2022) (cited on pages 20, 22, 38).

[67] Michael J. Mortonson and Wayne Hu. “Impact of reionization on CMB polarization tests of slow-roll inflation”. In: *Physical Review D* 77.4 (Feb. 2008). arXiv:0710.4162 [astro-ph], page 043506. ISSN: 1550-7998, 1550-2368. DOI: `10.1103/PhysRevD.77.043506`. URL: `http://arxiv.org/abs/0710.4162` (visited on 01/06/2023) (cited on page 20).

[68] G. Pisano et al. “Development of large radii half-wave plates for CMB satellite missions”. In: *Millimeter, Submillimeter, and Far-Infrared Detectors and Instrumentation for Astronomy VII.* Volume 9153. SPIE, July 2014, pages 385–400. DOI: `10.1117/12.2056380`. URL: `https://www.spiedigitallibrary.org/conference-proceedings-of-spie/9153/915317/Development-of-large-radii-half-wave-plates-for-CMB-satellite/10.1117/12.2056380.full` (visited on 10/16/2023) (cited on page 22).

[69] Satoru Takakura et al. “Performance of a continuously rotating half-wave plate on the POLARBEAR telescope”. en. In: *Journal of Cosmology and Astroparticle Physics* 2017.05 (May 2017), page 008. ISSN: 1475-7516. DOI: `10.1088/1475-7516/2017/05/008`. URL: `https://dx.doi.org/10.1088/1475-7516/2017/05/008` (visited on 10/16/2023) (cited on page 22).

[70] Adriaan J Duivenvoorden et al. “Probing frequency-dependent half-wave plate systematics for CMB experiments with full-sky beam convolution simulations”. In: *Monthly Notices of the Royal Astronomical Society* 502.3 (Apr. 2021), pages 4526–4539. ISSN: 0035-8711. DOI: `10.1093/mnras/stab317`. URL: `https://doi.org/10.1093/mnras/stab317` (visited on 01/11/2023) (cited on pages 22, 98).

[71] Ivan L. Padilla et al. “Two-year Cosmology Large Angular Scale Surveyor (CLASS) Observations: A Measurement of Circular Polarization at 40 GHz”. en. In: *The Astrophysical Journal* 889.2 (Jan. 2020). Publisher: The American Astronomical Society, page 105. ISSN: 0004-637X. DOI: `10.3847/1538-4357/ab61f8`. URL: `https://dx.doi.org/10.3847/1538-4357/ab61f8` (visited on 10/16/2023) (cited on page 22).

[72] Adriaan J Duivenvoorden, Jon E Gudmundsson, and Alexandra S Rahlin. “Full-sky beam convolution for cosmic microwave background applications”. In: *Monthly Notices of the Royal Astronomical Society* 486.4 (July 2019), pages 5448–5467. ISSN: 0035-8711. DOI: `10.1093/mnras/stz1143`. URL: `https://doi.org/10.1093/mnras/stz1143` (visited on 10/17/2023) (cited on pages 22, 34, 50).

[73] Giuseppe Puglisi et al. “Simulating Calibration and Beam Systematics for a Future CMB Space Mission with the TOAST Package”. en. In: *Research Notes of the AAS* 5.6 (June 2021). Publisher: The American Astronomical Society, page 137. ISSN: 2515-5172. DOI: `10.3847/2515-5172/ac0823`. URL: `https://dx.doi.org/10.3847/2515-5172/ac0823` (visited on 10/17/2023) (cited on pages 22, 34, 50, 98).

[74] Julien Peloton. *s4cmb*. original-date: 2017-07-02T21:00:50Z. Oct. 2021. URL: `https://github.com/JulienPeloton/s4cmb` (visited on 10/14/2022) (cited on pages 22, 34).

[75] Theodore Kisner. *Time Ordered Astrophysics Scalable Tools*. original-date: 2015-04-09T16:31:29Z. Oct. 2022. URL: `https://github.com/hpc4cmb/toast` (visited on 02/23/2023) (cited on pages 22, 34).

[76] Wayne Hu, Matthew M. Hedman, and Matias Zaldarriaga. "Benchmark parameters for CMB polarization experiments". In: *Physical Review D* 67.4 (Feb. 2003). Publisher: American Physical Society, page 043004. DOI: `10.1103/PhysRevD.67.043004`. URL: `https://link.aps.org/doi/10.1103/PhysRevD.67.043004` (visited on 10/16/2023) (cited on page 22).

[77] M. a. J. Ashdown et al. "Making sky maps from Planck data". en. In: *Astronomy & Astrophysics* 467.2 (May 2007). Number: 2 Publisher: EDP Sciences, pages 761–775. ISSN: 0004-6361, 1432-0746. DOI: `10.1051/0004-6361:20065829`. URL: `https://www.aanda.org/articles/aa/abs/2007/20/aa5829-06/aa5829-06.html` (visited on 02/23/2023) (cited on pages 22, 34).

[78] Ningfeng Zhu et al. "The Simons Observatory Large Aperture Telescope Receiver". en. In: *The Astrophysical Journal Supplement Series* 256.1 (Sept. 2021). Publisher: The American Astronomical Society, page 23. ISSN: 0067-0049. DOI: `10.3847/1538-4365/ac0db7`. URL: `https://dx.doi.org/10.3847/1538-4365/ac0db7` (visited on 02/15/2023) (cited on pages 23, 24, 26).

[79] Aamir M. Ali et al. "Small Aperture Telescopes for the Simons Observatory". en. In: *Journal of Low Temperature Physics* 200.5 (Sept. 2020), pages 461–471. ISSN: 1573-7357. DOI: `10.1007/s10909-020-02430-5`. URL: `https://doi.org/10.1007/s10909-020-02430-5` (visited on 02/15/2023) (cited on pages 23, 24).

[80] L. Montier et al. "Overview of the medium and high frequency telescopes of the LiteBIRD space mission". In: *Space Telescopes and Instrumentation 2020: Optical, Infrared, and Millimeter Wave*. Volume 11443. SPIE, Dec. 2020, pages 451–471. DOI: `10.1117/12.2562243`. URL: `https://www.spiedigitallibrary.org/conference-proceedings-of-spie/11443/114432G/Overview-of-the-medium-and-high-frequency-telescopes-of-the/10.1117/12.2562243.full` (visited on 02/15/2023) (cited on pages 23, 24).

[81] LiteBIRD Collaboration et al. "Probing Cosmic Inflation with the LiteBIRD Cosmic Microwave Background Polarization Survey". In: *Progress of Theoretical and Experimental Physics* (Nov. 2022), ptac150. ISSN: 2050-3911. DOI: `10.1093/ptep/ptac150`. URL: `https://doi.org/10.1093/ptep/ptac150` (visited on 02/15/2023) (cited on pages 23, 24).

[82] Michael Niemack. *Simons Observatory - Noise Calculator*. Aug. 2017. URL: `https://cmb-s4.uchicago.edu/wiki/images/SO_sensitivity_calcs_Niemack_20170825.pdf` (visited on 02/15/2023) (cited on pages 23, 24).

[83] Charles A. Hill et al. "BoloCalc: a sensitivity calculator for the design of Simons Observatory". In: *Millimeter, Submillimeter, and Far-Infrared Detectors and Instrumentation for Astronomy IX*. Volume 10708. SPIE, July 2018, pages 698–718. DOI: `10.1117/12.2313916`. URL: `https://www.spiedigitallibrary.org/conference-proceedings-of-spie/`

`10708/1070842/BoloCalc--a-sensitivity-calculator-for-the-design-of-Simons/10.1117/12.2313916.full` (visited on 02/16/2023) (cited on pages 23, 24).

[84] Nicholas Galitzki et al. "The Simons Observatory: instrument overview". In: *Millimeter, Submillimeter, and Far-Infrared Detectors and Instrumentation for Astronomy IX*. Volume 10708. SPIE, July 2018, page 1070804. DOI: `10.1117/12.2312985`. URL: `https://www.spiedigitallibrary.org/conference-proceedings-of-spie/10708/1070804/The-Simons-Observatory-instrument-overview/10.1117/12.2312985.full` (visited on 02/15/2023) (cited on pages 23, 24, 100).

[85] Peter Ade et al. "The Simons Observatory: science goals and forecasts". en. In: *Journal of Cosmology and Astroparticle Physics* 2019.02 (Feb. 2019), page 056. ISSN: 1475-7516. DOI: `10.1088/1475-7516/2019/02/056`. URL: `https://dx.doi.org/10.1088/1475-7516/2019/02/056` (visited on 02/15/2023) (cited on pages 23, 24).

[86] Matthew Hasselfield. *Simons Observatory - LAT Noise Calculator*. Technical report 181121. S4 Noise Tiger Team, Nov. 2021. URL: `https://cmb-s4.uchicago.edu/wiki/images/Lat-noise-181121.pdf` (visited on 02/15/2023) (cited on pages 23, 24).

[87] T. Matsumura et al. "LiteBIRD: Mission Overview and Focal Plane Layout". en. In: *Journal of Low Temperature Physics* 184.3 (Aug. 2016), pages 824–831. ISSN: 1573-7357. DOI: `10.1007/s10909-016-1542-8`. URL: `https://doi.org/10.1007/s10909-016-1542-8` (visited on 01/10/2023) (cited on pages 23, 24, 29, 31, 100, 106).

[88] A. Suzuki et al. "The LiteBIRD Satellite Mission: Sub-Kelvin Instrument". en. In: *Journal of Low Temperature Physics* 193.5 (Dec. 2018), pages 1048–1056. ISSN: 1573-7357. DOI: `10.1007/s10909-018-1947-7`. URL: `https://doi.org/10.1007/s10909-018-1947-7` (visited on 02/15/2023) (cited on pages 23, 24).

[89] M. Hazumi et al. "LiteBIRD: A Satellite for the Studies of B-Mode Polarization and Inflation from Cosmic Background Radiation Detection". en. In: *Journal of Low Temperature Physics* 194.5 (Mar. 2019), pages 443–452. ISSN: 1573-7357. DOI: `10.1007/s10909-019-02150-5`. URL: `https://doi.org/10.1007/s10909-019-02150-5` (visited on 02/15/2023) (cited on pages 23, 24).

[90] K. D. Irwin. "An application of electrothermal feedback for high resolution cryogenic particle detection". In: *Applied Physics Letters* 66.15 (Apr. 1995), pages 1998–2000. ISSN: 0003-6951. DOI: `10.1063/1.113674`. URL: `https://doi.org/10.1063/1.113674` (visited on 10/16/2023) (cited on page 25).

[91] B. Dober et al. "A microwave SQUID multiplexer optimized for bolometric applications". In: *Applied Physics Letters* 118.6 (Feb. 2021), page 062601. ISSN: 0003-6951. DOI: `10.1063/5.0033416`. URL: `https://doi.org/10.1063/5.0033416` (visited on 10/16/2023) (cited on page 25).

[92] S. Doyle et al. “Lumped Element Kinetic Inductance Detectors”. en. In: *Journal of Low Temperature Physics* 151.1 (Apr. 2008), pages 530–536. ISSN: 1573-7357. DOI: `10.1007/s10909-007-9685-2`. URL: `https://doi.org/10.1007/s10909-007-9685-2` (visited on 03/15/2023) (cited on pages 25, 102).

[93] Peter Barry. “On the development of SuperSpec: a fully integrated on-chip spectrometer for far-infrared astronomy”. en. Thesis. Cardiff University, 2014. URL: `https://orca.cardiff.ac.uk/id/eprint/71562/` (visited on 03/17/2023) (cited on pages 25, 102).

[94] Samuel Rowe. “Passive terahertz imaging with lumped element kinetic inductance detectors”. en. phd. Cardiff University, 2015. URL: `https://orca.cardiff.ac.uk/id/eprint/88242/` (visited on 10/17/2023) (cited on page 25).

[95] Amber Hornsby. “Development of microstrip-coupled Lumped-Element Kinetic Inductance Detectors for astronomy”. en. Thesis. Cardiff University, Nov. 2020. URL: `https://orca.cardiff.ac.uk/140909/` (visited on 11/26/2021) (cited on pages 25, 102, 104).

[96] J. Hubmayr et al. “Low-Temperature Detectors for CMB Imaging Arrays”. en. In: *Journal of Low Temperature Physics* 193.3 (Nov. 2018), pages 633–647. ISSN: 1573-7357. DOI: `10.1007/s10909-018-2029-6`. URL: `https://doi.org/10.1007/s10909-018-2029-6` (visited on 01/10/2023) (cited on page 25).

[97] B. Dober et al. “Optical Demonstration of THz, Dual-Polarization Sensitive Microwave Kinetic Inductance Detectors”. In: *Journal of Low Temperature Physics* 184.1-2 (July 2016). arXiv: 1603.02963, pages 173–179. ISSN: 0022-2291, 1573-7357. DOI: `10.1007/s10909-015-1434-3`. URL: `http://arxiv.org/abs/1603.02963` (visited on 07/28/2020) (cited on page 27).

[98] Justin Lazear et al. “The Primordial Inflation Polarization Explorer (PIPER)”. In: *Millimeter, Submillimeter, and Far-Infrared Detectors and Instrumentation for Astronomy VII*. Volume 9153. SPIE, July 2014, pages 529–539. DOI: `10.1117/12.2056806`. URL: `https://www.spiedigitallibrary.org/conference-proceedings-of-spie/9153/91531L/The-Primordial-Inflation-Polarization-Explorer-PIPER/10.1117/12.2056806.full` (visited on 02/16/2023) (cited on page 27).

[99] Alan Kogut et al. “Polarization properties of a multi-moded feed horn for the Primordial Inflation Explorer mission”. In: *Millimeter, Submillimeter, and Far-Infrared Detectors and Instrumentation for Astronomy VII*. Volume 9153. SPIE, July 2014, pages 401–412. DOI: `10.1117/12.2056873`. URL: `https://www.spiedigitallibrary.org/conference-proceedings-of-spie/9153/915318/Polarization-properties-of-a-multi-moded-feed-horn-for-the/10.1117/12.2056873.full` (visited on 02/16/2023) (cited on page 27).

[100] R. Gualtieri et al. “SPIDER: CMB Polarimetry from the Edge of Space”. en. In: *Journal of Low Temperature Physics* 193.5 (Dec. 2018), pages 1112–1121. ISSN: 1573-7357. DOI: `10.1007/s10909-018-2078-x`. URL: `https://doi.org/10.1007/s10909-018-2078-x` (visited on 02/16/2023) (cited on pages 27, 28).

[101] Ari Cukierman et al. “Hierarchical sinuous-antenna phased array for millimeter wavelengths”. In: *Applied Physics Letters* 112.13 (Mar. 2018), page 132601. ISSN: 0003-6951. DOI: `10.1063/1.5021962`. URL: `https://doi.org/10.1063/1.5021962` (visited on 10/16/2023) (cited on pages 27, 28).

[102] C. L. Kuo et al. “Antenna-coupled TES bolometer arrays for CMB polarimetry”. In: *Millimeter and Submillimeter Detectors and Instrumentation for Astronomy IV*. Volume 7020. SPIE, July 2008, pages 415–428. DOI: `10.1117/12.788588`. URL: `https://www.spiedigitallibrary org/conference-proceedings-of-spie/7020/70201I/Antenna-coupled-TES-bolometer-arrays-for-CMB-polarimetry/10.1117/12.788588.full` (visited on 02/16/2023) (cited on pages 27, 28).

[103] Sara M. Simon et al. “Feedhorn development and scalability for Simons Observatory and beyond”. In: *Millimeter, Submillimeter, and Far-Infrared Detectors and Instrumentation for Astronomy IX*. Volume 10708. SPIE, July 2018, pages 1145–1156. DOI: `10.1117/12.2313405`. URL: `https://www.spiedigitallibrary.org/conference-proceedings-of-spie/10708/107084B/Feedhorn-development-and-scalability-for-Simons-Observatory-and-beyond/10.1117/12.2313405.full` (visited on 10/16/2023) (cited on pages 27, 29, 30).

[104] P. Siritanasak et al. “The Broadband Anti-reflection Coated Extended Hemispherical Silicon Lenses for Polarbear-2 Experiment”. en. In: *Journal of Low Temperature Physics* 184.3 (Aug. 2016), pages 553–558. ISSN: 1573-7357. DOI: `10.1007/s10909-015-1386-7`. URL: `https://doi.org/10.1007/s10909-015-1386-7` (visited on 02/16/2023) (cited on pages 27, 106).

[105] Christopher M. McKenney et al. “Planar silicon metamaterial lenslet arrays for millimeter-wavelength imaging”. In: *Millimeter, Submillimeter, and Far-Infrared Detectors and Instrumentation for Astronomy X*. Volume 11453. SPIE, Dec. 2020, pages 43–58. DOI: `10.1117/12.2565532`. URL: `https://www.spiedigitallibrary.org/conference-proceedings-of-spie/11453/1145306/Planar-silicon-metamaterial-lenslet-arrays-for-millimeter-wavelength-imaging/10.1117/12.2565532.full` (visited on 02/16/2023) (cited on pages 27, 67, 106).

[106] S. Marnieros et al. “TES Bolometer Arrays for the QUBIC B-Mode CMB Experiment”. en. In: *Journal of Low Temperature Physics* 199.3 (May 2020), pages 955–961. ISSN: 1573-7357. DOI: `10.1007/s10909-019-02304-5`. URL: `https://doi.org/10.1007/s10909-019-02304-5` (visited on 10/16/2023) (cited on page 27).

[107] J. Aumont et al. *QUBIC Technical Design Report*. arXiv:1609.04372 [astro-ph]. May 2017. DOI: `10.48550/arXiv.1609.04372`. URL: `http://arxiv.org/abs/1609.04372` (visited on 10/16/2023) (cited on page 27).

[108] R. Adam et al. “The NIKA2 large-field-of-view millimetre continuum camera for the 30 m IRAM telescope”. en. In: *Astronomy & Astrophysics* 609 (Jan. 2018). Publisher: EDP Sciences, A115. ISSN: 0004-6361, 1432-0746. DOI: `10.1051/0004-6361/201731503`. URL:

`https://www.aanda.org/articles/aa/abs/2018/01/aa31503-17/aa31503-17.html` (visited on 10/16/2023) (cited on pages 27, 28).

[109] M. Calvo et al. “The NIKA2 Instrument, A Dual-Band Kilopixel KID Array for Millimetric Astronomy”. en. In: *Journal of Low Temperature Physics* 184.3 (Aug. 2016), pages 816–823. ISSN: 1573-7357. DOI: `10.1007/s10909-016-1582-0`. URL: `https://doi.org/10.1007/s10909-016-1582-0` (visited on 10/16/2023) (cited on page 28).

[110] A. Monfardini et al. “NIKA: A millimeter-wave kinetic inductance camera”. en. In: *Astronomy & Astrophysics* 521 (Oct. 2010). Publisher: EDP Sciences, A29. ISSN: 0004-6361, 1432-0746. DOI: `10.1051/0004-6361/201014727`. URL: `https://www.aanda.org/articles/aa/abs/2010/13/aa14727-10/aa14727-10.html` (visited on 10/17/2023) (cited on page 28).

[111] Rahul Datta et al. *Characterization of Low-noise Backshort-Under-Grid Kilopixel Transition Edge Sensor Arrays for PIPER*. arXiv:2212.01370 [astro-ph]. Dec. 2022. DOI: `10.48550/arXiv.2212.01370`. URL: `http://arxiv.org/abs/2212.01370` (visited on 10/16/2023) (cited on page 27).

[112] Adrian Liu et al. “Precision calibration of radio interferometers using redundant baselines”. In: *Monthly Notices of the Royal Astronomical Society* 408.2 (Oct. 2010), pages 1029–1050. ISSN: 0035-8711. DOI: `10.1111/j.1365-2966.2010.17174.x`. URL: `https://doi.org/10.1111/j.1365-2966.2010.17174.x` (visited on 10/16/2023) (cited on page 27).

[113] Louise Mousset. *Status of QUBIC, the Q&U Bolometric Interferometer for Cosmology*. arXiv:2203.08947 [astro-ph]. Mar. 2022. DOI: `10.48550/arXiv.2203.08947`. URL: `http://arxiv.org/abs/2203.08947` (visited on 10/16/2023) (cited on page 28).

[114] P. A. R. Ade et al. “Bicep2. II. Experiment and 3-year dataset”. en. In: *The Astrophysical Journal* 792.1 (Aug. 2014). Publisher: The American Astronomical Society, page 62. ISSN: 0004-637X. DOI: `10.1088/0004-637X/792/1/62`. URL: `https://dx.doi.org/10.1088/0004-637X/792/1/62` (visited on 10/16/2023) (cited on pages 28, 29).

[115] P. A. R. Ade et al. “Antenna-coupled TES bolometers used in BICEP2, Keck Array and SPIDER”. en. In: *The Astrophysical Journal* 812.2 (Oct. 2015). Publisher: The American Astronomical Society, page 176. ISSN: 0004-637X. DOI: `10.1088/0004-637X/812/2/176`. URL: `https://dx.doi.org/10.1088/0004-637X/812/2/176` (visited on 10/16/2023) (cited on page 29).

[116] James Bock et al. “The Experimental Probe of Inflationary Cosmology (EPIC): A Mission Concept Study for NASA’s Einstein Inflation Probe”. In: *arXiv:0805.4207 [astro-ph]* (May 2008). arXiv: 0805.4207. URL: `http://arxiv.org/abs/0805.4207` (visited on 02/08/2022) (cited on pages 29, 81).

[117] J. Leech et al. “Multiple flare-angle horn feeds for sub-mm astronomy and cosmic microwave background experiments”. en. In: *Astronomy & Astrophysics* 532 (Aug. 2011). Publisher: EDP Sciences, A61. ISSN: 0004-6361, 1432-0746. DOI: `10.1051/0004-6361/201117124`. URL: `https://www.aanda.org/articles/aa/abs/2011/08/aa17124-11/aa17124-11.html` (visited on 10/16/2023) (cited on page 29).

[118] Aamir M. Ali et al. “SiAl alloy feedhorn arrays: material properties, feedhorn design, and astrophysical applications”. In: *Millimeter, Submillimeter, and Far-Infrared Detectors and Instrumentation for Astronomy IX*. Volume 10708. SPIE, July 2018, pages 644–653. DOI: `10.1117/12.2312817`. URL: `https://www.spiedigitallibrary.org/conference-proceedings-of-spie/10708/107082P/SiAl-alloy-feedhorn-arrays--material-properties-feedhorn-design-and/10.1117/12.2312817.full` (visited on 10/16/2023) (cited on page 30).

[119] J. McMahon et al. “Planar Orthomode Transducers for Feedhorn-coupled TES Polarimeters”. In: *AIP Conference Proceedings* 1185.1 (Dec. 2009), pages 490–493. ISSN: 0094-243X. DOI: `10.1063/1.3292386`. URL: `https://doi.org/10.1063/1.3292386` (visited on 10/16/2023) (cited on page 30).

[120] S. Walker et al. “Demonstration of 220/280 GHz Multichroic Feedhorn-Coupled TES Polarimeter”. en. In: *Journal of Low Temperature Physics* 199.3 (May 2020), pages 891–897. ISSN: 1573-7357. DOI: `10.1007/s10909-019-02316-1`. URL: `https://doi.org/10.1007/s10909-019-02316-1` (visited on 10/16/2023) (cited on page 30).

[121] R. J. Thornton et al. “The Atacama Cosmology Telescope: The polarization-sensitive ACTPol instrument”. en. In: *The Astrophysical Journal Supplement Series* 227.2 (Dec. 2016). Publisher: The American Astronomical Society, page 21. ISSN: 0067-0049. DOI: `10.3847/1538-4365/227/2/21`. URL: `https://dx.doi.org/10.3847/1538-4365/227/2/21` (visited on 02/16/2023) (cited on page 30).

[122] J. Hubmayr et al. “Optical Characterization of OMT-Coupled TES Bolometers for LiteBIRD”. en. In: *Journal of Low Temperature Physics* 209.3 (Nov. 2022), pages 396–408. ISSN: 1573-7357. DOI: `10.1007/s10909-022-02808-7`. URL: `https://doi.org/10.1007/s10909-022-02808-7` (visited on 10/16/2023) (cited on page 30).

[123] Joe W. Britton et al. “Corrugated silicon platelet feed horn array for CMB polarimetry at 150 GHz”. In: *Millimeter, Submillimeter, and Far-Infrared Detectors and Instrumentation for Astronomy V*. Volume 7741. SPIE, July 2010, pages 229–239. DOI: `10.1117/12.857701`. URL: `https://www.spiedigitallibrary.org/conference-proceedings-of-spie/7741/77410T/Corrugated-silicon-platelet-feed-horn-array-for-CMB-polarimetry-at/10.1117/12.857701.full` (visited on 10/16/2023) (cited on page 30).

[124] D.F. Filipovic, S.S. Gearhart, and G.M. Rebeiz. “Double-slot antennas on extended hemispherical and elliptical silicon dielectric lenses”. In: *IEEE Transactions on Microwave Theory and Techniques* 41.10 (Oct. 1993). Conference Name: IEEE Transactions on Microwave

Theory and Techniques, pages 1738–1749. ISSN: 1557-9670. DOI: `10.1109/22.247919` (cited on pages 31, 68).

[125] Roger O'Brient et al. "A dual-polarized broadband planar antenna and channelizing filter bank for millimeter wavelengths". In: *Applied Physics Letters* 102.6 (Feb. 2013). Publisher: American Institute of Physics, page 063506. ISSN: 0003-6951. DOI: `10.1063/1.4791692`. URL: `https://aip.scitation.org/doi/10.1063/1.4791692` (visited on 07/08/2022) (cited on pages 31, 107).

[126] B. Westbrook et al. "Development of the Next Generation of Multi-chroic Antenna-Coupled Transition Edge Sensor Detectors for CMB Polarimetry". en. In: *Journal of Low Temperature Physics* 184.1 (July 2016), pages 74–81. ISSN: 1573-7357. DOI: `10.1007/s10909-016-1508-x`. URL: `https://doi.org/10.1007/s10909-016-1508-x` (visited on 10/16/2023) (cited on page 31).

[127] Stephen J. C. Yates et al. "Eliminating stray radiation inside large area imaging arrays". In: *Millimeter, Submillimeter, and Far-Infrared Detectors and Instrumentation for Astronomy IX*. Volume 10708. International Society for Optics and Photonics, July 2018, page 107081X. DOI: `10.1117/12.2315045`. URL: `https://www.spiedigitallibrary.org/conference-proceedings-of-spie/10708/107081X/Eliminating-stray-radiation-inside-large-area-imaging-arrays/10.1117/12.2315045.short` (visited on 11/18/2020) (cited on page 31).

[128] Giampaolo Pisano et al. "Dielectrically embedded flat mesh lens for millimeter waves applications". EN. In: *Applied Optics* 52.11 (Apr. 2013). Publisher: Optical Society of America, pages 2218–2225. ISSN: 2155-3165. DOI: `10.1364/AO.52.002218`. URL: `https://www.osapublishing.org/ao/abstract.cfm?uri=ao-52-11-2218` (visited on 11/30/2021) (cited on pages 32, 67, 71).

[129] Zui Tao et al. "High-Gain and High-Efficiency GRIN Metamaterial Lens Antenna With Uniform Amplitude and Phase Distributions on Aperture". In: *IEEE Transactions on Antennas and Propagation* 66.1 (Jan. 2018), pages 16–22. ISSN: 0018-926X, 1558-2221. DOI: `10.1109/TAP.2017.2767639`. URL: `http://ieeexplore.ieee.org/document/8089424/` (visited on 02/08/2022) (cited on page 32).

[130] I. B. Vendik and O. G. Vendik. "Metamaterials and their application in microwaves: A review". en. In: *Technical Physics* 58.1 (Jan. 2013), pages 1–24. ISSN: 1090-6525. DOI: `10.1134/S1063784213010234`. URL: `https://doi.org/10.1134/S1063784213010234` (visited on 01/03/2023) (cited on page 32).

[131] Willie J. Padilla and Richard D. Averitt. "Imaging with metamaterials". en. In: *Nature Reviews Physics* 4.2 (Feb. 2022). Number: 2 Publisher: Nature Publishing Group, pages 85–100. ISSN: 2522-5820. DOI: `10.1038/s42254-021-00394-3`. URL: `https://www.nature.com/articles/s42254-021-00394-3` (visited on 12/27/2022) (cited on pages 32, 52).

[132] Peter A. R. Ade et al. "A review of metal mesh filters". In: *Millimeter and Submillimeter Detectors and Instrumentation for Astronomy III.* Volume 6275. International Society for Optics and Photonics, June 2006, 62750U. DOI: `10.1117/12.673162`. URL: `https://www.spiedigitallibrary.org/conference-proceedings-of-spie/6275/62750U/A-review-of-metal-mesh-filters/10.1117/12.673162.short` (visited on 04/10/2020) (cited on pages 32, 56, 58, 118).

[133] Giampaolo Pisano et al. "Development of millimetre-wave quasi-optical devices based on the mesh technology". In: *The 8th European Conference on Antennas and Propagation (EuCAP 2014).* ISSN: 2164-3342. Apr. 2014, pages 2402–2406. DOI: `10.1109/EuCAP.2014.6902301` (cited on page 32).

[134] Joseph E. Golec et al. "Design and fabrication of metamaterial anti-reflection coatings for the Simons Observatory". In: *Advances in Optical and Mechanical Technologies for Telescopes and Instrumentation IV.* Volume 11451. SPIE, Dec. 2020, pages 1115–1122. DOI: `10.1117/12.2561720`. URL: `https://www.spiedigitallibrary.org/conference-proceedings-of-spie/11451/114515T/Design-and-fabrication-of-metamaterial-anti-reflection-coatings-for-the/10.1117/12.2561720.full` (visited on 10/17/2023) (cited on page 32).

[135] Jonathan Thompson. "Development of metamaterial lenslet arrays for cosmic microwave background experiments". en. Theses. Cardiff University, Jan. 2021. URL: `https://orca.cardiff.ac.uk/143553/` (visited on 11/26/2021) (cited on pages 32, 52, 67, 71, 73).

[136] N. Farias et al. "Simulated Performance of Laser-Machined Metamaterial Anti-reflection Coatings". en. In: *Journal of Low Temperature Physics* 209.5 (Dec. 2022), pages 1232–1241. ISSN: 1573-7357. DOI: `10.1007/s10909-022-02751-7`. URL: `https://doi.org/10.1007/s10909-022-02751-7` (visited on 10/17/2023) (cited on page 32).

[137] Giampaolo Pisano et al. "Thin flexible multi-octave metamaterial absorber for millimeter wavelengths". EN. In: *Applied Optics* 62.9 (Mar. 2023). Publisher: Optica Publishing Group, pages 2317–2328. ISSN: 2155-3165. DOI: `10.1364/AO.478842`. URL: `https://opg.optica.org/ao/abstract.cfm?uri=ao-62-9-2317` (visited on 10/29/2023) (cited on page 32).

[138] G. Pisano et al. "Planar mesh-lens arrays for millimeter and sub-mm wave focal planes". en. In: *2016 41st International Conference on Infrared, Millimeter, and Terahertz waves (IRMMW-THz).* Copenhagen, Denmark: IEEE, Sept. 2016, pages 1–2. ISBN: 978-1-4673-8485-8. DOI: `10.1109/IRMMW-THz.2016.7758897`. URL: `http://ieeexplore.ieee.org/document/7758897/` (visited on 11/28/2020) (cited on pages 32, 52, 73, 75).

[139] Xavier Dupac and Martin Giard. "Map-making methods for cosmic microwave background experiments". In: *Monthly Notices of the Royal Astronomical Society* 330.3 (Mar. 2002), pages 497–505. ISSN: 0035-8711. DOI: `10.1046/j.1365-8711.2002.05057.x`. URL: `https://doi.org/10.1046/j.1365-8711.2002.05057.x` (visited on 02/17/2023) (cited on page 34).

[140] E. Keihänen, H. Kurki-Suonio, and T. Poutanen. “Madam - a map-making method for CMB experiments”. In: *Monthly Notices of the Royal Astronomical Society* 360.1 (June 2005), pages 390–400. ISSN: 0035-8711. DOI: `10.1111/j.1365-2966.2005.09055.x`. URL: `https://doi.org/10.1111/j.1365-2966.2005.09055.x` (visited on 02/23/2023) (cited on page 34).

[141] S. Mitra et al. “Fast pixel space convolution for CMB surveys with asymmetric beams and complex scan strategies: FEBeCoP”. en. In: *The Astrophysical Journal Supplement Series* 193.1 (Jan. 2011). Publisher: The American Astronomical Society, page 5. ISSN: 0067-0049. DOI: `10.1088/0067-0049/193/1/5`. URL: `https://dx.doi.org/10.1088/0067-0049/193/1/5` (visited on 02/17/2023) (cited on page 34).

[142] Sanjit Mitra, Anand S. Sengupta, and Tarun Souradeep. “CMB power spectrum estimation using noncircular beams”. In: *Physical Review D* 70.10 (Nov. 2004). Publisher: American Physical Society, page 103002. DOI: `10.1103/PhysRevD.70.103002`. URL: `https://link.aps.org/doi/10.1103/PhysRevD.70.103002` (visited on 02/17/2023) (cited on page 34).

[143] Paul F. Goldsmith. *Quasioptical systems: Gaussian beam quasioptical propagation and applications*. IEEE Press/Chapman & Hall Publishers series on microwave technology and RF. Piscataway, NJ: IEEE Press, 1998. ISBN: 978-0-7803-3439-7 (cited on page 35).

[144] J. W. M. Baars et al. “Near-Field Radio Holography of Large Reflector Antennas”. In: *IEEE Antennas and Propagation Magazine* 49.5 (Oct. 2007). Conference Name: IEEE Antennas and Propagation Magazine, pages 24–41. ISSN: 1558-4143. DOI: `10.1109/MAP.2007.4395293`. URL: `https://ieeexplore.ieee.org/document/4395293` (visited on 10/20/2023) (cited on page 36).

[145] Grace E. Chesmore et al. “Simons Observatory: characterizing the Large Aperture Telescope Receiver with radio holography”. EN. In: *Applied Optics* 61.34 (Dec. 2022). Publisher: Optica Publishing Group, pages 10309–10319. ISSN: 2155-3165. DOI: `10.1364/AO.470138`. URL: `https://opg.optica.org/ao/abstract.cfm?uri=ao-61-34-10309` (visited on 10/20/2023) (cited on page 36).

[146] C. Aubry and D. Bitter. “Radiation pattern of a corrugated conical horn in terms of Laguerre-Gaussian functions”. en. In: *Electronics Letters* 11.7 (Apr. 1975). Publisher: IET Digital Library, pages 154–156. ISSN: 1350-911X. DOI: `10.1049/el:19750118`. URL: `https://digital-library.theiet.org/content/journals/10.1049/el_19750118` (visited on 11/26/2021) (cited on page 37).

[147] R. J. Wylde. “Millimetre-wave Gaussian beam-mode optics and corrugated feed horns”. en. In: *IEE Proceedings H (Microwaves, Optics and Antennas)* 131.4 (Aug. 1984). Publisher: IET Digital Library, pages 258–262. ISSN: 2053-7972. DOI: `10.1049/ip-h-1.1984.0053`. URL: `https://digital-library.theiet.org/content/journals/10.1049/ip-h-1.1984.0053` (visited on 09/22/2021) (cited on page 37).

[148] Nialh McCallum, Daniel B. Thomas, and Michael L. Brown. “Fast map-based simulations of systematics in CMB surveys including effects of the scanning strategy”. In: *Monthly Notices of the Royal Astronomical Society* 513.3 (May 2022). arXiv:2109.05038 [astro-ph], pages 3610–3626. ISSN: 0035-8711, 1365-2966. DOI: `10.1093/mnras/stac561`. URL: `http://arxiv.org/abs/2109.05038` (visited on 10/14/2022) (cited on pages 38, 42, 47).

[149] Daniel Baumann et al. “CMBPol Mission Concept Study: Probing Inflation with CMB Polarization”. In: *AIP Conference Proceedings*. arXiv:0811.3919 [astro-ph, physics:gr-qc, physics:hep-ph, physics:hep-th]. 2009, pages 10–120. DOI: `10.1063/1.3160885`. URL: `http://arxiv.org/abs/0811.3919` (visited on 10/14/2022) (cited on page 38).

[150] Meir Shimon et al. “CMB Polarization Systematics Due to Beam Asymmetry: Impact on Inflationary Science”. In: *Physical Review D* 77.8 (Apr. 2008). arXiv:0709.1513 [astro-ph], page 083003. ISSN: 1550-7998, 1550-2368. DOI: `10.1103/PhysRevD.77.083003`. URL: `http://arxiv.org/abs/0709.1513` (visited on 02/09/2023) (cited on page 38).

[151] Peter Hargrave et al. *Review and consolidation of Telescope Instrument Requirements*. Technical Notes TN1. Cardiff University, July 2011 (cited on pages 38, 39, 81).

[152] A. Ludwig. “The definition of cross polarization”. In: *IEEE Transactions on Antennas and Propagation* 21.1 (Jan. 1973). Conference Name: IEEE Transactions on Antennas and Propagation, pages 116–119. ISSN: 1558-2221. DOI: `10.1109/TAP.1973.1140406` (cited on page 39).

[153] A. D. Olver and Institution of Electrical Engineers, editors. *Microwave horns and feeds*. IEE electromagnetic waves series 39. OCLC: ocm31608524. London: IEE, 1994. ISBN: 978-0-85296-809-3 (cited on pages 39, 69).

[154] Maximilian H. Abitbol and CMB-S4. *CMB-S4 Technology Book, First Edition*. en. Technical report arXiv:1706.02464, FERMILAB–FN-1034-AE, 1414402. June 2017, arXiv:1706.02464, FERMILAB–FN–1034–AE, 1414402. DOI: `10.2172/1414402`. URL: `http://www.osti.gov/servlets/purl/1414402/` (visited on 02/15/2023) (cited on page 39).

[155] Virendra N. Mahajan. “Strehl ratio for primary aberrations: some analytical results for circular and annular pupils”. EN. In: *JOSA* 72.9 (Sept. 1982). Publisher: Optica Publishing Group, pages 1258–1266. DOI: `10.1364/JOSA.72.001258`. URL: `https://opg.optica.org/josa/abstract.cfm?uri=josa-72-9-1258` (visited on 10/20/2023) (cited on page 40).

[156] Virendra N. Mahajan. “Strehl ratio for primary aberrations in terms of their aberration variance”. EN. In: *JOSA* 73.6 (June 1983). Publisher: Optica Publishing Group, pages 860–861. DOI: `10.1364/JOSA.73.000860`. URL: `https://opg.optica.org/josa/abstract.cfm?uri=josa-73-6-860` (visited on 10/20/2023) (cited on page 40).

[157] Daniel O’Dea, Anthony Challinor, and Bradley R. Johnson. “Systematic errors in cosmic microwave background polarization measurements”. In: *Monthly Notices of the Royal Astronomical Society* 376.4 (Mar. 2007), pages 1767–1783. ISSN: 0035-8711. DOI: `10.1111/j.`

1365-2966.2007.11558.x. URL: https://doi.org/10.1111/j.1365-2966.2007.11558.x (visited on 02/23/2023) (cited on pages 42, 47).

[158] Eric Hivon, Sylvain Mottet, and Nicolas Ponthieu. “QuickPol: Fast calculation of effective beam matrices for CMB polarization”. en. In: *Astronomy & Astrophysics* 598 (Feb. 2017). Publisher: EDP Sciences, A25. ISSN: 0004-6361, 1432-0746. DOI: 10.1051/0004-6361/201629626. URL: https://www.aanda.org/articles/aa/abs/2017/02/aa29626-16/aa29626-16.html (visited on 02/23/2023) (cited on pages 42, 47).

[159] Christopher G. R. Wallis et al. “Optimal scan strategies for future CMB satellite experiments”. In: *Monthly Notices of the Royal Astronomical Society* 466.1 (Apr. 2017), pages 425–442. ISSN: 0035-8711. DOI: 10.1093/mnras/stw2577. URL: https://doi.org/10.1093/mnras/stw2577 (visited on 02/23/2023) (cited on pages 42, 47).

[160] Nialh McCallum et al. “Spin characterization of systematics in CMB surveys – a comprehensive formalism”. In: *Monthly Notices of the Royal Astronomical Society* 501.1 (Feb. 2021), pages 802–832. ISSN: 0035-8711. DOI: 10.1093/mnras/staa3609. URL: https://doi.org/10.1093/mnras/staa3609 (visited on 02/23/2023) (cited on pages 42, 47).

[161] M. Galloway et al. “BeyondPlanck- VIII. Efficient sidelobe convolution and corrections through spin harmonics”. en. In: *Astronomy & Astrophysics* 675 (July 2023). Publisher: EDP Sciences, A8. ISSN: 0004-6361, 1432-0746. DOI: 10.1051/0004-6361/202243138. URL: https://www.aanda.org/articles/aa/abs/2023/07/aa43138-22/aa43138-22.html (visited on 10/21/2023) (cited on page 42).

[162] T. Hasebe et al. “Sensitivity Modeling for LiteBIRD”. en. In: *Journal of Low Temperature Physics* (Dec. 2022). ISSN: 1573-7357. DOI: 10.1007/s10909-022-02921-7. URL: https://doi.org/10.1007/s10909-022-02921-7 (visited on 02/24/2023) (cited on page 43).

[163] Jeffrey McMahon. *CMB Analysis Summer School*. original-date: 2016-08-20T17:07:38Z. Aug. 2022. URL: https://github.com/jeffmcm1977/CMBAnalysis_SummerSchool (visited on 10/14/2022) (cited on page 44).

[164] Anthony Challinor and Antony Lewis. *CAMB — Code for Anisotropies in the Microwave Background (CAMB)*. 2014. URL: https://camb.info/ (visited on 01/09/2023) (cited on page 44).

[165] Planck Collaboration. *Planck Legacy Archive*. en. 2018. URL: http://pla.esac.esa.int/pla/#home (visited on 01/10/2023) (cited on pages 44, 45).

[166] Wayne Hu. “Weak lensing of the CMB: A harmonic approach”. In: *Physical Review D* 62.4 (July 2000). Publisher: American Physical Society, page 043007. DOI: 10.1103/PhysRevD.62.043007. URL: https://link.aps.org/doi/10.1103/PhysRevD.62.043007 (visited on 02/24/2023) (cited on page 44).

[167] Kendrick M. Smith. “Pseudo-C_ℓ estimators which do not mix E and B modes”. In: *Physical Review D* 74.8 (Oct. 2006). arXiv:astro-ph/0511629, page 083002. ISSN: 1550-7998, 1550-2368. DOI: `10.1103/PhysRevD.74.083002`. URL: `http://arxiv.org/abs/astro-ph/0511629` (visited on 01/13/2023) (cited on page 48).

[168] Viktor G. Veselago. “The electrodynamics of substances with simultaneously negative values of ε and μ”. en. In: *Soviet Physics Uspekhi* 10.4 (Apr. 1968). Publisher: IOP Publishing, page 509. ISSN: 0038-5670. DOI: `10.1070/PU1968v010n04ABEH003699`. URL: `https://iopscience.iop.org/article/10.1070/PU1968v010n04ABEH003699/meta` (visited on 02/27/2023) (cited on page 52).

[169] J. Clerk Maxwell. “A Dynamical Theory of the Electromagnetic Field”. In: *Philosophical Transactions of the Royal Society of London* 155 (1865). Publisher: The Royal Society, pages 459–512. ISSN: 0261-0523. URL: `https://www.jstor.org/stable/108892` (visited on 02/27/2023) (cited on page 52).

[170] S. Ramaseshan. “The centennial of the discovery of millimetre waves by Jagadis Chandra Bose (1858–1937)”. In: *Current Science* 70.2 (1996). Publisher: Temporary Publisher, pages 172–175. ISSN: 0011-3891. URL: `https://www.jstor.org/stable/24096992` (visited on 02/27/2023) (cited on page 52).

[171] W.E. Kock. “Metal-Lens Antennas”. In: *Proceedings of the IRE* 34.11 (Nov. 1946). Conference Name: Proceedings of the IRE, pages 828–836. ISSN: 2162-6634. DOI: `10.1109/JRPROC.1946.232264` (cited on page 52).

[172] J.B. Pendry et al. “Magnetism from conductors and enhanced nonlinear phenomena”. In: *IEEE Transactions on Microwave Theory and Techniques* 47.11 (Nov. 1999). Conference Name: IEEE Transactions on Microwave Theory and Techniques, pages 2075–2084. ISSN: 1557-9670. DOI: `10.1109/22.798002` (cited on pages 52, 56).

[173] J. B. Pendry, D. Schurig, and D. R. Smith. “Controlling Electromagnetic Fields”. In: *Science* 312.5781 (June 2006). Publisher: American Association for the Advancement of Science, pages 1780–1782. DOI: `10.1126/science.1125907`. URL: `https://www.science.org/doi/10.1126/science.1125907` (visited on 02/27/2023) (cited on page 52).

[174] Tolga Ergin et al. “Three-Dimensional Invisibility Cloak at Optical Wavelengths”. In: *Science* 328.5976 (Apr. 2010). Publisher: American Association for the Advancement of Science, pages 337–339. DOI: `10.1126/science.1186351`. URL: `https://www.science.org/doi/10.1126/science.1186351` (visited on 02/27/2023) (cited on page 52).

[175] Oliver Heaviside. *Electrical papers*. eng. 2nd ed. OCLC: 226973918. Providence: AMS Chelsea Publishing, 1892. ISBN: 978-0-8218-3463-3 (cited on page 55).

[176] David M. Pozar. *Microwave engineering*. 4th ed. OCLC: ocn714728044. Hoboken, NJ: Wiley, 2012. ISBN: 978-0-470-63155-3 (cited on page 55).

[177] Sophocles J. Orfanidis. *Electromagnetic waves and antennas*. English. 2d. 2016. URL: `https://www.ece.rutgers.edu/~orfanidi/ewa/` (cited on page 55).

[178] Sergej A. Tretjakov. *Analytical modeling in applied electromagnetics.* eng. Artech House electromagnetic analysis series. Boston, Mass.: Artech House, 2003. ISBN: 978-1-58053-367-6 (cited on page 59).

[179] Roger Petit, editor. *Electromagnetic Theory of Gratings.* Volume 22. Topics in Current Physics. Berlin, Heidelberg: Springer, 1980. ISBN: 978-3-642-81502-7 978-3-642-81500-3. DOI: `10.1007/978-3-642-81500-3`. URL: `http://link.springer.com/10.1007/978-3-642-81500-3` (visited on 10/24/2023) (cited on page 59).

[180] Chao-Chun Chen. “Transmission of Microwave Through Perforated Flat Plates of Finite Thickness”. In: *IEEE Transactions on Microwave Theory and Techniques* 21.1 (Jan. 1973). Conference Name: IEEE Transactions on Microwave Theory and Techniques, pages 1–6. ISSN: 1557-9670. DOI: `10.1109/TMTT.1973.1127906` (cited on page 59).

[181] Nathan Marcuvitz. *Waveguide handbook.* IEE electromagnetic waves series 21. London, UK: P. Peregrinus on behalf of the Institution of Electrical Engineers, 1986. ISBN: 978-0-86341-058-1 (cited on page 59).

[182] Shung-Wu Lee, G. Zarrillo, and Chak-Lam Law. “Simple formulas for transmission through periodic metal grids or plates”. In: *IEEE Transactions on Antennas and Propagation* 30.5 (Sept. 1982). Conference Name: IEEE Transactions on Antennas and Propagation, pages 904–909. ISSN: 1558-2221. DOI: `10.1109/TAP.1982.1142923` (cited on pages 59, 60, 62).

[183] T. Timusk and P. L. Richards. “Near millimeter wave bandpass filters”. EN. In: *Applied Optics* 20.8 (Apr. 1981). Publisher: Optical Society of America, pages 1355–1360. ISSN: 2155-3165. DOI: `10.1364/AO.20.001355`. URL: `https://www.osapublishing.org/ao/abstract.cfm?uri=ao-20-8-1355` (visited on 11/26/2021) (cited on page 59).

[184] R. Ulrich. “Far-infrared properties of metallic mesh and its complementary structure”. en. In: *Infrared Physics* 7.1 (Mar. 1967), pages 37–55. ISSN: 0020-0891. DOI: `10.1016/0020-0891(67)90028-0`. URL: `https://www.sciencedirect.com/science/article/pii/0020089167900280` (visited on 10/17/2022) (cited on pages 59, 65).

[185] T. Tamir and Shuzhang Zhang. “Modal transmission-line theory of multilayered grating structures”. In: *Journal of Lightwave Technology* 14.5 (May 1996). Conference Name: Journal of Lightwave Technology, pages 914–927. ISSN: 1558-2213. DOI: `10.1109/50.495177` (cited on page 65).

[186] R. J. Potton. “Reciprocity in optics”. en. In: *Reports on Progress in Physics* 67.5 (Apr. 2004), page 717. ISSN: 0034-4885. DOI: `10.1088/0034-4885/67/5/R03`. URL: `https://dx.doi.org/10.1088/0034-4885/67/5/R03` (visited on 01/03/2023) (cited on page 67).

[187] J.D. Kraus, M.E. Tiuri, and T.E. Martti. *Radio Astronomy.* McGraw-Hill, 1966. ISBN: 978-0-07-035392-3 (cited on page 67).

[188] P. Moseley. “Novel RF quasi-optical components for THZ astronomy”. eng. Pages: ?-? Publication Title: Doctoral thesis, UCL (University College London). Doctoral. UCL (University College London), July 2015. URL: `https://discovery.ucl.ac.uk/id/eprint/1469687/` (visited on 11/26/2021) (cited on page 67).

[189] Giampaolo Pisano et al. “Development of Flat Silicon-Based Mesh Lens Arrays for Millimeter and Sub-millimeter Wave Astronomy”. en. In: *Journal of Low Temperature Physics* (Jan. 2020). ISSN: 1573-7357. DOI: `10.1007/s10909-019-02327-y`. URL: `https://doi.org/10.1007/s10909-019-02327-y` (visited on 04/10/2020) (cited on pages 67, 75, 76).

[190] A. Suzuki et al. “Multi-Chroic Dual-Polarization Bolometric Detectors for Studies of the Cosmic Microwave Background”. en. In: *Journal of Low Temperature Physics* 176.5 (Sept. 2014), pages 650–656. ISSN: 1573-7357. DOI: `10.1007/s10909-013-1049-5`. URL: `https://doi.org/10.1007/s10909-013-1049-5` (visited on 10/16/2023) (cited on page 68).

[191] Roger OBrient. “A Log-Periodic Focal-Plane Architecture for Cosmic Microwave Background Polarimetry”. en. PhD thesis. UC Berkeley, 2010. URL: `https://escholarship.org/uc/item/8bh7z0pb` (visited on 10/25/2023) (cited on page 68).

[192] J. Zhang et al. “New artificial dielectric metamaterial and its application as a terahertz antireflection coating”. EN. In: *Applied Optics* 48.35 (Dec. 2009). Publisher: Optica Publishing Group, pages 6635–6642. ISSN: 2155-3165. DOI: `10.1364/AO.48.006635`. URL: `https://opg.optica.org/ao/abstract.cfm?uri=ao-48-35-6635` (visited on 10/25/2023) (cited on page 73).

[193] Zeyong Wei et al. “Broadband polarization transformation via enhanced asymmetric transmission through arrays of twisted complementary split-ring resonators”. In: *Applied Physics Letters* 99.22 (Nov. 2011), page 221907. ISSN: 0003-6951. DOI: `10.1063/1.3664774`. URL: `https://doi.org/10.1063/1.3664774` (visited on 10/26/2023) (cited on page 73).

[194] Qiu Wang et al. “A Broadband Metasurface-Based Terahertz Flat-Lens Array”. In: *Advanced Optical Materials* 3.6 (2015). _eprint: https://onlinelibrary.wiley.com/doi/pdf/10.1002/adom.20 pages 779–785. ISSN: 2195-1071. DOI: `10.1002/adom.201400557`. URL: `https://onlinelibrary.wiley.com/doi/abs/10.1002/adom.201400557` (visited on 10/26/2023) (cited on page 73).

[195] Oskar Dahlberg, Guido Valerio, and Oscar Quevedo-Teruel. “Fully Metallic Flat Lens Based on Locally Twist-Symmetric Array of Complementary Split-Ring Resonators”. en. In: *Symmetry* 11.4 (Apr. 2019). Number: 4 Publisher: Multidisciplinary Digital Publishing Institute, page 581. ISSN: 2073-8994. DOI: `10.3390/sym11040581`. URL: `https://www.mdpi.com/2073-8994/11/4/581` (visited on 10/26/2023) (cited on page 73).

[196] Oscar Quevedo-Teruel, Oskar Dahlberg, and Guido Valerio. “Propagation in Waveguides With Transversal Twist-Symmetric Holey Metallic Plates”. In: *IEEE Microwave and Wireless Components Letters* 28.10 (Oct. 2018). Conference Name: IEEE Microwave and Wireless Components Letters, pages 858–860. ISSN: 1558-1764. DOI: `10.1109/LMWC.2018.2863718`. URL: `https://ieeexplore.ieee.org/document/8457218` (visited on 10/26/2023) (cited on page 73).

[197] Randol W. Aikin et al. “Optical performance of the BICEP2 Telescope at the South Pole”. In: *Millimeter, Submillimeter, and Far-Infrared Detectors and Instrumentation for Astronomy V*. Volume 7741. SPIE, July 2010, pages 246–254. DOI: `10.1117/12.857868`. URL: `https://www.spiedigitallibrary.org/conference-proceedings-of-spie/7741/77410V/Optical-performance-of-the-BICEP2-Telescope-at-the-South-Pole/10.1117/12.857868.full` (visited on 12/28/2022) (cited on page 81).

[198] John S. Ward. “Phase Noise Induced by a Vibrating Antenna”. In: *IEEE Transactions on Microwave Theory and Techniques* 65.11 (Nov. 2017). Conference Name: IEEE Transactions on Microwave Theory and Techniques, pages 4148–4153. ISSN: 1557-9670. DOI: `10.1109/TMTT.2017.2699682` (cited on page 89).

[199] C. A. Edwards and H. M. Presby. “Coupling-sensitivity comparison of hemispheric and hyperbolic microlenses”. EN. In: *Applied Optics* 32.9 (Mar. 1993). Publisher: Optica Publishing Group, pages 1573–1577. ISSN: 2155-3165. DOI: `10.1364/AO.32.001573`. URL: `https://opg.optica.org/ao/abstract.cfm?uri=ao-32-9-1573` (visited on 03/29/2023) (cited on page 97).

[200] C. M. Posada et al. “Fabrication of Detector Arrays for the SPT-3G Receiver”. en. In: *Journal of Low Temperature Physics* 193.5 (Dec. 2018), pages 703–711. ISSN: 1573-7357. DOI: `10.1007/s10909-018-1924-1`. URL: `https://doi.org/10.1007/s10909-018-1924-1` (visited on 07/08/2022) (cited on pages 101, 107).

[201] Gethin Robson et al. *The Simulation and Design of an On-Chip Superconducting Millimetre Filter-Bank Spectrometer*. arXiv:2111.04632 [astro-ph, physics:physics]. June 2022. DOI: `10.1007/s10909-022-02747-3`. URL: `http://arxiv.org/abs/2111.04632` (visited on 07/07/2022) (cited on page 101).

[202] Jonas Zmuidzinas. “Superconducting Microresonators: Physics and Applications”. en. In: *Annual Review of Condensed Matter Physics* 3.1 (Mar. 2012), pages 169–214. ISSN: 1947-5454, 1947-5462. DOI: `10.1146/annurev-conmatphys-020911-125022`. URL: `https://www.annualreviews.org/doi/10.1146/annurev-conmatphys-020911-125022` (visited on 03/29/2023) (cited on pages 102, 103).

[203] P. J. de Visser et al. “Fluctuations in the electron system of a superconductor exposed to a photon flux”. en. In: *Nature Communications* 5.1 (Feb. 2014). Number: 1 Publisher: Nature Publishing Group, page 3130. ISSN: 2041-1723. DOI: `10.1038/ncomms4130`. URL: `https://www.nature.com/articles/ncomms4130` (visited on 03/29/2023) (cited on pages 104, 116).

[204] J. M. Lamarre. “Photon noise in photometric instruments at far-infrared and submillimeter wavelengths”. EN. In: *Applied Optics* 25.6 (Mar. 1986). Publisher: Optica Publishing Group, pages 870–876. ISSN: 2155-3165. DOI: `10.1364/AO.25.000870`. URL: `https://opg.optica.org/ao/abstract.cfm?uri=ao-25-6-870` (visited on 03/29/2023) (cited on page 104).

[205] P. S. Barry et al. “Design and Performance of the Antenna-Coupled Lumped-Element Kinetic Inductance Detector”. en. In: *Journal of Low Temperature Physics* 193.3 (Nov. 2018), pages 176–183. ISSN: 1573-7357. DOI: `10.1007/s10909-018-1943-y`. URL: `https://doi.org/10.1007/s10909-018-1943-y` (visited on 11/26/2021) (cited on page 104).

[206] R. Barends et al. “Contribution of dielectrics to frequency and noise of NbTiN superconducting resonators”. In: *Applied Physics Letters* 92.22 (June 2008). Publisher: American Institute of Physics, page 223502. ISSN: 0003-6951. DOI: `10.1063/1.2937837`. URL: `https://aip.scitation.org/doi/10.1063/1.2937837` (visited on 03/24/2023) (cited on pages 104, 111, 116).

[207] G. Deschamps. “Impedance properties of complementary multiterminal planar structures”. In: *IRE Transactions on Antennas and Propagation* 7.5 (Dec. 1959). Conference Name: IRE Transactions on Antennas and Propagation, pages 371–378. ISSN: 1558-3643. DOI: `10.1109/TAP.1959.1144717` (cited on pages 105, 108).

[208] A. J. Anderson et al. “SPT-3G: A Multichroic Receiver for the South Pole Telescope”. en. In: *Journal of Low Temperature Physics* 193.5 (Dec. 2018), pages 1057–1065. ISSN: 1573-7357. DOI: `10.1007/s10909-018-2007-z`. URL: `https://doi.org/10.1007/s10909-018-2007-z` (visited on 02/16/2023) (cited on page 106).

[209] G. Chattopadhyay and J. Zmuidzinas. “A dual-polarized slot antenna for millimeter waves”. In: *IEEE Transactions on Antennas and Propagation* 46.5 (May 1998). Conference Name: IEEE Transactions on Antennas and Propagation, pages 736–737. ISSN: 1558-2221. DOI: `10.1109/8.668920` (cited on page 106).

[210] J. Meinke et al. “Planar Self-similar Antennas for Broadband Millimeter-Wave Measurements”. en. In: *Journal of Low Temperature Physics* 199.1 (Apr. 2020), pages 281–288. ISSN: 1573-7357. DOI: `10.1007/s10909-020-02427-0`. URL: `https://doi.org/10.1007/s10909-020-02427-0` (visited on 07/08/2022) (cited on page 106).

[211] Kamaljeet Singh Saini and Richard F. Bradley. “The sinuous antenna: A dual-polarized element for wideband phased array feed application”. en. In: (Feb. 1996), page 20 (cited on page 106).

[212] R. DuHamel and D. Isbell. “Broadband logarithmically periodic antenna structures”. In: *1958 IRE International Convention Record*. Volume 5. Mar. 1957, pages 119–128. DOI: `10.1109/IRECON.1957.1150566` (cited on page 106).

[213] Francesco Aieta et al. “Aberrations of flat lenses and aplanatic metasurfaces”. EN. In: *Optics Express* 21.25 (Dec. 2013). Publisher: Optica Publishing Group, pages 31530–31539. ISSN: 1094-4087. DOI: `10.1364/OE.21.031530`. URL: `https://opg.optica.org/oe/abstract.cfm?uri=oe-21-25-31530` (visited on 07/08/2022) (cited on page 110).

[214] A. L. Hornsby et al. “Reducing the Susceptibility of Lumped-Element KIDs to Two-Level System Effects”. en. In: *Journal of Low Temperature Physics* 200.5 (Sept. 2020), pages 239–246. ISSN: 1573-7357. DOI: `10.1007/s10909-020-02501-7`. URL: `https://doi.org/10.1007/s10909-020-02501-7` (visited on 03/24/2023) (cited on page 111).

[215] Carole E. Tucker and Peter A. R. Ade. “Thermal filtering for large aperture cryogenic detector arrays”. In: *Millimeter and Submillimeter Detectors and Instrumentation for Astronomy III.* Volume 6275. SPIE, June 2006, pages 239–247. DOI: `10.1117/12.673159`. URL: `https://www.spiedigitallibrary.org/conference-proceedings-of-spie/6275/62750T/Thermal-filtering-for-large-aperture-cryogenic-detector-arrays/10.1117/12.673159.full` (visited on 03/23/2023) (cited on page 118).

[216] Toptica. *TeraScan - Frequency-Domain Terahertz Platform.* en-US. 2001. URL: `https://www.toptica.com/products/terahertz-systems/frequency-domain/terascan` (visited on 03/24/2023) (cited on page 119).

Appendices

A. C_l from Planck 2018

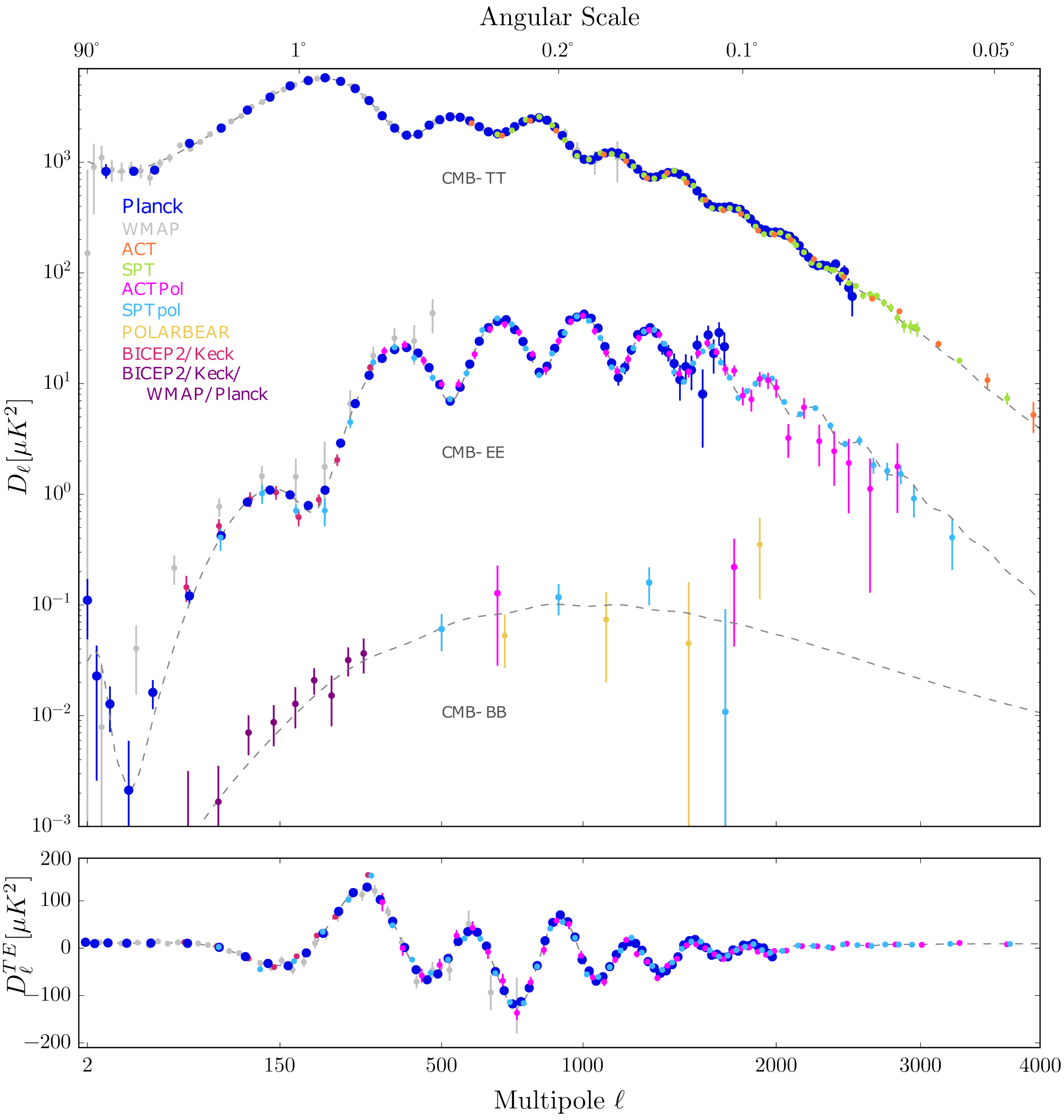

Figure A.1: *$D_\ell^{TT,EE,BB}$, top to bottom, and D_ℓ^{TE}, from the 2018 release of result analysis of the Planck mission.*

B. GBeam Python Class

Here follows a reduced version of the Python code at the base of the LGB decomposition and fitting procedure used to post-process beams simulated in ANSYS-HFSS or measured throughout this work.

```
'''
Created on 20 April 2019

@author: Mr Thomas Gascard

Aim: Give a Laguerre-Gaussian Beam description usable for fitting experimental data or generate a Gaussian beam.

'''
import numpy as np
from scipy import integrate
from scipy.special import laguerre, j0, j1
import scipy.constants as sc
from lmfit import Model

class gBeam():
 """
 .. versionadded:: 1.1

 Give a Laguerre-Gaussian Beam description
 """

 def __init__(self, f, z, w0):
     """
     Initialisation of the gBeam class
```

```
        :param f: Frequency of the beam
        :param z: Distance at which the beam is described from its phase centre, in m
        :param w0: Beam waist, in m
        :type f: float
        :type z: float
        :type w0: float
        :return None

        """
        self.raw = True
        self.f = f
        self.z = z
        self.w0 = w0

    def calculate_fEvars(self, th, p):
        """
        Calculate the characteristics of the beam

        :param th: Angular span of the beam
        :param p: Order of the mode of concern
        :type th: array of floats
        :type p: int
        :return lmb: Wavelength, in m
        :return k: Wave number
        :return w: Beam width, in m
        :return R: Beam radius, in m
        :return r: Array of transversal radii corresponding to the azimutal (theta) range
            at z, in m
        :return u: Transversal diameter fraction
        :return phi0: Phase, in rad
        :return Pn: Laguerre ordinary polynomial of order p function
        :return Lu: Array of Laguerre ordinary polynomial of order p calculated for u
        :rtype lmb: float
        :rtype k: float
        :rtype w: float
        :rtype R: float
        :rtype r: array of floats
        :rtype u: array of floats
        :rtype phi0: float
        :rtype Pn: method
        :rtype Lu: array of floats
```

```
    """
    lmb = sc.c/(self.f*10**9)
    k = 2*np.pi/lmb
    w = self.w0*np.sqrt(1 + (lmb*self.z/(np.pi*(self.w0**2)))**2)
    R = self.z + (1/self.z)*((np.pi*(self.w0**2)/lmb)**2)
    r = R*np.sin(th*np.pi/180.)
    u = (2*r**2/w**2)
    phi0 = np.arctan(lmb*self.z/(np.pi*self.w0**2))
    Pn = laguerre(p)
    Lu = Pn(u)
    th0 = np.arctan(lmb*np.sqrt(2*np.log(2))/(2*np.pi*self.w0))

    return lmb, k, w, R, r, u, phi0, Pn, Lu

def calculate_fEvars_aperture(self, th, w, R, p, hwhm):
    """
    Calculate the characteristics of the beam in the case of a circular aperture

    :param th: Angular span of the beam
    :param w: Beam width, in m
    :param R: Beam radius, in m
    :param p: Order of the mode of concern
    :param hwhm: Beam waist, in m
    :type th: array of floats
    :type w: float
    :type R: float
    :type p: int
    :type hwhm: float
    :return wl: Wavelength, in m
    :return k: Wave number
    :return z: Distance at which the beam is described/observed in m
    :return w0: Beam waist, in m
    :return r: Array of transversal radii corresponding to the azimutal (theta) range
       at z, in m
    :return u: Transversal diameter fraction
    :return phi0: Phase, in rad
    :return Pn: Laguerre ordinary polynomial of order p function
    :return Lu: Array of Laguerre ordinary polynomial of order p calculated for u
    :rtype wl: float
    :rtype k: float
    :rtype w: float
    :rtype R: float
    :rtype r: array of floats
```

```
    :rtype u: array of floats
    :rtype phi0: float
    :rtype Pn: method
    :rtype Lu: array of floats

    """
    wl = sc.c/(self.f*10**9)
    k = 2*np.pi/wl
    z = R/(1 + (wl*R/(np.pi*w**2))**2)
    w0 = hwhm
    r = R*np.sin(th*np.pi/180.)
    u = (2*r**2/w**2)
    phi0 = np.arctan(wl*z/(np.pi*w0**2))
    Pn = laguerre(p)
    Lu = Pn(u)

    return wl, k, z, w0, r, u, phi0, Pn, Lu

def calculate_Ap(self, alpha, Phip):
    """
    Calculate the complex amplitude of the p-th mode in a genrral form

    :param alpha: Maximal amplitude of the p-th mode
    :param Phip: Gouy Phase of the p-th mode, in rad
    :type alpha: float
    :type Phip: float
    :return Ap: Complex amplitude of the p-th mode
    :rtype Ap: complex float

    """
    Ap = alpha*np.exp(-1j*Phip)

    return Ap

def calculate_Ap_aperture(self, th, w, R, alpha, Phip, p):
    """
    Calculate the complex amplitude of the p-th mode in the case of a circular aperture

    :param th: Angular span of the beam
    :param w: Beam width at the distance z, in m
    :param R: Beam radius at the dcistance z, in m
    :param alpha: Maximal amplitude of the p-th mode
    :param Phip: Gouy Phase of the p-th mode, in rad
```

```
    :param p: Order of the mode of concern
    :type th: array of floats
    :type w: float
    :type R: float
    :type alpha: float
    :type Phip: float
    :type p: int
    :return Ap: Complex amplitude of the p-th mode
    :rtype Ap: complex float

    """
    wl = sc.c/(self.f*10**9)
    w0 = w/np.sqrt(1 + (np.pi*w**2/(wl*R))**2)
    z = R / (1+(wl*R/(np.pi*w**2)**2))
    ra_stp = 1/(len(th)-1)
    ra = np.arange(0,1+ra_stp, ra_stp)
    Pn = laguerre(p)
    Lr = Pn(alpha**2*ra**2)
    phi0 = np.arctan(-z*wl/(np.pi*w0**2))
    th_Ap = (2*p+1)*phi0 + Phip
    Ap = (4*alpha)*integrate.trapz(ra*j0(2.4048*ra)*Lr*np.exp(-((alpha*ra)**2)/2), x =
       ra)*np.exp(-1j*th_Ap)

    return Ap

def eGp(self, th, p):
    """
    Calculate the complex LGB field of p-th order, non weighed by diffraction effects

    :param th: Azimutal range, in rad
    :param p: Order of the LGB
    :type alpha: array of floats
    :type Phip: int
    :return eGp: Complex LGB field of the p-th mode
    :rtype eGp: complex float

    """
    fEvars = self.calculate_fEvars(th, p)
    lmb = fEvars[0]
    k = fEvars[1]
    w = fEvars[2]
    R = fEvars[3]
    r = fEvars[4]
```

```
    phi0 = fEvars[6]
    Lu = fEvars[8]
    eGp = np.sqrt(2/(np.pi*(w**2)))*Lu*np.exp(-((r/w)**2) -1j*(np.pi*r**2/(lmb*R) +
        k*self.z - (2*p+1)*phi0))

    return eGp

def eGp_aperture(self, th, w, R, p, hwhm):
    """
    Calculate the complex LGB field of p-th order, non weighed by diffraction effects,
        in the case of a circular aperture model

    :param th: Azimutal range, in rad
    :param w: Beam width, in m
    :param R: Beam radius, in m
    :param p: Order of the mode of concern
    :param hwhm: Beam waist, in m
    :type th: array of floats
    :type w: float
    :type R: float
    :type p: int
    :type hwhm: float
    :return eGp: Complex LGB field of the p-th mode
    :rtype eGp: complex float

    """
    fEvars = self.calculate_fEvars_aperture(th, w, R, p, hwhm)
    wl = fEvars[0]
    z = fEvars[2]
    r = fEvars[4]
    phi0 = fEvars[6]
    Lu = fEvars[8]
    eGp = np.sqrt(2/(np.pi*w**2))*Lu*np.exp(-(r/w)**2 -1j*(np.pi*r**2/(wl*R) -
        (2*p+1)*phi0))

    return eGp

def fEN(self, fEc):
    """
    Calculate the complex LGB field of p-th order

    :param fEc: Complex LGB field
    :type fEc: array of complex floats
```

```
        :return np.real(np.conj(fEc)*fEc): Real LGB field of the input LGB field
        :rtype np.real(np.conj(fEc)*fEc): array of floats

        """
        return np.real(np.conj(fEc)*fEc)

    def eLGp0(self, th, alpha0, Phi0):
        """
        Calculate the complex LGB field of 0-th order, weighed by diffraction effects

        :param th: Azimutal range, in rad
        :param alpha0: Maximal amplitude of the 0-th mode
        :param Phi0: Gouy Phase of the 0-th mode, in rad
        :type th: array of floats
        :type alpha0: float
        :type Phi0: float
        :return eLGp0: Complex LGB field of order 0
        :rtype eLGp0: array of complex floats

        """
        eG0 = self.eGp(th, 0)
        A0 = self.calculate_Ap(alpha0, Phi0)
        eLGp0 = self.fEN(A0*eG0)

        return eLGp0

    def eLGp1(self, th, alpha0, Phi0, alpha1, Phi1):
        """
        Calculate the complex LGB field with mode contributions up to the 1st order, weighed by diffraction effects

        :param th: Azimutal range, in rad
        :param alpha0: Maximal amplitude of the 0-th mode
        :param Phi0: Gouy Phase of the 0-th mode, in rad
        :param alpha1: Maximal amplitude of the 1st mode
        :param Phi1: Gouy Phase of the 1st mode, in rad
        :type th: array of floats
        :type alpha0: float
        :type Phi0: float
        :type alpha1: float
        :type Phi1: float
        :return eLGp1: Complex LGB field of order 1
        :rtype eLGp1: array of complex floats
```

```
        """
        eG0 = self.eGp(th, 0)
        eG1 = self.eGp(th, 1)
        A0 = self.calculate_Ap(alpha0, Phi0)
        A1 = self.calculate_Ap(alpha1, Phi1)
        eLGp0 = A0*eG0
        eLGp1 = A1*eG1
        eLGp1 = self.fEN(eLGp0 + eLGp1)

        return eLGp1

    def eLGp2(self, th, alpha0, Phi0, alpha1, Phi1, alpha2, Phi2):
        """
        As eLGp1, up to the 2d order...

        """
        eG0 = self.eGp(th, 0)
        eG1 = self.eGp(th, 1)
        eG2 = self.eGp(th, 2)
        A0 = self.calculate_Ap(alpha0, Phi0)
        A1 = self.calculate_Ap(alpha1, Phi1)
        A2 = self.calculate_Ap(alpha2, Phi2)
        eLGp0 = A0*eG0
        eLGp1 = A1*eG1
        eLGp2 = A2*eG2
        eLGp2 = self.fEN(eLGp0 + eLGp1 + eLGp2)

        return eLGp2

    def eLGp3(self, th, alpha0, Phi0, alpha1, Phi1, alpha2, Phi2, alpha3, Phi3):
        """
        As eLGp1, up to the 3d order...

        """
        eG0 = self.eGp(th, 0)
        eG1 = self.eGp(th, 1)
        eG2 = self.eGp(th, 2)
        eG3 = self.eGp(th, 3)
        A0 = self.calculate_Ap(alpha0, Phi0)
        A1 = self.calculate_Ap(alpha1, Phi1)
        A2 = self.calculate_Ap(alpha2, Phi2)
        A3 = self.calculate_Ap(alpha3, Phi3)
```

```
    eLGp0 = A0*eG0
    eLGp1 = A1*eG1
    eLGp2 = A2*eG2
    eLGp3 = A3*eG3
    eLGp3 = self.fEN(eLGp0 + eLGp1 + eLGp2 + eLGp3)

    return eLGp3

def eLGp4(self, th, alpha0, Phi0, alpha1, Phi1, alpha2, Phi2, alpha3, Phi3, alpha4,
    Phi4):
    """
    As eLGp1, up to the 4th order...

    """
    eG0 = self.eGp(th, 0)
    eG1 = self.eGp(th, 1)
    eG2 = self.eGp(th, 2)
    eG3 = self.eGp(th, 3)
    eG4 = self.eGp(th, 4)
    A0 = self.calculate_Ap(alpha0, Phi0)
    A1 = self.calculate_Ap(alpha1, Phi1)
    A2 = self.calculate_Ap(alpha2, Phi2)
    A3 = self.calculate_Ap(alpha3, Phi3)
    A4 = self.calculate_Ap(alpha4, Phi4)
    eLGp0 = A0*eG0
    eLGp1 = A1*eG1
    eLGp2 = A2*eG2
    eLGp3 = A3*eG3
    eLGp4 = A4*eG4
    eLGp4 = self.fEN(eLGp0 + eLGp1 + eLGp2 + eLGp3 + eLGp4)

    return eLGp4

def eLGp5(self, th, alpha0, Phi0, alpha1, Phi1, alpha2, Phi2, alpha3, Phi3, alpha4,
    Phi4, alpha5, Phi5):
    """
    As eLGp1, up to the 5th order...

    """
    eG0 = self.eGp(th, 0)
    eG1 = self.eGp(th, 1)
    eG2 = self.eGp(th, 2)
    eG3 = self.eGp(th, 3)
```

```
        eG4 = self.eGp(th, 4)
        eG5 = self.eGp(th, 5)
        A0 = self.calculate_Ap(alpha0, Phi0)
        A1 = self.calculate_Ap(alpha1, Phi1)
        A2 = self.calculate_Ap(alpha2, Phi2)
        A3 = self.calculate_Ap(alpha3, Phi3)
        A4 = self.calculate_Ap(alpha4, Phi4)
        A5 = self.calculate_Ap(alpha5, Phi5)
        eLGp0 = A0*eG0
        eLGp1 = A1*eG1
        eLGp2 = A2*eG2
        eLGp3 = A3*eG3
        eLGp4 = A4*eG4
        eLGp5 = A5*eG5
        eLGp0_sub = self.fEN(eLGp0)
        eLGp1_sub = self.fEN(eLGp1)
        eLGp2_sub = self.fEN(eLGp2)
        eLGp3_sub = self.fEN(eLGp3)
        eLGp4_sub = self.fEN(eLGp4)
        eLGp5_sub = self.fEN(eLGp5)
        eLGp5 = self.fEN(eLGp0 + eLGp1 + eLGp2 + eLGp3 + eLGp4 + eLGp5)

        return eLGp5

    def eLGp5_aperture(self, th, w, R, alpha0, Phi0, alpha1, Phi1, alpha2, Phi2, alpha3,
        Phi3, alpha4, Phi4, alpha5, Phi5):
        """
        As eLGp1, up to the 5th order, considering diffraction effects from a circular
            aperture...

        .. note:: May be extended to higher orders

        """
        hwhm = self.w0
        eG0 = self.eGp_aperture(th, w, R, 0, hwhm)
        eG1 = self.eGp_aperture(th, w, R, 1, hwhm)
        eG2 = self.eGp_aperture(th, w, R, 2, hwhm)
        eG3 = self.eGp_aperture(th, w, R, 3, hwhm)
        eG4 = self.eGp_aperture(th, w, R, 4, hwhm)
        eG5 = self.eGp_aperture(th, w, R, 5, hwhm)
        A0 = self.calculate_Ap_aperture(th, w, R, alpha0, Phi0, 0)
        A1 = self.calculate_Ap_aperture(th, w, R, alpha1, Phi1, 1)
        A2 = self.calculate_Ap_aperture(th, w, R, alpha2, Phi2, 2)
```

```
        A3 = self.calculate_Ap_aperture(th, w, R, alpha3, Phi3, 3)
        A4 = self.calculate_Ap_aperture(th, w, R, alpha4, Phi4, 4)
        A5 = self.calculate_Ap_aperture(th, w, R, alpha5, Phi5, 5)
        eLGp0 = A0*eG0
        eLGp1 = A1*eG1
        eLGp2 = A2*eG2
        eLGp3 = A3*eG3
        eLGp4 = A4*eG4
        eLGp5 = A5*eG5
        eLGp5 = self.fEN(eLGp0 + eLGp1 + eLGp2 + eLGp3 + eLGp4 + eLGp5)

        return eLGp5

    def edge_taper(self, r_a, w):
        """
        Calculate the edge taper of a circular aperture for a beam with a given width

        :param r_a: Aperture radius, in m
        :param w: Beam width, in m
        :type r_a: float
        :type w: float
        :return Te: Edge taper
        :rtype Te: float

        """
        we = w/np.sqrt(2*np.log(2))
        Te = np.exp(-2*((r_a/we)**2))

        return Te

    def edge_taper_from_z(self, r_a, z):
        """
        Calculate the edge taper of a circular aperture for a beam at a given distance z

        :param r_a: Aperture radius, in m
        :param z: Distance from beam phase centre, in m
        :type r_a: float
        :type z: float
        :return Te: Edge taper
        :rtype Te: float

        """
        lmb = sc.c/(self.f*10**9)
```

```
        w = self.w0*np.sqrt(1 + (lmb*z/(np.pi*(self.w0**2)))**2)
        we = w/np.sqrt(2*np.log(2))
        Te = np.exp(-2*((r_a/we)**2))

        return Te, w

    def eGp0N_init(self, th, w, R, hwhm):
        """
        Calculate the real 0th order LGB field, non weighed by diffraction effects

        :param th: Azimutal range, in rad
        :param w: Beam width, in m
        :param R: Beam radius, in m
        :param hwhm: Beam waist, in m
        :type th: array of floats
        :type w: float
        :type R: float
        :type hwhm: float
        :return eGp0N: real 0th order LGB field
        :rtype eGp0N: array of floats

        """
        return self.fEN(self.eGp_aperture(th, w, R, 0, hwhm))

    def lgb0_fit_aperture(self, a, theta_fit, field_to_fit, w, R):
        """
        Example fit of a 0th order LGB field, weighed by diffraction effects from a
            circular aperture

        :param a: Aperture diameter, in m
        :param theta_fit: Azimutal range, in rad
        :param field_to_fit: Beam radius, in m
        :param w: Beam width, in m
        :param R: Beam radius, in m
        :type a: float
        :type theta_fit: array of floats
        :type field_to_fit: array of floats
        :type w: float
        :type R: float
        :return fit0: Fitted real 0th order LGB field
        :return alpha0_fit: Corresponding amplitude of the diffraction field contribution
        :return Phi0_fit: Corresponding gouy phase of the diffraction field contribution
        :return w: Fitted w
```

```
    :return R: Fitted R
    :rtype fit0: array of floats
    :rtype alpha0_fit: float
    :rtype Phi0_fit: float
    :rtype w: float
    :rtype R: float

    .. note:: May be extended to higher orders

    """
    hwhm = self.w0
    modelG0_init = Model(self.eGp0N_init, independent_vars=["th", "hwhm"])
    params0 = modelG0_init.make_params(w = w, R= R)
    params0["w"].set(min=0.0001*a)
    params0["R"].set(min=0.0001*a)
    res0_init = modelG0_init.fit(field_to_fit, params0, th = theta_fit, hwhm = hwhm)
    w = res0_init.best_values["w"]
    R = res0_init.best_values["R"]

    model0 = Model(self.eLGp0_aperture, independent_vars=["th", "w", "R", "hwhm"])
    params0 = model0.make_params(alpha0 = 1, Phi0 = 0)
    res0 = model0.fit(field_to_fit, params0, th = theta_fit, w = w, R = R, hwhm = hwhm)
    rsq0 = 1 - res0.residual.var() / np.var(field_to_fit)
    fit0 = res0.best_fit
    alpha0_fit = res0.best_values["alpha0"]
    Phi0_fit = res0.best_values["Phi0"]

    return fit0, alpha0_fit, Phi0_fit, w, R

def lgb0_fit(self, theta_fit, field_to_fit):
    """
    Example fit of a 0th order LGB field, weighed by diffraction effects

    :param theta_fit: Azimutal range, in rad
    :param field_to_fit: Beam radius, in m
    :type theta_fit: array of floats
    :type field_to_fit: array of floats
    :return fit0: Fitted real 0th order LGB field
    :return alpha0_fit: Corresponding amplitude of the diffraction field contribution
    :return Phi0_fit: Corresponding gouy phase of the diffraction field contribution
    :rtype fit0: array of floats
    :rtype alpha0_fit: float
    :rtype Phi0_fit: float
```

```
    .. note:: May be extended to higher orders

    """
    hwhm = self.w0
    model0 = Model(self.eLGp0, independent_vars=["th"])
    params0 = model0.make_params(alpha0 = 1., Phi0 = 0.)
    res0 = model0.fit(field_to_fit, params0, th = theta_fit)
    rsq0 = 1 - res0.residual.var() / np.var(field_to_fit)
    fit0 = res0.best_fit
    alpha0_fit = res0.best_values["alpha0"]
    Phi0_fit = res0.best_values["Phi0"]

    return fit0, alpha0_fit, Phi0_fit
```

C. PhaseEngin Python Class

Here follows the Python code used to establish a similar approach to the phase engineering design method used to create the MetaL prototype discussed in this work.

```
'''
Created on 27 May 2020

@author: Mr Thomas Gascard

Aim: From an input phase profile and frequency band:
- determine suitable unite-cell size,
- discretise the profile,
- resolve a TL model for each column.

Notes:
'''


### Imports ###
import numpy as np
import cmath
import scipy.constants as sc
from sphinx.util import ws_re
from plotly.subplots import make_subplots
import pandas as pd
from scipy.interpolate import interp1d

### Class Definition ###
class PhaseEngin:
    """
    .. versionadded:: 0.1
```

```
    Provides a set of functions to establish e slice of the lens geometry.

    """

    def __init__(self):

        self.c = sc.c
    #####################

    def find_g(self, bandf, trs_lim, safeg = True):
        """
        Determine the optimal unit-cell size for a given frequency band-stop.

        :param bandf: Frequency band [GHz]
        :param trs_lim: Transmissivity threshold
        :type bandf: numpy array
        :type trs_lim: float
        :return : ?
        :rtype : ?

        .. note::

        """

        valid = True
        i = 0; j = 0
        flim = np.arange(1,10)*bandf[-1] # k = 1,2,3... * banf[-1]
        lmb_lim = sc.c/flim
        g_arr = np.linspace(0.,1.5*lmb_lim)
        while i < len(g_arr) and valid:
            g = g_arr[i]
            a = 0.9*g  # ~ Worst case scenario
            while j < len(flim) and valid:
                [lmb, Z0, DPhi, tau2N] = self.patch_freq_response(bandf, a, g)
                if tau2N >= trs_lim:
                    valid = False
                    print("Unit-cell size found!")
                j = j + 1
            i = i + 1
        if safeg:
            g = 0.8*g
```

```
    return g
####################

def patch_band_response_ulrich(self, bandf, a, g):
    """
    Provides the characteristic impedance, phase shift and transmittnce of a
        geometrically defined patch over a frequency band.

    :param bandf: Frequency band [GHz]
    :param a: Half-gap between patches = k*g, k in [0,1]
    :param g: Unit-cell size [m]
    :type bandf: numpy array
    :type a: float
    :type g: float
    :return z0: Patch iImpedance in Ohm
    :return DPhi: Phase shift operated by the patch
    :return tau2N: Trasmittance of the patch
    :rtype z0: float
    :rtype DPhi: float
    :rtype tau2N: float

    .. note::
    """

    lmb = sc.c/(bandf*10**9)
    kappa0 = 1 - 0.27*(a/g)
    kappa = g/lmb
    omega = (kappa/kappa0) - (kappa0/kappa)

    Z0 = 1/( 2*np.log(1/np.sin(np.pi*a/(2*g))) )
    DPhi = np.pi - np.arctan((Z0*omega))
    tau2N = (Z0*omega)**2/(1+(Z0*omega)**2)

    return kappa, omega, Z0, DPhi, tau2N
####################

def patch_freq_response_ulrich(self, fop, a, g):
    """
    Provides the characteristic impedance, phase shift and transmittance of a
        geometrically defined patch over a frequency band.

    :param fop: Operating frequency [GHz]
    :param a: Half-gap between patches = k*g, k in [0,1]
```

```
    :param g: Unit-cell size [m]
    :type fop: float
    :type a: float
    :type g: float
    :return z0: Patch iImpedance in Ohm
    :return DPhi: Phase shift operated by the patch
    :return tau2N: Trasmittance of the patch
    :rtype z0: float
    :rtype DPhi: float
    :rtype tau2N: float

    .. note::
    """

    lmb = sc.c/(fop*10**9)
    kappa0 = 1 - 0.27*(a/g)
    kappaN = g/lmb
    omega = (kappaN/kappa0) - (kappa0/kappaN)

    Z0 = 1/( 2*np.log(1/np.sin(np.pi*a/(2*g))) )
    DPhi = np.pi - np.arctan((Z0*omega))
    tau2N = (Z0*omega)**2/(1+(Z0*omega)**2)

    return lmb, Z0, DPhi, tau2N
####################

def fss_response_lee(self, fop, a, g, n1, l1, patch = True):
    """
    Provides the characteristic impedance, phase shift and transmittance of a
       geometrically defined patch over a frequency band.

    :param fop: Operating frequency [GHz]
    :param a: Half-gap between patches = k*g, k in [0,1]
    :param g: Unit-cell size [m]
    :param n1: Admittance of the dielectric before the patch, equal to its
       refractive index [None]
    :param l1: Total width of layer(s) prior to the patch
    :param patch: Flag selecting square "patch" or "wire" FSS
    :type fop: float
    :type a: float
    :type g: float
    :type n1: float
    :type l1: float
```

```
    :type patch: boolean
    :return DPhi: Phase shift operated by the patch
    :return tau2N: Trasmittance of the patch
    :return rho2N: Reflectance of the patch
    :return S: Scattering matrix of the patch np.array([S11, S12, S21, S22])
    :rtype DPhi: float
    :rtype tau2N: float
    :rtype rho2N: float
    :rtype S: 2 x 2 np array

    .. note::
    """

    lmb = sc.c/(fop*10**9)/n1
    k = 2*np.pi/lmb
    beta = (1 - 0.41*(a/g))/(g/lmb)
    Z0 = -1j*(beta-(1/beta))*( ((g/(g-(2*a)))+(0.5*(g/lmb)**2))/
        np.log(1/np.sin(np.pi*a/(2*g))) )
    Y0 = 1/Z0
    if not(patch):
        print("Wire !")
        Y0 = Z0
        Z0 = 1/Y0
    tau0 = 1/(1+Y0)
    rho0 = 1-tau0
    tau2N = abs(tau0)
    rho2N = 1-tau2N
    DPhi = np.angle(tau0)
    S = np.array([[tau0*(1-(rho0/tau0)**2) , (rho0/tau0)*np.exp(1j*2*k*l1)],
        [(-rho0/tau0)*np.exp(-1j*2*k*l1), 1/tau0]])
    tau0_S = S[0][0][:] - ((S[0][1][:]*S[1][0][:])/S[1][1][:])
    tau2N_S = abs(tau0_S)
    DPhi_S = np.angle(tau0_S)

    return DPhi, tau2N, rho2N, S
####################

def fss_response_chen(self, fop, a, g, n1, l1, patch = True):
    """
    Provides the characteristic impedance, phase shift and transmittance of a
        geometrically defined patch over a frequency band.

    :param fop: Operating frequency [GHz]
```

```
        :param a: Half-gap between patches = k*g, k in [0,1]
        :param g: Unit-cell size [m]
        :param n1: Admittance of the dielectric before the patch, equal to its
            refractive index [None]
        :param l1: Total width of layer(s) prior to the patch
        :param patch: Flag selecting square "patch" or "wire" FSS
        :type fop: float
        :type a: float
        :type g: float
        :type n1: float
        :type l1: float
        :type patch: boolean
        :return DPhi: Phase shift operated by the patch
        :return tau2N: Trasmittance of the patch
        :return rho2N: Reflectance of the patch
        :return S: Scattering matrix of the patch np.array([S11, S12, S21, S22])
        :rtype DPhi: float
        :rtype tau2N: float
        :rtype rho2N: float
        :rtype S: 2 x 2 np array

        .. note::
        """

        lmb = sc.c/(fop*10**9)/n1
        k = 2*np.pi/lmb
        Z0 = ((-1j)**2) * np.sqrt( ((lmb/g)**2) - 1 ) * ( np.cos(np.pi*(g-(2*a))/g) /
            (1-(2*(g-(2*a))/g)**2) )**2 - \
            ( 1/np.sqrt(((lmb/g)**2)-1) ) * ( np.sin(np.pi*(g-(2*a))/g) /
               (np.pi*(g-(2*a))/g) )**2 + \
            ( np.sqrt((2*(lmb/g)**2)-1) ) - ( 1/np.sqrt((2*(lmb/g)**2)-1) ) * \
            ( ( np.cos(np.pi*(g-(2*a))/g) / (1-(2*(g-(2*a))/g)**2) )**2 ) * ( (
               np.sin(np.pi*(g-(2*a))/g) / (np.pi*(g-(2*a))/g) )**2 )
        Y0 = 1/Z0
        if not(patch):
            print("Wire !")
            Y0 = Z0
            Z0 = 1/Y0
        tau0 = 1/(1+Y0)
        rho0 = 1-tau0
        tau2N = abs(tau0)
        rho2N = 1-tau2N
        DPhi = np.angle(tau0)
```

```
    S = np.array([[tau0*(1-(rho0/tau0)**2) , (rho0/tau0)*np.exp(1j*2*k*l1)],
       [(-rho0/tau0)*np.exp(-1j*2*k*l1), 1/tau0]])
    tau0_S = S[0][0][:] - ((S[0][1][:]*S[1][0][:])/S[1][1][:])
    tau2N_S = abs(tau0_S)
    DPhi_S = np.angle(tau0_S)

    return DPhi, tau2N, rho2N, S
####################

def fss_response_ulrich(self, fop, a, g, n1, l1, patch = True):
    """
    Provides the characteristic impedance, phase shift and transmittance of a
       geometrically defined patch over a frequency band.

    :param fop: Operating frequency [GHz]
    :param a: Half-gap between patches = k*g, k in [0,1]
    :param g: Unit-cell size [m]
    :param n1: Admittance of the dielectric before the patch, equal to its
       refractive index [None]
    :param l1: Total width of layer(s) prior to the patch
    :param patch: Flag selecting square "patch" or "wire" FSS
    :type fop: float
    :type a: float
    :type g: float
    :type n1: float
    :type l1: float
    :type patch: boolean
    :return DPhi: Phase shift operated by the patch
    :return tau2N: Trasmittance of the patch
    :return rho2N: Reflectance of the patch
    :return S: Scattering matrix of the patch np.array([S11, S12, S21, S22])
    :rtype DPhi: float
    :rtype tau2N: float
    :rtype rho2N: float
    :rtype S: 2 x 2 np array

    .. note::
    """

    lmb = sc.c/(fop*10**9)/n1
    k = 2*np.pi/lmb
    beta = (1 - 0.27*(a/g))/(g/lmb)
    Z0 = -1j*(beta-(1/beta))*( 1 / np.log(1/np.sin(np.pi*a/(2*g))) )
```

```
    Y0 = 1/Z0
    if not(patch):
        print("Wire !")
        Y0 = Z0
        Z0 = 1/Y0
    tau0 = 1/(1+Y0)
    rho0 = 1-tau0
    tau2N = abs(tau0)
    rho2N = 1-tau2N
    DPhi = np.angle(tau0)
    S = np.array([[tau0*(1-(rho0/tau0)**2) , (rho0/tau0)*np.exp(1j*2*k*l1)],
        [(-rho0/tau0)*np.exp(-1j*2*k*l1), 1/tau0]])
    tau0_S = S[0][0][:] - ((S[0][1][:]*S[1][0][:])/S[1][1][:])
    tau2N_S = abs(tau0_S)
    DPhi_S = np.angle(tau0_S)

    return DPhi, tau2N, rho2N, S
####################

def diel_response(self, fop, epsr, d, n1, l1):
    """
    Provides the characteristic impedance, phase shift and transmittance of a
        geometrically defined dielectric over a frequency band.

    :param fop: Operating frequency/ies [GHz]
    :param n: dielectric refractive index [None]
    :param d: dielectric thickness [m]
    :param n1: Admittance of the dielectric before the patch, equal to its
        refractive index [None]
    :param l1: Total width of layer(s) prior to the patch
    :type fop: float / array of floats
    :type n: float
    :type d: float
    :type n1: float
    :type l1: float
    :return gamma: Phase shift operated by the dielectric
    :return tau2N: Trasmittance of the dielectric
    :return rho2N: Reflectance of the dielectric
    :return S: Scattering matrix of the patch np.array([S11, S12, S21, S22])
    :rtype gamma: float
    :rtype tau2N: float
    :rtype rho2N: float
    :rtype S: 2 x 2 np array
```

```
    .. note::
    """

    lmb = sc.c/(fop*10**9)/n1
    k = 2*np.pi/lmb
    kp = k*np.sqrt(epsr)
    r = (1-np.sqrt(epsr))/(1+np.sqrt(epsr))
    tau0 = np.exp(1j*(k-kp)*d) * (1 - r**2)/(1 - (np.exp(-1j*2*kp*d)*r**2))
    rho0 = np.exp(1j*k*d) * r*(1 - (np.exp(-1j*2*kp*d)))/(1 -
        (np.exp(-1j*2*kp*d)*r**2))
    tau2N = abs(tau0)
    rho2N = 1- tau2N
    DPhi = np.angle(tau0)
    S = np.array([[tau0*(1-(rho0/tau0)**2) , (rho0/tau0)*np.exp(1j*2*k*l1)],
        [(-rho0/tau0)*np.exp(-1j*2*k*l1), 1/tau0]])

    return DPhi, tau2N, rho2N, S

def rought_estimate_n(self,rho2N):
    """
    Estimates the refractive index of an element (FSS), assuming permeability of 1.
    :param rho2N: Reflection coeffcicient of the element of concern
    :type: float
    :return n: Refractive index of the element
    :rtype n: float

    .. note::
    """

    n = (rho2N-1)/(1+rho2N)

    return n
####################

def make_column(self, patch, g, f_lim, fop, l_out, n_out, l_diel, n_diel, DPhi_obj,
    DPhi_delta, N_lim, tau_lim):
    """
    Generate a column of patches to reach the desired phase shift

    :param patch: Flag selecting "square" patch or "wire" FSS
    :param g: Unit-cell size [m]
    :param f_lim: Frequency limit [GHz]
```

```
        :param fop: Frequency band [GHz]
        :param l_out: thickness of the top and bottom layer surrounding the column [m]
        :param n_out: refractive index of the layer surrounding the column
        :param l_diel: thickness of the dielectric embedding the column [m]
        :param n_diel: refrective index of the dielectric embedding the column
        :param DPhi_obj: Desired Phase shift [rad]
        :param DPhi_delta: Desired Phase shift error [rad]
        :param N_lim: Max # of layers, starting from layer 0
        :param tau_lim: transmission lower limit
        :type patch: boolean
        :type g: float
        :type f_lim: float
        :type fop: numpy array of floats
        :type l_out: float
        :type n_out: float
        :type l_diel: float
        :type n_diel: float
        :type DPhi_obj: float
        :type DPhi_delta: float
        :type Nlim: int
        :type tau_lim: float
        :return aN: Array of patch sizes
        :return DPhi: Phase shift operated by the column
        :return tau2N: Trasmittance of the column
        :rtype aN: np array of floats
        :rtype DPhi: float
        :rtype tau2N: float

        .. note::
        """
        N = 0; valid = False; flag_break = False
        DPhi = 0.; tau2N = 1.
        a = np.linspace(1/100,1-1/100,99)*g
        a = a[::-1]
        a = np.atleast_3d(a)[0]
        aN = np.array([])
        n1 = n_out; l1 = 0.
        S_N = np.ones((2,2, len(a), len(fop)))
        S_N[0,1] = np.zeros(len(fop))
        S_N[1,0] = np.zeros(len(fop))
        S_diel = np.ones((2,2, len(a), len(fop)))
        S_diel[0,1] = np.zeros(len(fop))
        S_diel[1,0] = np.zeros(len(fop))
```

```
while N <= N_lim and not(valid) and not(flag_break):
    if N > 0:
        n1 = n_diel
        l1 = l1 + l_diel
        S_N = np.repeat(S_N[:, :, np.newaxis], len(a), axis=2)
    [DPhi_a, tau2N_a, rho2N_a, S_a] = self.fss_response_lee(fop, a, g, n1, l1,
        patch)
    if n_diel == 1.:
        S_Na = np.einsum(’mnop,nqop->mqop’, S_a, S_N)
    else:
        print("Dielectric-Embedded!")
        [DPhi_diel, tau2N_diel, rho2N_diel, S_diel] = self.diel_response(fop,
            n_diel**2, l_diel, n_diel, l1)
        S_diel = np.repeat(S_diel[:, :, np.newaxis], len(a), axis=2)
        S_Na = np.einsum(’mnop,nqop->mqop’, np.einsum(’mnop,nqop->mqop’, S_a,
            S_diel), S_N)
    tau0 = S_Na[0,0] - ((S_Na[0,1]*S_Na[1,0])/S_Na[1,1])
    tau2N = abs(tau0)
    tau2N_sub = tau2N[:,:int(f_lim)]
    tau2N_test = tau2N_sub[np.where((tau2N_sub > tau_lim).all(axis = 1))] # axis
        = 1
    DPhi = np.angle(tau0)
    DPhi = np.unwrap(DPhi, axis=0)
    DPhi_sub = DPhi[:,:int(f_lim)]
    DPhi_test = DPhi_sub[np.where((tau2N_sub > tau_lim).all(axis = 1))] # axis = 1
    if len(tau2N_test) == 0 or len(DPhi_test) == 0:
        flag_break = True
        print("tau limit too hard! Try reducing it, or the unit-cell size or the
            dielectric thickness...")

    test = np.logical_and( np.logical_and( abs(DPhi_test[:,-1]) <= abs(DPhi_obj)
        + DPhi_delta, abs(DPhi_test[:,-1]) >= abs(DPhi_obj) - DPhi_delta) ,
        tau2N_test[:,-1] >= tau_lim )
    idx_res = np.where(test)[0]
    a_res = a[idx_res]
    if not(flag_break):
        if not(a_res.size == 0):
            DPhi_print = DPhi[idx_res[0],int(f_lim)]
            tau2N_print = tau2N[idx_res[0],int(f_lim)]
            print("N = " + str(N) + ", a/g = " +
                str(np.format_float_positional(100*a_res[0]/g, precision = 2)) +
                "%, DPhi = " + str(np.format_float_positional(DPhi_print,
                precision = 3)) + ", tau2N = " +
```

```
                    str(np.format_float_positional(tau2N_print, precision = 3)))
                aN = np.append(aN,a_res[0])
                S_N = S_Na[:,:,idx_res[0]]
                valid = True
                print("Sucess!")
            else:
                test = (DPhi_test == DPhi_test.min()).any(axis = 1)
                idx_res = np.where(test)[0]
                DPhi_print = DPhi[idx_res[0],int(f_lim)]
                tau2N_print = tau2N[idx_res[0],int(f_lim)]
                a_res = a[idx_res]
                print("N = " + str(N) + ", a/g = " +
                    str(np.format_float_positional(100*a_res[0]/g, precision = 2)) +
                    "%, DPhi = " + str(np.format_float_positional(DPhi_print,
                    precision = 3)) + ", tau2N = " +
                    str(np.format_float_positional(tau2N_print, precision = 3)))
                aN = np.append(aN,a_res[0])
                S_N = S_Na[:,:,idx_res[0]]
                print("Defeat...")

            N = N + 1

    return aN, DPhi, tau2N
####################

def make_column_custom(self, patch, a, g, fop, n_init, l_init, l_diel, n_diel,
    N_lim):
    """
    Generate a column of patches to reach the desired phase shift

    :param patch: Flag selecting "square" patch or "wire" FSSs
    :param g: Unit-cell size [m]
    :param f_lim: Frequency limit [GHz]
    :param fop: Frequency band [GHz]
    :param l_init: thickness of the top and bottom layer surrounding the column [m]
    :param n_init: refractive index of the top and bottom layer surrounding the
        column
    :param l_diel: thickness of the dielectric embedding the column [m]
    :param n_diel: refractive index of the dielectric embedding the column
    :param DPhi_obj: Desired Phase shift [rad]
    :param DPhi_delta: Desired Phase shift error [rad]
    :param N_lim: Max # of layers, starting from layer 0
    :param tau_lim: transmission lower limit
```

```
        :type patch: boolean
        :type g: float
        :type f_lim: float
        :type fop: numpy array of floats
        :type l_out: float
        :type n_out: float
        :type l_diel: float
        :type n_diel: float
        :type DPhi_obj: float
        :type DPhi_delta: float
        :type Nlim: int
        :type tau_lim: float
        :return aN: Array of patch sizes
        :return DPhi: Phase shift operated by the column
        :return tau2N: Trasmittance of the column
        :rtype aN: np array of floats
        :rtype DPhi: float
        :rtype tau2N: float

        .. note::
        """
        N = 0
        l_diel = l_diel/2 # centering
        DPhi = 0.; tau2N = 1.
        n1 = n_init; l1 = 0.
        S_N = np.ones((2,2, len(fop)))
        S_N[0,1] = np.zeros(len(fop))
        S_N[1,0] = np.zeros(len(fop))
        S_diel = np.ones((2,2, len(fop)))
        S_diel[0,1] = np.zeros(len(fop))
        S_diel[1,0] = np.zeros(len(fop))

        while N <= N_lim: # + 1
            if N == 0:
                [DPhi_diel, tau2N_diel, rho2N_diel, S_diel] = self.diel_response(fop,
                    n_init**2, l_init*0.01, n_init, l_init)
                S_N = np.einsum('mno,nqo->mqo', S_diel, S_N)
                l1 = l1 + l_init
                DPhi += DPhi_diel
            if N > 0 and N <= N_lim:
                n1 = n_diel
                l1 = l1 + l_diel
                [DPhi_a, tau2N_a, rho2N_a, S_a] = self.fss_response_lee(fop, a, g, n1,
```

```
                l1, patch)
            DPhi += DPhi_a

            if n_diel == 1.:
                S_N = np.einsum('mno,nqo->mqo', S_a, S_N)
            else:
                [DPhi_diel, tau2N_diel, rho2N_diel, S_diel] = self.diel_response(fop,
                    n1**2, l_diel, n_diel, l1)
                S_N = np.einsum('mno,nqo->mqo', np.einsum('mno,nqo->mqo', S_diel,
                    S_a), S_N)
                DPhi += DPhi_diel

        N = N + 1

    tau0 = S_N[0,0] - ((S_N[0,1]*S_N[1,0])/S_N[1,1])
    rho0 = - (S_N[1,0]/S_N[1,1])
    tau2N = abs(tau0)
    rho2N = 1 - tau2N

    return DPhi, tau2N, rho2N
####################

def make_column_custom_filter(self, patches, a_s, g, fop, n_init, l_init, l_diel_s,
    n_diel_s, N_lim):
    """
    Generate a column of patches to reach the desired phase shift

    :param patch: Flag selecting "square" patch or "wire" FSSs
    :param g: Unit-cell size [m]
    :param f_lim: Frequency limit [GHz]
    :param fop: Frequency band [GHz]
    :param l_init: thickness of the top and bottom layer surrounding the column [m]
    :param n_init: refractive index of the top and bottom layer surrounding the
        column
    :param l_diel: thickness of the dielectric embedding the column [m]
    :param n_diel: refractive index of the dielectric embedding the column
    :param DPhi_obj: Desired Phase shift [rad]
    :param DPhi_delta: Desired Phase shift error [rad]
    :param N_lim: Max # of layers, starting from layer 0
    :param tau_lim: transmission lower limit
    :type patch: boolean
    :type g: float
    :type f_lim: float
```

```
    :type fop: numpy array of floats
    :type l_out: float
    :type n_out: float
    :type l_diel: float
    :type n_diel: float
    :type DPhi_obj: float
    :type DPhi_delta: float
    :type Nlim: int
    :type tau_lim: float
    :return aN: Array of patch sizes
    :return DPhi: Phase shift operated by the column
    :return tau2N: Trasmittance of the column
    :rtype aN: np array of floats
    :rtype DPhi: float
    :rtype tau2N: float

    .. note::
    """
    N = 0
    DPhi = 0.; tau2N = 1.
    n1 = n_init; l1 = 0.
    S_N = np.ones((2,2, len(fop)))
    S_N[0,1] = np.zeros(len(fop))
    S_N[1,0] = np.zeros(len(fop))
    S_diel = np.ones((2,2, len(fop)))
    S_diel[0,1] = np.zeros(len(fop))
    S_diel[1,0] = np.zeros(len(fop))

    while N <= N_lim: # + 1
        if N == 0:
            [DPhi_diel, tau2N_diel, rho2N_diel, S_diel] = self.diel_response(fop,
                n_init**2, l_init*0.01, n_init, l_init)
            S_N = np.einsum('mno,nqo->mqo', S_diel, S_N)
            l1 = l1 + l_init
            DPhi += DPhi_diel
        if N > 0 and N <= N_lim:
            n1 = n_diel_s[N-1]
            a = a_s[N-1]
            patch = patches[N-1]
            l1 = l1 + l_diel_s[N-1]
            [DPhi_a, tau2N_a, rho2N_a, S_a] = self.fss_response_lee(fop, a, g, n1,
                l1, patch)
            DPhi += DPhi_a
```

```
                [DPhi_diel, tau2N_diel, rho2N_diel, S_diel] = self.diel_response(fop,
                    n1**2, l_diel_s[N-1], n_diel_s[N-1], l1)
                S_N = np.einsum('mno,nqo->mqo', np.einsum('mno,nqo->mqo', S_diel, S_a),
                    S_N)
                DPhi += DPhi_diel

            N = N + 1

        tau0 = S_N[0,0] - ((S_N[0,1]*S_N[1,0])/S_N[1,1])
        rho0 = - (S_N[1,0]/S_N[1,1])
        tau2N = abs(tau0)
        rho2N = 1 - tau2N
        DPhi = np.angle(tau0)

        return DPhi, tau2N, rho2N
    ####################

    def build_DPhi_req(self, fop, fmin, fmax, fc, DPhimin, DPhimax, DPhic):
        F = np.array([0., fmin, fc,fmax])
        DPHI = np.array([0., DPhimin, DPhic, DPhimax])

        DPhi_interp = interp1d(F, DPHI)
        DPhi_req = DPhi_interp(fop)

        return DPhi_req

    def optimise_column_filter(self, fop, g, a_min, a_max, a_step, epsr_wafer,
        thk_wafer, n_init, l_init, N_lim, DPhi_req, delta_DPhi_req, tau_threshold):
        patches = np.ones(N_lim, dtype = bool)
        l_diel_s = np.ones(N_lim)*thk_wafer
        n_diel_s = np.ones(N_lim)*np.sqrt(epsr_wafer)
        a_k = np.arange(a_min, a_max, a_step)
        a_s = np.zeros(N_lim)
        a_f = np.zeros(N_lim)
        DPhi_flag = False
        N = 1
        df = pd.DataFrame()
        while N <= N_lim and not(DPhi_flag):
            df_tau = pd.DataFrame()
            df_tau_new = pd.DataFrame()
            print("# of layers = " + str(N))
            for a in a_k:
                if not(DPhi_flag):
```

```
                a_s = a_f
                a_s[N-1] = a
                DPhi, tau2N, rho2N = self.make_column_custom_filter(patches, a_s, g,
                    fop, n_init, l_init, l_diel_s, n_diel_s, N)
                DPhi_check = np.unwrap(DPhi, axis = 0)*(180/np.pi)
                df_i = pd.DataFrame(
                            np.array([np.ones(len(fop))*N, np.ones(len(fop))*a, fop,
                                DPhi, DPhi_check, tau2N]).T,
                            columns = ["N", "a", "f", "dphi", "dphi_cangdeg", "tau"]
                            )
                df_i = df_i[df_i["tau"] >= tau_threshold]
                if len(df_i[df_i["tau"] >= tau_threshold]["f"]) == len(fop):
                    if np.all(np.less(df_i["dphi_cangdeg"].values,
                        DPhi_req+delta_DPhi_req)) and
                        np.all(np.greater(df_i["dphi_cangdeg"].values,
                        DPhi_req-delta_DPhi_req)):
                        print("Success!")
                        DPhi_flag = True
                        df = pd.concat([df, df_i])
                        a_f[N-1] = df_i["a"].unique()
                    else:
                        df_tau = pd.concat([df_tau, df_i])
        if df_tau.empty and not(DPhi_flag):
            print("Oh no...")
            N = N + 1
        else:
            if not(DPhi_flag):
                if N == N_lim: print("Failed...")
                else: print("Failed. Moving to next layer")
                df_tau_new = df_tau[df_tau["a"] == df_tau["a"].unique()[-1]]
                print(df_tau_new["a"].unique())
                a_f[N-1] = df_tau_new["a"].unique()
                df = pd.concat([df, df_tau_new])
                N = N + 1
    return df, df_tau, df_tau_new, a_f
```